STRUCTURAL STUDIES OF ALPHA-AMYLASE INHIBITION

by

Leslie Karen Williams

B.Sc., The University of British Columbia, 2007
M.A., The University of Toronto, 1997
B.A., The University of British Columbia, 1996

A THESIS SUBMITTED IN PARTIAL FULFILLMENT OF
THE REQUIREMENTS FOR THE DEGREE OF

DOCTOR OF PHILOSOPHY

in

The Faculty of Graduate and Postdoctoral Studies

(Biochemistry and Molecular Biology)

THE UNIVERSITY OF BRITISH COLUMBIA

(Vancouver)

June 2014

Abstract

The increasing prevalence of type 2 diabetes has stimulated research aimed at discovering new drugs to treat the condition. Human Pancreatic α-Amylase (HPA) is responsible for cleaving starch into the smaller oligosaccharides that then become the substrates for the intestinal disaccharidases that hydrolyze them into glucose. Inhibition of HPA activity correlates to a reduction in postprandial blood glucose levels. This thesis uses x-ray crystallography to characterize the binding interactions between α-amylases and several newly discovered inhibitors that have potential therapeutic value, as well as one compound, voglibose, currently in clinical use.

Voglibose is an excellent inhibitor of the intestinal disaccharidases, but a poor inhibitor of α-amylase. The HPA-voglibose complex is the first structure of voglibose with any α-glucosidase, and reveals a surprising binding mode for this inhibitor.

Montbretin A is a glycosylated acyl flavonol that inhibits HPA with a K_i of 8 nM. This inhibitor exhibits a unique binding mode that allows it to fill the volume of the active site cleft near the enzyme's three catalytic carboxylates. Two montbretin A fragments, myricetin and ethyl caffeate,

also inhibit HPA with K_i values of 100 μM and 1.3 mM, and the crystal structures of their complexes with HPA were also solved. These two inhibitors impede enzyme activity through opposite mechanisms: myricetin blocks the active site, aided by increased order in an active site loop, and ethyl caffeate increases disorder in four loops that form part of the substrate binding cleft. The HPA-ethyl caffeate complex structure is also the first of HPA bound to a noncompetitive inhibitor.

Amystatin is a 44 amino acid peptide that exhibits nanomolar inhibition of HPA. The crystal structure of the porcine pancreatic α-amylase-amystatin complex, reveals that this peptide represents a brand new class of HPA inhibitor.

Preface

Portions of chapter 3 have been published as,

> Williams, L.K., Li, C., Withers, S.G. and Brayer, G.D. (2012). Order and Disorder: Differential Structural Impacts of Myricetin and Ethyl Caffeate on Human Amylase, an Antidiabetic Target. J. Med. Chem. 55, 10177-10186 (*1*).

I isolated, purified and crystallized the protein used, collected the diffraction data, and performed all of the structural determination and analysis. I also wrote most of the manuscript, with revisions by Prof. Gary Brayer. I performed the crystal-inhibitor soaks with help from Dr. Chunmin Li. The research that identified myricetin and ethyl caffeate as valuable structural targets was performed by members of Prof. Steve Withers' group and has been published elsewhere (*2*).

Chapter 4 is based on work conducted in Prof. Gary Brayer's laboratory in collaboration with the groups of Prof. Steve Withers and Prof. Raymond Andersen. The montbretin A used was isolated from the corms of *Crocosmia crocosmiflora* at UBC's Centre for Drug Research and Development. The HPA H299N mutant was produced by Dr. Anjuman Begum,

and I took charge of the expression and purification. Crystallization of the HPA-monbretin A complex was performed in conjunction with Dr. Chunmin Li, and Nham Nguyen. I performed all of the data collection, structural determination and analysis. I also isolated and purified all wild-type HPA used during the crystallization trials.

Chapter 5 is also based on work conducted in Prof. Gary Brayer's laboratory in collaboration with the groups of Prof. Steve Withers and Prof. Raymond Andersen. The PPA used in the PPA-amystatin complex was bought from Sigma and then further purified by Dr. Adeleke Aguda. Crystallization trials for the α-amylase-amystatin complex were performed by Dr. Chunmin Li, Nham Nguyen, and myself. I isolated and purified most of the HPA used in the crystallization trials using constructs provided by Dr. Chunmin Li, Dr. Ran Zhang and Emily Kwan. Some protein used during crystallization trials was also purified by Emily Kwan.

All of the research in this thesis is part of a longtime collaboration between the laboratories of Prof. Gary Brayer and Prof. Steve Withers to analyze structure-function relationships in HPA. Profs. Raymond Andersen and John McNeill joined for the diabetes-related inhibitor studies.

Table of Contents

List of Tables

List of Figures

List of Abbreviations

αG3F α-maltotriosyl fluoride

αGF α-glucosyl-fluoride

5Fido 5-fluoro-idose

5FidoF 5-fluoro-idosylfluoride

AA Auxiliary activities

AAI Amaranth α-Amylase Inhibitor

Amy13A α-Amylase from *Roseburia inulinivorans*

Amy13B α-Amylase from *Butyfibrio fibrisolvens*

BASI Barley α-amylase/subtilisin inhibitor

CAZy Carbohydrate Active Enzyme

CBM Carbohydrate-binding modules

CCBN Canadian Chemical Biology Network

CDRD Centre for Drug Research and Design

CE Carbohydrate esterase

CNP-G3 2-chloro-4-nitrophenyl α-maltotrioside

CNS Crystallography and NMR Systems

COOT Crystallographic Object-Oriented Toolkit

DMSO Dimethyl Sulfoxide

DTNB 5,5-dithio-bis-(2-nitrobenzoic acid)

EC Enzyme Commission

EDTA Ethylenediaminetetraacetic acid

G3F α-maltotriosyl fluoride

GH Glycoside hydrolase

Glc Glucose

GHIL D-gluconohydroximino-1,5-lactam

GT Glycosyltransferase

HPA Human Pancreatic α-Amylase

HSA Human Salivary α-Amylase

MbA Montbretin A

MbB Montbretin B

MbC Montbretin C

MbD Montbretin D

MbE Montbretin E

MeG2F 4′-O-methyl-α-maltosyl fluoride

MPD 2-methylpentane-2,4-diol

MS Mass spectrometry

NCI National Cancer Institute

NMR Nuclear Magnetic Resonance

IUBMB International Union of Biochemistry and Molecular Biology

PAGE Polyacrylamide Gel Electrophoresis

PL Polysaccharide lyase

PDB Protein Data Bank

PISA Protein interfaces, surfaces and assemblies

PPA Porcine Pancreatic α-Amylase

PSAIA Protein Structure and Interaction Analyzer

RBI Ragi bifunctional α-amylase/trypsin inhibitor

RCSB Research Collaboratory for Structural Bioinformatics

Rha Rhamnose

RMSD Root mean square deviation

SDS Sodium Dodecyl Sulphate

SSRL Stanford Synchrotron Radiation Lightsource

TIM Triose Phosphate Isomerase

TMA *Tenebrio molitor* α-Amylase

UBC The University of British Columbia

WT Wild-Type

Xyl Xylose

ZDF Zucker diabetic fatty

Acknowledgements

I would like to thank my supervisor, Professor Gary Brayer, for his help and support through all of my success and failures. I would also like to thank Dr. Robert Maurus and my supervisory committee, Professors Steve Withers and Filip van Petegem for the advice they have given, and Professor Roger Brownsey for stepping in when Gary was not available.

I appreciate the efforts of Dr. Chunmin Li, Dr. Ran Zhang, and Dr. Jacqueline Wicki to teach me about crystallography and enzyme kinetics, and those of Nham Nguyen, Emily Kwan, Yili Wang and Tara Hill who provided technical expertise and support. I am also grateful for the kinetic assays carried out by numerous colleagues, including Dr. Ran Zhang, Dr. Christopher Tarling, Dr. Jacqueline Wicki, and Xiaohua Zhang, and the work done to isolate and identify inhibitors done by Dr. Kate Woods and Dr. Robert Keysers. Thanks are also due to Dr. John Coleman of UBC's Centre for Drug Research and Development, and Dr. Adeleke Aguda for providing some of the starting materials for my experiments.

I must also thank NSERC for their financial support, provided through an Alexander Graham Bell Canada Graduate Scholarship.

Finally, I thank my family who have always encouraged me, and without whom nothing would have been possible.

For Mom and Lynne

Chapter 1

General Introduction

Type 2 diabetes is a serious endocrine disorder involving insulin resistance and insulin deficiency. Without proper management, the resulting high blood glucose levels (hyperglycemia) lead to increased risk of cardiovascular disease, stroke, kidney failure, blindness, and nerve damage (*3*–*5*). People with diabetes have double the risk of death of their non-diabetic peers (*6*). Aging populations and more sedentary lifestyles mean that the incidence of diabetes is rising and set to double by the year 2030 (*7*, *8*). This will pose a major burden on healthcare systems worldwide. Current oral therapies for type 2 diabetes do one of four things: they stimulate the pancreas to produce or release more insulin, they inhibit the production and release of glucose from the liver, they improve cells' sensitivity to insulin, or they block the action of digestive enzymes that break down carbohydrates. Insulin itself may also be administered subcutaneously if blood glucose levels remain elevated after treatment with oral drugs.

The drugs that block digestive enzyme activity, the α-glucosidase inhibitors (acarbose, miglitol, voglibose), slow, but do not stop glucose production. They are also non-specific, and target many different α-glucosidases. In fact, the goal of early searches for α-glucosidase inhibitors for

the treatment of diabetes was to find something that inhibited both starch and disaccharide digestion (*9*). This prevention of the degradation of carbohydrates into glucose allows complex carbohydrates to reach the gut where they are fermented by bacteria, and leads to the associated side effects of α-glucosidase inhibitor treatment of type 2 diabetes. These side effects include flatulence, bloating and diarrhea and contribute to a high rate of patient non-compliance (*10*, *11*). Specific inhibition of α-amylase has been shown to correlate to lower postprandial blood glucose levels in diabetic patients (*12*), and it is hoped that the development of new high-affinity and specific inhibitors for this enzyme will increase the efficacy of this class of drug, lessen gastrointestinal side effects, and lead to the elimination of postprandial hyperglycemia itself.

The work in this thesis takes a structural approach to characterize several new α-amylase inhibitors that target Human Pancreatic α-Amylase (HPA) that will hopefully lead toward more effective treatments for type 2 diabetes and prevention of the complications associated with it.

1.1 Starch Digestion in Humans

1.1.1 Dietary Carbohydrates

Glucose is the primary source of energy for many organisms, but free glucose is a potentially dangerous molecule, because it contains a reactive

aldehyde functionality that readily forms adducts with proteins such as hemoglobin and other biological molecules. These non-enzymatic reactions are particularly dangerous for proteins that have low turnover rate, and contribute significantly to the complications of diabetes.

To avoid these problems, organisms have developed ways to limit the number of free reducing ends of stored glucose. Plants store glucose as starch, a large, branched polymer, while mammals store it as glycogen, a branched polymer that is very similar to starch, and many bacteria store it as pullulan. These polymers generally have only one reactive reducing end for thousands of glucose units. Some organisms even eliminate the reducing ends of stored glucose entirely in molecules such as cyclodextrins and trehalose.

1.1.1.1 Starch

Starch is the predominant source of dietary glucose in most human diets. It is composed of two large polymers, amylose and amylopectin (Figure 1.1). Amylose is an almost linear chain of glucose units attached to each other by α(1,4)-glycosidic bonds, with very rare α(1,6)-linked branches occurring approximately every 1000 glucose units. Amylopectin, is a much larger, and highly branched, polymer composed of three types of glucose chain, and a large number of α(1,6)-links. The C-chain contains amylopectin's only free reducing group, and A- and B- chains are linked to

it. B chains have other A and B chains attached to them, while A chains are analogous to amylose, and form terminal chains of the molecule (*13*).

In solution, a hydrogen bond forms between the 3 and 2′ hydroxyl groups of maltose, the α(1,4)-linked glucose disaccharide. This induces a helical conformation for amylose and other α(1,4)-linked polymers. The 6-hydroxyls are found outside the helix, and starch is thus a series of helices bound together through α(1,6)-glycosidic bonds. Amylolytic endoglucanases have large, open active site clefts that can accommodate these starch helices.

1.1.2 The Digestion of Starch into Glucose

Only sugar monomers can be transported across the intestinal lumen to provide energy; thus, starch granules must be entirely decomposed. This process starts in the mouth, where Human Salivary α-Amylase (HSA) breaks some of the starch into smaller oligosaccharides, but most of it is digested in the small intestine (*18*), since HSA is largely inactivated by the acid and the proteases in the stomach. HPA then continues the breakdown of these oligosaccharides and any remaining starch in the small intestine, producing maltose, maltotriose and limit dextrins that contain the α-(1,6) branch points. The disaccharidases, sucrase-isomaltase and maltase-glucoamylase, are embedded in the brush border of the small intestine and process the products produced by the α-amylases into glucose. Unlike HSA and HPA that work on the internal bonds of starch and

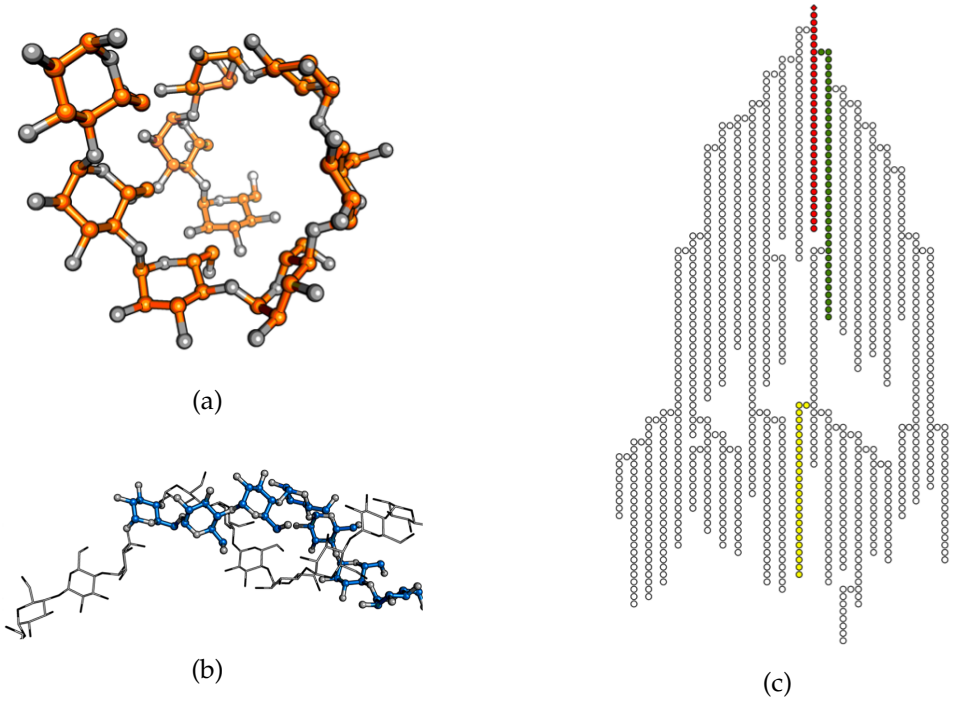

Figure 1.1: The Structure of Starch. (a) Amylose is a polymer composed of α-(1,4)-linked glucose monomers and can be over 1000 units long. It forms a helical coil due to hydrogen bonding between the 3 and 2′ hydroxyls of maltose units. (b) Amylopectin is a highly branched polymer consisting of an amylose chain with α-(1,6)-branches. In amylopectin, two linked chains can form a double helix. The first α-(1,4)-linked chain is shown in thin lines except at the α-(1,6) branch point. The linking sugar and the new α-(1,4)-chain are shown in blue sticks. (c) Diagram representing the highly branched structure of amylopectin. Examples of an 'A' chain, 'B' chain and 'C' chain are highlighted in yellow, green and red, respectively. Circles represent glucose monomers and the only reducing sugar is shown as a diamond. The coordinates used for (a) and (b) are from references (*14*) and (*15*). The coordinates were obtained from the Protein Data Bank (PDB) (*16*) and PolySac3Db (*17*).

release product from the reducing end, the disaccharidases are exoglucosidases that liberate glucose monomers from the non-reducing end. These glucose monomers are then transported through the intestinal wall and released into the bloodstream. The disaccharidases, *in vitro*, can work on substrates larger than the maltose, maltotrioside and limit dextrins produced by HPA, although they do so poorly and have little affinity for starch itself (*19*).

1.2 Classification of Carbohydrate Active Enzymes

1.2.1 The CAZy Database

The Carbohydrate Active Enzyme (CAZy) database represents the most thorough attempt to classify enzymes that work upon carbohydrate-based substrates (*20*). It primarily uses the amino acid sequence information available to organize them into five enzyme classes: Glycoside hydrolase (GH), Glycosyltransferase (GT), Polysaccharide lyase (PL), Carbohydrate esterase (CE) and Auxiliary activities (AA). This last class was added due to the discovery of lytic polysaccharide monooxygenase activity in some glycoside hydrolases (*21*). All of the enzymes currently in the AA class are involved in the degradation of lignocellulose. The CAZy database also includes categories for Carbohydrate-binding modules (CBM) (*21*).

Each of the enzyme classes is further divided into families that are designated by Arabic numerals (e.g., GH13). These are expanded into subgroups and subfamilies that share similarities that indicate a more recent common ancestor and thus, greater correspondence in primary sequence (e.g., GH13_24). Another division within the CAZy hierarchy is the clan, designated by a hyphen and a letter (e.g., GH-H); clans group families of enzymes that are distantly related, sharing structural and mechanistic similarity despite great variation in amino acid sequence (*22*).

Grouping the complex array of carbohydrate active enzymes by amino acid sequence does not always account for differences in substrate specificity. Family GH13, for instance, includes α-amylases, pullulanases, and trehalose synthases, and enzymes with many other functions. The converse is also true, with different enzymes having the same function being classified into different families. The CAZy database thus sorts enzymes according to evolutionary, rather than functional, relationships.

1.2.2 Enzyme Commission Numbers

The International Union of Biochemistry and Molecular Biology (IUBMB), in contrast, classifies enzymes by function using Enzyme Commission (EC) numbers (*23*). These are composed of 4 integers separated by points that progressively denote finer classes of the reaction catalyzed. α-Amylases, for instance, are given the number EC 3.2.1.1, where the first number indicates that it is a hydrolase, the second, that it is a glycosylase, and the

third denotes that it acts on either an O- or an S- linked compound. The final number is a unique identifier for the reaction: in the case of α-amylases it indicates the cleavage of the α-(1,4)-links between glucose residues in the polysaccharide chains of starch, glycogen, and similar compounds with retention of configuration at the anomeric carbon. The EC numbering system becomes complex very quickly, since the meaning of each number depends on the identity of all of those preceding it. This system does not attempt to show evolutionary relationships or common fold among enzymes.

1.2.3 Family GH 13

α-Amylases are among the most studied of the carbohydrate active enzymes due to their importance for both health and industry. Most α-amylases are found in family GH13 in the CAZy database, but they are also found in families GH57, GH119, and GH126 (for a review, see Janeček, Svensson, and MacGregor (*24*)).

Family GH13 is among the largest in the CAZy database, containing more than 15,000 members as of November 2013. These members include not only α-amylases, but also enzymes with other specificities such as α-glucosidases, isoamylases, pullulanases, trehalose synthases, amylopullulanases, neopullulanases and cyclodextran glucanotransferases (*22*, *25*–*28*).

Regardless of the varied specificities of the GH13 enzymes, they all share four characteristics: (1) all of them cleave α-(1,4)-glycosidic linkages with retention of stereochemistry at the anomeric carbon, although a few also have some exoglucosidase activity (*29*) (2) they all fold into a $(\beta/\alpha)_8$ barrel that makes up the catalytic domain, (3) they all have the same catalytic machinery comprised of an aspartic acid nucleophile on strand $\beta 4$ of the $(\beta/\alpha)_8$ barrel, a glutamic acid proton donor/acceptor on strand $\beta 5$ and an aspartic acid that acts as a transition state stabilizer on strand $\beta 7$. They also share between 4 and 7 short regions of conserved amino acid sequence (*30*, *31*). These regions are found mostly within the β strands of the $(\beta/\alpha)_8$ barrel, and often are a better indicator of enzyme specificity than the sequences as a whole (for a review, MacGregor, Janeček, and Svensson (*31*)).

To cope with the large number of proteins in family 13, it has been divided into subfamilies that indicate closer evolutionary relationships (*32*). Even so, subfamilies do not necessarily indicate identical substrate and product profiles for the enzymes within them. An overview of each of the GH13_subfamilies can be found in Janeček, Svensson, and MacGregor (*24*).

1.2.3.1 Structure of GH 13 Enzymes

Although they vary widely in primary sequence, most GH13 α-amylases are three domain proteins, with a large $(\beta/\alpha)_8$ barrel making up domain A

and containing the active site and catalytic residues; these three residues are the only ones conserved across all of the retaining GH13 enzymes. Domain B is a smaller, ordered loop structure protruding from the side of the barrel between strand β3 and helix α3 of domain A. Domain B contains no conserved topology and is the most variable domain of the GH13 α-amylases. Domain C is also attached to domain A, but at the C-terminal end; it assumes an antiparallel β-sandwich fold and is likely a carbohydrate binding domain (*33*–*36*). These canonical domains were first identified in Taka-amylase A from *Aspergillus oryzae* (*37*). In addition, some GH13 α-amylases also contain other domains attached to either terminus of their polypeptide chain. Many of these additional domains help bind starch, glycogen or other, similar, polysaccharides (*24*, *38*, *39*). Variation in domain structure of α-amylases across several GH13 subfamilies is shown in Figure 1.2.

HPA is contained within subfamily GH 13_24, which contains mostly animal α-amylases. These enzymes are made up of only the three canonical domains A, B, and C. Domain A in HPA contains the substrate binding cleft, which can be seen as groove across one side of the protein surface (Figure 1.3) (*45*). This large groove allows the binding of amylose coils within the active site. Within the active site cleft, the invariant catalytic carboxylates form a triangle with the distance between the nucleophile (D197) and acid base catalyst (E233) being approximately 5 Å. This small distance is necessary for the nucleophile to be able to attack the anomeric

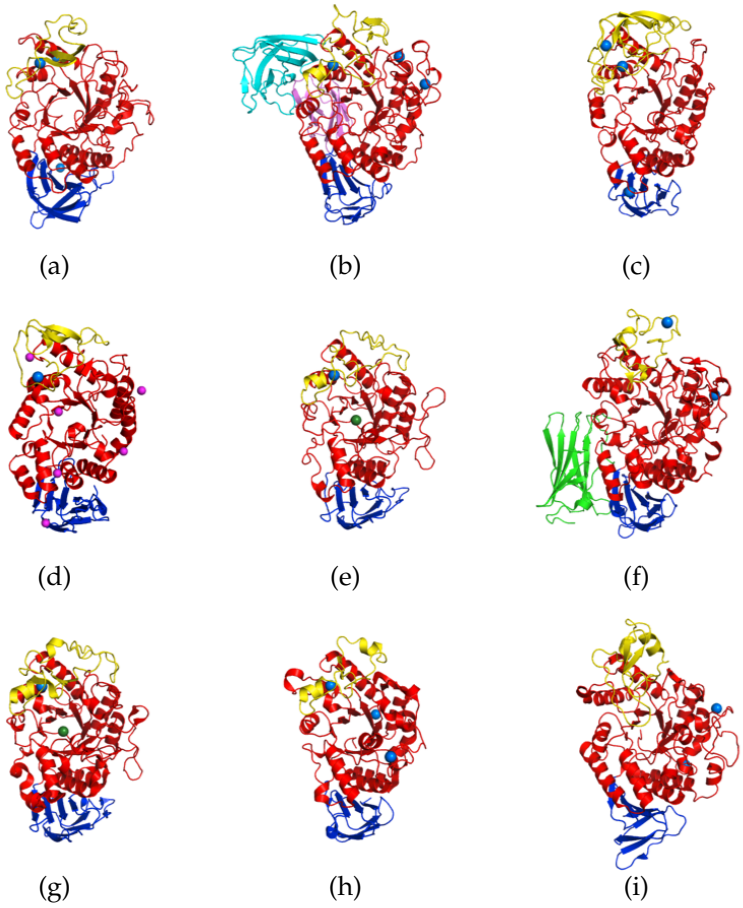

Figure 1.2: α-Amylases from 9 Glycoside Hydrolase Subfamilies. (a) GH13_1 TAKA-Amylase A (*37*) (b) GH13_2 Novamyl (*40*). (c) GH13_5 *Bacillus licheniformis* α-amylase (*41*) (d) GH13_7 (*42*). The pink spheres are zinc ions. (e) GH13_15 *Tenebrio molitor* larval α-amylase (*43*) (f) GH13_21 *Thermoactinomyces vulgaris* R-47 α-amylase 1 (*44*) (g) GH13_24 Human pancreatic α-amylase (*45*). (h) GH13_28 *Bacillus subtilis* α-amylase (*46*) (i) GH13_36 *Halothermothrix orenii* α-amylase A (*47*). Domain A of each enzyme is colored red, domain B, yellow, and domain C is dark blue. Novamyl (b) has two extra C-terminal domains colored pink and cyan, while *Thermoactinomyces vulgaris* R-47 α-amylase 1 (f) has an N-terminal domain colored green. Blue spheres represent calcium ions, and dark green spheres, chloride ions. All of the enzymes are shown in the same orientation.

centre. In contrast, the distance between the two catalytic residues in inverting glycosidases, is about 10 Å to leave room for a water molecule to act as the nucleophile (*25*). The third conserved catalytic residue (D300) in HPA is approximately 7 Å from the acid/base catalyst and 9.5 Å from the catalytic nucleophile. This configuration has led to speculation that this third residue may participate in, but is not essential for, acid-base catalysis in the mechanism of α-amylases (*48*). When substrate is bound, this residue forms a hydrogen bond to the O2 hydroxyl of the aglycone glucose in the -1 binding subsite (*49*, *50*). This leads to a charge separation between the O2 and H2, and negatively polarizes the O2 oxygen, favoring the development of a positive charge during the enzyme's transition state. In the crystal structure of the CGTase-substrate complex, the sugar in the -1 subsite is distorted, and flattened compared to that of a $^4C_1$ chair. This distortion is also promoted by steric conflict with the third catalytic carboxylate and suggests that this residue also helps push the substrate towards a transition state conformation (*49*).

Another important residue within the active site of HPA is Arginine 195. This residue, along with N298 and R337, binds a chloride ion. R195 and N298 are conserved in most α-amylases, whether or not they are chloride dependent, and they help orient the catalytic carboxylates and modulate their pK_a values (*52*). Only the chloride dependent amylases have a basic residue at the R337 position, and a R337Q mutation produces a chloride independent enzyme, indicating that one of the functions of the

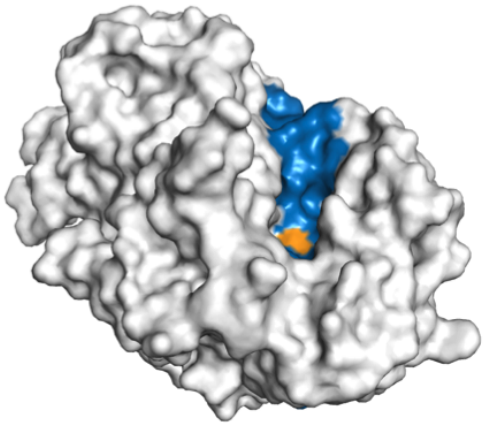

Figure 1.3: HPA's Substrate Binding Cleft. A surface representation of HPA showing the enzyme's extended substrate-binding cleft in blue. The catalytic nucleophile, D197, has been colored orange. The HPA coordinates used were from reference (*51*).

chloride ion is to shield the active site from this arginine's positive charge (*52*).

Domain B in HPA (residues 100-169) binds a calcium ion in a small pocket formed between an α-helix and a small β-strand. The calcium ion also rests against a bend in domain A between sheet β4 and helix α4 (*45*, *51*). The calcium ion helps maintain the protein fold and stabilize the loop that contains the catalytic nucleophile, D197 (*53*). Higher calcium ion concentrations appear to prevent heat denaturation of the protein (*54*).

Domain C (residues 405-496) forms an 8-stranded greek-key barrel motif. Experiments with barley α-amylase isozyme 1, a GH13_6 enzyme, revealed that this functions as a starch binding domain (*55*, *56*). The presence

of domain C is also essential for the activity of some α-amylases, including that of *Bacillus stearothermophilus* (GH13_5) (*57*, *58*). While extensive studies of domain C in subfamily 13_24 have yet to be performed, it is likely that it also functions as a carbohydrate-binding module.

1.3 Mechanism of HPA and Other Retaining Glycosidases

HPA is a key enzyme involved in the breakdown of starch. It cleaves the α-1,4-linked glycosidic bonds in amylose and amylopectin to produce maltose and other small oligosaccharides as well as limit dextrins with retention of the anomeric conformation of the substrate. The enzyme accomplishes this through a double displacement mechanism (Figure 1.4) (*59*). Two carboxylic acid residues, D197 and E233, are intimately involved in this process (*60*). D197 acts as a nucleophile, attacking the anomeric carbon of the substrate, while E233 acts as a general acid catalyst and protonates the leaving group. This forms a covalent glycosyl-enzyme intermediate, with the substrate now attached to D197. As the new covalent bond forms, the substrate goes through a transition state with oxocarbenium ion-like character. In the second step, E233, which previously acted as a general acid catalyst, now acts as a general base and deprotonates a water molecule. The water engages in nucleophilic attack on the anomeric carbon to regenerate the enzyme and release the shortened substrate. This

proceeds through a second oxocarbenium ion-like transition state. (for a review, see (*61–64*)).

HPA also has a third essential carboxylic acid, D300, that is also needed for efficient catalysis. This residue may help deform the sugar in the -1 binding subsite (i.e., the subsite on the non-reducing end of the cleavage point), and push the substrate towards the conformation of the transition state, consistent with its role in CTGase (*49*, *60*). D300 may also increase the electrophilicity of the anomeric carbon at the cleavage point through a hydrogen bond with the oxygen at the C2 position (*49*). Structural studies of HPA indicate that this residue plays a crucial role in hydrogen bonding the water molecule involved in the deglycosylation step of the mechanism (*45*, *50*).

1.3.1 The Catalytic Nucleophile

All GH13 enzymes employ a carboxylate (Glu or Asp) as a nucleophile in the first step of the double displacement mechanism. Carboxylates perform this role well, for they are reasonably good nucleophiles, and can displace the saccharide leaving group of the carbohydrate substrate; they form easily cleaved covalent intermediates, allowing hydrolysis and they are negatively charged and can stabilize the cationic character of the oxocarbenium ion-like transition state.

The evidence for the use of carboxylates as catalytic nucleophiles comes primarily from crystallographic studies of many glycosidases (*65*) and from

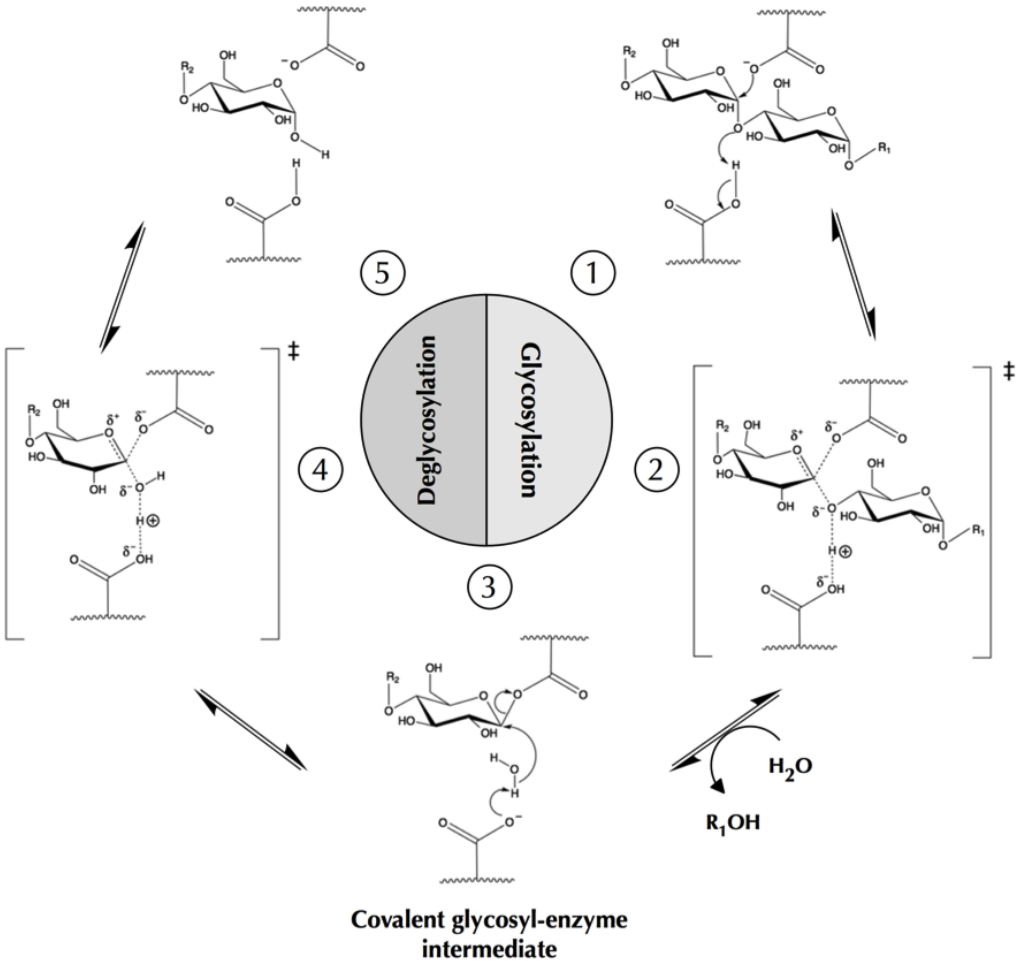

Figure 1.4: The Double Displacement Mechanism of Retaining α-Glycosidases. The substrate is attacked by an enzymatic nucleophile and a proton is donated to the leaving group through general acid catalysis (1). This goes through an oxocarbenium ion-like transition state (2) to form the glycosyl enzyme intermediate (3). The covalent intermediate is cleaved when general base catalysis, performed by the same enzymatic residue that acts as the acid catalyst in step 1, deprotonates a water molecule that becomes the nucleophile in the deglycosylation step. This goes through a second oxocarbenium ion-like transition state to release the substrate and regenerate the enzyme.

trapping studies using mechanism-based inhibitors (*64*) or cryogenic temperatures (*66*), with significant contributions from kinetic studies of purported nucelophile mutants (*48*, *67*, *68*). Nucleophile mutants show dramatic decreases in enzymatic activity with reaction rates typically 10^6 times slower than the wild type enzyme. The loss of activity can be partially restored by adding nucleophilic anions such as acetate, azide and formate to occupy the place of the mutated amino acid. This, of course, alters the product, resulting in inverted stereochemistry at the anomeric carbon (*67*–*69*).

Kinetic studies provide some of the best evidence for the role of D197 in the catalytic mechanism of HPA. Mutants of D197 had the lowest k_{cat}/K_m values of all the HPA mutants tested (*48*, *60*). Since the K_m of the D197N and D197A mutants increased by only 3 and 10 times, respectively, and there were no structural changes in the enzyme caused by these mutations, the dramatic decrease in enzymatic activity can be explained by catastrophic damage to the catalytic machinery itself. Azide rescue studies increased the reaction rate of the D197A mutant 10-fold, but even after 24 hours incubation, there was insufficient accumulated product for Nuclear Magnetic Resonance (NMR) characterization (*48*). Confirming the results of these kinetic studies, later crystallographic studies of the trapped glycosyl-enzyme intermediate clearly show D197 covalently bound to a mechanism based inhibitor, 5-fluoro-idosylfluoride (5FidoF) (*70*). The fluorine at the C5 position slows the endocyclic oxygen's contribution of a

lone pair of electrons into the formation of the oxocarbenium ion-like transition state, while the fluorine at the C1 position, ensures that deglycosylation is the rate limiting step. 5-fluoro-idose (5Fido) itself has little effect on HPA activity; however, the elongation agents 4'-O-methyl-α-maltosyl fluoride (MeG2F) and α-maltotriosyl fluoride (G3F) greatly increased the efficacy of this inhibitor by capitalizing on the enzyme's ability to transglycosylate monosaccharide inhibitors to increase affinity *in situ* (*70*, *71*).

1.3.2 The General Acid/Base Catalyst

The general acid/base catalyst plays a dual role in a double displacement mechanism. It acts as a general acid to promote cleavage of the glycosidic bond, and then acts as a general base to activate the water molecule that cleaves the glycosyl-enzyme intermediate. Kinetic studies have been used in conjunction with nucleophilic rescue experiments to identify the acid/base catalyst of glycosidases (*60*, *67*, *72*). The identity of the acid catalyst can be determined by kinetic studies of mutant enzymes. The rate of the glycosylation step depends strongly on the substrate's ability to form a good leaving group. When fluorine, for instance, replaces the aglycone sugar, there is no longer any need for an acid-base catalyst for the glycosylation step, and the rate enhancement induced by such an activated substrate will be different for the wild type enzyme and an acid catalyst mutant.

Regardless of the substrate used, cleavage of the glycosyl-enzyme intermediate is slowed when the acid/base catalyst is missing. Rescue experiments with anions such as azide, formate or acetate, help identify acid/base catalyst mutants, because they produce an altered product that retains the anomeric configuration of the substrate. If an amino acid other than the acid/base catalyst is mutated, steric clash and charge repulsion prevent these anions from performing the role of the deglycosylating nucleophile, and the primary product remains that of the wild-type enzyme.

Such anion rescue experiments have identified the acid/base catalyst of HPA as E233 (*48*, *60*). The k_{cat}/K_m value of wild type HPA was 10^4 times higher than that of the E233 mutants when maltopentaose was used as a substrate. Changing the substrate to G3F increased k_{cat}/K_m value of the wild-type enzyme only 6-fold, but the same change of substrate using HPA E233A resulted in a k_{cat}/K_m value that was 5000 times higher. This difference indicates that E233 likely acts as HPA's acid catalyst (*48*). In addition, the activity of this mutant doubled upon the addition of azide, which is consistent with rescue of acid/base catalyst mutants in other retaining glycosidases (*73*).

1.4 Kinetics of Enzyme Inhibition

The study of the changes in enzyme reaction rates reveals much about how an inhibitor impedes enzymatic activity, and how effective the inhibitor is.

There are three main categories of enzyme inhibitor: competitive, uncompetitive, and noncompetitive. A competitive inhibitor cannot bind to the enzyme if the substrate is already bound and vice versa; an uncompetitive inhibitor can only bind to the enzyme-substrate complex, and a noncompetitive inhibitor can bind either to the free enzyme or to the enzyme substrate complex. True noncompetitive inhibition occurs only when an inhibitor has equal affinity for the free enzyme and enzyme-substrate complex. In reality, this is rare, and most inhibitors designated 'noncompetitive' actually exhibit mixed inhibition, and have different binding constants for these two enzymatic states. A more detailed description of the kinetics of enzyme inhibition can be found in appendix A.

1.5 α-Glucosidase Inhibitors

The use of α-glucosidase inhibitors as antidiabetic agents was developed by Puls, Keup, Krause, Thomas, and Hoffmeister (*9*) as a means of controlling postprandial hyperglycemia through the prevention of glucose release from complex polysaccharides. Acarbose was found during a screen to find inhibitors of α-amylase, sucrase, and maltase activity (*74*), and was introduced as a drug in 1990. Three α-glucosidase inhibitors are currently used therapeutically for the treatment of type 2 diabetes: acarbose, miglitol, and voglibose (Figure 1.5).

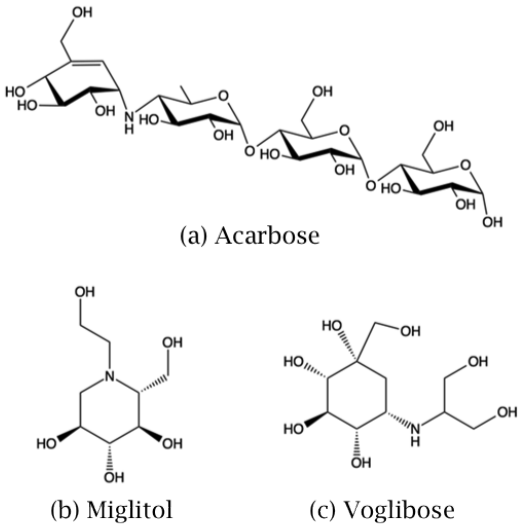

Figure 1.5: Chemical structures of the three α-glucosidase inhibitors currently available as treatments for type 2 diabetes, acarbose (a), miglitol (b), and voglibose (c).

Acarbose is a pseudotetrasaccharide composed of valienamine linked through a nitrogen atom to 6-deoxyglucose which is attached through an α-(1,4)-glycosidic bond to α-D-maltose. It acts as a transition state analog for α-glucosidases, including HPA (*73*, *75*). Miglitol is a derivative of 1-deoxynojirimycin, the iminosugar analog of glucose, and voglibose is a product of the reductive alkylation of valiolamine (*76*). The first of these is a general α-glycosidase inhibitor and is thought to be a transition state analog for enzymes such as α-glucosidases, α-amylases, including HPA, cyclomaltodextrin glucanyltransferases and dextransucrases, among others. Miglitol and voglibose, as monosaccharide mimics have greater affinity for enzymes requiring smaller substrates, such as the sucrase, and mal-

tase of the intestinal brush border. The administration of all three of these medications is accompanied by severe gastrointestinal side effects caused by the fermentation of polysaccharides that would normally be digested in the upper gastrointestinal tract, by bacteria in the colon. This leads to an increase in the amount of carbon dioxide and hydrogen gas produced in the lower bowel (*77*).

Tight binding HPA inhibitors have the potential to become new therapeutics for the treatment of type 2 diabetes and obesity, and much effort has been made to search for inhibitors that display both high affinity and specificity for this enzyme (*2*, *78*, *79*). The inhibitors that have been found generally fall into 3 categories, carbohydrate-based inhibitors and carbohydrate mimics, polyphenolic compounds, and proteinaceous inhibitors.

1.5.1 Carbohydrate-Based Inhibitors

Sugar-mimicking glycosidase inhibitors have been shown to have enormous potential as treatments for diabetes, viral infection and lysosomal storage disorders (*80–83*). These carbohydrate mimics are classified into three categories: carbaglycosylamines, iminosugars, and thiosugars. Carbaglycosylamines are glycosylamines in which the ring oxygen has been replaced by a methylene group, while iminosugars and thiosugars have a nitrogen or a sulphur atom in place of the ring oxygen. Their effect on glycosidases can be explained by their resemblance to substrate molecules and, in some cases, to enzymatic transition states.

1.5.1.1 Acarbose

Acarbose, a carbaglycosylamine compound, is by far the most studied α-glucosidase inhibitor, and is currently used therapeutically to prevent postprandial hyperglycemia in type 2 diabetics. Acarbose inhibits all of the intestinal α-glucosidases with the exception of isomaltase, which cleaves α-(1,6), rather than α-(1,4) linked glucosidic bonds (*84*).

Acarbose was first isolated from *Actinoplanetes* in 1977, and was very quickly seen as a possible treatment for hypoglycemia and obesity, in part because it inhibited both α-amylase and sucrase activity (*9*, *74*). Its structure is very similar to malto-tetraose, containing a maltose and a pseudo-maltose moiety (see Figure 1.5). This pseudo-maltose is composed of a valienamine moiety N-linked to the 4-hydroxyl of 6-deoxyglucose. The half-chair conformation of the cyclohexenol ring resembles that of the oxocarbenium ion-like transition state of the GH13 α-glucosidases, and the nitrogen, when protonated, confers a positive charge. The nitrogen-linked pseudo-glycosidic bond renders this acarviosyl group immune to hydrolysis. Acarbose itself, however, can act as a substrate for hydrolysis, condensation and transglycosylation reactions within the active site of HPA and other α-amylases, and significantly altered inhibitors are found in crystal structures of α-amylase/acarbose complexes (*50*, *85–89*). The conformation of the final rearranged product varies by enzyme, but acarbose's acarviosyl group consistently spans the substrate cleavage point in a conformation consistent with acarviosine being a transition state analog.

The rearranged acarbose structure that binds within the active site of HPA crystals is a pseudo pentasaccharide that spans the -3 to +2 binding subsites (Figure 1.6) (*50*). Substrate-binding subsites designate the sugars that bind on the non-reducing end of the cleavage point with negative numbers, and those on the reducing end with positive numbers. Cleavage occurs between the -1 and +1 binding subsites (*90*). For HPA, the only productive binding mode for a pentasaccharide is from the -3 to +2 binding subsites , because the only product of enzymatic cleavage of maltopentaose is maltose (*50*). Studies employing both shorter and longer oligosaccharides (maltotetraose through maltoheptaose) as substrates for HPA revealed an enzymatic preference for maltose in the aglycon (+n) sites to produce optimal reaction rates. This tendency, however, is offset by a competing mode in which three sugars bind in the glycon (-n) subsites. HPA cleavage of maltotetraose produces both maltose and glucose, while maltose and maltotriose are produced when maltohexaose is the substrate. HPA's substrate cleavage preferences reveal 5 binding subsites, all of which are occupied in the crystal structure of the HPA-acarbose complex (*50*).

This need for larger carbohydrate inhibitors for strong binding to HPA limits the number of strong inhibitors for this enzyme, while many inhibitors are available for GH 13 enzymes that process monosaccharides. These enzymes have the same mechanism, and a similar transition state structure to HPA, and work has been done to determine whether small

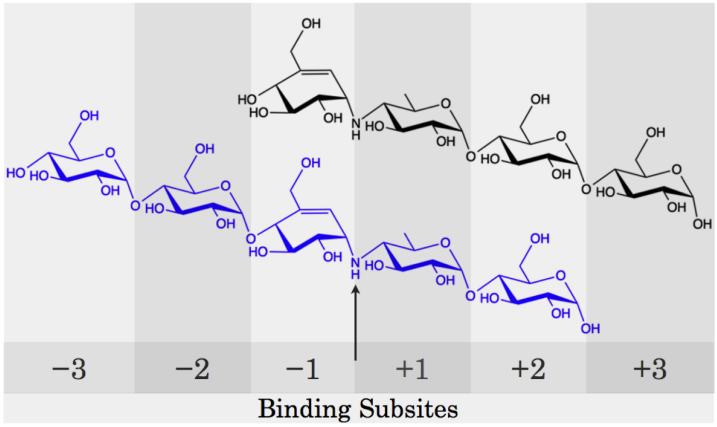

Figure 1.6: The Rearrangement of Acarbose in HPA Crystals. When acarbose (black) is soaked into HPA crystals, it is transglycosylated to form a pseudopentasaccharide (blue) that binds in the enzyme's -3 to +1 binding subsites. Normal substrate cleavage takes place between the +1 and 1 binding subsites, as marked by the arrow. The black drawing indicates how acarbose would be expected to bind if it were inert to HPA catalysis.

monosaccharidase inhibitors can be transglycosylated *in situ* to form HPA inhibitors upon incubation of the inhibitor with an activated glucosyl fluoride. This strategy has been effective in producing elongated HPA inhibitors from D-gluconohydroximino-1,5-lactam (GHIL) (*71*) and 5FidoF (*70*, *71*). The success of these studies encouraged the use of elongating agents during a new screen for HPA inhibitors, developed by Dr. Christopher Tarling from Prof. Steve Withers' group. In this study, crude extract and pure compound libraries were screened for HPA inhibition with and without the addition of α-glucosyl-fluoride (αGF). While this screen did not result in any promising, elongatable inhibitors, the two strongest

leads, a glycosylated flavonol and a peptide, are discussed in chapters 4 and 5 of this thesis.

1.5.1.2 Voglibose

Voglibose is a monosaccharide mimic derived from valiolamine (*91*). It is a potent inhibitor of human maltase and sucrase with K_i values of 3.8 nM and 0.2 nM, respectively (*92*). It is a much poorer inhibitor of α-amylases, being approximately 104 times less effective than acarbose (*92*). No structural studies showing an α-glucosidase-voglibose complex are currently available, but it is thought that this inhibitor may use the 2-hydroxy-1-(hydroxymethyl) ethyl group attached to the nitrogen to imitate the C-3' hydroxyl of either sucrose or maltose by rotating around the pseudoglycosidic bond between valiolamine and $CH(CH_2OH)_2$ (*91*).

1.5.1.3 Miglitol – an iminosugar

Iminosugars are small organic compounds that mimic sugars or their hydrolysis transition states, but have replaced the endocyclic oxygen with nitrogen (*93*, *94*). The nitrogen will be protonated at physiological pH, helping these inhibitors by mimicking the charge of an oxocarbenim ion. The nitrogen of acarbose, on the other hand, more closely resembles the exocyclic oxygen of the substrate as it is being protonated by the acid/base catalyst.

One of the most used iminosugar inhibitors of human α-glucosidases is miglitol (see Figure 1.5). It is an excellent disaccharidase inhibitor, but has no known effect on HPA or other α-amylases (*95*). It is a derivative of 1-deoxynojirimycin, the imino sugar of glucose and the active ingredient in mulberry bark, a traditional Chinese medicine for the treatment of diabetes. Despite excellent *in vitro* α-glucosidase inhibition, 1-deoxynojirimycin showed little effect *in vivo* (*80*). Derivatives of this compound were then investigated to increase *in vivo* efficacy. Miglitol was the best of these derivatives. Unlike acarbose, little of which is absorbed through the intestinal wall, miglitol is almost completely absorbed. It is not metabolized and is excreted intact by the kidneys (*96*).

1.5.1.4 Salacinol – a Thiosugar

Sulfonium ions can be used to mimic the developing charge on the endocyclic oxygen at the oxocarbenium ion like transition state. The first such compound to be made was a sulfonium salt (Fig 1.7a) that inhibited liver α-mannosidase (*97*).

One of the best studied thiosugar inhibitors of α-glucosidase is salacinol, a furanose mimic (Figure 1.7b). This inhibitor has a zwitterionic sulfonium sulfate structure (*98*). It is a competitive inhibitor of intestinal α-glucosidases *in vitro*, and its K_i for maltase and sucrase is nearly identical to that of acarbose; however, it shows much greater isomaltase inhibitory activity than the pseudotetrasaccharide. It inhibits HPA with a

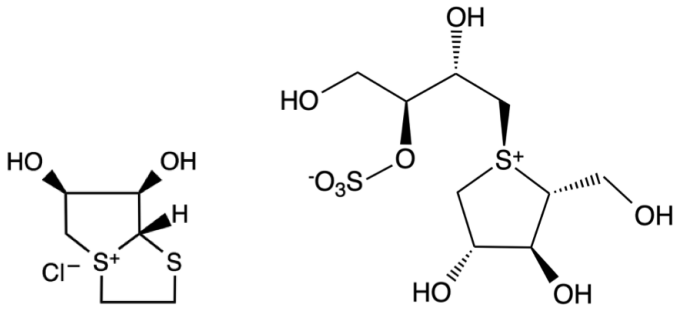

(a) (b)

Figure 1.7: The Chemical Structure of Two Sulfonium Ion α-Glycosidase Inhibitors. (a) The sulfonium salt first described by Siriwardena, Chiaroni, Riche, El-Daher, Winchester, and Grierson (*97*); (b) salacinol

K_i of 75 μM (*99*). Salacinol is used as a treatment for diabetes in traditional Indian medicine.

1.5.2 Polyphenolic Compounds

Polyphenolic compounds are present in almost all plant-derived foods. There are many classes of these compounds, but the most common in the diet are anthocyanins, flavanols, flavonols, phenolic acids, isoflavones, ellagitannins, flavones and flavanones (Figure 1.8) (*100*). These are often found covalently bound to sugars either by O-glycosidic, or more rarely, by C-glycosidic bonds. Many studies have shown a link between the consumption of polyphenol-containing foods and a reduction in glycemic index, a measure of how quickly postprandial blood sugar is elevated after consuming a specific food, and polyphenolic compounds are the active in-

gredients in many traditional medicines for type 2 diabetes (*101*, *102*); in Ayurvedic medicine alone, over 800 plants are said to have antidiabetic properties (*102*). Such a reduction in glycemic index was observed for red wine, coffee, chocolate, and American ginseng, among many other foods (see *100*, *101*, *103*, *104*, for reviews).

In vitro assays have shown α-amylase and α-glucosidase inhibitory compounds in many plant extracts. A review of these inhibitory extracts, (*102*), lists 155 plant species whose raw extracts contain anti-HPA or Porcine Pancreatic α-Amylase (PPA) activity, and that number continues to

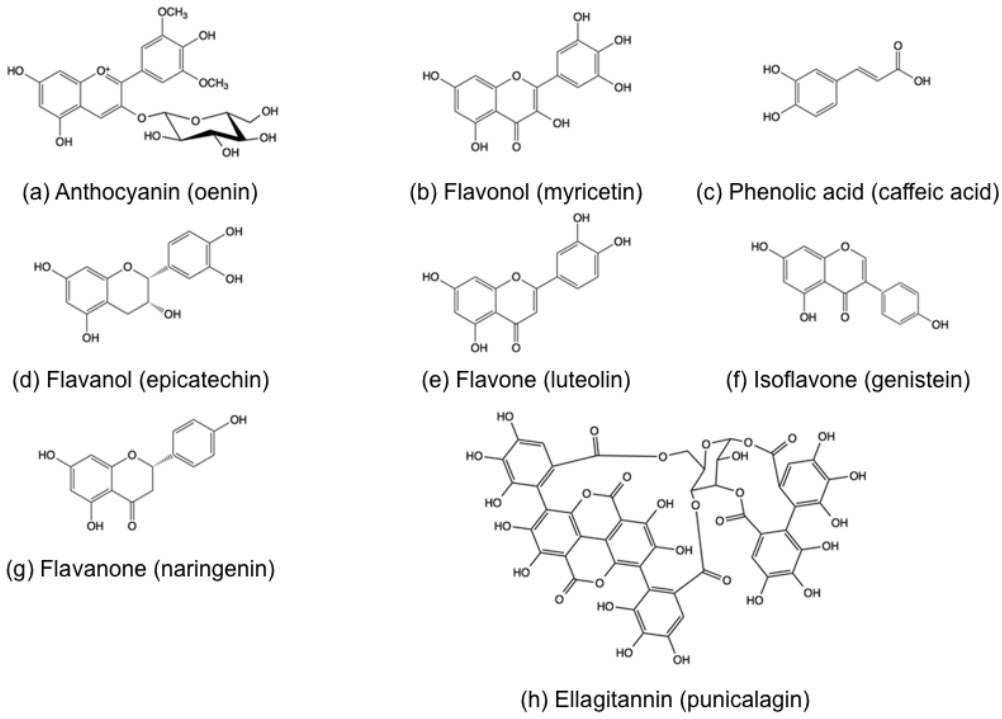

Figure 1.8: Examples of Dietary Polyphenolic Compounds.

grow as new studies are published (see, for example, references *105*, *106*). The active compounds of most of these extracts have not been characterized. Some of the polyphenolic α-amylase and α-glucosidase inhibitors that have been characterized are listed in Table 1.1.

Initial kinetic studies have shown that polyphenols, in general, are fairly poor α-glycosidase inhibitors, but this inhibitory activity can be increased with the addition of sugar residues or sugar analogues. 5-O-caffeoylquinic acid, for instance, which exhibits mixed inhibition of PPA, has a K_i of 0.2 mM, and a K_i' of 0.05 mM, which indicate its ability to bind to the free enzyme and enzyme-substrate complexes, respectively; caffeic acid alone had a K_i of 1.6 mM and a K_i' of 0.25 mM (*107*). Another caffeic acid derivative, ethyl caffeate, inhibits HPA noncompetitively with a K_i of 1.3 mM (*2*). How this inhibitor interacts with the enzyme will be discussed in Chapter 3 of this thesis.

Few structural studies have examined the complexes formed between α-amylase and this large class of phenolic inhibitors. The most comprehensive to date is an *in silico* study of flavonol binding in the active site of HSA (*108*). The flavonols in this study form hydrogen bonds with the catalytic carboxylates, and a conjugated π-stacking interaction with the side chain of Trp59. Two possible configurations were found for flavonol binding, flipped 180°relative to each other. In one, the A-ring hydroxyls hydrogen bond to D197, while in the other those of the AC ring system do. This second pose forms at the expense of the π-stacking interactions seen

Table 1.1: Phenolic Compounds that Inhibit α-Amylase or α-Glucosidase *In Vitro*

	Inhibition of α-Amylase (References)	**Inhibition of α-Glucosidases (References)**
Anthocyanins		
cyanidin 3-sambubioside	(*111*)	(*112*)
acylated anthocyanins		(*113*, *114*)
Catechins		
catechin		(*115*)
catechin-gallate		(*115*)
epi(gallo)catechin		(*115–117*)
epi(gallo)catechin gallate		(*111*, *118*, *119*)
theaflavin gallate		(*118*)
Flavonols, flavones and flavanones		(*120*)
quercetin	(*108*, *120*)	(*115*, *120*, *121*)
quercetin 3-rhamnoside		(*122*)
myricetin	(*1*, *2*, *108*, *120*)	(*120*)
myricetin-3-O-rhamnoside	(*123*)	(*123*)
luteolin	(*108*, *120*)	(*120*)
luteolin 7-glucoside	(*124*)	(*124*)
isookanin	(*125*)	
europetein-3-O-rhamnoside	(*123*)	
tiliroside	(*126*)	
vitexin		(*127*)
isovitexin		(*127*)
5,7,3,4-Tetramethoxyflavone		(*128*)
5,7,4-trimethoxyflavone		(*128*)
3,5,7,30,4-pentamethoxyflavone		(*128*)
isorhamnetin		(*121*)
rutin		(*129*)
kazinol A		(*130*)
Isoflavones		
genistein		(*120*, *131*)
dadzein		(*108*, *120*, *124*)
Phenolic acids		

continued on next page

	Inhibition of α-Amylase (References)	**Inhibition of α-Glucosidases (References)**
caffeic acid	(*2*, *107*)	(*116*, *117*, *122*)
6-O-caffeoylsophorose	(*132*)	(*132*)
chlorogenic acid	(*133*, *134*)	(*111*, *115*)
p-coumaric acid		(*116*, *117*)
ferulic acid		(*116*, *117*, *135*)
gallic acid		(*116*, *117*)
tannic acid	(*133*)	(*116*, *117*, *136*)
4,5-dicaffeoyl quinic acid	(*137*)	
hydrolyzable tannins		(*138*, *139*)
Ellagitannins	(*134*)	
Proanthocyanidins	(*140*)	(*140*, *141*)
Other phenolics		
quercitylcinnamate		(*142*)
curcumin	(*143*)	
coumestrol		(*144*)
saponarin		(*145*)
saponarin II		(*146*)
hispidin		(*147*)
hispolon		(*147*)
inotilone		(*147*)
bis(2,3-dibromo-4,5-dihydroxybenzyl) ether		(*148*)

in pose 1. This computer docking study provides a huge step towards understanding α-amylase-flavonol binding interactions; however, it cannot indicate with certainty how these inhibitors bind, because it does not allow for any significant movement in the enzyme's polypeptide chain, and previous x-ray crystallographic studies of HPA, HSA and PPA showed that the mobile loop from residues 303-311 can move upon the binding of an inhibitor (*50*, *86*, *109*, *110*). In inhibitor-free HPA, the side chain of His305

packs against Trp59, (*51*) and movement of this loop could affect flavonol binding.

1.5.3 Proteinaceous Inhibitors

Proteinaceous inhibitors of α-amylases have been isolated from bacteria and higher plants (*79*, *149*). They are most likely produced to protect an organism from predatory pathogens and pests. These protein inhibitors can be classified into seven categories according to similarities in primary sequence and three-dimensional structure (*79*, *149*). Six of these categories are produced by higher plants, while the seventh is produced by *Streptomyces spp*. Peptide-based α-amylase inhibitors have also been produced artificially through directed evolution of peptides developed from the cellulose binding domain of *Trichoderma reesei* cellobiohydrolase Cel7A (*150*) or dromedary VHH antibody domains that have been raised against PPA (*151*). Only the naturally-occurring peptide will be discussed here. For a review of the designed inhibitors, see Svensson, Fukuda, Nielsen, and Bønsager (*79*).

1.5.3.1 *Streptomyces Inhibitors*

The most studied of these protein-based α-amylase inhibitors is tendamistat, which was isolated from *Streptomyces tendae* (Figure 1.9). It is an extremely potent inhibitor of mammalian α-amylases with a K_i of 9×10^{-12}

M for PPA (*152*). It is also the first protein to have three-dimensional structures solved by both NMR spectroscopy and X-ray crystallography (*153*, *154*).

Tendamistat is a small protein, only 74 amino acids long; it binds to an extended cleft in PPA and blocks substrate access to the active site (*155*). Four short stretches of its polypeptide chain form various salt bridges, hydrogen bonds and hydrophobic interactions with PPA. A single β-turn that includes residues 18-20 interacts directly with the catalytic residues of PPA with strong electrostatic interactions. In fact, the Trp18-Arg19-Tyr20 motif of this turn is highly conserved in other inhibitors in this class (*156*–*158*). Arg19 engages in a salt bridge with E233, the acid/base catalyst. Many studies have tried to replicate this β-turn structure in smaller peptides; however, none of these retain the picomolar inhibition of the larger protein, and have K_i values in the micromolar range (*79*, *159*). A compar-

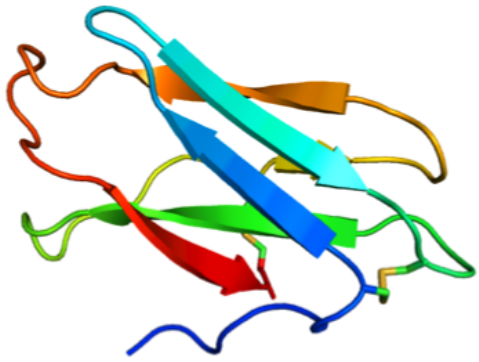

Figure 1.9: The tertiary structure of tendamistat. The inhibitor forms a 6-stranded barrel-like structure (PDB ID: 1BVN *155*).

ison of the crystal structures of the PPA-tendamistat and PPA-amystatin complexes will be presented in Chapter 5.

1.5.3.2 Knottins

Knottins are small peptides that are defined by their peptide bond topology. They have three disulfide bonds in a characteristic 1-4, 2-5, 3-6 pattern, where cysteine 1 is bound to cysteine 4, cysteine 2 to cysteine 5, and cysteine 3 to cysteine 6. These peptides are called 'knottins', because one disulfide bond penetrates a macrocycle formed by the other two. These peptides are known to be carboxypeptidase, and squash trypsin inhibitors (*160*, *161*). They are also found in spider, scorpion and cone snail venoms (*162*). There is no three-dimensional structure common to all knottins.

One example of a knottin α-amylase inhibitor is Amaranth α-Amylase Inhibitor (AAI) from *Amaranthus hypochondriacus* (Figure 1.10). AAI is one of the smallest known peptide-based α-amylase inhibitors, being only 32 amino acids long. It specifically inhibits insect α-amylases, and has little effect on its mammalian homologs (*163*). A comparison of PPA to *Tenebrio molitor* α-Amylase (TMA) revealed that this is likely due to the loss of important hydrogen bonding interactions in the region of PPA's mobile loop from residues 303-311 (*164*).

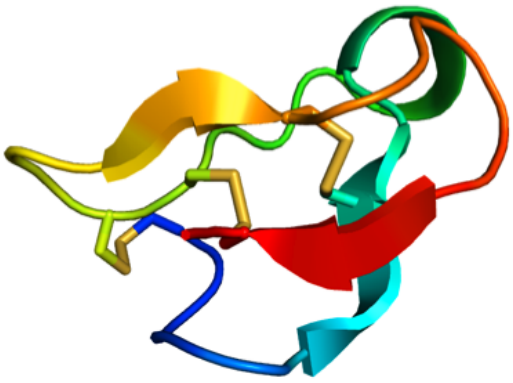

Figure 1.10: The tertiary structure of Amaranth Amylase Inhibitor. The polypeptide backbone is shown as a cartoon, and the disulfide bonds are shown as sticks. The middle disulfide bond penetrates a macrocycle formed by the other two. (PDB ID: 1CLV, *164*)

1.5.3.3 γ-Thionins

γ-Thionins, also known as plant defensins, are small peptides that defend the plant against parasites. They are small, basic peptides that contain four disulfide bonds and share a common fold comprised of a three-stranded β-sheet with an α-helix in parallel (see, for example *165*). The core of this global fold consists of a disulfide bridge stabilized α-helix β-sheet (CS$\alpha\beta$) motif where two cysteine residues, one turn apart on the α-helix form disulfide bridges to two cysteines separated by a single amino acid on the last strand of the β-sheet. SIα1, SIα2, and SIα3, isolated from sorghum, strongly inhibit insect α-amylases (*166*).

Plant defensins are so named due to their resemblance to mammalian defensins, which were first found in rabbits (*167*). The mammalian α- and β-defensins differ in the arrangement of their cysteine residues and the

topology of their disulfide bonds, but both classes share a common fold (*168*, *169*). The mammalian α-defensins do not contain the α-helix found in the plant defensins. Mammalian β-defensins, on the other hand, can include a short α-helix that usually precedes the small β-sheet; this is different than the plant defensins where the helix is found at the C-terminus of the peptide. The β-defensin fold is also found in snake venom and sea anemone toxins (*170*).

In silico docking has been used to examine binding interactions between VuD1, a plant defensin from cowpea, and a weevil α-amylase (*171*). VuD1 is an excellent inhibitor of weevil α-amylase, but has little effect on its mammalian homologs. This study suggests that VuD1 might interact with the enzyme's catalytic nucleophile, Asp204. While some caution must be taken in interpreting their results, since the structure of the enzyme, the peptide inhibitor and of the enzyme-inhibitor complex were all determined *in silico*, the comparison of their model to the crystal structure of PPA (*109*) shows that the specificity of VuD1 to insect α-amylases may result from three loops present in PPA, but absent in the insect enzyme. These include the mobile loop from residues 303-311 (PPA numbering). These loops may therefore be essential in determining the specificity of this type of peptide inhibitor. Unfortunately, the coordinates are not available publically for further analysis.

The solution structure exists for another α-amylase inhibitor, VrD1 from mung bean (*172*) (Figure 1.11). VrD2, also from mung bean, shows no α-

amylase inhibitory activity. Experiments to transform VrD2 into an amylase inhibitory peptide revealed that inhibition depends strongly on loop length and the distribution of charged amino acids (*173*). The actual binding interactions between α-amylase and VrD1 or the mutant VrD2 are still not known.

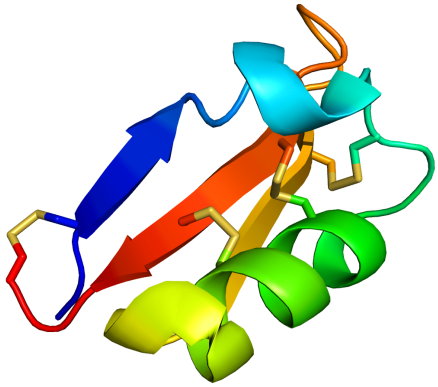

Figure 1.11: Structure of VrD1, an insect α-amylase inhibitor. The structure show the fold of plant defensins, with two disulfide bonds on consecutive turns of the α-helix bound to the middle β-strand of an antiparallel β-sheet. (PDB ID: 1TI5, *172*).

1.5.3.4 CM-Proteins

CM-proteins are small, salt-soluble proteins found in chloroform:methanol (2:1, v/v) extracts of cereal endosperm. They are between 120 and 160 amino acids long and contain five disulfide bonds (*79*, *174*, *175*). Many are bifunctional trypsin/α-amylase inhibitors (*174–177*), while some inhibit only α-amylase (*178*) or trypsin (*179*). The crystal structure of Ragi bifunctional α-amylase/trypsin inhibitor (RBI) (Figure 1.12) has been solved in complex with *Tenebrio molitor* α-amylase (TMA) (*180*). This structure

shows that the N-terminal segment of the peptide (residues 1-11) interacts with the enzyme's substrate binding cleft, and Ser 1 forms hydrogen bonds with Asp185 and Glu222, the enzyme's catalytic nucleophile and acid/base catalysts. It is likely that the N-terminal nitrogen is protonated under the crystal growing conditions (pH 8.0) and thus, it may form a strong salt bridge with these two residues. Val2 and Ser5 interact with the third catalytic carboxylate, Asp287. The structure of the inhibitor was solved both by x-ray crystallography and by NMR spectroscopy (*181*, *182*), and these reveal that the binding of RBI to the enzyme induces the formation of one α-helical turn at the N-terminus of the peptide (residues 2-5). Kinetic studies of this bifunctional inhibitor showed it to inhibit PPA with a K_i of 11 nM (*177*); an N-terminal fragment containing only the first 7 residues of RBI, also inhibited PPA with a K_i of 335 nM while other fragments did not inhibit the enzyme at all (*183*). This confirms that the N-terminal region is crucial for α-amylase inhibition. *In silico* modeling studies suggest that the RBI-PPA complex may gain additional enzyme-inhibitor interactions absent in the RBI-TMA complex structure due to the longer loops within the substrate-binding cleft (*180*).

1.5.3.5 Kunitz-Type Inhibitors

Kunitz-type inhibitors are so named because they share sequence similarity to Kunitz soybean trypsin inhibitor (*184*). While at first thought to inhibit only subtilisin, a Kunitz-type inhibitor from barley was later

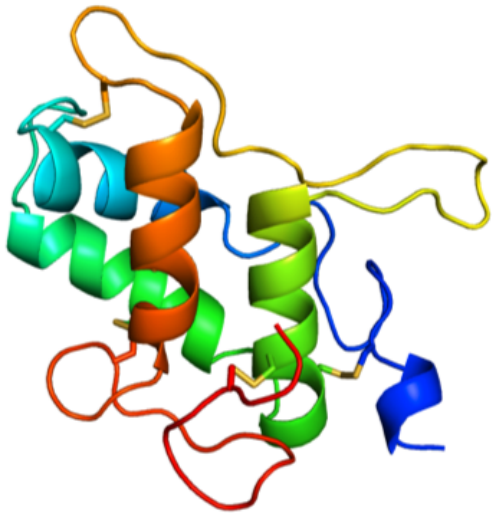

Figure 1.12: The tertiary structure of Ragi Bifunctional Inhibitor (RBI). Only the N-terminal region (blue) is important for α-amylase binding. (Strobl, Maskos, Wiegand, Huber, Gomis-Rüth, and Glockshuber (PDB ID: 1TMQ, *180*))

found to bind with an endogenous α-amylase (Figure 1.13); Barley α-amylase/subtilisin inhibitor (BASI) inhibits barley α-amylase 2 (AMY2) with a K_i of 0.22 nM (*185*). The binding of BASI to AMY2 creates a calcium-binding pocket in which the coordination sphere of a fully solvated calcium ion coordinates water molecules that hydrogen bond to all three of the enzyme's catalytic carboxylates and to the inhibitor. This is a feature unique to this type of inhibitor.

1.5.3.6 Thaumatin-like Inhibitors

The primary sequence of zeamatin (Figure 1.14), a protein isolated from corn, resembles that of thaumatin; it has antifungal properties and inhibits

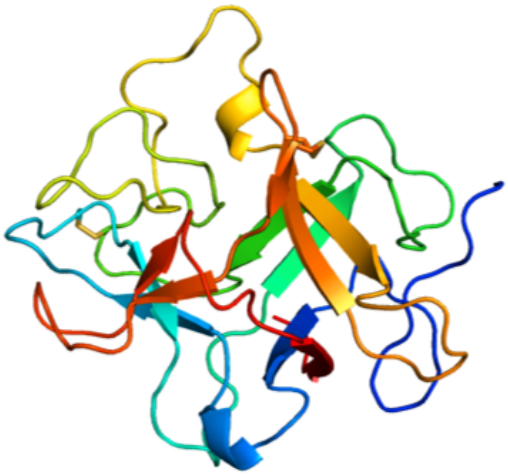

Figure 1.13: The tertiary structure of Barley Amylase/Subtilisin Inhibitor (BASI) (PDB ID, 1AVA, *185*).

both α-amylase and trypsin (*186*). Schimoler-O'Rourke, Richardson, and Selitrennikoff (*186*), testing for α-amylase residual activity, found that it has significant inhibitory activity towards insect α-amylases, but does not affect the activity of their mammalian or plant homologues. There is no crystal structure of this inhibitor in complex with an α-amylase, but the crystal structure of the inhibitor by itself reveals it to be composed of an 11 stranded β-sandwich against which an arm-like projection packs to form a distinct cleft (*187*). Further studies are needed to determine how this protein interacts with α-amylase, including how tightly it binds to the enzyme.

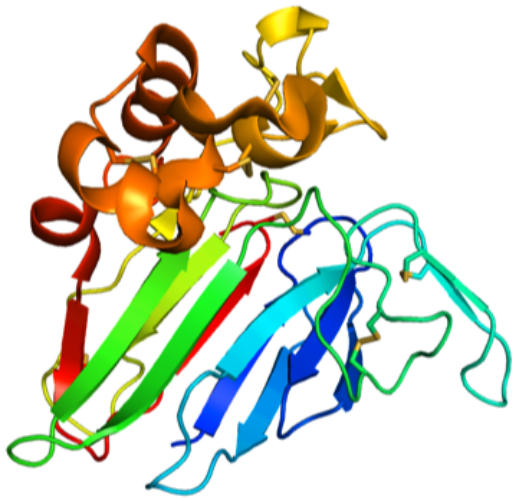

Figure 1.14: The crystal structure of zeamatin. This protein from maize inhibits both α-amylase and trypsin, as well as having antifungal properties (PDB ID: 1DU5, *187*, *188*).

1.5.3.7 Lectin-like Inhibitors

Three proteins from kidney bean inhibit α-amylases: αAI1 (Figure 1.15) inhibits mammalian and some insect α-amylases, while αAI2 inhibits insect α-amylases, for example those from *Zabrotes spp.*, but not those inhibited by αAI1; αAI3 is a more general inhibitor, and inhibits both mammalian and *Zabrotes subfasciatus* enzymes (*149*, *189–191*). Comparison of the sequences of the first two inhibitors and mutational studies show that this change in activity might be due to a Trp-Ser-Tyr motif near the C-terminal (residues 188-190) of αAI1 (*192*). Crystal structures of αAI1 in complex with PPA and TMA show that Tyr186, Tyr37, and Tyr190 of the inhibitor hydrogen bond with the enzyme's acid/base catalyst, nucleophile, and

third essential carboxylic acid (*193–197*). Although the active site cleft loops are shorter in TMA than in its mammalian homologs, it appears that the inhibitor maintains the same hydrogen bonding interactions in both TMA and PPA (*196*). This differs from the inhibitory action of the plant defensins, where differences in the sequence of active site loops of these two enzymes seem to relate to inhibitor specificity. The crystal structure of *Z. subfasciatus* α-amylase is not available for comparison, and the reason for αAI2 specificity is still unknown.

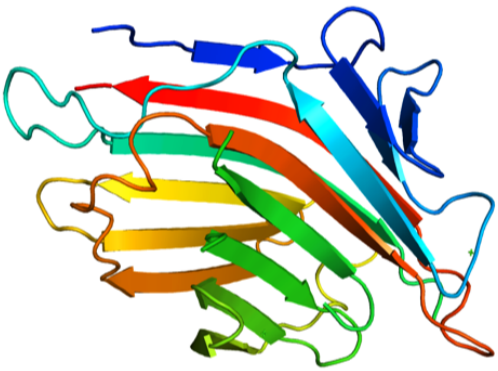

Figure 1.15: The structure of αAI1 from kidney bean as bound to PPA. The red and light blue loops on the right side of the diagram extend into the active site and interact with the catalytic carboxylates ((PDB ID: 1DHK, *193*)).

1.5.3.8 α-Amylase and Proteinaceous Inhibitor Complexes in the Protein Data Bank

The Protein Data Bank (PDB) contains 7 crystal structures of α-amylases in complex with proteinaceous inhibitors (Table 1.2). Six are naturally oc-

curring inhibitors such as those described above. Most are competitive inhibitors that block the active site of their target enzymes and prevent substrate binding, but some do show mixed noncompetitive inhibition. Generally, they have K_i values in the low nanomolar to picomolar range.

BASI (PDB ID, 1AVA) inhibits α-amylase by blocking the entire substrate-binding cleft, but does not enter the active site itself. The minimum distance between any of the catalytic carboxylates and this inhibitor is 4.5 Å. The other natural proteinaceous inhibitors all form hydrogen bonds to at least one of the catalytic carboxylates. The N-terminus of RBI (PDB ID, 1TMQ) hydrogen bonds with the third catalytic carboxylate (D300, HPA numbering), but the other three inhibitors, tendamistat, AAI and bean lectin-like inhibitor, all place a tyrosine near the catalytic nucleophile or acid/base catalyst. Tendamistat and AAI also form salt bridges to their respective enzymes through arginine residues; bean lectin-like inhibitor replaces this with a different salt bridge between an inhibitor aspartate and enzymatic histidine (H201, HPA numbering). The remaining crystal structure is a complex between PPA and an anti-PPA camelid VHH antibody (PDB ID, 1KXQ; K_i 10 nM). This small protein binds across the substrate-binding cleft to block substrate access. In this respect, it is most similar to BASI, although individual contacts with the enzyme are different, and the distance to the catalytic carboxylates is even greater at 8.5 Å.

Regardless of the differing structures of these peptide inhibitors, they all bind to α-amylase in one of two ways–they either act as a patch over

Table 1.2: Three Dimensional Structures of α-Amylase-Proteinaceous Inhibitor Complexes

Inhibitor Name	**α-Amylase**	**PDB ID**	**K_i or K_d (nM)**	**Reference**
Streptomyces inhibitors				
Tendamistat	Pig (pancreatic)	1BVN	0.009	(*152*, *155*)
Knottins				
AAI	Yellow meal worm	1CLV	–	(*164*)
CM Proteins				
RBI from Ragi	Yellow meal worm	1TMQ	15	(*43*, *177*, *180*)
Kunitz-type				
BASI	Barley Amy2	1AVA	0.22	(*185*)
Lectin-like				
Bean lectin-like inhibitor (-AI1)	Pig (pancreas)	1DKH	0.1	(*193*, *198*)
	Yellow meal worm	1VIW	–	(*196*)
Man-made				
Camelid VHH domain	Pig (pancreas)	1KXQ	10	(*151*)

the active site without approaching the catalytic residues, or they employ a combination of a salt bridge and a tyrosine that is placed next to or near the catalytic carboxylates. The repetition of these motifs in the various classes of peptide and protein inhibitors may indicate that there are very few ways in which a protein can achieve nano- or pico-molar inhibition of α-amylase.

1.6 HPA Inhibitor Screening

All but one of the inhibitors described in this thesis were found through a high-throughput screening process designed by Dr. Christopher Tarling from Prof Steve Withers' group. In this screen, large libraries of crude extracts from various organisms and known chemical compounds were screened for HPA inhibitory activity. These libraries included one from the National Cancer Institute, USA (crude extract), and the Canadian Chemical Biology Network; a library of marine product extracts provided by Prof. Raymond Andersen was also examined. The screen also took advantage of HPA's ability to transglycosylate glucose-based substrates and glucose analogs: the residual enzyme activity was compared between replicates with and without elongation agents. By plotting the residual activity for each extract/compound against its replicate with added elongation agent, any inhibitor hits that allowed for enzymatic rearrangement would have different residual activity when αGF was added; those that did not

would appear on the diagonal of the plot. These reactions used the chromogenic 2-chloro-4-nitrophenyl α-maltotrioside (CNP-G3) as a substrate, and were monitored by UV/Vis spectrophotometry at 405 nm.

In total, approximately 30 'hits' were identified and the most potent of these were subjected to bioassay-guided purification and structural elucidation by NMR and mass spectrometry (MS). The purification and identification process was carried out by Dr. Kate Woods and Dr. Rob Keysers from Prof. Raymond Andersen's group. Kinetic characterization of these purified inhibitors was carried out by Dr. Chris Tarling, Dr. Jacqueline Wicki, and Dr. Ran Zhang of Prof. Steve Withers' group.

Two of the inhibitors studied in this thesis were found through this screening process: montbretin A and amystatin. These were the most potent of the inhibitors found, eliminating almost all residual HPA activity. Montbretin A is a glycosylated acyl flavonoid isolated from an extract of the corms from *Crocosmia crocosmiflora*, and amystatin is a 44 amino acid peptide isolated from tissue of the Caribbean sea anemone *Stichodactyla helianthus*. Both are competitive inhibitors of HPA. Montbretin A inhibits HPA competitively with a K_i of 8 nM, while amystatin is a 44 amino acid peptide that contains 3 disulfide bonds and has a K_i of 2 nM. Both montbretin A and amystatin are highly specific for HPA, and inhibit other glycosidases poorly (*2*, *199*). Two montbretin A fragments, myricetin and ethyl caffeate are also HPA inhibitors with K_i values of 110 μM and 1.3 mM under competitive and noncompetitive models, respectively.

1.7 Specific Aims of this Study

The goal of this study is to characterize HPA-inhibitor complexes, using x-ray crystallography to gain insight about the enzyme and gain information that will lead to the development of new antidiabetic drugs. The main focus is on new high-affinity inhibitors that were discovered during screening of National Cancer Institute (NCI) and Canadian Chemical Biology Network (CCBN) natural product and known compound libraries for HPA inhibition.

The goal of the Montbretin A study is to use x-ray crystallography to show how this inhibitor binds to HPA, and to gain information about why it binds tightly. This is information that can be used to create new, derivative compounds that can act as lead compounds in the development of new drugs to treat type 2 diabetes and obesity. To help with this endeavour, the crystal structures of both the HPA-myricetin and HPA-ethyl caffeate complex structures will also be examined. The resulting model is also used to analyze the basis of the inhibitor's specificity for HPA.

The amystatin study has many of the same aims (i.e., the use of x-ray crystallography to elucidate the binding of this inhibitor to α-amylase). Also important is determining the tertiary structure of the peptide inhibitor itself, as well as its disulfide bond topology. The information so gained is crucial for expanding our knowledge of peptide inhibitors of α-glucosidases, most of which are derived from plant or bacterial sources.

Other peptides with similar binding affinity are much larger than amystatin, and the crystal structure of amystatin bound to HPA will either show which portions of these larger peptides are essential for inhibition, or will introduce a new class of α-amylase inhibitor. It will also lead to new ideas for possible drugs for the treatment of type 2 diabetes.

Chapter 2

General Methodology

This study serves to characterize the mode of action of strong binding inhibitors of HPA that show potential as drug candidates for the treatment of type II diabetes. The specific inhibitors analysed were discovered in a uniquely designed high-throughput screening process that examined over 70,000 compounds and natural product extracts for HPA inhibition. My work in this area took a structure/function approach, using protein x-ray crystallography techniques to elucidate how these inhibitory compounds interact with this enzyme and influence its mechanism. This information is critical as a base for the future improvement of lead compounds by suggesting molecular enhancements that can potentially enhance their usefulness as therapeutics.

2.1 Overview of Experimental Approach

As outlined in the preceding chapter, the global objective of this work is to gain a comprehensive understanding of how novel inhibitors bind to, and interact with, HPA in order to determine which features contribute to their affinity and specificity for this enzyme. This was a complex pro-

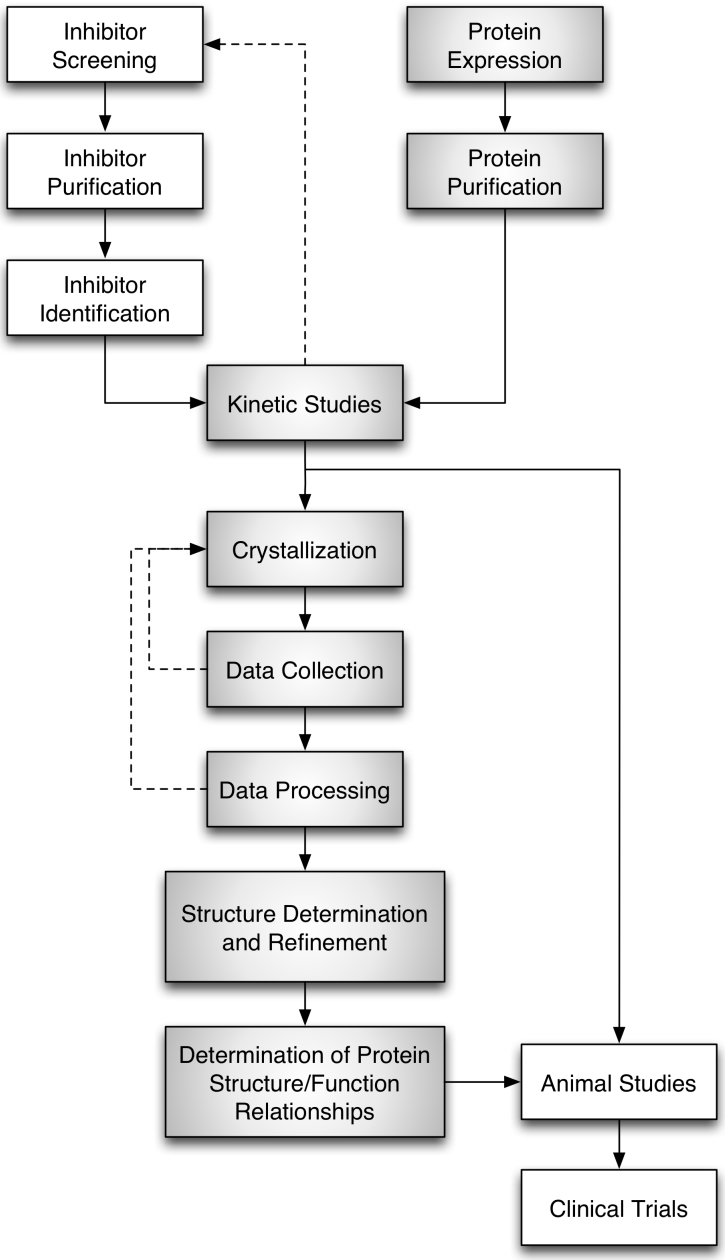

Figure 2.1: General Approach to HPA-inhibitor Identification and Characterization Used in this Study. The shaded boxes indicate areas in which experiments were performed as part of the work described in this thesis. Dashed lines indicate the location of decision points where a return to a previous step often proved to be necessary.

cess involving a number of steps as outlined in Figure 2.1. Initially, based on previous kinetic analyses of HPA (*60*, *71*), a two step high-throughput screening process was developed and used to examine a series of comprehensive sample libraries for potential inhibitor candidates that exhibit high affinity and specificity for HPA (*2*). In this screen, both known chemical and natural product libraries were analyzed. It is worth pointing out that prior to these studies the only high affinity carbohydrate-based HPA inhibitor identified had been acarbose, which was shown to undergo a number of enzymatic reactions before reaching its optimal inhibitory form (*200*). Unfortunately, acarbose lacks specificity for HPA and was found to bind tightly to a number of other α-glucosidases (*201*), thereby limiting its usefulness in medical applications related to HPA activity (*201*, *202*).

The active compounds from the best hits of inhibitor screening were identified and purified. These purified compounds were then subjected to kinetic tests against HPA to determine inhibition constants and the type of inhibition. The best of these proceeded to x-ray crystallographic and animal studies. These included the novel inhibitors montbretin A and amystatin, both of which are intensively analysed in this thesis.

The results of the crystallographic studies were compared to the structures of HPA by itself and in complex with known inhibitors, identifying features of the new inhibitors that are both novel and unique. The goal being to use the information so gained to form the groundwork that allows these inhibitors to be optimized for use as potential therapeutics in

the treatment of Type II diabetes. Indeed, animal testing in a diabetic rat model system has already demonstrated the efficacy of one of these inhibitors (*203*).

2.2 Source of Protein

2.2.1 HPA Expression and Purification

For my studies, HPA was expressed and purified using procedures developed by Dr. Edwin Rydberg of Prof. Steve Withers' group (*51*). The *Pichia pastoris* cells containing a pPIC9 vector with the human pancreatic α-amylase gene were provided by Dr. Chunmin Li and Dr. Ran Zhang. These cells were plated on MD plates (3 g agar, 160 mL distilled water, 20 mL 10X yeast nitrogen base, 0.4 mL 500X biotin, 20 mL 10X dextrose for 6 plates), and left to incubate at 30°C for 3 days until colonies were visible. Single colonies were then transferred to 5mL samples of BMGY medium (80 g yeast extract, 160 g peptone, 5600 mL distilled water, 800 mL 1M potassium phosphate buffer, pH 6.0, 800 mL 10X yeast nitrogen base, 16 mL 500X biotin, 800 mL glycerol). These samples were grown overnight at 30 °C and then were transferred to 2L baffled flasks containing 500 mL of the same medium, and 200 µL of antifoam C (Sigma) was added to each flask. These were incubated for another 2 days at 30°C.

After 2 days, the cells were spun down at 6000 rpm for 15 minutes at 4°C. The supernatant was discarded and the cells were resuspended in 100 mL of BMMY media (10 g yeast extract, 20 g peptone, 700 mL distilled water, 100 mL 10X yeast nitrogen base, 2 mL 500X biotin, 100 mL 10% (v/v) methanol, 100 mL 1M potassium phosphate buffer, pH 6.0). Additionally, 50 μL of antifoam C was added to each flask. The cells were then grown in the shaker at 30°C for 2 days, adding 1 mL of 50% (v/v) methanol twice daily. Samples of the supernatant were collected every day to run 12% SDS PAGE gels to monitor expression. After 2 days, the cells were spun down again in exactly the same manner as described above. The salt concentration of the supernatant was adjusted to 0.5 M NaCl by adding the necessary amount of 5 M NaCl, and the cells were discarded.

The amylase was then purified by filtering the supernatant through a 0.45 μm filter and then loading it onto a 30 mL Phenyl Sepharose column equilibrated with 0.5 M NaCl, 100 mM potassium phosphate buffer, pH 7.5 (loading buffer). The column was then washed with 300 mL of loading buffer before eluting with distilled water on a GradFrac system, collecting 5 mL fractions.

The fractions containing HPA also contained a vivid green contaminant. In order to remove this, the positive fractions were concentrated down to a total volume of 4 mL, by forcing the supernatant through 30 kDa Amicon filters at 3500 rpm and 18°C. The resulting concentrate was a very dark green colour. The pH and salt concentrations of the concen-

trate were then adjusted to 20 mM potassium phosphate, pH 6.9 and 25 mM NaCl (cutting buffer). Then, 5 μL of Endoglycosidase F solution (0.05 U/μL), prepared by Emily Kwan, was added to the sample which was left to incubate at 4°C for 2 days in order to deglycosylate the HPA.

Finally, to remove the green contaminant and the endoglycosidase F, a 5 mL Q-Sepharose column was prepared and equilibrated with 50 mL of the cutting buffer. The sample was loaded onto the column, and the eluent, which contained the HPA, was collected. This protein was now ready to be transferred to the crystallization buffer. The HPA H299N variant protein used in the montbretin A studies was isolated in the same manner, and was provided by Yili Wang.

2.2.2 Purification of Porcine Pancreatic α-Amylase

PPA was kindly provided by Dr. Adeleke Aguda. Starting with PPA ordered from Sigma (A4268), he further purified it by diluting 10 mg of the purchased protein solution in 20 mM Tris, pH 8.0 and loading it onto a mono Q ion exchange column. PPA was then eluted against a gradient of 20 mM Tris, pH 8.0, 1 M NaCl. Fractions of the purified protein were then pooled together and concentrated by buffer exchange to 10 mg/mL in 0.1 M Tris, pH 8.5.

2.3 Protein Crystallization

Protein crystallography is the primary technique used in the studies herein, and as a first step requires the growth of suitable crystals of the molecular structure to be solved. This section describes the general characteristics of protein crystals and introduces the methodology used to produce the amylase crystals used in this study. For a more detailed description of protein crystallization methods, the reader is referred to McPherson (*204*), and Bergfors (*205*).

2.3.1 The Crystalline State

Protein crystals are an ordered, three-dimensional array of molecules, held together by non-covalent interactions. They are made up of many repetitions of a minimal unit, called the unit cell, stacked together like bricks. The unit cell is the smallest volume that can represent the contents of the crystal as a whole. This often consists of more than one protein molecule, because it represents not only the volume of the protein molecule itself, but also symmetry relations between adjacent protein molecules. A crystal can thus be described using three parameters: a space group, indicating how the protein molecules are packed together, the unit cell dimensions, and the angles between the axes formed by the unit cell. The unit cell is itself most often composed of one or more 'asymmetric units' that represent the minimal repeating unit of the crystal without any indication of

symmetry relationships. The goal of an x-ray crystallography experiment is to determine the contents of this unique asymmetric unit.

2.3.2 Preparation of Protein Crystals

Protein crystals are most often grown by dissolving the protein in a suitable buffer solution that contains a precipitation agent at a concentration just below that which will cause the protein to fall out of solution. The concentration of the precipitation agent is then slowly increased so that an equilibrium forms in which the protein exists in both solid and liquid states. Crystal nuclei can then form and the crystal grows by joining these units together, adding blocks to the crystal lattice. The formation of optimal interactions between protein molecules and the release of solvent drive crystal growth.

Unfortunately, there is no way to determine *a priori* which buffer and precipitant combinations or concentrations will allow crystals to form; thus, many possibilities must be tested before crystals can be grown. Furthermore, even initially identified successful combinations must be further optimized to control the rate of crystal growth and finally produce a diffraction quality crystal of sufficient size for use in structure determination experiments.

2.3.3 Hanging Drop Vapour Diffusion

Hanging drop vapour diffusion is one method that can be used to slowly change the precipitant concentration of a protein in order to form crystals. In this technique, a small drop of protein solution (usually 1-5 μl) is mixed with another drop of solution containing the precipitation agent on a microscope cover slide (usually in a 1:1 (v/v) ratio). The slide is then sealed over a large volume (1 mL) of the undiluted precipitant solution. A diagram of the setup for this type of experiment is shown in Figure 2.2.

Since the precipitant concentration is much greater in the reservoir, as the system equilibrates, there is a net movement of water molecules through the vapour phase from the suspended drop to the reservoir. If the protein slowly reaches a state of supersaturation during this process, crystals can form. Note that to identify the proper conditions for crystal growth, many such crystallization trials must be conducted over a wide range of parameters altering the buffer, precipitant, temperature, and additives. For this reason these experiments are usually conducted in multi-well plates that allow for a gradation of solution conditions to be examined.

All of the crystals used in this thesis were grown with the hanging drop vapour diffusion method and descriptions of the exact conditions used can be found in subsequent chapters.

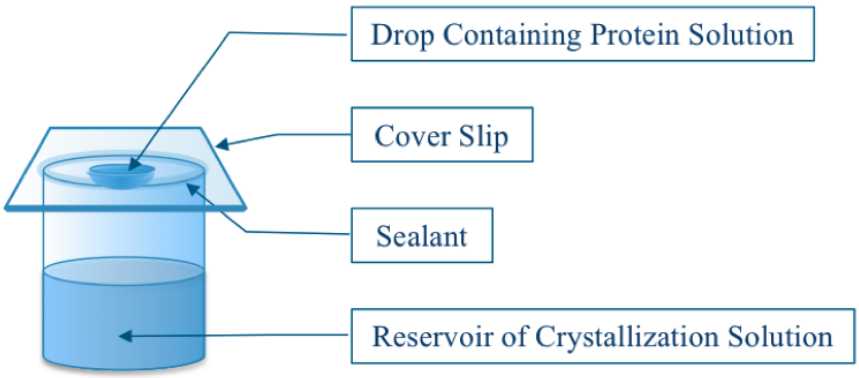

Figure 2.2: The Hanging Drop Vapour Diffusion Method for Protein Crystallization.

2.4 Theory of X-Ray Diffraction

This section describes in brief the diffraction of x-rays by crystals and the mathematics used to obtain atomic structure from a diffraction pattern. This discussion is by no means comprehensive, and the reader is referred to Blundell, and Johnson (*206*), Stout, and Jensen (*207*), Rhodes (*208*), McRee (*209*), Drenth (*210*) and Giacovazzo (*211*) for more detailed treatments of the subject.

2.4.1 Diffraction of X-Rays by Matter

X-rays are electromagnetic radiation with wavelengths between 10^{-8} and 10^{-11} m. When these high-energy waves interact with matter, their electric field exerts a force on charged particles causing them to oscillate at the

same frequency as the radiation. The charged particles then emit radiation that is scattered in all directions. The electric field, E_d, of the scattered radiation is proportional to the square of the charge and inversely proportional to its mass. When we observe the electric field at a point defined by positional vector, r, in the x,y plane at time t, we observe that

$$\mathbf{E}_d = \mathbf{E}_{0d} \exp\left[2\pi i\nu\left(t - \frac{\mathbf{r}}{c}\right) - i\alpha\right] \tag{2.1}$$

and

$$\mathbf{E}_{0d} = \frac{1}{\mathbf{r}} E_{0i}\left(\frac{e^2}{mc^2}\right) \sin\psi \tag{2.2}$$

where $\mathbf{E}_0$ is the amplitude of the wave, ν is its frequency, α is the phase lag with which the electron reemits the radiation and ψ is the angle between the direction of acceleration and the direction of observation. The quantity (e^2/mc^2) is the scattering amplitude of the electron, where e is the charge and m is the particle's mass. This last quantity explains the absence of scattering by neutrons, and the poor scattering power of protons, whose factor $(e/m)^2$ is tiny compared to that of the electron.

Each electron acts as an independent scatterer, but the waves emitted in a single direction by all of the electrons in an atom are superimposed to form the atomic scattering factor, $\mathbf{F}$.

$$\mathbf{F}(\boldsymbol{S}) = \int_\nu \rho(\mathbf{r}) e^{(2\pi i \mathbf{r}\cdot S)} dV \tag{2.3}$$

This equation describes the total wave scattered (F) as the sum of all individual waves scattered by the electron density (ρ) at position r integrated over the volume (V) of the atom. (S) is the scattering vector; that is, the vector needed to turn the incident x-ray to the direction of the scattered x-ray. Each atom type has its own characteristic scattering factor.

2.4.2 Diffraction of X-rays by the Crystal Lattice

Bragg's Law stipulates that under specific conditions, we can treat the waves scattered by the crystal as though they are reflected by planes in the crystal lattice. This concept is illustrated in Figure 2.3. When treating scattering in this way, planes are drawn through the crystal lattice points, and are defined by the Miller indices, h, k, and l. Each set of equidistant, parallel planes acts as a single diffractor that produces a single reflection as long as the angle of incidence, θ, remains constant. Using this construction, we can relate the electron density in the real space unit cell to the structure factors of the sets of planes, F_{hkl}.

$$\rho(x, y, z) = \frac{1}{V} \sum_{h} \sum_{k} \sum_{l} F_{hkl} e^{-2\pi i(hx+ky+lz)} \tag{2.4}$$

The structure factor contains information about both the phase and the intensity of the waves reflected from the planes.

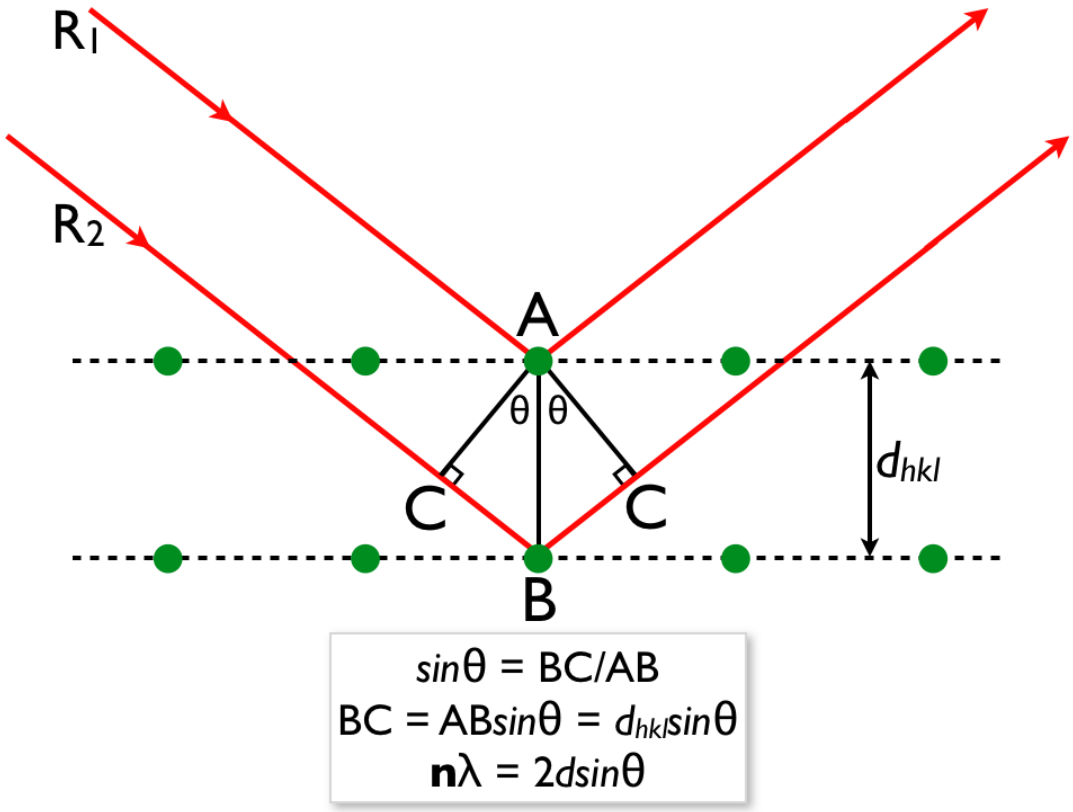

Figure 2.3: Bragg's Law and the Conditions Necessary for Constructive Interference. θ is the angle of incidence, d_{hkl} is the distance between the planes formed by the crystal lattice, R_1 and R_2 are parallel x-ray waves, n is any positive integer, and λ is the wavelength. For a constant value of θ, constructive interference only occurs if Bragg's Law, $n\lambda = 2d_{hkl}\sin\theta$ is true.

2.4.3 The Crystallographic Phase Problem

The structure factor, F_{hkl}, can be broken down into its component parts: an amplitude term, $|F_{hkl}|$, proportional to the intensity of the recorded reflections, and a phase term, α_{hkl}.

$$\rho(x, y, x) = \frac{1}{V} \sum_{h} \sum_{k} \sum_{l} |F_{hkl}| e^{i\alpha_{hkl}} e^{-2\pi i(hx+ky+lz)} \tag{2.5}$$

One of the significant hurdles in determining the structure of a macromolecule by x-ray crystallography is that the phases of the diffracted waves cannot be measured, and thus a significant proportion of the information needed to solve the structure is missing. A number of methods have been devised to overcome this problem, and acquire estimates of the phases that can be used to begin structure refinement. The method used for all of the crystal structures in this study is called molecular replacement.

2.4.4 Molecular Replacement

When phases from the structure factors of known protein models are used as initial phase estimates for a new crystal structure, this is known as molecular replacement, and the model from which the phases were taken is the phasing model. In this study, both isomorphous and non-isomorphous models were used for phasing. The advantage of using isomorphous phasing models is that the electron density of the target protein can often be

calculated directly from the phases of the phasing model:

$$\rho(x, y, z) = \frac{1}{V} \sum_{h} \sum_{k} \sum_{l} \left| F_{hkl}^{target} \right| e^{-2\pi i(hx+ky+lz-\alpha_{hkl}^{model})} \tag{2.6}$$

This method can only work when the space group for both phasing model and target dataset are the same, and the dimensions of the two unit cells are similar (within 1-2%).

When the location of the atoms in the unit cell of the target protein is too different from the location of the same atoms in the phasing model (a non-isomorphous model), we must superimpose the asymmetric unit of the phasing model, or portions thereof, onto that of the target protein before calculating the initial phase estimates. This is done in two steps.

Firstly, the best rotational orientation of the phasing model's unit cell is calculated using a Patterson and a rotation function:

$$P(u, v, w) = \frac{1}{V} \sum_{h} \sum_{k} \sum_{l} |F_{hkl}|^2 e^{-2\pi i(hu+kv+lw)} \tag{2.7}$$

$$R(\psi, \phi, \chi) = \int_{u,v,w} p^{target}(u, v, w) p^{model} \{(u, v, w) \times [\psi, \phi, \chi]\} \, du \, dv \, dw \tag{2.8}$$

The Patterson function calculates a map of vectors between all atoms in the unit cell while the rotation function evaluates the correlation between Patterson maps for the phasing model and target model. If one Patterson map has a peak where the other does not, the product will be 0, and thus,

maxima occur when the Patterson map of the phasing model has been rotated into an orientation that best describes the Patterson map of the target. This method gives a set of possible orientations for the unit cell of the phasing model. In order to determine which, if any, of these orientations can be used to phase the target structure, a further translation search must first be performed.

This second, translation function search in non-isomorphous molecular replacement compares the structure factor amplitudes calculated from the phasing model in a specific trial location to those observed in the target dataset. Correspondence is measured as an R-factor as the unit cell of the phasing model is moved through a 3-dimensional grid.

$$R = \frac{\sum ||\mathbf{F}_{obs}| - |\mathbf{F}_{calc}||}{\sum |\mathbf{F}_{obs}|} \tag{2.9}$$

The lower the R-factor, the better the trial location of the phasing model's unit cell is, given a specific solution to the rotation function (Eq. 2.8) above. The phases calculated from the new location and orientation of the phasing model's unit cell can then be inserted into equation 2.6 and, along with the structure factor amplitudes from the new dataset, be used to generate the first electron density map of the target structure. These initial phase estimates will gradually be improved using an iterative refinement process that leads to a structure that is in good agreement with the observed structure factor amplitude data measured for the target molecule.

2.5 Data Collection, Processing and Refinement

This section describes how the data used in this study were collected, and then processed to obtain structure factor amplitudes from the images of the diffraction pattern. It also explains how the data were refined to a final structure once phase estimates were added, and how the validity of the models was judged.

2.5.1 Synchrotron Radiation

The x-rays used in all of my crystallographic studies were generated using a synchrotron. A synchrotron works by bending the path of electrons that have been accelerated to near-relativistic velocities. The acceleration exerted on these electrons by the bending magnets causes them to emit radiation that is proportional to their kinetic energy and to the angular frequency of the arc of the bent path. The kinetic energy of the electrons depends on the energy of the synchrotron's storage ring.

Even though radiation is emitted by these accelerated electrons in all directions, to an observer in the lab frame, it is seen as being emitted as a cone of light tangential to the electron's path. This is due to a Doppler shift caused by the particles' motion. Once emitted, the radiation is directed to beam lines placed tangentially to the path of the storage ring. The beam lines focus and filter the light so that only a narrow beam of the desired wavelength reaches the hutch where the X-ray diffraction ex-

periment takes place. Each beam line has monochromators that handle the light differently, not only because different types of experiments need different wavelengths of incident radiation, but also because the properties of the light itself depend on the configuration of the magnetic fields used to generate it. Thus, each beamline is optimized for a specific type of experiment.

A more detailed description of synchrotron radiation and associated instrumentation can be found in Hofmann (*212*) and Willmott (*213*).

2.5.2 Data Collection

In the hutch at the synchrotron beam line, the protein crystal of interest, having been mounted onto a nylon loop and flash frozen in liquid nitrogen, is mounted by a robot onto a goniometer, a device that holds it in the correct position for a diffraction experiment. The crystal is kept frozen by being surrounded by a stream of nitrogen gas cooled to liquid nitrogen temperatures. Test images are then taken, allowing a strategy for the rest of the data collection run to be devised. Once decisions about beam strength, beam size, exposure time, oscillation angle, and detector distance have been made, data were collected and processed using either of the software packages: Mosflm (*214*, *215*) or XDS (*216*). In both of these programs, diffraction intensities are integrated using a profile fitting routine described by Rossmann, Leslie, Abdel-Meguid, and Tsukihara (*217*). In this method, the level of background radiation is measured from the ob-

served intensity surrounding the measured and integrated intensity peaks on the diffraction images. Partial reflections that span two or more measured diffraction frames are combined to form single reflections, and corrections are then made to the full data set; these include Lorrentz and polarization corrections for the beam geometry and crystal orientation used, as well as any necessary corrections specific to the detector.

To this point, each observation of a single reflection has been treated independently, but before any can be used to calculate structure factors, they are scaled to compensate for fluctuating beam intensity, and radiation damage, and then identical reflections related through unit cell symmetry are merged. Structure factor amplitudes and estimated errors are then calculated from the intensities using the following equation:

$$F = \sqrt{I} \pm \frac{1}{2} \cdot \frac{\sigma(I)}{\sqrt{I}} \tag{2.10}$$

These structure factor amplitudes are then combined with the initial phase estimates determined by molecular replacement to calculate the first electron density map of the molecular structure being examined.

2.5.3 Iterative Refinement of Initial Models

The structure of the phasing model used, not only enables the calculation of phase estimates as described in section 2.4.4, but also becomes the first structural model, or at least in part depending on similarity to the

target molecule, of the protein to be placed within the electron density map. Subsequently, this initial model is improved by alternating least squares refinements of the atomic coordinates and manual adjustments of the model, moving atoms where necessary and in the case of complexes, building inhibitors into the available remaining empty density. The progress of structural refinement is monitored with the crystallographic R-factor, which measures the agreement between the structure factors from the experimental dataset and those calculated from the structural model:

$$R_{cryst} = \frac{\sum_{hkl} \left| \left| F_{hkl}^{obs} \right| - \left| F_{hkl}^{calc} \right| \right|}{\sum_{hkl} \left| F_{hkl}^{obs} \right|} \tag{2.11}$$

A low R-factor means that there is good agreement between the structural model and the experimental data. Experience has shown that for well-refined structures, the final R_{cryst} for the refined model should be between 0.10 and 0.20.

In this study, structural refinements were carried out using a maximum likelihood function that describes the posterior probability that we will observe the original dataset given the structural model, $\mathtt{prob}(\mathtt{data}|\mathtt{model})$ (*218*). The aim of refinement is to minimize the residual of the target function:

$$E_{ML} = \sum_{hkl \in \text{working set}} \left(\frac{1}{\sigma_{ML}^2} \right) \left(|F_o| - \langle |F_o| \rangle \right)^2 \tag{2.12}$$

In this equation, we calculate the difference between the observed structure factors, F_o, obtained from the experimental data, and the expected value $\langle F_0 \rangle$, which is derived from F_0, the structure factors calculated from the model, F_c, and σ_A, a statistical weighting term that accounts for errors and incompleteness in the model and is calculated from a portion of the data set kept aside for cross-validation. σ_{ML} is also derived from F_o, F_c and σ_A; it estimates the error in both the experimental data and the structural model. It is also important to note that refinement only takes place over the reflections in the working set, leaving the rest unrefined for cross-validation purposes. During refinement, the stereochemical parameters of the structural model are held within acceptable bounds using restraints that define bond distances, angles, planar groups, chiral centres, torsion angles, hydrogen bonds, non-bonded contacts and thermal motion.

Importantly, between rounds of *in silico* refinement, the refined structural model and its associated electron density are carefully examined and adjusted manually in order to correct positional errors remaining due to the small radius of convergence of the target function. The most important tool for manual adjustments is the difference electron density map, the equation of which is an expansion of equation 2.5.

$$\Delta\rho(x,y,z) = \frac{1}{V}\sum_{h}\sum_{k}\sum_{l}\left(\left|F^{obs}_{hkl}\right| - \left|F^{calc}_{hkl}\right|\right) e^{-2\pi i(hx+ky+lz)} \qquad (2.13)$$

Electron density calculated in this way shows positive peaks where there should be atoms in the structure that are not yet present in the refinement model, while negative peaks will be present in the map wherever there are atoms in the model, the presence of which is not supported by the experimental data.

A common variation of this type of map is the $2\mathbf{F}_o$-$\mathbf{F}_c$ map which uses the same form as equation 2.13, only $\mathbf{F}_{hkl}^{obs}$ is replaced by $2\mathbf{F}_{hkl}^{obs}$, thereby increasing the size of the positive peaks. This superimposes the native $\mathbf{F}_o$ map onto the difference map, in order to make interpretation easier. Another useful modification of the difference electron density map is the omit electron density map where the atoms of the part of the model under scrutiny are deleted before calculating $\mathbf{F}_{calc}$ and α_{calc}. In many cases this serves to remove bias that might be generated by errors in that portion of the structural model and thereby assist in the clarification of any structural corrections needed. In the structural analyses conducted in thesis, it was the practice to calculate difference, $2\mathbf{F}_o$-$\mathbf{F}_c$ and omit electron density maps over the entire course of the polypeptide chain to assure the best fit of the structural model to the experimentally measured structure factors.

2.5.4 Evaluating the Validity of the Refinement Structural Model

In order to cross-validate the structural model, the R-factor described in equation 2.11 is calculated twice: once as R_{cryst} on the working set of reflections that are used in refinement, and once as R_{free} on a test set of reflections that are omitted from refinement (usually 5-10% of the total data set). The R_{free} value calculated from the structure factors of the unrefined test set is a measure of the phase accuracy of the structure and is related to the mean phase error (*219*). Ideally these two R-factors will have comparable values. Notably, the R_{free} value is less prone to overfitting than the R_{cryst} value, and can suggest how to reduce the errors in the model caused by atoms built into what is noise in the electron density maps. However it is important to remember that these R-factors are a global measure of model accuracy and do not preclude local errors in the atomic structure even when both are low and in close agreement.

From a structural geometry perspective, the software programs, PROCHECK (*220*) and MolProbity (*221*) were used after each round of refinement and helped identify potential problem areas within the structures being refined. Both programs compare properties of the refinement model, such as stereochemistry, backbone torsion angles and interatomic distances to the values expected based on a large collection of known structures. PROCHECK is particularly useful in identifying geometry pa-

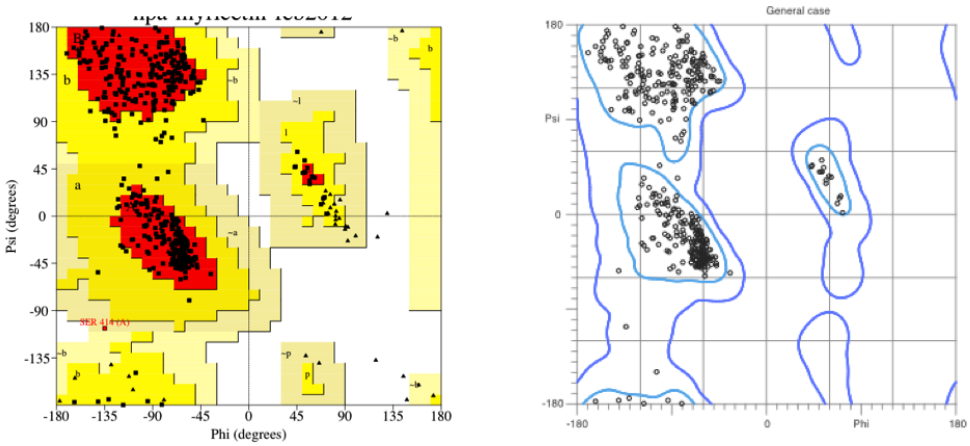

(a) PROCHECK (b) Molprobity

Figure 2.4: Comparison of Ramachandran plots generated by (a) PROCHECK and (b) Molprobity, for the HPA+myricetin structure (PDB code: 4GQR) described in this thesis. The triangles in plot (a) represent glycine residues, and are not shown in plot (b). Note that the boundaries in each plot are slightly different, with the older, PROCHECK plot having a more generous allowable area (in yellow) than Molprobity (darker blue line).

rameter outliers and also provides a Ramachandran plot that highlights potential problems with backbone torsion angles. MolProbity accomplishes many of the same tasks as PROCHECK, but adds hydrogen bonds to all residues before analysing the structure for potential close contacts or other geometry problems. This allows for an investigation of hydrogen bonding networks, as well as a more sensitive assessment for all atom contact analyses. Any significant deviations from ideal geometry identified by these programs were examined in electron density maps to verify whether they were, in reality, outliers and were corrected, if necessary. All close contacts and overlaps were adjusted to conform to the ideal values. A comparison of the Ramachandran plots output by PROCHECK and Molprobity is shown in Figure 2.4.

Chapter 3

Structural Studies of Small Molecule Inhibitors of Human Pancreatic α-Amylase

3.1 General Introduction

The most studied α-amylase inhibitor is acarbose, a naturally occurring inhibitor that is used as an antihyperglycemic drug. This pseudotetrasaccharide comprises a valienamine moiety linked through a nitrogen in a pseudo α-1,4 linked bond to deoxymaltotriose (see Figure 1.5 on page 21). When acarbose binds to HPA it is not inert; in fact, it undergoes a series of transglycosylation reactions that add a maltosyl group to the non-reducing end of valienamine and remove a glucose from the reducing end (*60*, *200*). Indeed, such transglcosylation reactions are common for α-amylases (*85*, *87*, *88*), and have been used to reveal substantial information regarding the enzyme and its mechanism (*70*, *71*, *222*). These studies capitalise on α-amylase's ability to elongate inhibitors to produce a molecule that binds more stably to the enzyme, and reveal much about the manner in which the amylase binds its natural polymeric substrate. This is because they must bind with the enzyme in a manner similar enough to

that of amylose that the enzyme is not completely inhibited, and that they become substrates themselves. What such inhibitors cannot do is reveal novel interactions with a foreign molecule, interactions that are essential to the development of new and better drugs for type II diabetes.

Three small molecules have been chosen to examine the possibility of new protein-inhibitor interactions: voglibose, myricetin and ethyl caffeate. Voglibose, an N-substitued derivative of valiolamine (*91*) , is currently used as an antihyperglycemic therapy to prevent spiking of blood glucose levels after meals. Its primary targets are the brush border disaccharidases, but it is also a weak α-amylase inhibitor (*92*). It is made up of a valiolamine ring attached through the nitrogen atom to a 1,3 propane diol. While structurally similar to the valienamine of acarbose, voglibose is unlikely to form the stable half-chair conformation that makes acarbose a good transition state analog, and as a monosaccharide mimic it is expected to bind poorly to HPA's existing carbohydrate binding subsites. This opens up the possibility of new interactions forming between this inhibitor and the protein.

Bioflavonoids are secondary plant metabolites, and have been shown to have many potential health benefits for humans including lower prevalence of heart disease and some types of cancer (*223–226*). This occurs due to their antioxidant properties as well as the ability to act as enzyme inhibitors. Flavonols, a subclass of flavonoids, have been studied as α-glycosidase inhibitors (*108*, *120*, *124*, *129*, *134*, *227*). Myricetin (Figure 3.1)

is a flavonol that acts as a competitive inhibitor of HPA with a K_i of 110 μM; it also forms the core of a much more potent, 8 nM, HPA inhibitor, montbretin A (*2*). Montbretin A will be discussed in detail in the following chapter.

The planar structure of myricetin imposes many constraints on the way it can bind to the enzyme and obviates its use of the enzyme's standard polysaccharide binding subsites (*71*). This makes it a good candidate for structural studies aimed at discovering new HPA inhibitor binding modes.

The final inhibitor to be discussed in this chapter is ethyl caffeate (Figure 3.1). This was chosen for two reasons. Firstly, like myricetin, it forms part of the 8 nM HPA inhibitor, montbretin A; it is also a noncompetitive inhibitor of this enzyme, with a K_i of 1.3 mM (*2*). Caffeic acid derivatives have been studied as α-glycosidase inhibitors (*135*, *228–230*), but only a few studies have revealed a noncompetitive mode of inhibition (*231*, *232*), and none of these have included structural data. Since the binding of ethyl caffeate does not preclude substrate binding in the active site, and all HPA

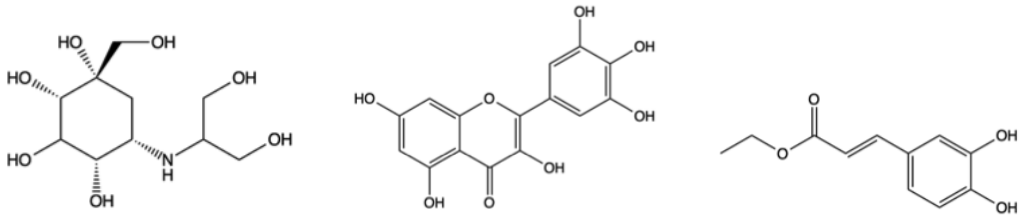

(a) (b) (c)

Figure 3.1: The chemical structures of voglibose (a), myricetin (b), and ethyl caffeate (c).

inhibitor studies to date show either competitive or uncompetitive kinetics when they become substrates themselves, it is an ideal candidate for structural studies to reveal new modes of action and new relationships with the enzyme.

3.2 Specific Aims of this Study

Small molecule inhibitors that cannot be transglycosylated were chosen for crystallographic studies to show how these small molecules interact with HPA, and demonstrate how these binding modes differ from those of inhibitors that can act as substrates for the enzyme. Voglibose was used in part due to its clinical use as an α-glucosidase inhibitor to prevent postprandial hyperglycemia. It is also a monosaccharide mimic that is inert to the enzyme's activity.

Myricetin and ethyl caffeate were chosen to elucidate the interactions between flavonols or caffeic acid derivatives and HPA. It was expected that these would reveal new binding modes and relationships, since neither can mimic the enzyme's carbohydrate substrate. They were also chosen because a much stronger HPA inhibitor, montbretin A, contains both. It was hoped that studying the small molecule inhibitors in isolation would uncover additional information about how this larger molecule becomes an 8 nM HPA inhibitor. Discussion of these molecules in relation to montbretin A will occur in chapter 4. It was also hoped that analysis of the

crystal structures of voglibose, myricetin and ethyl caffeate in complex with HPA would reveal novel interactions with the enzyme that could be exploited in the design of future α-amylase inhibitors.

3.3 Methods

3.3.1 Expression, and Purification of Wild-Type HPA

Details of the protocols used for the expression and purification of HPA can be found in section 2.2.1

3.3.2 Crystallization of Wild Type HPA

Wild type HPA was crystallized using the hanging drop vapour diffusion method according to established procedures (*51*). The crystallization media were prepared by mixing the HPA crystallization buffer (100 mM sodium cacodylate, pH 7.5) with an equal volume of 40%-60% MPD (2-methyl-2,4-pentanediol) (v/v), preparing 5 different MPD solutions. 1 ml of each crystallization medium was added to 12 wells in a 24 well tissue culture plate. The hanging drops were prepared by placing 4 μL drops of the purified HPA solution onto siliconized cover slips and then adding an equal volume of crystallization medium from the well to each drop. These slides were then inverted and sealed over the wells using vacuum grease.

The plates were stored at room temperature for 3 months before crystals appeared.

3.3.3 Inhibitor Soaking

All crystal soaking experiments described in this chapter were conducted in collaboration with Dr. Chunmin Li.

3.3.3.1 Soaking Voglibose into Wild-Type HPA Crystals

To prepare the inhibitor solution used to soak the HPA crystals, 500µl of mother liquor was removed from the crystallization well and the well was resealed. A small amount of voglibose was added to the solution and mixed. If the solution remained clear, more voglibose was added and the solution was mixed again. The goal was to create a solution of mother liquor that was saturated with voglibose. When no more inhibitor would dissolve, the solution was left overnight at room temperature and was then centrifuged to force any solid particles into a pellet at the bottom of the tube. The supernatant was used to soak the HPA crystals.

Once the soaking solution had been prepared, the well was re-opened and 100 µl of the mother liquor was added to a well in a glass plate. The crystals were then transferred from the cover slide to the liquid in this well. This was performed under the microscope to observe any visible changes to the crystal structure. When none were observed, 200 µl of the

voglibose solution was added to the well in 20μl aliquots, checking for any visible signs of damage to the crystals after each addition. The well was then covered and left at room temperature as the inhibitor diffused into the crystals. Crystals were removed from the well at 30 minute intervals, mounted on nylon loops and flash frozen in liquid nitrogen, ready for data collection at the Stanford Synchrotron Radiation Lightsource (SSRL) in California.

3.3.3.2 Creating the HPA-Myricetin Complex Crystals

The HPA-myricetin complex crystals were created by soaking myricetin into wild-type HPA crystals as described in section 3.3.3.1. A small amount of solid myricetin was then added to one edge of the mother liquor in the soaking well, as far as possible from the crystals. A small mound of undissolved myricetin remained in the well for the rest of the experiment, gradually increasing the amount of inhibitor available to bind to the crystals until a saturated solution formed. This was done because previous attempts to soak flavonols into HPA crystals had failed due to the low solubility of the inhibitors. Soaking studies with geraldol, fisetin, quercetin, and scutellarein had been attempted without success: the crystals either did not diffract or did not contain enough inhibitor to be seen in electron density maps. Adding Dimethyl Sulfoxide (DMSO) to the soaking solution to increase solubility had swiftly destroyed the crystals. Success with the myricetin crystal soaking trials is likely due to the large number

of hydroxyl groups on this particular flavonol. After solid myricetin was added to the wells, crystals were removed from the solution and frozen at half hour intervals. The crystals that diffracted to give usable data had been soaked for three hours.

3.3.3.3 Soaking Ethyl Caffeate into Wild-Type HPA Crystals

The HPA-ethyl caffeate crystals were formed by soaking ethyl caffeate into wild-type HPA crystals in the same manner as described in section 3.3.3.2. Crystals were collected from the soaking solution at half hour intervals for 8 hours. Another soaking solution was prepared in the same manner and left overnight. The crystals that diffracted to give usable data had been soaked for fifteen hours.

3.3.4 Data Collection and Processing

High-resolution data for HPA-voglibose complex crystals were collected remotely on an ADSC Quantum 315R detector using beam line 7-1 at the SSRL (*233–235*). 180 frames of data were collected at a wavelength of 0.9794 Å using a 1° oscillation.

Data for the HPA-myricetin and ethyl caffeate complex crystals were collected remotely on a Mar 325-CCD detector using beam line 11-1 at the SSRL (*233–235*). 120 frames of data were collected at a wavelength of 0.9794 Å using a 1° oscillation. Data were processed using Mosflm and

scaled using Scala (*236*, *237*). Data collection, processing and refinement statistics are summarized in Table 3.1.

3.3.5 Structure Phasing

Initial phases for the HPA-voglibose complex structure were obtained through molecular replacement using the coordinates of HPA as expressed in *Pichia pastoris* (PDB code 1BSI, *51*) as a starting model. Of the two crystal forms of the native HPA crystals, this was most dissimilar to the unit cell dimensions shown in the HPA-voglibose data. A clear solution was found after running the cross rotation and translation scripts in CNS (*238*). This was followed by rigid body refinement, and the resulting coordinates were used for subsequent structural refinement.

Phasing for the HPA-myricetin and HPA-ethyl caffeate complex structures was done in the same manner as for the HPA-voglibose complex using HPA isolated from human pancreas as the starting model (PDB code 1HNY, *45*). Unlike the myricetin complex, which has a similar unit cell to 1BSI, the unit cell of the ethyl-caffeate complex differed from both structures of wild-type HPA, being much shorter on the 'c' axis.

3.3.6 Structure Refinement

Refinement of all three HPA-inhibitor complexes was carried out in CNS (*238*) alternating positional and b-factor refinement. After each round of

Table 3.1: Data Collection, Processing and Refinement Statistics

Complex Structure	**HPA-e voglibose**	**HPA-myricetin**	**HPA-ethyl caffeate**
Data Collection Parameters			
Space group	$P2_12_12_1$	$P2_12_12_1$	$P2_12_12_1$
Unit cell dimensions (Å)			
a	52.4	52.1	52.1
b	73.0	67.4	68.1
c	135.1	129.9	125.9
Resolution range (Å)	64.24-1.7	43.3-1.2	52.1-1.35
Highest Resolution Shell (Å)	1.79-1.7	1.26-1.2	1.42-1.35
No. of unique reflections	57601	140097	98452
Mean $I/\sigma I$[a]	23.0 (9.9)	14.7 (5.4)	19.8 (6.8)
Multiplicity[a]	6.7 (6.5)	4.6 (4.7)	4.8 (4.7)
Merging R-factor (%)[a]	5.2 (15.7)	6.4 (28.2)	5.0 (20.1)
Structure Refinement Values			
Number of reflections	57479	140013	98366
Completeness (%)[a]	99.6 (99.3)	97.8 (98.1)	99.5 (98.2)
No. protein atoms	3946	3946	3946
No. inhibitor atoms	54	23	30
No. solvent atoms	375	651	240
Average thermal factors ($Å^2$)			
Protein atoms	15.9	10.2	19.1
Inhibitor atoms	32.4	52.0	18.9
Solvent atoms	41.1	29.7	32.0
Overall	18.3	13.4	20.4
Final R-free value (%)	22.0	19.0	22.9
Final R-factor (%)	19.2	16.8	19.3
Structure Stereochemistry			r.m.s. deviations
bonds (Å)	0.01	0.02	0.02
angles (σ)	1.4	2.3	2.4

[a] The number in brackets indicate data for the highest resolution shell.

refinement, the model was checked with Fo-Fc, sigmaa weighted 2mFo-DFc, and omit density maps, Necessary adjustments were made manually in Coot (*239*). All three structures were refined to convergence, with R-free values below 25%. Inhibitor topologies and restraints were obtained from the PRODRG server (*240*). Hydrogen bonding patterns described in subsequent sections were determined manually.

3.3.6.1 HPA-Voglibose

Rigid body refinement of the model obtained from molecular replacement clearly revealed the position of three voglibose molecules bound to the surface of the enzyme in initial Fo-Fc maps. All inhibitor atoms were refined at full occupancy. A summary of refinement statistics can be found in table 3.1, and Ramachandran plots of the final coordinates can be found in figure 3.2.

3.3.6.2 HPA-Myricetin

The initial Fo-Fc maps after rigid body refinement showed something bound in the active site of HPA. Myricetin was built into this density after the coordinates of the protein alone had been adjusted and refined to an R-factor below 25%. All inhibitor atoms were refined at full occupancy; however, Fo-Fc maps showed negative density for the inhibitor. The occupancy was then estimated using CNS which gave different occupancies for each atom of the inhibitor. These were then adjusted manually and the final refine-

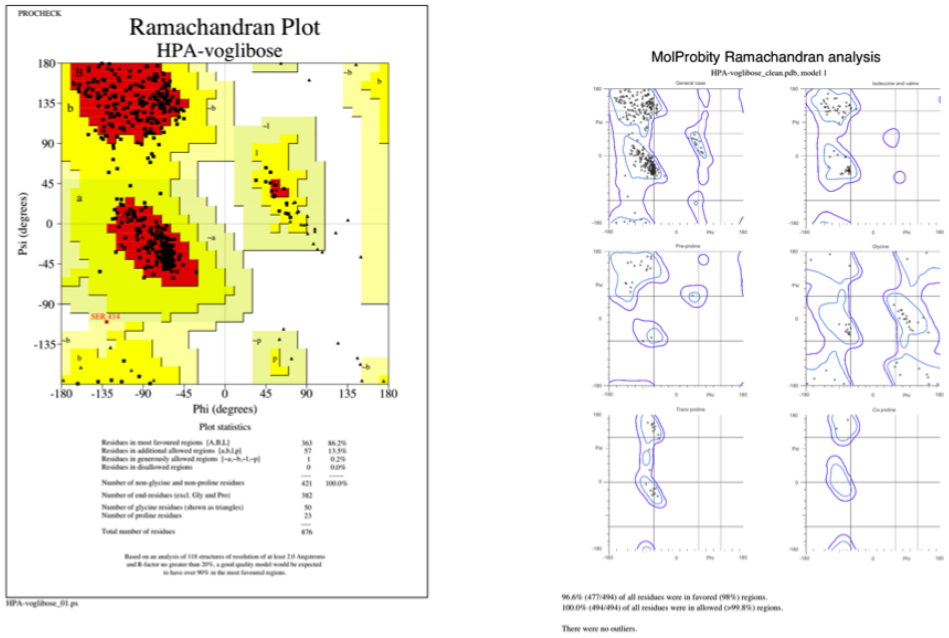

(a) (b)

Figure 3.2: Ramachandran Plots of the Final Model of the HPA-Voglibose Complex Crystal. The plots shown were generated by (a) Procheck (*220*) and (b) Molprobity (*221*, *241*). The residue shown in red in the Procheck plot is S414, which is involved in a γ-turn.

ment run was repeated, each iteration testing values within the range suggested by CNS. The result for each run was checked using Fo-Fc and omit density maps. An occupancy level of 40% produced the clearest maps and the lowest R-free value. A summary of refinement statistics can be found in table 3.1, and Ramachandran plots of the final coordinates can be found in figure 3.3.

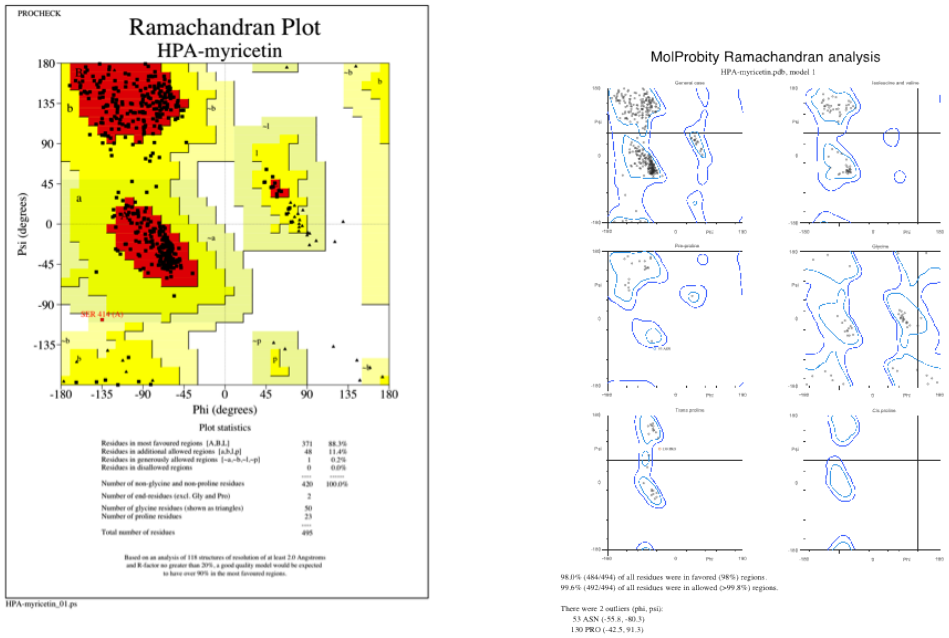

(a) (b)

Figure 3.3: Ramachandran Plots of the Final Model of the HPA-Myricetin Crystal. The plots shown were generated by (a) Procheck (*220*) and (b) Molprobity (*221*, *241*). The residue shown in red in the Procheck plot is S414, which is involved in a γ-turn. The coordinates used are those in the Protein Data Bank (PDB code, 4GQR ((*1*)).

3.3.6.3 HPA-Ethyl Caffeate

Initial Fo-Fc maps revealed three ethyl caffeate molecules bound to the surface of the enzyme well away from the active site. These molecules were very clearly defined, while segments of the protein structure that are usually well-ordered in most HPA-inhibitor complexes were ill-defined in omit electron density maps; nevertheless, the complete protein sequence was built into the available density. This disorder likely accounts for the R-factors in Table 3.1, which are higher than normal for HPA. Analysis of the Ψ and Φ angles of the final model are shown in Figure 3.4.

3.4 The HPA-Voglibose Complex Structure

Voglibose, (1S,2S,3R,4S,5S)-5-(1,3-dihydroxypropan-2-ylamino)-1-(hydroxymethyl)cyclohexane-1,2,3,4-tetraol) is a relatively weak α-amylase inhibitor with approximately 1/3000 of the inhibitory activity of acarbose (*92*). This is likely due to its being a monosaccharide mimic, while human α-amylase has evolved to bind large, polymeric substrates to produce maltose. Its efficacy against the intestinal dissaccharidases has nevertheless made it a common adjunct therapy for type II diabetes.

Voglibose inhibits the N- and C- terminal subunits of human maltase-glucoamylase with K_i values of 2.6 μM and 1.7 μM, respectively (*242*); no K_i for HPA inhibition by voglibose has been reported in the literature.

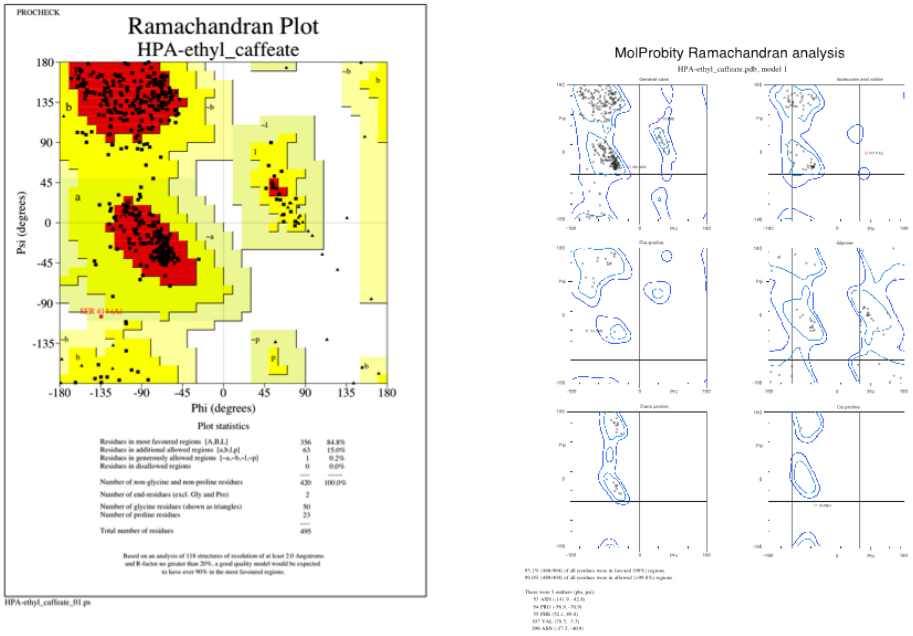

(a) (b)

Figure 3.4: Ramachandran Plots of the Final Model of the HPA-Ethyl Caffeate Crystal. The plots shown were generated by (a) Procheck (*220*) and (b) Molprobity (*221*, *241*). The residue shown in red in the Procheck plot is S414, which is involved in a γ-turn. The coordinates used are those in the Protein Data Bank (PDB code, 4GQQ *1*).

Although voglibose is a monosaccharide mimic, it does not obviate all of the interactions that a disaccharide would have with the enzyme. This is because the distance between carbon 2 of its dihydroxypropane moiety and either hydroxyl group closely approximates that between the C4 and O3 of a glucose molecule, albeit the hydroxyl attached to the propane is more mobile.

In doing this experiment, we hoped that the crystal structure of the HPA-voglibose complex would reveal not only how an important clinical α-glucosidase inhibitor interacts with HPA, but reveal information about how an isolated monosaccharide might bind to the enzyme, and reveal new HPA-inhibitor interactions that can be exploited in the design of new, higher affinity inhibitors.

3.4.1 Description of the HPA-Voglibose Complex

Electron density maps of the HPA-voglibose complex structure revealed three inhibitor molecules bound to the surface of the protein: one bound within the enzyme's active site, one near the calcium binding site in domain B, and one bound on the opposite side of the enzyme, 21 Å away from the catalytic nucleophile, and 28 Å from the bound calcium ion (Figures 3.5 and 3.6). The first and second voglibose molecules are nearly equidistant from the calcium ion, at a distance of approximately 10.5 Å.

The voglibose molecule within the substrate binding cleft forms 5 hydrogen bonds with the enzyme, all but one involving the catalytic nu-

cleophile and acid/base catalyst, D197 and E233 (Figure 3.7a). The hydroxyl on C4 forms a bifurcated interaction with the side chains of both carboxylates. The orientation of bound voglibose is further stabilized by

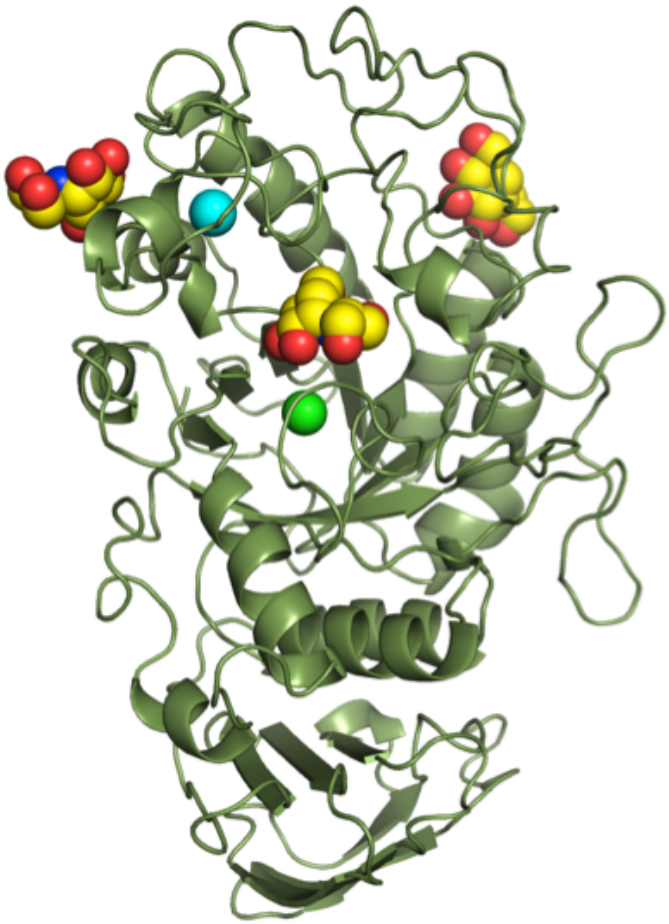

Figure 3.5: The Three Voglibose Binding Sites. The voglibose molecules are shown as yellow spheres. The calcium ion is cyan and the chloride ion, light green. The voglibose molecule in the middle is bound within the enzyme's active site cleft.

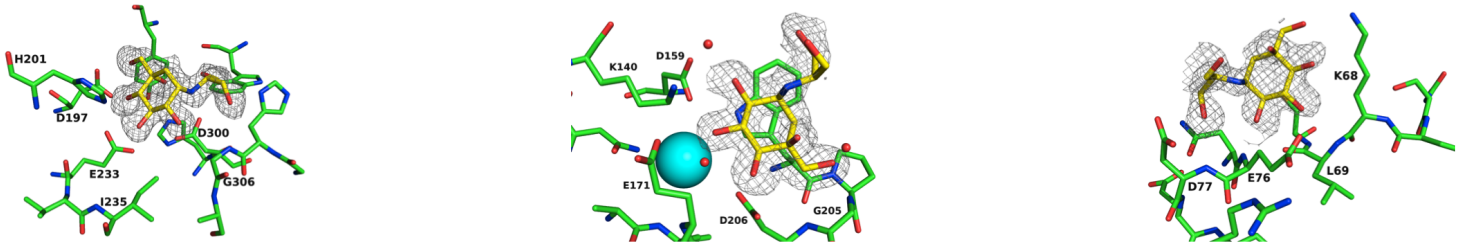

(a) (b) (c)

Figure 3.6: Omit Electron Density Maps of the Three Voglibose Binding Sites. These sites are found (a) within the enzyme's active site, (b) near the calcium binding site, and (c) on the protein's surface 21 Å away from the catalytic carboxylates. None are found on domain C of the protein. The cyan sphere in (b) is a calcium ion. All of the maps are at contour level 2σ, and all inhibitor atoms were refined at full occupancy.

the side chain of L162 that packs against the inhibitor's cyclohexane ring, and by an extended hydrogen-bonding network that employs five water molecules to expand the number of interactions with the protein (Figure 3.7b). D300, HPA's third essential catalytic carboxylate participates in this enlarged network.

The second voglibose binds to the surface of the enzyme near the calcium binding site. It is held in place by three hydrogen bonds to the protein, to the side chains of K140, E171, and D206. These are accompanied by three water-mediated hydrogen bonds that extend the interactions to include the side chain of D159 and the main chain nitrogen of G205. The side chain of W203 also serves to orient the position of the bound inhibitor (Figure 3.8a).

The third voglibose molecule that binds to HPA forms five hydrogen bonds to the enzyme (Figure 3.8b). One oxygen of the inhibitor also packs against the main chain nitrogen of L69 at a distance of 3.10 Å, but the angle makes a hydrogen bond unlikely. Unlike the other two inhibitor molecules found in this structure, there are no water molecules that act as intermediaries between the enzyme and the inhibitor, and the cyclohexanol ring does not pack against a hydrophobic residue, but against the disulfide bond between C70 and C115.

The binding of voglibose does not significantly alter the tertiary structure of the enzyme, and the average RMSD of the Cα from their positions in the free enzyme is a mere 0.27 Å (Figure 3.9). The largest difference

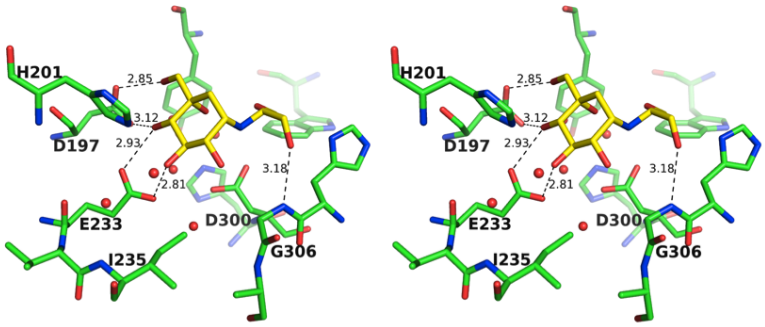

(a)

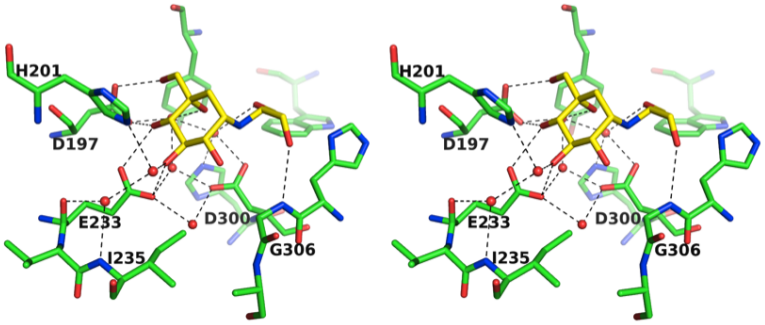

(b)

Figure 3.7: Stereo View of Voglibose in the Active Site of HPA. The first image (a) shows the hydrogen bonds between the inhibitor and the protein. Voglibose forms hydrogen bonds with two of the three catalytic carboxylates, D197 and E233. The numbers indicate hydrogen bond length in Ångstroms. To the second image (b), the water-mediated hydrogen bond network that helps stabilize voglibose binding has been added. This would increase the stability of the HPA-voglibose complex

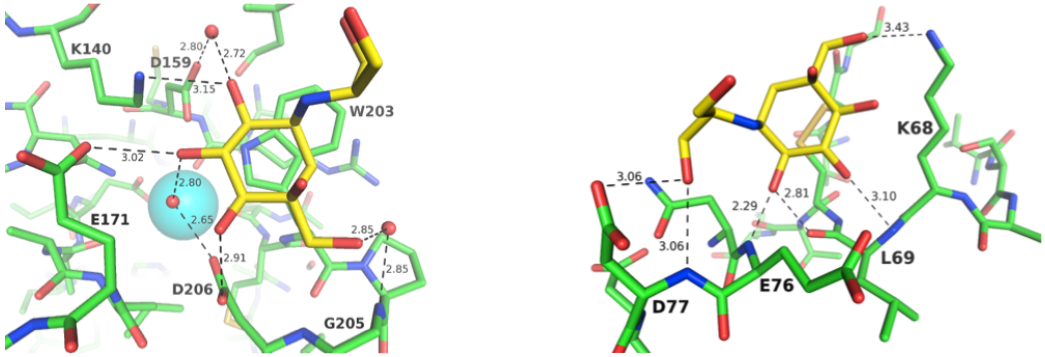

(a) (b)

Figure 3.8: The Hydrogen-Bonding Network Formed by Voglibose Binding on the Surface of HPA. (a) shows the binding site near the calcium ion. The inhibitor forms 4 hydrogen bonds directly with HPA. These are supplemented by 3 more water-mediated hydrogen bonds. (b) shows the binding of voglibose in the remaining surface pocket. The inhibitor forms 5 strong hydrogen bonds with the enzyme. The geometry of the final hydrogen bond to L69/N would be highly strained and may only indicate a close contact. The numbers in both pictures indicate hydrogen bond distances in Ångstroms.

occurs at H305, which moves 4.8 Å when voglibose binds. This residue is part of a highly mobile loop from residues 304-310 that is known to stabilize the binding of substrate molecules (*50*). This loop fulfills the same role in the HPA-voglibose structure, but with one key difference. Here, a hydrogen bond forms between the nitrogen of G306 and one of the hydroxyl groups of voglibose's dihydroxypropan-2-ylamino moiety, whereas in previous studies, it has been H305 that interacts directly with the inhibitor (*50*, *60*, *71*, *200*).

3.4.2 Discussion

Although it is a weak HPA inhibitor, voglibose forms five hydrogen bonds to the enzyme, two each to D197 and E233, and one to the nitrogen atom

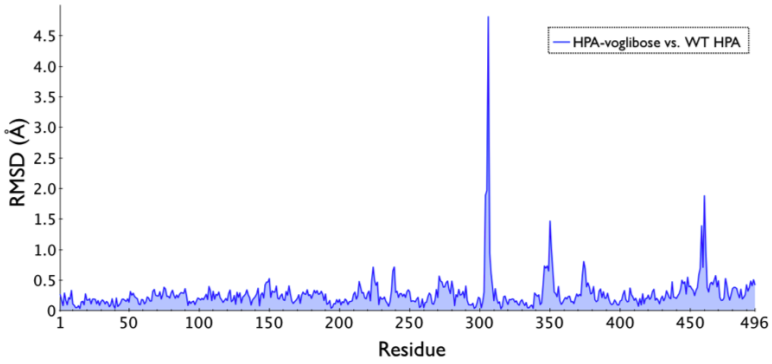

Figure 3.9: Average Root Mean Squared Differences in Main Chain Atomic Positions between the HPA-Voglibose Complex and Wild-Type HPA (PDB ID 1HNY) (*45*)). Notably, voglibose binding perturbs a flexible loop adjacent to the catalytic residue D300, shifting its position by 4.8 Å. The smaller peaks near residues 350 and 460 are due to flipped peptide bonds in surface loops of the enzyme.

of G306. This occludes both the catalytic nucleophile and acid/base catalyst, thereby accounting for any inhibitory activity. Surprisingly, it does not bind within any of the carbohydrate binding subsites that bind the enzyme's usual polymeric substrate (*50*); instead, it spans the +1 to -2 binding subsites with the cyclohexanol ring positioning itself at an approximately 106° angle to the position of bound acarbose's valienamine moiety. (Figure 3.10). It is unlikely that this displacement from all of the usual positions of bound sugars in the active site is due to the steric encumbrance caused by the additional oxygen at the C5 position of voglibose, since the enzyme is able to bind 5Fido, with a bulkier hydroxymethyl group at this position, in subsite +1 (*70*). However, the loss of the hydrogen bond between the 5OH of 5Fido and H305/O of HPA, and the possible introduction of electronic repulsion between voglibose's additional O5 and G306/CA may make binding in subsite +1 impossible. Voglibose, consequently, does not act as a substrate mimic for HPA.

Previous studies (*50*, *200*) have shown that the binding of acarbose within the active site of HPA, induces a shift in the position of a mobile loop from residues 304-310, so that the side chain of H305 can hydrogen bond, through atom ND1, to the sugar bound in the -2 subsite. Voglibose binds instead to the nitrogen of G306 at the +1 subsite, an interaction never observed in any other HPA-inhibitor complex. In order to be able to do this, the peptide bond from H305 to G306 is flipped, and the loop moves an extra 1.1 Å into the active site cleft. Interestingly, the position of

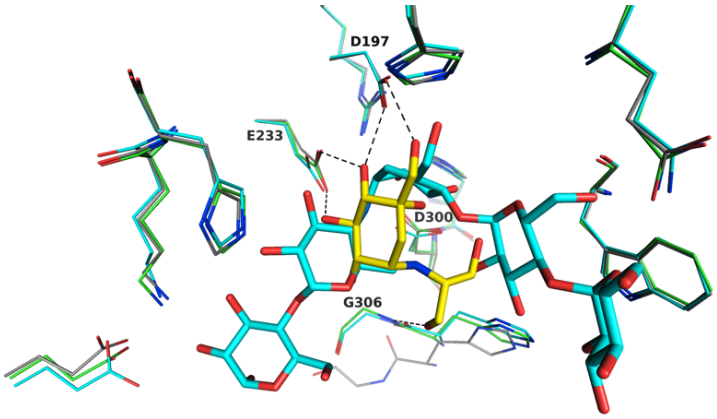

Figure 3.10: Comparison of the binding orientations of voglibose (yellow sticks) and acarbose (cyan sticks) to HPA. The voglibose molecule does not bind in the usual carbohydrate binding subsites. Instead, it spans the -2 to +1 subsites. The HPA-voglibose complex is shown in green (enzyme) and yellow (inhibitor); the HPA-acarbose complex (*50*) is shown in cyan, and the wild type enzyme with no inhibitor (*45*) is gray. The hydrogen bonds shown are the same as those of Figure 3.8a.

this loop remains stable when idose, fluorinated at C5, is covalently bound to the nucleophile (*70*), whether or not this inhibitor has been elongated to have a sugar in the -2 subsite (Figure 3.11). This may indicate that this loop has a smaller role in stabilizing the covalent intermediate than in orienting bound substrate. That G306 in the HPA-voglibose structure is drawn into to the active site to stabilize the inhibitor molecule that bridges the -2 to +1 subsites shows us that this loop is even more flexible than previously thought, a property that could be exploited in future inhibitor design.

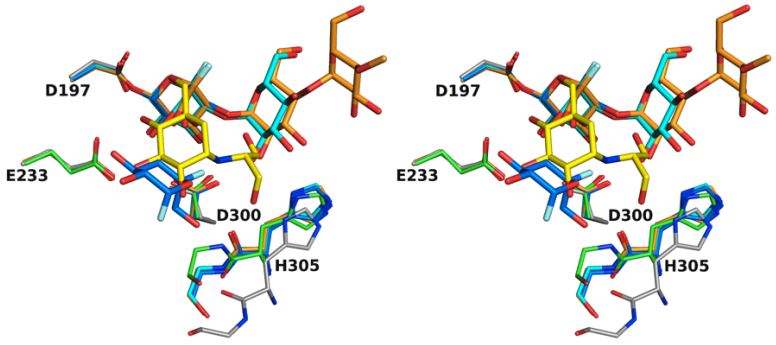

Figure 3.11: Stereo plots comparing the orientation of voglibose (yellow) bound in the active site of HPA (green) with the structures of the enzyme's covalent intermediate in elongated and unelongated forms (PDB codes, 3IJ7 (orange), 3IJ8 (cyan) and 3IJ9 (blue); (*70*)). The free enzyme (PDB code, 1HNY; (*45*) is shown in gray. Voglibose does not bind in the enzyme's high-affinity binding subsites, and forms a bridge between subsites -2 to +1 instead. This may mean that potential monosaccharide substrates or monosaccharide-mimic inhibitors cannot not bind stably to these subsites in the absence of a polysaccharide bound in the active site. Also shown in the figure is the shift in the position of the mobile loop from residues 304-310, showing a slight narrowing of the active site when voglibose is bound.

Two additional voglibose molecules bind to surface sites far from the enzyme's active site. Remote binding sites have been observed for HPA before (*70*, *71*, *200*), and it has been suggested that these may be involved in starch binding. Two other x-ray crystal structures of HPA-inhibitor complexes even show the binding site near the calcium ion. Both involve the covalent inhibitor 5FidoF (*70*), and, like voglibose, high inhibitor concentrations are almost certainly involved in forcing the interaction. All three inhibitor molecules share structural similarities with monomeric glucose and form many of the same hydrogen bonds to the protein (Figure 3.12). The main differences between the binding of voglibose and the binding of 5FidoF to this surface site involve hydrogen bonds to the endocyclic oxygen.

The binding of the third voglibose molecule may also approximate the binding of maltose or a polysaccharide substrate since the distance between the O4 oxygen of the cyclohexanol ring and the terminal oxygen of the dihydroxypropan-2-ylamino tail closely approximate that between the O2 and O3' oxygens of maltose. Voglibose's similarities to both glucose and maltose indicates that this binding pocket could be preformed in the free enzyme, and thus may help the enzyme bind to starch.

While it is a poor α-amylase inhibitor, the crystal structure of the HPA-voglibose complex reveals much about the flexibility of the enzyme's active site cleft, showing that the loop at residues 304-310 helps modulate the active site structure, activity that can be exploited both to promote or

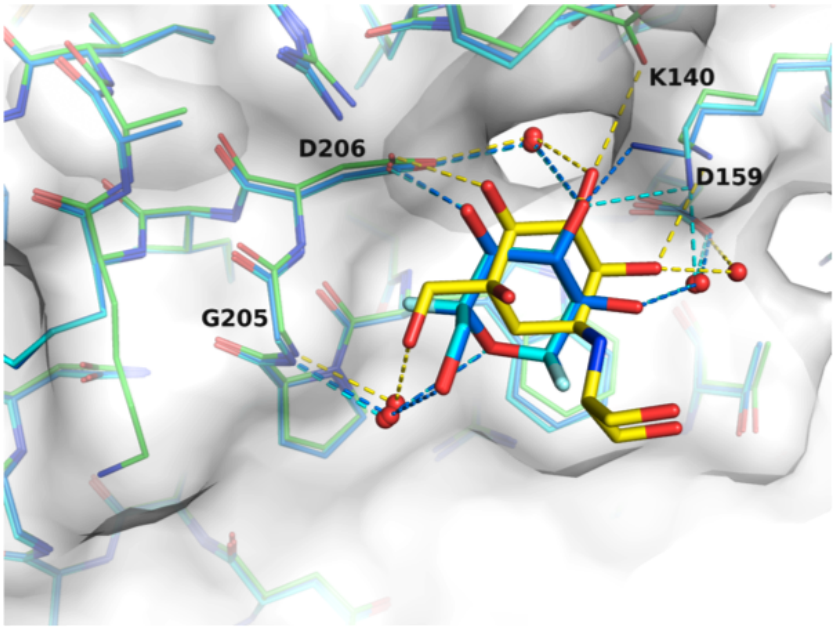

Figure 3.12: Diagram of the Voglibose Binding Site near the Calcium Ion. Voglibose (yellow) binds to domain B of HPA (green) in the same way as 5FidoF (PDB code, 3IJ8 (blue), 3IJ9 (cyan) (*70*)), forming the same hydrogen bonds to the protein. This indicates that this binding pocket may be preformed and could help bind the enzyme's polysaccharide starch substrate.

inhibit enzyme activity. It also provides another piece in the puzzle of how the enzyme binds to a polymeric starch substrate.

3.4.3 Conclusions

Several major discoveries can be drawn from the HPA-voglibose complex structure. The first is that a monosaccharide, or monosaccharide mimic, may not bind as expected in the enzyme's high affinity carbohydrate binding subsites; this must impact the design of any future small molecule in-

hibitors of HPA. The binding of voglibose in an unusual location within the active site cleft in the crystal structure also reveals a novel role for the mobile loop from residues 304-310, for it moves farther into the active site than has been seen before. This newly found flexibility of the mobile loop has implications for future inhibitor design, since it unveils a possibility for the development of inhibitors that can remodel the active site in order to prevent starch binding.

3.5 The HPA-Ethyl Caffeate Complex Structure

Caffeic acid derivatives, including caffeic acid glycosides, have been studied as antihyperglycemic agents and α-glucosidase inhibitors (*135*, *228*–

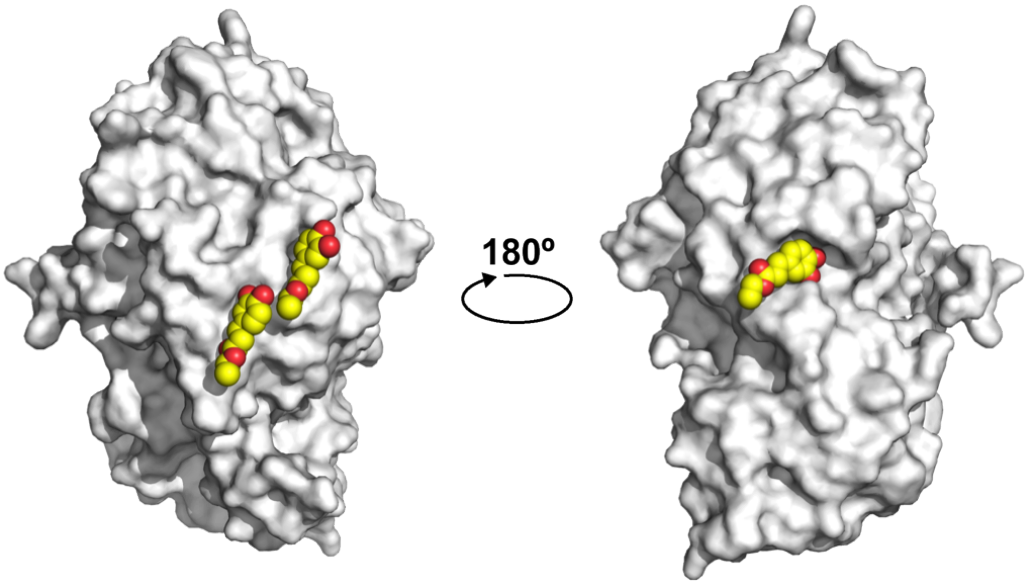

Figure 3.13: The Three Ethyl Caffeate Binding Sites.

230). No previous structural studies have been undertaken to determine how these molecules accomplish this inhibition.

Ethyl caffeate is a noncompetitive HPA inhibitor with a K_i of 1.3 mM (*2*). HPA is not known to have any allosteric regulators, and how this inhibitor inactivates the enzyme without preventing substrate from binding has never been studied. Solving the crystal structure of the HPA-ethyl caffeate complex thus has the potential to unveil completely new HPA-inhibitor interactions that can be utilized in the design of future inhibitors.

3.5.1 Description of the HPA-Ethyl Caffeate Complex

Electron density maps show three ethyl caffeate molecules bound to the surface of HPA (Figure 3.13). Each binds tightly in a separate pocket on the surface, shown by clear electron density for each inhibitor (Figure 3.14), and thermal factors averaging 15 $Å^2$, 17 $Å^2$ and 25 $Å^2$ for each molecule, respectively. This is commensurate with those of the entire polypeptide chain, which averages 19 $Å^2$. The binding pockets, appear to be preformed, since the binding of ethyl caffeate does not perturb the position of the main chain atoms immediately surrounding the binding sites.

All three binding sites are located along the wall formed by the helices between the β-strands of the central TIM barrel, involving helices 2, 3 and 5. These binding sites are also more than 20 Å away from the active site and catalytic residues, making this the first noncompetitive α-amylase in-

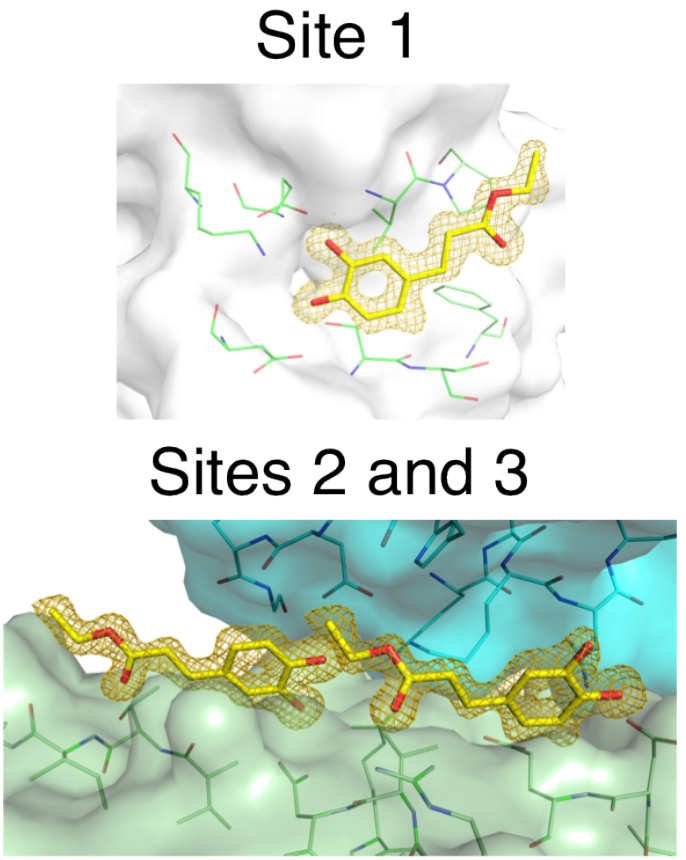

Figure 3.14: Omit Difference Electron Density Maps of Bound Ethyl Caffeate in the Three Binding Pockets on the Surface of HPA. Ethyl caffeate is shown in yellow, the polypeptide chain of HPA is shown in green, and the polypeptide chain from a symmetry-related HPA molecule is shown in cyan. All maps are shown at a contour level of 2.5σ.

hibitor for which we have a x-ray crystal structure of its complex with the enzyme.

One of the three ethyl caffeate molecules forms particularly close interactions with HPA, sharing 5 hydrogen bonds with the protein (Figure 3.15). The other two ethyl caffeates bind next to each other, but do not share any of the same interactions with the protein nor do they have any interaction with each other.

A unique feature of ethyl caffeate binding is that these three inhibitor molecules cause part of the polypeptide chain with the enzyme's active site to become disordered, and, as a result, only poor or patchy electron density is observed for residues 51-56, 104-111, 298-315, and 343-358 (Figure 3.16). In all but one case, these atoms are well resolved in the structure of the inhibitor-free enzyme, where they assume a single stable conformation. The exception is from residues 298-315, which is an expansion of a normally disordered loop from residues 304-310 (*51*, *243*). This disorder is reflected in the displacement and thermal factors of the main chain atoms of the enzyme (Figure 3.17).

The loop from residues 304-310 normally converges around substrate and inhibitor molecules that are bound in the active site, with H305 forming hydrogen bonds with sugars bound in the -3 binding subsite (*50*, *70*, *71*). The extension of disorder into new polypeptide segments means that D300, one of the essential catalytic carboxylates, is disordered in this struc-

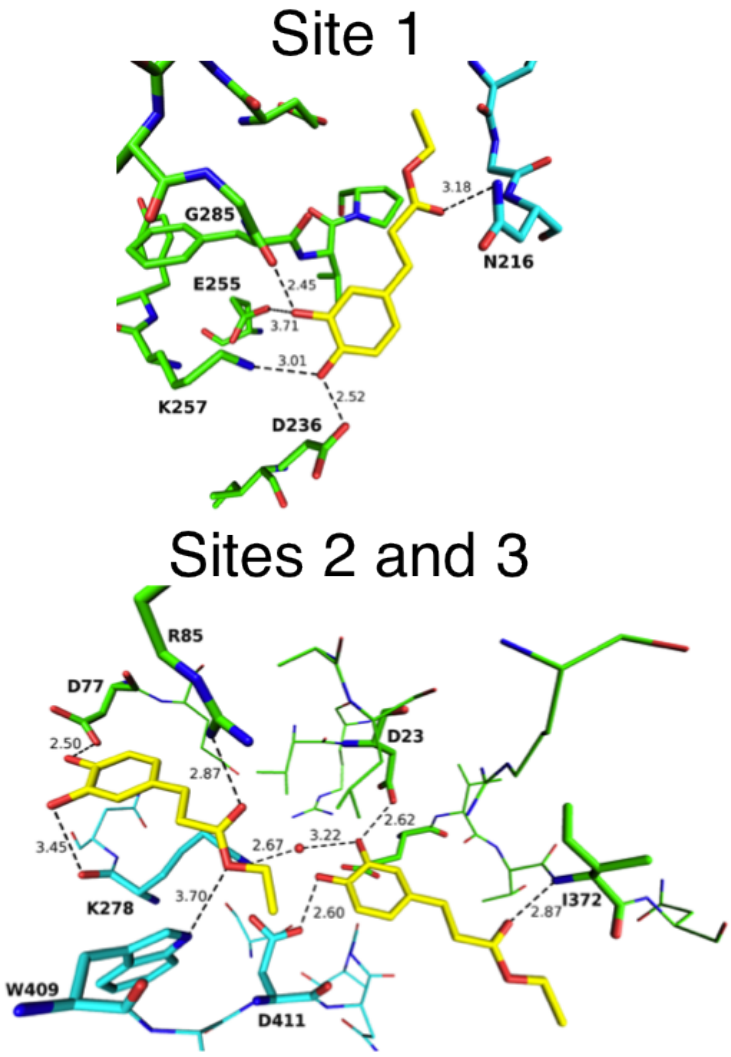

Figure 3.15: Hydrogen Bonding in the Three Ethyl Caffeate Binding Sites. Ethyl caffeate is in yellow, the polypeptide chain of HPA is green, and the polypeptide chain of a symmetry-related molecule is cyan. Numbers indicate distances in Ångstroms

ture; this likely accounts for the drop in enzyme activity during ethyl caffeate inhibition of HPA.

All four of the disordered loops are located within the substrate-binding cleft of HPA at the C-terminal end of the β-barrel that forms domain A, and each occurs in a loop that immediately succeeds one of the β-strands in the barrel and precedes the helical crossover. Thus, the disordered regions occur between strands β2 and β3, β3 and β4, β7 and β8, and β8 and β1.

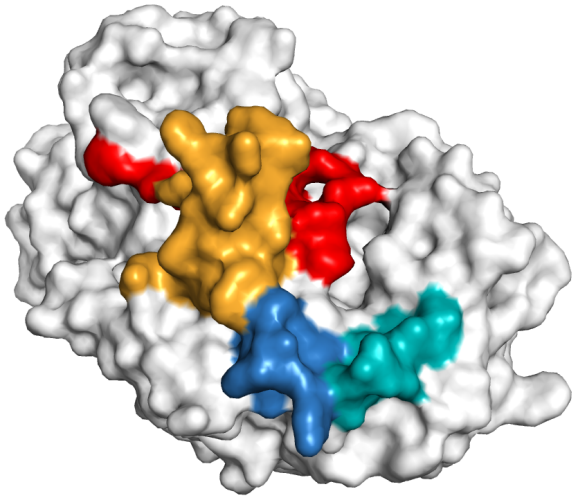

Figure 3.16: The Four HPA Surface Loops Disordered by Ethyl Caffeate Binding. Residues 51-56 are shown in blue, 104-111 in teal, 298-311 in red, and 343-358 in orange. The large groove at the top of the figure is the enzyme's substrate binding cleft. The orientation is that shown in Figure 1.3.

3.5.2 Discussion

Caffeic acids and caffeic acid derivatives have been studied as potential anti-diabetic agents (*228–230*). Little work, however, has been done previously to show the specific interactions between the inhibitors and α-amylase that enable them to achieve their anti-hyperglycemic effect.The structural studies in this thesis clearly show that ethyl caffeate represents a new class of α-amylase inhibitor that acts both remotely and precisely to disorder specific loops within the active site of HPA. No other inhibitor found to date has affected enzymatic activity in this manner.

Of the three bound ethyl caffeate molecules, the one bound in site 1 (Figure 3.14) is likely responsible for much of the observed disordering effect. This is because it is closer than either of the two others to one of the disordered loops, and can influence the position of residues 298-315 in multiple ways. Firstly, the 3- and 4- hydroxyls of ethyl caffeate hydrogen bond to K257/NZ and G285/O which anchor the beginning of α-helix 6 of the enzyme's β-barrel, and the end of the loop before β-strand 7. These atoms hydrogen bond to each other in inhibitor-free HPA (*45*, *51*). The presence of the ethyl caffeate molecule, and the change in the endpoints of this helix-loop combination may help destabilize residues 305-311, which normally pack against it.

Two more direct interactions are also involved with the destabilization of residues 298-315. The hydrogen bond between K257/O and K261/N completes the first turn of helix 6. Within this turn, A260/O hydrogen

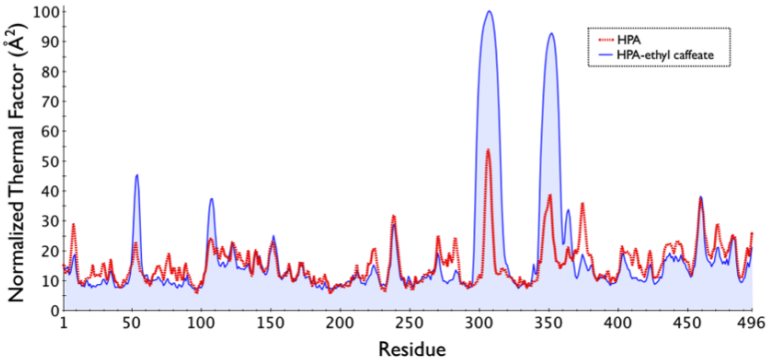

(a)

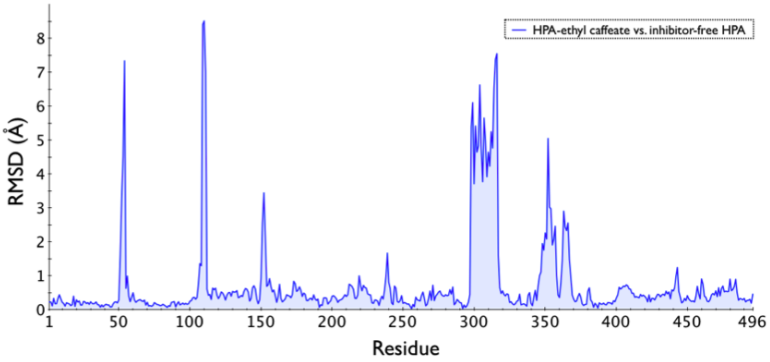

(b)

Figure 3.17: Normalized Thermal Factor and RMSD Graphs for the HPA-Ethyl Caffeate Complex. (a) The normalized thermal factors of the HPA-ethyl caffeate complex (blue lines and shading) overlaid with the normalized thermal factors of the free enzyme (red dashes) (PDB ID, 1BSI (*51*)). The binding of ethyl caffeate causes a significant increase in disorder for four loops centered about residues 53, 107, 306, and 350. (b) Average root mean squared differences in main chain atomic positions between the HPA-ethyl caffeate complex and wild-type HPA (PDB ID, 1BSI). The three ethyl caffeates bound at remote sites on the surface of HPA have a large impact, causing the four polypeptide chains located near the active site to move away from their usual place.

bonds to S311/SG in inhibitor-free HPA, to anchor the end of the active site mobile loop from residues 304-310. This hydrogen bond is clearly disrupted by the presence of bound ethyl caffeate which almost certainly accounts for the extension of the highly mobile region to residue 315.

The ethyl caffeate molecule in site 1 also hydrogen bonds weakly to E255/OD2 through the 3-OH. E255 hydrogen bonds to K257 through OD1 (distance 2.82 Å). This hydrogen bond replaces the one to G285/O that is present in the uninhibited enzyme. The binding of ethyl caffeate and the change in hydrogen bond pattern must affect the properties of the bridging residue, F256, even though its positional coordinates do not change. The side chain of F256 comes into close contact with N298/ND2 in the absence of ethyl caffeate (distance 3.6 Å), an interaction that is stabilized both by the interaction between this atom and the chloride ion, and by a t-shaped π-stacking arrangement between F256 with F295. Changes to F256 very likely account for the C-terminal extension of the mobile loop from residues 304-310 to include N298. The disorder in this loop would then be transmitted along the surface of the protein to the remaining disordered regions, possibly by disrupting interactions between R303 and D356, as well as W357 and P54. This may allow for the loop from residues 51-56 to displace itself form new contacts with the loop from residues 104-111, accounting for the disorder seen there.

While ethyl caffeate has an unprecedented effect on the structure of HPA, the low binding affinity of ethyl caffeate to the enzyme (K_i 1.3 mM)

does limit the possibility of using this molecule as an antihyperglycemic agent. One can envisage this being improved by the addition of functional groups that would increase its affinity for the enzyme, or perhaps, ethyl caffeate could be used in a novel approach to α-glycosidase inhibition, using it to induce structural changes that allow a higher-affinity competitive inhibitor to bind within the active site itself. Such an inhibitor could potentially stabilize a completely new and inactive form of the enzyme.

3.5.3 Conclusions

These results are important because it is the first crystal structure of a non-competitive inhibitor in complex with HPA, a structure that reveals a surprising flexibility in the structure of a very stable enzyme. The binding of ethyl caffeate to three remote binding sites on the surface of HPA causes the enzyme to undergo significant structural changes: four ordered loops on one side of the protein become disordered. This disordered region covers the position of one of the three catalytic carboxylates that are necessary for efficient enzyme activity, D300. This effect appears to be caused by changes involving the hydrogen bonding pattern of K257. Developing inhibitors that specifically target site 1 may give future researchers the ability to manipulate the enzyme's active site structure in the development of new drugs for the treatment of diabetes.

3.6 The HPA-Myricetin Complex

Flavonols and flavonoids have long been studied for their antidiabetic properties, and appear to be the active ingredient in many traditional medicines for type II diabetes acting as α-glucosidase inhibitors (*223–226*). It is unknown, however, how these molecules interact with their enzyme targets. Few analogies can be drawn between these planar, rigid compounds and the more flexible sugar substrate of these enzymes.

Previous structural studies of flavonoid inhibition of α-amylases used *in silico* modeling to determine how these inhibitors interact with the enzyme (*108*). While the results of these studies may be substantially correct, they cannot predict any dramatic changes in protein structure or model individual solvent molecules. These shortcoming of an *in silico* method to structure determination can result in huge errors in the results. An x-ray crystallographic study is thus needed to verify the accuracy of the computer-generated results, and to show protein-inhibitor interactions ignored by the algorithms. The HPA-myricetin complex structure does this, and reveals surprising roles for D300 and the mobile loop from residues 304-310 in the inhibition of α-amylases by flavonols.

3.6.1 Description

Myricetin binds non-covalently in the active site of HPA contiguous to the active site carboxylates, D197 and E233 (Figure 3.21). It spans binding

subsites -1 to -3 and forms 7 hydrogen bonds directly to the enzyme, all along the more hydroxylated face of the inhibitor (Figure 3.18). Three of these are interactions with the side chains of the catalytic carboxylates, D197 and E233, with another connection to E233 mediated through a water molecule. The other four hydrogen bonds are formed with the main chain oxygens of W59 and Y62, and with the carbonyl oxygen of the side chain of Q63.

The binding of myricetin to HPA has little effect on the overall fold of the enzyme, with the main chain RMSD between the HPA-flavonol complex structure and the uncomplexed wild-type enzyme being a mere 0.27 Å. There are, however, perturbations to the position of the main chain atoms within the active site itself (Figure 3.19). Two segments move significantly to accommodate the planar myricetin. The first is a short loop containing glycines 238 and 239, which forms part of the -1 and -2 binding subsites, and the second is a loop from residues 305-310 that is highly mobile in most HPA-inhibitor complex structures (Figure 3.20). Both of these regions show a modest drop in thermal factors compared to the inhibitor-free enzyme (Figure 3.17), indicating a further effect of flavonol binding.

Although it doesn't hydrogen bond to myricetin, D300, the third essential catalytic carboxylate (*60*) is greatly affected by the presence of the flavonol in the active site. If the side chain of D300 were to remain in the position found in the uncomplexed protein structure, the very polar carboxylate group would pack against the B ring of myricetin, a role much

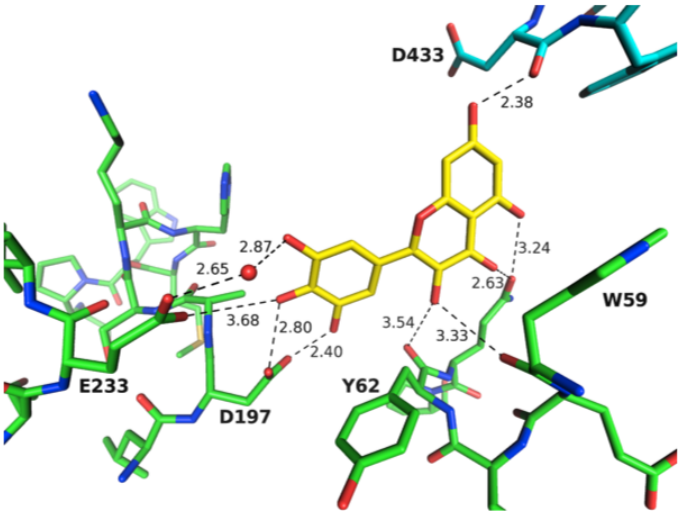

Figure 3.18: The Hydrogen Bonding Pattern of Myricetin Bound to HPA. Myricetin is shown in yellow, and the enzyme's polypeptide chain is in green. The polypeptide chain of a symmetry related molecule of HPA is shown in cyan.

better suited to a hydrophobic amino acid. To stabilize the binding of myricetin, D300 turns by approximately 76° around its $\chi 1$ torsional angle, pushing the loop from residues 304-310 away from the active site so that the side chain of H305 packs against the ordered loop from residues 342-360. This is very different from the HPA-acarbose complex structure (*200*) where H305 is drawn into the active site cleft to hydrogen bond with the inhibitor. The loop from residues 304-310 is highly mobile, and in all other crystal structures of HPA to date the electron density in this region is patchy (*45*, *51*, *52*, *70*, *71*, *200*, *244*, *245*). In the HPA-myricetin complex structure, the position of this loop is stabilized and clear electron density is present for its entire length, despite being composed, save for H305, en-

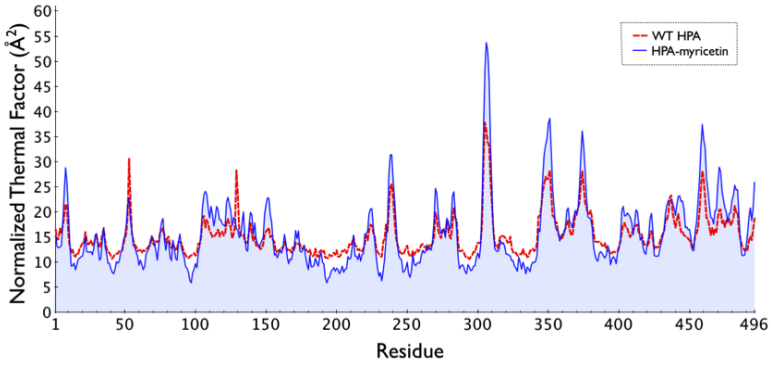

(a)

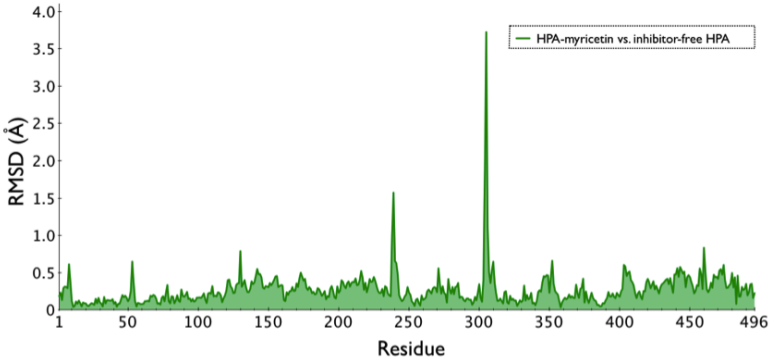

(b)

Figure 3.19: Normalized Thermal factor and RMSD Graphs for the HPA-Myricetin Complex. (a) The normalized thermal factors of the HPA-myricetin complex (blue lines and shading) overlaid with the normalized thermal factors of the free enzyme (red line) (PDB ID, 1BSI, (*51*). The binding of myricetin leads to less disorder in an active site loop near D300. (b) Average root mean squared differences in main chain atomic positions between the HPA-myricetin complex and wild-type HPA (PDB ID 1BSI). Myricetin binding in the active site disturbs the position of a mobile loop in the enzyme's active site.

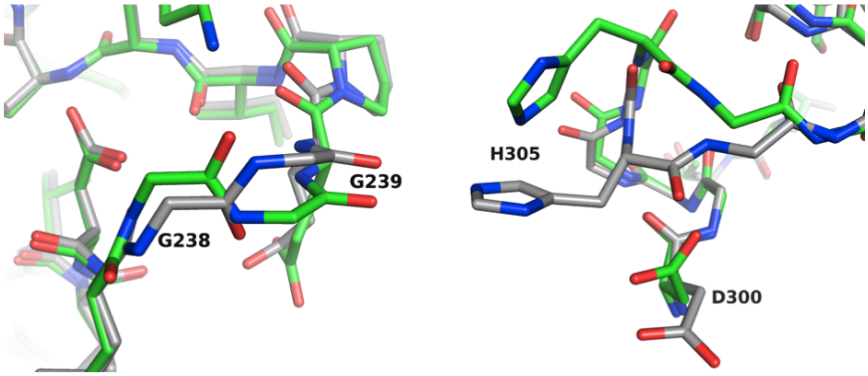

(a) (b)

Figure 3.20: Displacement of Atoms within the Active Site upon the Binding of Myricetin. Two regions show a significant displacement of main chain atoms : (a) residues 238-239, and (b) residues 304-306. The HPA-myricetin complex structure is green, while inhibitor-free HPA is gray. Panel (b) also shows the shift of the side chain of D300. This shift forces the displacement of H305.

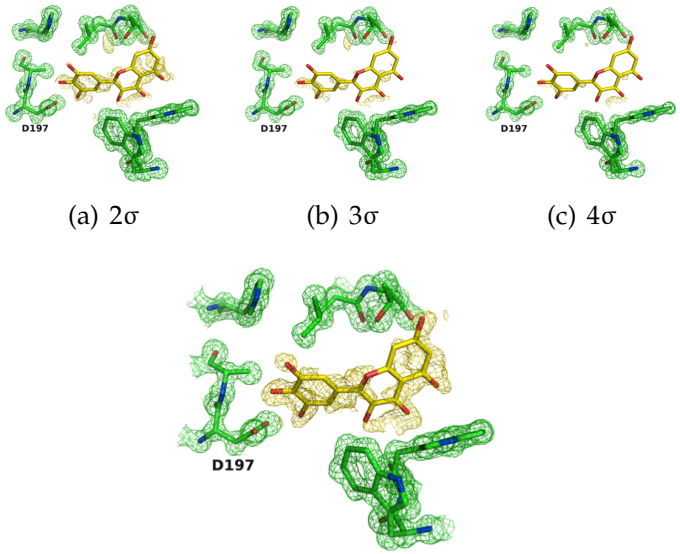

(a) 2σ (b) 3σ (c) 4σ

(d)

Figure 3.21: Electron Density Maps of Myricetin Bound in the Active Site of HPA. Omit maps are shown at contour levels 2σ (a), 3σ (b) and 4σ (c). A sigma weighted 2mFo-Fc map at 1.0σ is shown in (d). HPA is green and myricetin is yellow.

tirely of glycine and alanine residues. This stability is maintained through an extensive, solvent-mediated hydrogen-bonding network that involves the side chains of both D300 and E233.

3.6.2 Discussion

The binding of myricetin to HPA is distinct from other inhibitors, both covalent and non-covalent, for which we have structural data; these include acarbose (*50*), 5FidoF (*70*), and lactams (*71*). These inhibitors mimic the polysaccharide scaffold of the enzyme's natural substrate. Myricetin, however, binds differently.

The catalytic nucleophile and acid/base catalyst, residues D197 and E233, engage directly with myricetin, hydrogen bonding to the 3', 4' and 5' hydroxyls of the inhibitor's B ring. This blocks substrate access to these residues and neutralizes their function. The B-ring also hydrogen bonds to a water molecule believed to be the nucleophile that hydrolyzes the covalent bond of the glycosyl-enzyme intermediate.

Unlike the carbohydrate-based inhibitors, steric and electrostatic conflicts shift the placement of the side chain of D300, turning it away from the active site, thereby forcing the substrate-binding loop from residues 304-310 into a more stable, yet nonfunctional conformation. Myricetin binding thus blocks all three catalytic carboxylates, and impairs substrate binding in a region approximately 10 Å away from the catalytic nucleophile.

3.6.2.1 Comparision of the HPA-Myricetin Structure to HPA in Complex with Acarbose

When we compare the structure of HPA in complex with myricetin to the previously published structure of HPA with acarbose (PDB ID: 1CPU) (*50*), we see that both inhibitors span the -1 to -3 binding subsites thought to have the highest affinity for the substrate (Figure 3.22). Acarbose is a pseudo-tetrasaccharide that is transglycosylated by HPA to form a pseudo-pentasaccharide with a valienamine moiety next to the catalytic cleavage point. Acarbose's glucose moieties bind to HPA in a manner thought to be analogous to the enzyme's natural starch substrate. The flavonol, myricetin, takes advantage of these preformed binding pockets and shares hydrogen bonds with many of the same amino acids. It also forms a new interaction with the side chain hydroxyl of Y62 that is absent in the HPA-acarbose complex. Although acarbose does not hydrogen bond to Y62, this residue plays a key role in the active site during catalysis, using hydrophobic interactions to help orient the sugar rings.

Unlike acarbose, however, myricetin forms hydrogen bonds to only two of the three essential catalytic residues. As seen in figure 3.15, myricetin is hydrogen bonded to the catalytic nucleophile, D197 as well as to the acid-base catalyst, E233. Steric conflicts leave the side chain of D300 free to rotate into a new position with profound effects on the structure of a mobile loop near the active site.

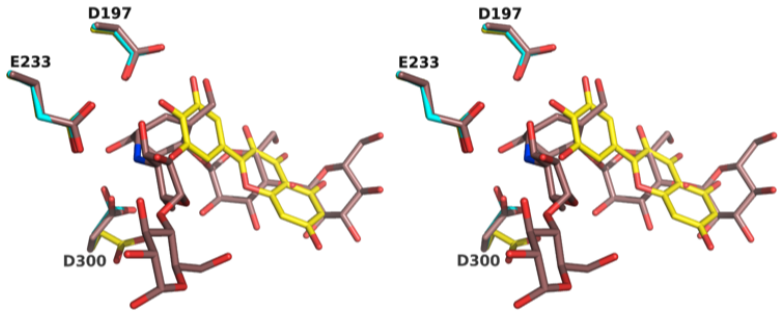

Figure 3.22: Stereo diagram of the binding orientations of myricetin (yellow) and transglycosylated acarbose (brown) (PDB ID 1CPU, (*50*) within the active site of HPA. Myricetin spans the -1 to -3 carbohydrate binding subsites, and the side chain of D300 turns away from the active site. WT HPA with no inhibitor (PDB ID 1BSI, (*51*)) is shown in cyan, showing that a carbohydrate-like inhibitor does not have the same effect on the enzyme.

While the positions of the other catalytic residues do not change when myricetin is soaked into the crystal, the side chain of D300 in the HPA-myricetin structure is rotated by approximately 76° relative to the same residue in both the structure of wild-type HPA (PDB ID: 1BSI) ((*51*) and in that of its complex with acarbose. Steric conflict would occur between the side chain of D300 and the backbone oxygen of H305 were they to appear in the same location shown in the structures of the wild-type enzyme and of the HPA-acarbose complex. As a result, the backbone oxygen of H305 has moved to a new position, 4.99 Å away from the D300 side chain. This new orientation of D300 appears to help stabilize the position of the amino acids in the highly mobile region from residues 304-310. This is reflected in

slightly lower thermal factors for these residues . Surprisingly, the lower B-values of this loop in the HPA-myricetin structure do not correspond to any new hydrogen bonds between the loop and other parts of the protein. A new water molecule appears where the backbone nitrogen of H305 was in the other structures (*50*, *51*).

In crystal structures of the interactions of carbohydrate-based inhibitors, including acarbose, with HPA, the structure of the active site remains fairly static, with minimal shifts in the positions of the main chain atoms, and only small rotations of the torsional angles of the side chains. Flavonol binding reveals a heretofore unexploited flexibility in active site structure.

3.6.2.2 Comparison to Flavonoid Modeling Studies

Flavonoids are very common secondary metabolites in plants, and have long been studied to reveal any potential health benefits, including any ability to alleviate the symptoms of diabetes (*2*, *108*, *120*, *124*, *129*, *246–248*). These studies have shown that these molecules act as competitive inhibitors of α-glycosidases, including α-amylases.

The only structural study to date has been an *in silico* docking study of flavonol binding in the active site of human salivary α-amylase (HSA) (*108*). These results can be expected to be comparable to those for HPA, given the high degree of homology between the two enzymes (*45*, *249*).

While the results of the *in silico* study are substantially correct, reflecting the position of the molecule within the enzyme's active site with the

B ring adjacent to the catalytic nucleophile and acid/base catalyst, there are significant differences in both the hydrogen bonding pattern and planar group stacking interactions between it and the structure determined by x-ray crystallography. Most notable are the interactions with the catalytic residues, D197 and E233. The *in silico* study suggests a bifurcated hydrogen bond between one side chain oxygen of D197 and the 4′ and 5′ hydroxyls of the flavonol inhibitor, whereas the crystal structure shows a much stronger interaction, where both side chain oxygens of D197 are involved in hydrogen bonds with the same two inhibitor atoms. Lo Piparo, Scheib, Frei, Williamson, Grigorov, and Chou (*108*) also underestimate the importance of E233, suggesting that the 4′ hydroxyl also hydrogen bonds to E233. This also occurs in the crystal structure, but the presence of the 3′ hydroxyl allows for an additional, water-mediated hydrogen bond to E233. This water molecule is present in other α-amylase crystal structures, and is believed to be the nucleophile that attacks the anomeric carbon of the deglycosylation step of the enzyme's mechanism. The interactions with the enzyme are thus influenced by the presence of individual solvent molecules, which are ignored in most modeling studies.

The biggest, and unanticipated, change to the enzyme upon myricetin binding is the rotation of the side chain of D300 away from the active site and the concomitant change in the position of the mobile loop from residues 304-310, a loop that moves towards the active site when more substrate-like inhibitors bind in order to stabilize sugar binding (*71*, *200*).

This shift in the position of D300 is not predicted by the modeling studies, for similar results were obtained with or without having the computer model changes to the enzyme surface.

The π-stacking interactions suggested *in silico* are also either absent or significantly different in the HPA-myricetin complex structure. This again is due to the shifting of D300 and the loop from residues 304-310 upon binding of the flavonol. The position of the A-C ring moiety shifts relative to that hypothesized in the *in silico* study, adapting to the changed environment, and rendering most of the suggested π-stacking interactions highly improbable. Complicating matters, the crystal structure also shows a substantially different position for H305 meaning it cannot form any planar stacking interactions with the inhibitor.

Nevertheless, Lo Piparo, Scheib, Frei, Williamson, Grigorov, and Chou (*108*) suggest one intriguing possibility: namely, that the flavonols tested may assume more than one binding conformation with the enzyme. In this second configuration, the A-C ring structure is placed adjacent to D197 and E233, and from a purely spatial point of view, this seems feasible. This change, however, would come at a cost for myricetin, since there would be only two, rather than three, hydroxyl groups able to hydrogen bond to the catalytic residues. The larger planar ring system would also limit the inhibitor's ability to interact with other groups within the enzyme's active site. This second configuration, however, may be exploited by other

flavonols, with the binding orientation depending upon the position of the hydroxyl groups within the inhibitor.

3.6.3 Conclusions

The HPA-myricetin complex structure reveals that the active site of the enzyme is not static upon the binding of the flavonol. Steric and electrostatic conflicts turn D300, an essential catalytic residue, away the active site, neutralizing it. The new position of D300 causes the mobile loop from residues 304-310 to coalesce into a new, stable conformation. This loop is usually highly mobile and ill defined in electron density maps. The end result is a widening of the active site cleft that has never been seen in any other HPA-inhibitor complex structure.

These results can be used to design new, stronger binding HPA inhibitors that take advantage of this newly found ability of the enzyme to remodel itself.

3.7 General Conclusions and Future Directions

All three HPA-inhibitor complexes discussed in this chapter reveal a never before seen flexibility in the structure of the active site of HPA. All three inhibitors rely on or affect the position of the mobile loop from residues 304-310, with ethyl caffeate causing the most dramatic change in enzyme structure by disordering four contiguous loops on the protein's surface.

These results open up the possibility of inducing changes in the enzyme's structure by designing inhibitors that capitalize on these effects to lead to greater inhibitor specificity.

All three of these inhibitors avoid binding in the preformed carbohydrate binding subsites within HPA's active site, and affect the position of residues 304-310. Further studies would be needed to determine whether this effect is common to most small inhibitors that cannot be transglycosylated by the enzyme.

Chapter 4

Origins of the Affinity and Specificity of Montbretin A Inhibition of HPA

4.1 Introduction

Montbretin A was first isolated from *Crocosmia crocosmiflora* in 1988 and forms part of a larger family of acylated flavonols collectively called the montbretins (*250*). Kinetic studies have shown it to be a high affinity inhibitor of HPA with a K_i of 4.4 nM (*251*). It is also a selective inhibitor for this enzyme, with 0.1 μM montbretin A reducing HPA activity by 91% while having virtually no effect on the other α- and β glycosidases tested (*2*).

All of the montbretins contain a myricetin flavonol core, glycosylated at the 3 and 4′ positions. A disaccharide containing an L-rhamnopyranosyl-(α-1,4)-D- xylopyranose is β-linked at the 4′ position of the flavonol. D-glucopyranosyl-(β-1,2)-glucopyanosyl-(β-1,2)-rhamnopyranose is attached at carbon 3. The middle glucose of this trisaccharide is joined to a 6-O-cinnamic ester. The substituents at the 3 position of the cinnamic acid ester

and at the 7 position of the flavonol differ between the family members (Figure 4.1).

4.1.1 Kinetic Studies of the Montbretin Isoforms

Crocosmia crocosmiflora produces at least five montbretin variants, the structures of which are shown in figure 4.1. Given that Montbretin A (MbA) is a low nanomolar inhibitor of HPA, montbretins B-E were also tested for

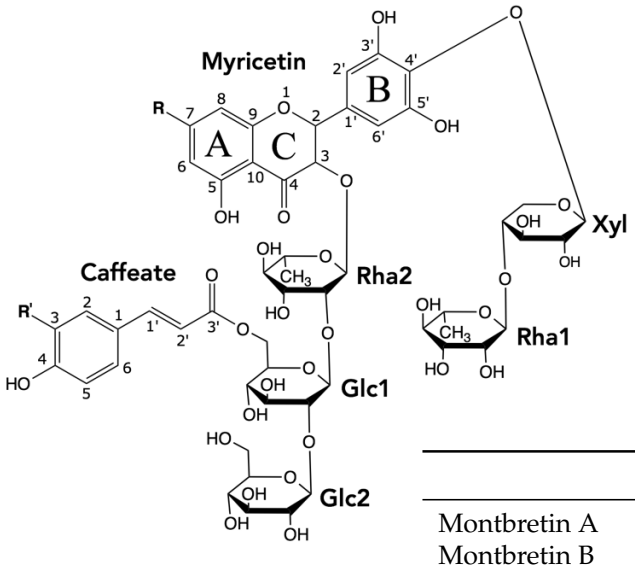

	R′	R	K_i (nM)
Montbretin A	OH	OH	8
Montbretin B	H	OH	3600
Montbretin C	OMe	OH	6100
Montbretin D	H	Glucose	890
Montbretin E	OH	Glucose	730

Figure 4.1: Chemical Structure of Montbretins A-E (*2*, *252*). The identities of the sugar rings are labeled, and ring designations and atom numbering are indicated for the myricetin and caffeate moieties. Groups specific to montbretins A-E and K_i values measured for the inhibition of HPA are indicated in the inset table (*2*, *251*, *253*)

α-amylase inhibitory activity and a K_i was determined for each by Drs. Jacqueline Wicki and Christopher Tarling of the Withers laboratory. The inhibition constants that they found for these molecules can be found in figure 4.1.

Montbretin B exchanges the 3OH of the caffeate group of MbA for a hydrogen atom. Surprisingly, this leads to a 1000-fold decrease in inhibitory activity (*2*), demonstrating the importance of this single hydroxyl for MbA binding. The switch of this same atom to an OMe group in Montbretin C (MbC) diminishes the activity even further. Montbretin D (MbD) and Montbretin E (MbE) both replace the 7OH of myricetin with glucose, while the 3OH of the caffeate moiety is replaced by a hydrogen atom or remains unchanged. The added glucose on the 7OH in MbD and MbE was expected to help stabilize the enzyme inhibitor complex, but instead destabilized binding even further. The removal of the terminal glucose (Glc2) had almost no effect on MbA's inhibitory ability.

4.1.2 MbA's Inhibitory Effect on Other Glycosidases

Due to its profound effect on HPA activity, MbA was also tested for specificity for α-amylase. Dr. Christopher Tarling of Dr. Stephen Withers' group measured the residual activity of six different glycosidases (β-glucosidase (*Agrobacterium sp.*), β -galactosidase (*E. coli*), β-hexosaminidase (jack bean), α-mannosidase (jack bean), α-galactosidase (green coffee bean), α-glucosidase (brewers' yeast)) in the presence of 0.1 μM MbA (*2*). None

showed any significant inhibition by MbA, and all had residual activities between 97% and 100%. This is dramatically different than the 11% residual activity for HPA using the same assay. These studies show that MbA is not a general glycosidase inhibitor, and is very likely specific for HPA and its homologs.

4.1.3 *In Vivo* Use of MbA as an Antihyperglycemic Drug

The success of the affinity and specificity studies led to the testing of MbA as a potential therapeutic agent for the treatment of type II diabetes using a rat model. Six groups of rats were used: lean, lean+acarbose, lean+MbA, Zucker diabetic fatty (ZDF) , ZDF+acarbose, and ZDF+MbA (*203*). The results showed that MbA significantly lowered plasma glucose levels in the ZDF rats, while having no effect on the lean ones. It also worked at a lower dose than acarbose. Toxicity studies were also promising, with the rats showing no ill effects after being treated with MbA for 9 weeks. This made MbA a very promising drug candidate warranting structural studies.

4.1.4 Specific Aims of this Study

The aim of my experiments into the inhibition of HPA by MbA is to determine structurally the basis of this inhibitor's specificity and affinity. The information so gained will elucidate the interactions between this inhibitor

and the enzyme and explain why small changes to the chemical structure between the montbretin family members significantly alters their ability to inhibit HPA. This will allow the development of a single, minimal unit that retains MbA's powerful inhibitory action.

4.2 Methods

4.2.1 Discovering the Structure of the HPA-MbA Complex

The MbA used in these studies was initially obtained from Katharine Woods from Dr. Raymond Andersen's group, and later from John Coleman at the Centre for Drug Research and Design (CDRD). Both had isolated the compound from the corms of *Crocosmia crocosmiflora*, var. Emily McKenzie. The crystal screening process was performed in collaboration with Nham Nguyen and Dr. Chunmin Li. Crystallization trials were conducted using both wild-type and variant HPA enzymes. The HPA H299N, N298S and R195Q mutants were employed due to a temporary difficulty in obtaining sufficient quantities of wild-type enzyme. This allowed crystallization trials to continue while new stocks of *Pichia pastoris* cells expressing the wild-type enzyme were prepared.

4.2.1.1 Expression, Purification and Crystallization of Wild-Type and Mutant HPA

The procedures for the expression and purification and crystallization of wild-type and mutant HPA can be found in section 2.2.1; crystallization methods are in sections 2.3.2 and 3.3.2. *Pichia pastoris* cells containing a plasmid for HPA H299N were provided by Yili Wang, while the R195Q and N298S mutants were provided by Dr. Anjuman Begum. Protein was expressed and purified using the method described in section 2.2.1.

4.2.1.2 MbA Soaking Studies.

Although MbA is a large inhibitor, crystal soaking experiments were conducted to determine whether or not an HPA-MbA complex crystal could be obtained in this manner. The data obtained from these crystals indicated that MbA was too large to fit into the solvent channels in the crystal, so a larger co-crystallization trial was launched.

4.2.1.3 Co-Crystallization of the HPA-MbA Complex

Initially, a grid search was conducted around the crystallization conditions for WT HPA, using all available WT HPA and mutant HPA protein. The H299N variant produced the best results. The HPA H299N-MbA complex was crystallized using the hanging drop vapour diffusion method. The conditions are essentially the same as those for the uninhibited enzyme

(HPA H299N 12.3 mg/ml, 58% MPD, 100 mM sodium cacodylate, pH 7.5) to which MbA was added in a 10:1 MbA to protein ratio. These wells were then sealed and crystals allowed to form. Crystals appeared over the course of one month. These were mounted on nylon loops and flash frozen in liquid nitrogen before being sent to the SSRL for data collection.

4.2.1.4 *In Silico* Docking and Model Building

While crystallization trials were underway, one of the undergraduates in our lab, AmirAli Mahpour attempted to use *in silico* docking to place MbA into the active site of HPA using Autodock 4.0 (*254*). We hoped that this model would provide some initial insights into how MbA might bind to the enzyme. The best of the models he produced, or rather, the one that best fit our expectations, placed the 5OH and 7OH of MbA's myricetin group near the catalytic triad consisting of D197, E233, and D300 (Figure 4.2). In this model the inhibitor's sugar residues do not bind in the enzyme's high-affinity binding subsites, and the ethyl caffeate extends outside the active site cleft so that the 3OH hydrogen bonds to the side chain of S145. None of these features provided any clear understanding of why changing substituents on the cinnamic acid reduced MbA's inhibitory activity by a factor of 1000 or how it achieved its remarkable affinity for the enzyme.

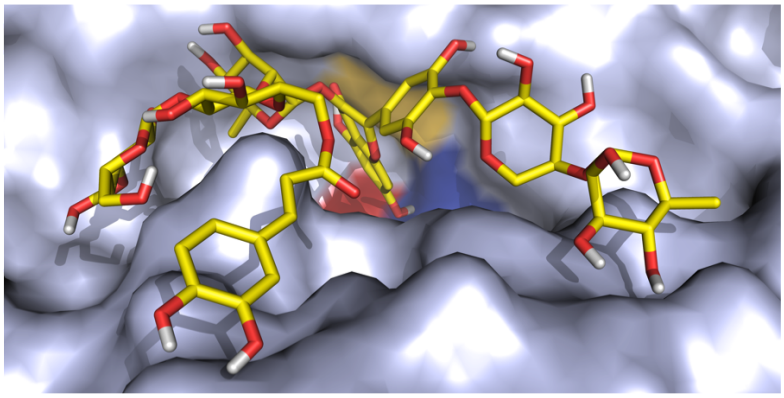

Figure 4.2: Results of *In Silico* Docking of MbA within the Active Site of HPA. *In silico* docking places MbA in the amylase active site with the myricetin fragment interacting with D197 (red), and E233 (blue). D300 is shown in yellow on the surface of the protein.

4.2.1.5 Diffraction Data Collection and Processing

Diffraction data from an HPA H299N-MbA complex crystal were collected on beam line 7-1 at the SSRL at 100 K, a wavelength of 0.98 Å and an oscillation of 1°, using an ADSC Quantum 315R CCD detector. These data were processed and reduced using Mosflm (*214*, *215*) and then scaled using Scala (*237*, *255*, *256*). Observed space group and unit cell dimensions (Table 4.1) indicated that this complex containing crystal was isomorphous with that of wild-type HPA (*51*), and this latter structure was subsequently used as a starting model for molecular replacement using the Crystallography and NMR Systems (CNS) software package (*238*, *257*). All subsequent refinement of the structural model of the H299N HPA/MbA complex was accomplished with CNS, using alternating cycles of simulated annealing, positional and thermal factor B refinements. During this process, the com-

plete polypeptide chain for the inhibitor complex was examined periodically with F_o-F_c, sigmaa weighted 2mFo-DFc and composite omit electron density maps. Where necessary, manual model rebuilding was performed with Crystallographic Object-Oriented Toolkit (COOT) (*239*).

4.2.1.6 Structure Refinement and Verification

That MbA was bound in the active site of HPA H299N was evident in the initial difference electron density maps calculated during refinement of the polypeptide chain of the enzyme. MbA was built into this well-defined density in segments, starting with the myricetin group and then gradually adding the sugar moieties in each subsequent refinement cycle. The caffeoyl group was the last to be added to the model. The HIC-Up database (*258*, *259*) was used to obtain the initial models and parameter files for each sugar; initial models for both the flavonol and ethyl caffeate moieties were generated using the PRODRG server (*240*). Subsequent refinement of both the MbA and polypeptide chain placement was carried out to convergence, the inhibitor atoms at full occupancy.

Difference electron density maps also indicated the presence of an N-acetylglucosamine group covalently bound to the side chain of N461 and two 2-methylpentane-2,4-diol (MPD) molecules hydrogen bonded to the surface of the protein. These were added to the model before adding solvent molecules. The validity of the water molecules was evaluated on the basis of hydrogen bonding potential to protein and inhibitor atoms, and

Table 4.1: Data Collection, Processing and Refinement Statistics

	HPA H299N-MbA
Data Collection Parameters	
Space group	$P2_12_12_1$
Unit cell dimensions (Å)	
a	52.69
b	74.74
c	135.48
Resolution range (Å)	37.37-1.75
Highest Resolution Shell (Å)	1.84-1.75
No. of unique reflections	52965
Mean $I/\sigma I$[a]	18.8 (10.2)
Multiplicity[a]	5.0 (5.2)
Merging R-factor (%)[a]	5.6 (10.5)
Structure Refinement Values	
Number of reflections	52813
Completeness (%)[a]	96.9 (99.5)
No. protein atoms	3943
No. inhibitor atoms	86
No. solvent atoms	566
Average thermal factors ($Å^2$)	
Protein atoms	13.6
Inhibitor atoms	22.7
Solvent atoms	35.5
Overall	25.6
Final R-free value (%)	21.6
Final R-factor (%)	18.6
Structure Stereochemistry	r.m.s. deviations
bonds (Å)	0.014
angles (°)	1.76

[a] The number in brackets indicate data for the highest resolution shell.

the refinement of thermal factors to less than 65 Å^2. Table 4.1 provides a summary of data collection, processing and refinement statistics for the HPA H299N-MbA complex structure. The torsion angles between amino acids was evaluated using both PROCHECK (*220*) and Mosflm (*241*). The Ramachandran plots obtained can be seen in figure 4.3.

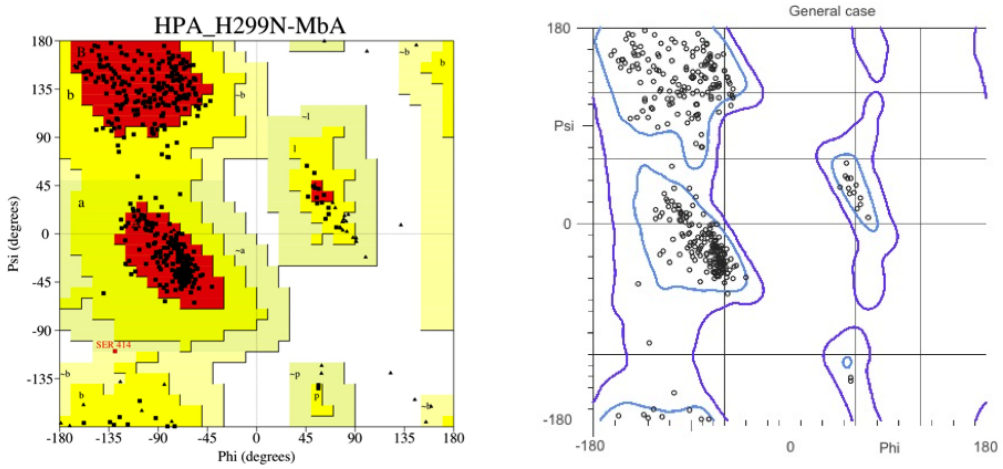

(a) (b)

Figure 4.3: Main Chain Dihedral Angles in the Final Model of the HPA H299N-MbA Complex. The Ramachandran plots were produced by (a) PROCHECK (*220*), and (b) Molprobity ((*241*)). Serine 414 is outside the preferred area in the PROCHECK plot because it participates in a γ-turn.

4.2.2 Isolation and Crystallization Trials of Two α-Amylases Produced by the Microbiota in the Human Gut

Since the inhibition of α-amylases from bacteria in the human gut could help prevent the flatulence, diarrhea and pain associated with clinical use of α-glucosidase inhibitors for the treatment of type II diabetes, we selected two bacteria from the human gut microbiome, *Roseburia inulinivorans* and *Butyrivibrio fibrisolvens*, to use as models for MbA inhibition of bacterial α-amylase. These were chosen, because the clones containing the α-amylase genes could be obtained from Dr. Harry Flint, and expression and purification protocols had already been established (*260*). The first step was to obtain crystal structures of the enzyme alone and then, if successful, to proceed to co-crystallization trials with MbA, as well as soaking studies with acarbose, to give us insight into the workings of human gut microbiota and the process of digestion itself. The experiments describing the isolation and crystallization trials of these two enzymes can be found in Appendix B.

4.3 Results

4.3.1 Crystal Structure of HPA H299N/MbA Complex

To investigate the powerful binding of MbA to HPA, co-crystallization trials were undertaken to crystalize the complex between MbA and wild-type HPA and several of its mutants. Diffraction quality crystals were obtained from wells containing HPA H299N. After molecular replacement and initial positional refinement, the Fo-Fc maps of the entire polypeptide chain and omit density maps of the active site residues clearly showed a large, well-defined inhibitor in the active site. A model of MbA was built into this density, and the final, refined model of the inhibitor can be seen in figure 4.4. Density was also seen for two molecules of 2-methylpentane-2,4-diol between two symmetry-related polypeptide chains.

4.3.1.1 How MbA Binds to HPA

MbA is a very large and complex inhibitor with a molecular weight of 1228.3 Da (see Figure 4.1). It binds non-covalently within the active site cleft of HPA next to the catalytic residues D197, E233 and D300 (Figure 4.4). It fills nearly all of the available volume and clearly inhibits the enzyme by blocking both substrate and solvent access to the enzyme's catalytic machinery, rather than through a mechanism-based approach.

In the conformation bound to the enzyme, a parallel displaced π-stacking interaction occurs intramolecularly between MbA's myricetin A ring

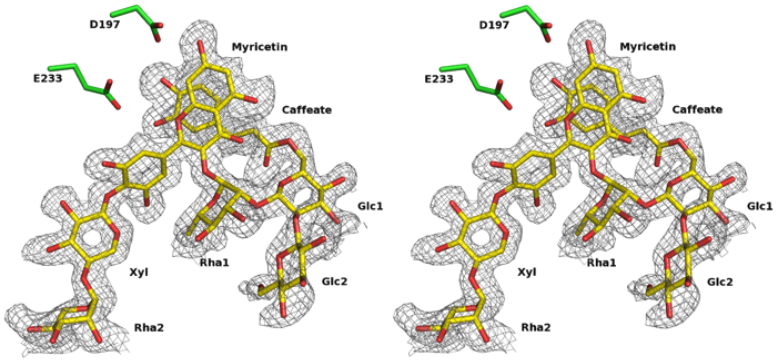

Figure 4.4: Stereo Diagram of the Bound Conformation of MbA in the Active Site of HPA H299N. The omit map is contoured at the 2σ level, and the catalytic nucleophile, D197 and acid-base catalyst, E233, of HPA are shown in green. Notice the π-stacking between MbA's caffeate and flavonol groups. This is markedly different than the *in silico* model shown in figure 4.2.

and the aromatic portion of the caffeate. This can be seen in Figure 4.4: the midline of ethyl caffeate's aromatic ring rests on the junction between the A and C rings of myricetin. The distance between the two planar moieties corresponds to the width of a pyranose ring, and as a unit, they block HPA's -1 binding subsite almost exactly. The parallel displaced π-stacking arrangement is energetically favorable because it avoids charge repulsion between the more positive centres of the aromatic rings (Figure 4.5).

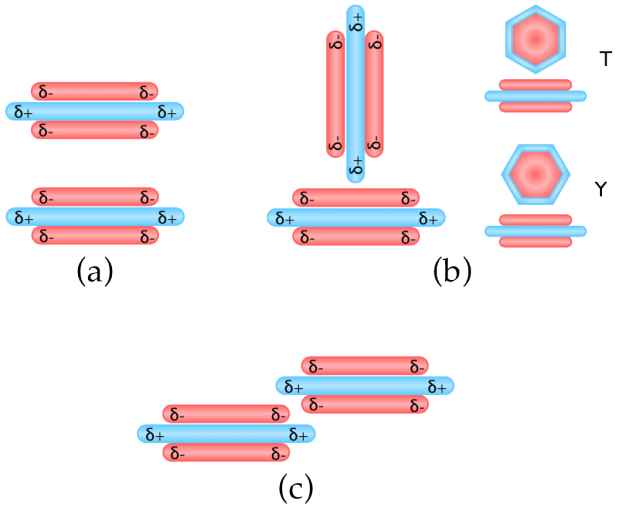

Figure 4.5: π-Stacking Aromatic Interactions. The cartoons qualitatively represent the quadrupole moments in benzene rings, with red indicating positive, and blue, negative partial charges. The face centered 'sandwich' conformation in (a) is disfavored due to electrostatic repulsion. (b) presents an edge to face conformation. The two smaller drawings show its two variants. In the t-shaped interaction (T) a single hydrogen atom from one benzene points toward the aromatic plane of another. The y-conformation (Y) is slightly more stable since two hydrogens point toward the plane. (c) shows a model of parallel displaced stacking. This conformation is very common for single or bicyclic aromatic ring systems. (Adapted from reference (*261*).)

4.3.1.2 Hydrogen Bonding.

Unlike many carbohydrate-containing inhibitors (*70*, *71*, *200*, *244*), MbA is not modified by the enzyme. It is unique in that while it maintains many of the hydrogen bonds found in other HPA-inhibitor complexes, it does not occupy the usual binding subsites (*50*). Instead of having one pyranose ring in each subsite, both the myricetin core and the ethyl caffeate arm of MbA occupy the +1 and -1 binding subsites and hydrogen bond either directly or through key water molecules to the three catalytic carboxylates, D197, E233 and D300 (Figure 4.6).

The myricetin moiety also binds directly to H101/NE2 and through water-mediated bonds to Q63/NE2, Y151/OH and the O5 of the xylose in MbA itself. The ethyl caffeate also participates in several water-mediated hydrogen bonds with N298/ND2 and D300/OD2. Between them, the two glucoses of the inhibitor participate in a single hydrogen bond to the protein from Glc1/O2 to T163/OG1. The second, terminal glucose does not interact with the protein at all, but may help stabilize the inhibitor's folded conformation with an intramolecular hydrogen bond between Glc2/O5 and the O3 of Rha1 (see figure 4.1 for MbA atom numbering).

This rhamnose, acting as a bridge between the myricetin and glucose portions of MbA, does not interact directly with the protein either, but its O4 does participate in a water-mediated hydrogen bond with the side chain oxygen of Y151, the aromatic portion of which packs against the xylose.

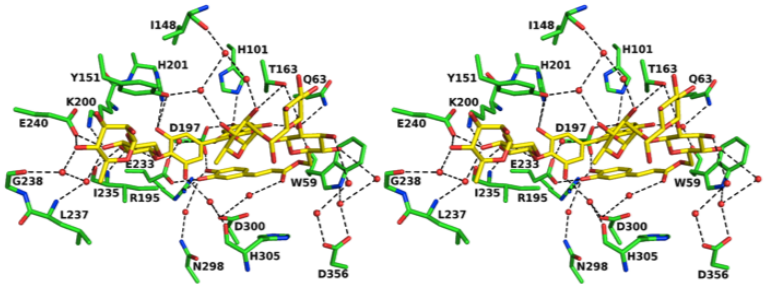

(a)

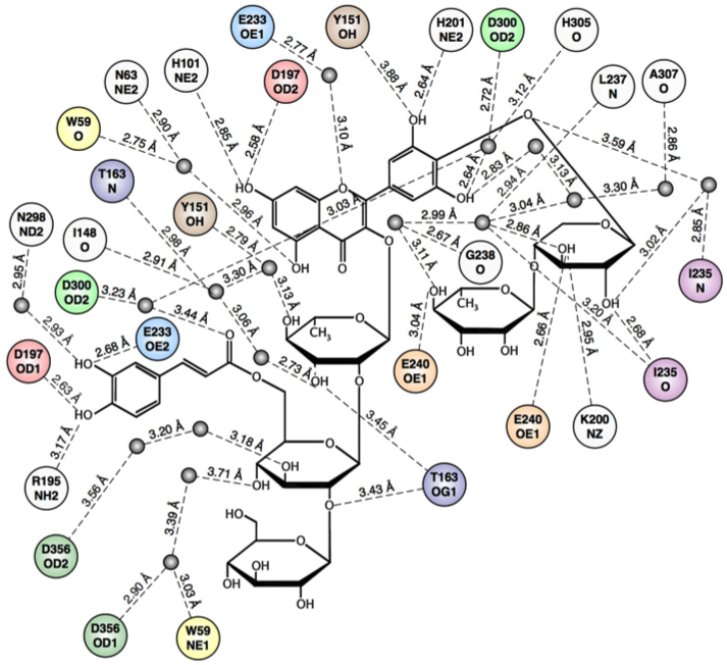

(b)

Figure 4.6: (a) Stereo diagram of the hydrogen bonding network formed upon the binding of MbA (yellow) to HPA H299N (green). Water molecules are drawn as small red spheres. (b) A schematic drawing of this hydrogen bonding network with distances shown in Ångstroms. Protein residues with more than one hydrogen bond to MbA have been shaded the same colour. Water molecules are shown as small grey spheres.

In total, MbA forms 14 hydrogen bonds directly to the protein, 10 hydrogen bonds mediated through one water molecule and 4 that go through two water molecules. This forms a very complex hydrogen-bonding network in which six of the thirteen water molecules form more than two hydrogen bonds. Water is thus an indispensable 'glue' that helps MbA bind to the protein.

4.3.1.3 Inhibitor Folding

One key feature of MbA binding to HPA is the folded conformation of the inhibitor itself. This consists of a purely hydrophobic π-stacking interaction observed between the planar A- and C- rings of the myricetin group and the ring of the caffeate group, in a parallel displaced formation (see figure 4.4). This substructure appropriately positions the hydroxyl groups next to the catalytic residues in the correct orientation to form strong hydrogen bonds. Interestingly, a ROESY NMR analysis conducted by Dr. David Williams of Raymond Andersen's lab suggests that this interplanar relationship occurs spontaneously in solution in the absence of any enzyme (Figure 4.7). This π-stacking primes the inhibitor for binding with HPA, albeit one alteration is needed: in MbA bound within the active site of HPA, the caffeoyl moiety is flipped by 180°. This second conformation is likely present in a small proportion of the molecules in solution, with only a small energy barrier between the two forms.

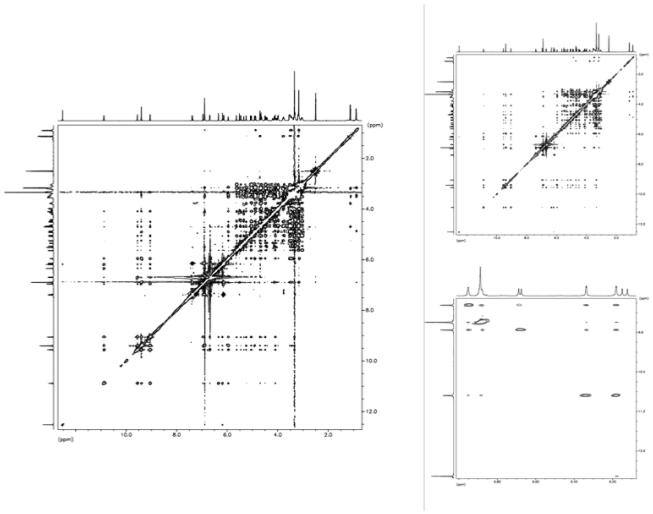

(a)

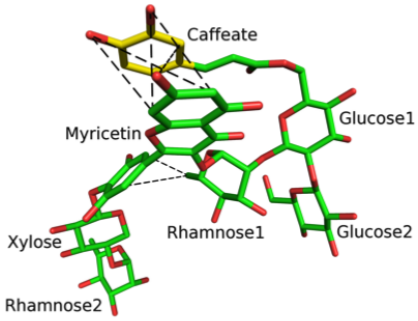

(b) MbA solution conformation

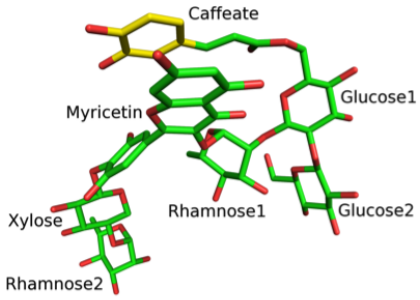

(c) MbA conformation bound to HPA

Figure 4.7: The Solution Structure of MBA. (a) Plots from a ROESY NMR experiment used to model the conformation of MbA in solution. (b) These data indicate that the myricetin and ethyl caffeate ring moieties participate in π-stacking in solution. Strong interactions between groups that have been identified through NMR have been drawn with dashed lines. (c) Comparison with the bound conformation of MbA in the active site of HPA shows that it is very similar to that found in solution. The major difference is a 180° flip of the plane of the caffeate ring (colored yellow). The plots in (a) were provided by Dr. Raymond Andersen.

4.3.1.4 Hydrophobic Interactions

Equally important in establishing the specificity and affinity of MbA for HPA are the hydrophobic interactions: near the catalytic triad, the caffeate and myricetin moieties stack together, with the ring plane of the dihydroxyphenyl of the caffeate being absolutely parallel to the benzopyrone of myricetin. Helping to stabilize this conformation, are several hydrophobic residues: W58 interacts with the plane of the caffeate ring while Y62 is at nearly a 90° angle to it and L162 and L165 pack against the benzopyrone of myricetin. The phenyl moiety of myricetin also has a hydrophobic partner in the protein and packs against the side chain of I235. Even the sugars also take advantage of the placement of hydrophobic residues in the active site: the hydrophobic side of the side chain of T163 packs against the C1 carbon of rhamnose 1, while its side chain oxygen hydrogen bonds to glucose1, Y151 packs against the xylose residue. Interestingly, its side chain oxygen also hydrogen-bonds to the inhibitor. These hydrophobic interactions, while fairly weak individually, help create an extremely tight fit for MbA in the enzyme's active site, and contribute greatly to the its affinity for HPA.

4.3.1.5 Effect of HPA H299N Mutation on MbA Binding

The MbA does not interact at all with the site of the H299N mutation, at their closest, they remain 6 Å apart. The void created by the mutation

is filled by a water molecule near the asparagine, indicating that there is space enough for the histidine of the wild-type enzyme to occupy the same position without disturbing the inhibitor. Indeed, a histidine here would still be more than 4 Å away from bound MbA. A poorer K_i of 124 nM observed for MbA inhibition of HPA H299N (vs. 8 nM for the wild-type enzyme) may reflect this less structured, more hydrated region of the enzyme-inhibitor interface (Figure 4.8). The kinetic study of MbA inhibition of HPA H299N was performed by Xiaohua Zhang from Prof. Steve Withers' group (*262*, personal communication); her results are shown in figure 4.9.

4.3.1.6 Effects of Mutation and MbA on Protein Structure

Neither the use of the H299N variant, nor the binding of MbA significantly affected the protein fold: the average root mean squared distance between corresponding main chain atoms of the H299N-MbA complex and the wild-type, inhibitor-free amylase is only 0.26 Å. A residue-by-residue analysis of the mainchain positional changes is shown in Figure 4.10. The peaks seen at residues 305, 350, and 459 can be attributed to positional changes in H305, which is flipped relative to its counterpart in the wild-type protein, a flipped peptide bond at N350 and variations in the position of a beta-turn at residue 459. The changes at residues 305 and 459 may not be significant due to the poor electron density seen in maps of these areas, which indicates high mobility in these loops. More inter-

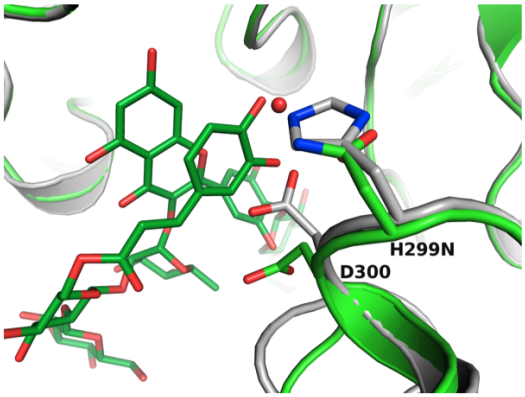

Figure 4.8: The Site of the H299N Mutation. HPA H299N is shown in green with bound MbA as sticks. The structure in silver is the wild-type enzyme (*51*). NE2 of the histidine is replaced by a water molecule in the mutant enzyme. The shift in the position of D300 is unlikely to be caused by the mutation due to the proximity of one of MbA's aromatic rings.

esting, however, is the smaller peak in the distance graph at residue 240: E240 hydrogen bonds to the rhamnose2 and xylose groups of MbA, and these interactions force a small deviation in the main-chain position in this region of the protein. Interestingly, in the structure of HPA with bound myricetin (*1*), this same area is pulled toward the active site, rather than pushed away from it. The average thermal factors for each residue show very similar patterns in the H299N-MbA complex and wild-type HPA. A small drop in B-values is seen near residue 375 of the MbA structure that is not present in any of the other HPA structures (Figure 4.11). This change is likely due to the proximity of a symmetry-related MbA molecule (5.9 Å) and the resultant changes in solvent structure near residue 375. This is evidenced by the addition of an extra ordered water molecule hydrogen bonded to D375 in the MbA complex structure; this ordered water

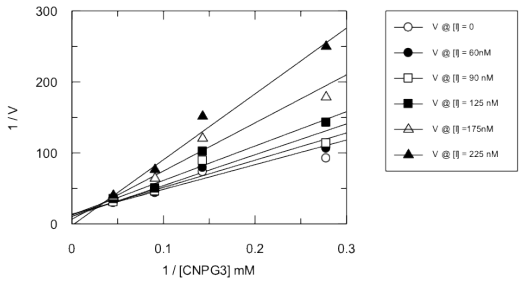

(a)

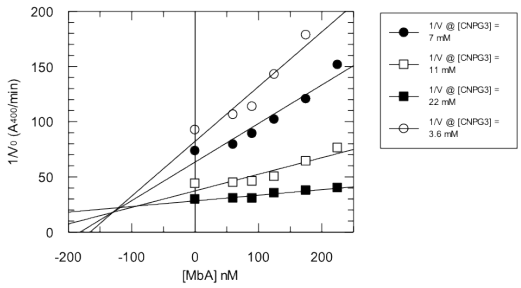

(b)

Figure 4.9: Kinetics of MbA Inhibition of HPA H299N. (a) Linewear-Burk plot, and (b) Dixon plots show that MbA inhibits HPA H299N competitively with a K_i of 124 ± 14 nM.

molecule is not present in any other HPA-inhibitor complex. The drop in thermal factors at residue 305 is caused by a hydrogen bond that has formed between its side chain and that of D300. The HPA-MbA complex structure is the first in which this hydrogen bond appears. The binding of MbA to the free enzyme also causes a positional shift near residue 305 (see Figure 4.10). This is part of a highly mobile loop from residues 303-310 that stabilizes bound substrates in the -2 binding subsite. This loop is disordered in the free enzyme, but becomes more ordered as it coalesces around bound substrate mimics (*50*). In these structures, the side chain of

H305 shifts towards the inhibitor to hydrogen bond with it. The binding of MbA, however, causes the opposite effect, and H305 moves away from the active site to avoid steric conflicts with the large inhibitor. As H305 shifts away, the rest of the 303-310 loop moves with it. In conjunction with the change in position of residues 303-310, the side chain of the catalytic residue D300 also moves away from the active site through an approximately 90° rotation, since this would also clash with the inhibitor were it to remain in the same position as in the free enzyme. As a result, D300 now forms a hydrogen bond with the side chain of H305 (figure 4.12). This interaction has never been seen in any other HPA crystal structure. The final two regions of polypeptide chain displacement near residues 350 and 459 occur farther from the active site, and involve a flipped peptide bond at N350 and a β-turn variant at N459. These changes occur in regions of high polypeptide chain mobility, and should not be considered definite since they are poorly determined in electron density maps.

4.4 Discussion

The crystal structure of the HPA H299N-MbA complex shows just how essential the ethyl caffeate moiety is in establishing how this inhibitor binds to the enzyme. When bound, the ethyl caffeate sits right next to the catalytic carboxylates, forming hydrogen bonds with the catalytic nucelophile, D197 and the acid-base catalyst, E233 as well as the side chain of R195, a

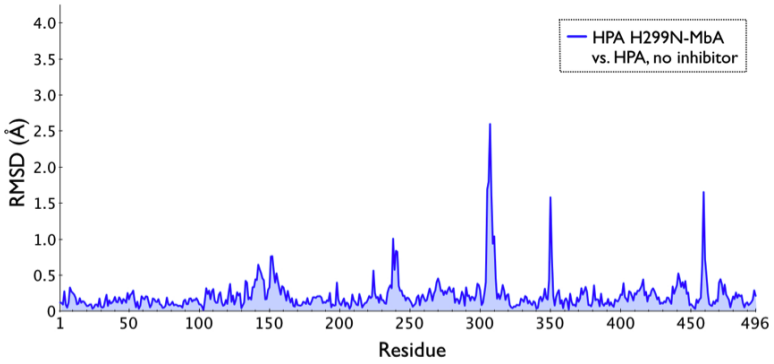

Figure 4.10: Plot of the average root mean square differences in Ångstroms between the Cα atoms of the HPA H299N-MbA structure and wild type HPA with no inhibitor (*50*). The highest peak at residue 305 is due to the high mobility in a substrate binding loop in the enzyme's active site. The small peak near residue 240 is due to displacement of the polypeptide chain as E240 hydrogen bonds to MbA. The other peaks are due to flipped peptide bonds in solvent-exposed loops on the protein's surface.

residue known to bind and stabilize the chloride ion that modulates the electrostatic environment of the active site (*52*, *244*, *245*). If this network is extended to include solvent molecules, the caffeoyl group also interacts through an intermediary water molecule with the side chain of the third catalytic carboxylate, D300 and the side chain of N298, also known to bind the chloride ion (*52*, *244*, *245*). This is consistent with the results of kinetic experiments with Montbretin B (MbB) and MbD.

The hydrophobic interactions of the aromatic cinnamate are also indispensable for MbA inhibition of HPA. The aromatic A rings of myricetin π-stack against the caffeoyl group, and together, they form a block that is very nearly the same width as a pyranose ring, and this block slides into

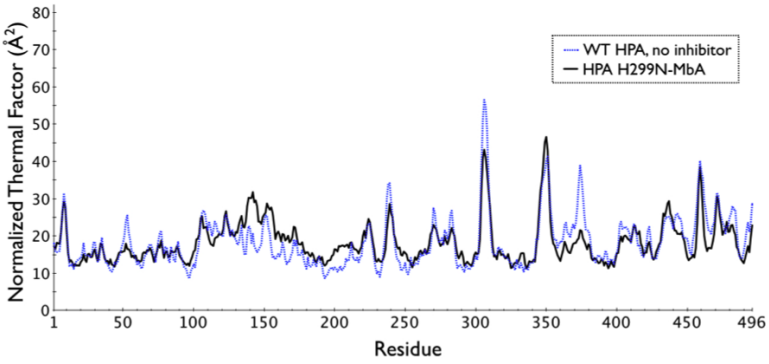

Figure 4.11: Comparison of the Main Chain Thermal Factors of the HPA H299N-MbA Complex (solid black line) and WT HPA without any Inhibitor Present (*50*, dotted blue line)). The values have been normalized so that the two sets of data have the same mean. The modest drop in thermal factors near residue 375 of the MbA complex structure is not seen upon the binding of other inhibitors and may be due to the proximity of a symmetry-related MbA molecule and the resultant changes in nearby solvent structure. The drop at residue 305 is due to a new hydrogen bond formed between H305 and D300 as the latter turns away from its usual position in the active site.

the active site to form hydrophobic interactions with W59, Y62, L162 and L165. Without the caffeoyl group, the inhibitor would not fit as tightly into the active site.

The hydrophilic and hydrophobic contacts formed by MbA's caffeoyl group severely restrict the orientation of MbA near the catalytic carboxylates, and provide an explanation of the tremendous differences in kinetic parameters for HPA inhibition by montbretins A through E. In studies conducted by Drs. Chris Tarling and Jacqueline Wicki of Prof. Steve Withers' group, the replacement of the 3OH of the caffeate of MbA with a hydrogen in MbB, and the subsequent 1000 fold decrease in inhibitory activity can

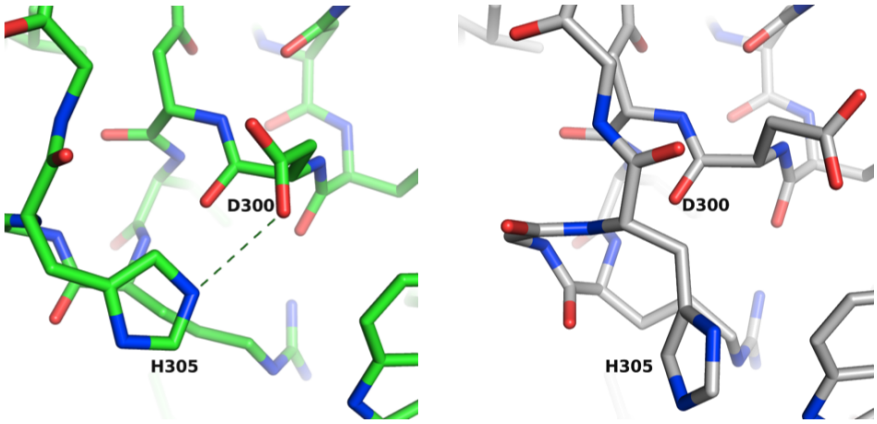

(a) (b)

Figure 4.12: The Shift in Atom Positions of HPA's Substrate Binding Loop (Residues 303-310) upon the Binding of MbA. (a) In the HPA-MbA complex structure, D300 and H305 hydrogen bond, stabilizing the position of the mobile loop. The hydrogen bond is shown as a dashed line. (b) The position of the same residues in uninhibited HPA. Note how the side chain of D300 is turned towards the active site, whereas in (a) it turns towards the substrate binding loop.

be explained by the loss of the hydrogen bonds with E233 and, through a water molecule, with N298. It is also possible that the presence of this hydroxyl helps stabilize the folded conformation of MbA, with it interacting either with myricetin's 7OH in the predominant form in solution, or with O1 in the conformation seen bound in HPA (see figure 4.7).

The addition of a methoxy group to carbon 3 of MbA's cinnamate ring in MbC would cause the same hydrogen bond loss as seen with MbB; it would also be paired with a steric repulsion that would prevent a folded MbC from binding in the enzyme's active site in the same orientation as

MbA. This montbretin variant is an even weaker inhibitor of HPA, and its K_i is twice that MbB.

The kinetics of MbD and MbE inhibition of HPA show the effect of an additional glucose added to the 7-OH of myricetin in MbB and MbA, respectively. It is impossible for these first two inhibitors to bind to the enzyme in the same manner as that seen in the crystal structure of the HPA H299N-MbA complex, since the glucose at the 7 position would clash sterically with the protein. Montbretins D and E, however, do inhibit HPA, with K_i values of 830 and 790 nM. This is only possible if there exists a second, different binding mode for these variants. Surprisingly, the addition of this glucose has a smaller effect on the binding affinity of the montbretins than the replacement of the ethyl caffeate 4-OH of MbA with either a -H or -OMe group. I suggest that this might be a result of a flattened conformation for montbretins D and E if the 7-glucose can prevent the hydrophobic stacking between myricetin and ethyl caffeate that is seen in both the ROESY NMR study of MbA in solution and the crystal structure of the MbA-HPA complex. A more extended conformation of montbretins D and E in solution may also explain why this second binding mode is largely inaccessible to the other montbretins: it may depend upon crucial enzyme-inhibitor interactions that are obstructed by inhibitor folding. If the difference in kinetic parameters of the montbretin variants is due to the formation or lack of formation of a compact inhibitor structure, this

would mean that the solvent itself plays a vital role in the affinity of these inhibitors for the enzyme.

4.4.1 Comparison to the HPA-Acarbose Complex Structure

One of the primary differences between the inhibition of HPA by acarbose and by MbA is that the enzyme actively alters the first by cleaving and transglycosylating the inhibitor to produce a new compound with higher affinity for the enzyme (*50*, *71*, *200*) while MbA remains untouched by any catalytic process despite the presence of several glucose residues. This is because none of the carbohydrate portions of MbA bind adjacent to the three catalytic carboxylates, D197, E233 and D300. Instead, the π-stacked myricetin and ethyl caffeate moieties insert themselves into the active site and hydrogen bond directly with D197 and E233, and through water-mediated contacts, with D300.

When the HPA-acarbose and HPA H299N-MbA complex structures are superimposed, only the myricetin moiety overlaps with the conformation of bound acarbose, acting as a bridge between the -1 and +1 binding subsites, covering the position of the scissile bond (Figure 4.13). The gap between the π-stacked groups of MbA blocks the -1 subsite almost exactly, with the 3OH of the caffeate moiety corresponding to the position of the

nitrogen joining the two rings of acarbose's valienamine. Both of these atoms hydrogen bond with the side chain of E233.

Regardless of the differences in the structures of MbA and transglycosylated acarbose, the two inhibitors share key hydrogen bonds to specific enzymatic residues, including W59, H101, D197, H201, E233 and E240 with MbA forming 14 direct hydrogen bonds with the enzyme, while transglycosylated acarbose has 15. This similarity is reflected in the K_i for each inhibitor: 8 nM for MbA (*2*) and 15 nM for transglycosylated acarbose (*200*), indicating the MbA binds to the enzyme as strongly as the transition state mimic.

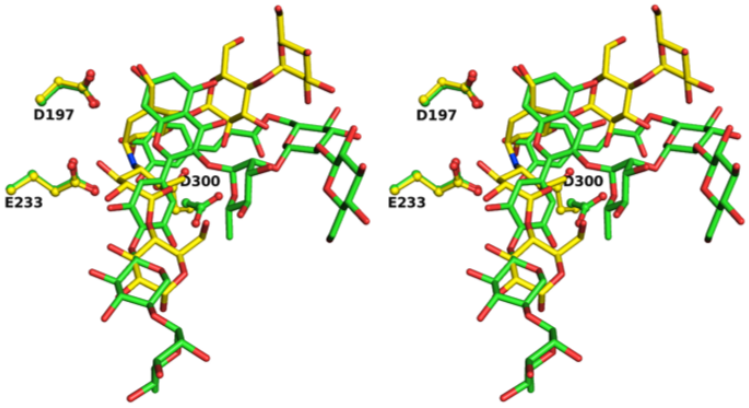

Figure 4.13: Stereo diagram of the conformations of the bound inhibitors MbA (green) and acarbose (yellow) in the active site of HPA. The side chains of the catalytic carboxylates are shown in ball and stick format. MbA has a very different mode of binding than the transition state analogue, and the distance between the π-stacked aromatic rings of MbA corresponds almost exactly to the diameter of acarbose's valienamine. D300 also rotates away from the active site cleft.

The binding of MbA to the enzyme's active site causes two structural changes that do not occur when acarbose is bound. The first is that the side chain of D300 rotates away from the active site, a rotation that has previously been seen only when the flavonol myricetin binds; the second is that this rotation is accompanied by a shift in the position of the mobile loop from residues 303-310, as it moves away from the active site. This displacement, shown in figure 4.12, enables a hydrogen bond to form between the side chains of D300 and H305. In the HPA-acarbose complex, this same loop moves into the active site so that H305 hydrogen bonds with the inhibitor in the -2 binding subsite.

Another key difference between acarbose and MbA, is that MbA appears to inhibit HPA specifically, while acarbose acts indiscriminately as a general α-glucosidase inhibitor, affecting the activity not only of HPA, but of many other α-glucosidases as well (*82*, *263*). This is due to the very different structures of each inhibitor. As a transition-state mimic, the valienamine moiety of acarbose can be expected to bind to many α-glucosidases that share HPA's double displacement mechanism (*264*). Acarbose, is therefore capable of binding to, and inhibiting all of the human digestive α-glucosidases.

4.4.2 Comparison to HPA-Myricetin Complex

Many flavonols and substituted flavonols have been shown to have α-amylase inhibitory activity (*108*, *120*, *126*, *265*). The myricetin core of MbA

is among these, and it inhibits HPA with a K_i of 110 μM. While the binding modes of MbA and myricetin share some characteristics in common, overall they are very different.

Both myricetin and MbA's myricetin core bind to HPA adjacent to the catalytic residues and significantly, within the same plane (Figure 4.14). Also similar is the displacement of D300 and H305, as well as the movement of the substrate-binding loop from residues 303-310 away from the active site cleft; in contrast, the positions of D197 and E233 do not change at all. The orientation of myricetin's aromatic rings, is however, distinct in each structure. Myricetin by itself binds in such a way its B-ring occupies the same position as the C-ring of the flavonol in MbA. This is accompanied by an approximately 120° rotation of the myricetin group so that there is no overlap between the B- and C-rings of myricetin alone and the rest of MbA. This rotation increases the number of hydrogen bonds that the smaller inhibitor can form within the active site, and is very likely preferred for this reason. It also follows a path that more closely resembles that of a normal substrate. MbA cannot orient itself in this way, as it is constrained by bulky constituents that determine where and how the myricetin moiety can bind.

4.4.3 Comparison to HPA-Ethyl Caffeate Complex

Before the crystal structures of the HPA H299N-MbA and HPA-ethyl caffeate complexes were available, it was assumed that ethyl caffeate would

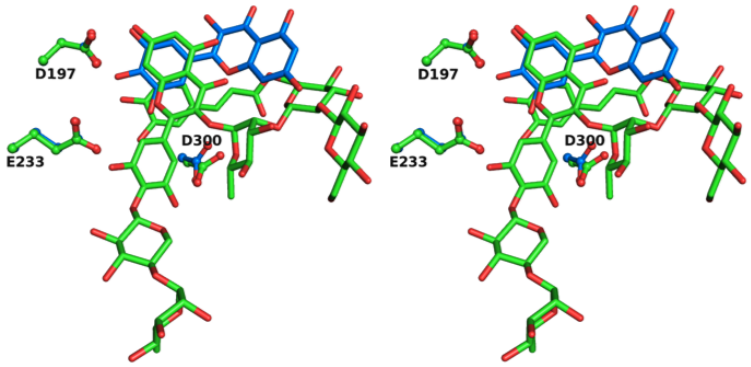

Figure 4.14: Stereo representation of MbA (green) and myricetin (*1*, blue) bound in the active site of HPA. The three catalytic residues appear in ball and stick format. In both of these structures, the side chain of D300 turns away from the active site and the bound inhibitor. Interestingly, the B ring of myricetin binds in the same position of the C ring of MbA, and the myricetin molecule has rotated within this plane to maximize the number of hydrogen bonds formed to D197 and E233.

play a similar role in the inhibition of the enzyme in both cases. My structural studies clearly show the importance of the ethyl caffeate moiety in MbA's inhibition of HPA. This moiety forms many hydrogen bonds to key enzymatic residues, including D197, E233, and R195, one of the residues that helps bind the chloride ion that modulates the electrostatic environment of the active site (*52*, *244*, *245*). It also interacts through a water molecule with N298 and the third catalytic carboxylate, D300. Removing a single hydroxyl group from MbA's ethyl caffeate decreases the binding affinity by three orders of magnitude (*2*). The π-stacking interaction between the ethyl caffeate and myricetin aromatic rings also allows for addi-

tional hydrophobic interactions with the side chains of W59 and Y62, L162 and L165.

Ethyl caffeate, by itself, also a weak inhibitor of HPA with a K_i of 1.3 mM, inhibits the enzyme by a completely different mechanism than MbA. Instead of blocking the enzyme's active site as does MbA, ethyl caffeate is a non-competitive inhibitor that binds to three separate binding pockets on the enzyme's surface approximately 20 Å away from the catalytic triad. Ethyl caffeate binding at these three sites causes four normally ordered loops to become disordered. These loops make up most of HPA's extended substrate binding cleft, and disordering them keeps them from orienting any bound substrate in a productive conformation. This difference in both binding conformation and mode of action means that the crystal structure of the HPA-ethyl caffeate complex cannot shed much light on HPA inhibition by MbA. It does however, remind this researcher that assumptions should never be taken as givens.

4.4.4 Comparison to the HPA-Voglibose Complex

No significant variation on the position of Cα atoms or in the thermal factors occurs when comparing the structures of HPA with bound MbA or bound voglibose. The variations that do occur have been discussed relative to the enzyme with no inhibitor in section 4.3.1.6. Interestingly, however, voglibose's cyclohexanol ring binds in nearly the same plane as

MbA's myricetin core, both groups packing against the side chain of L162 (Figure 4.15).

While the presence of the π-stacked caffeate group severely limits where and how MbA can bind to the enzyme, the fact that both free myricetin and voglibose bind in the same plane as MbA's flavonol core may indicate that this orientation may not be determined entirely by the inhibitor's folded conformation, and that L162 is perfectly placed to stabilize the binding of moieties that have little affinity for the enzyme's binding subsites, yet still hydrogen bond to D197 and E233.

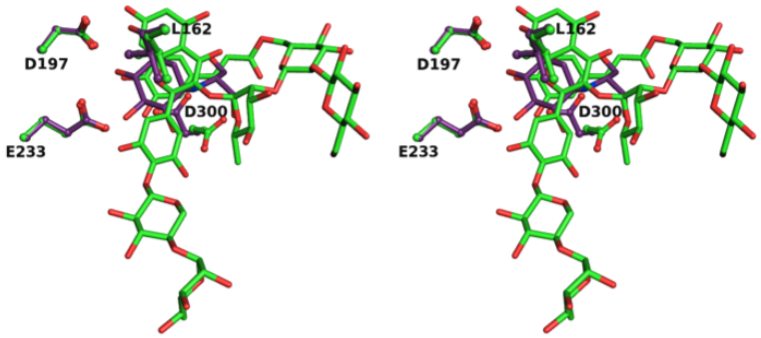

Figure 4.15: Stereo representation of the binding of MbA (green) and voglibose (purple) in the active site of HPA. Protein residues are shown in ball and stick format. Both voglibose and MbA's π-stacked core hydrogen bond with the catalytic carboxylates, D197 and E233, and MbA's myricetin and voglibose's cyclohexanol also pack against the side chain of L162 with the rings in nearly the same plane.

4.4.5 Flavonol Caffeoglycosides and Inhibitor Specificity

Yoshida, Hishida, Iida, Hosokawa, and Kawabata (*230*) showed that flavonol caffeoylglycosides can also inhibit rat intestinal maltase, with quercetin 3-O-(6-O-caffeoyl)-β-galactoside having a K_i of 110 μM. These larger compounds inhibited the enzyme better than either the isolated flavonol or the caffeoylglycoside alone. The linker region between the flavonol's 3OH and the caffeoyl group is longer in MbA, consisting of a rhamnopyranose and a glucopyranose ring compared to a single galactose in the maltase study. It would be possible, however, for the smaller flavonol galactoside to fold so that the two aromatic moieties interact if the sugar were to assume a $^1C_4$ configuration. Perhaps this is what confers the greater inhibitory power to the flavonol caffeoylglycoside over either moiety alone. If so, this opens the door to bespoke inhibitors designed to bind to each α-glucosidase specifically by altering not only the length of the linker, but also the other substituents attached to the flavonol core.

4.5 Conclusions

These structural studies clearly show that MbA binds to the HPA in a completely different manner than any inhibitor previously observed. Instead of binding to the high affinity binding subsites established in studies of the transition state mimic, acarbose (*50*, *51*, *71*, *200*), it places two stacked, planar aromatic groups across the -1 subsite to engage enzymatic residues,

including two of the catalytic carboxylates, in multiple hydrogen bonds while taking advantage of the presence of hydrophobic residues lining the active site cleft to further stabilize the protein-inhibitor complex. These inhibitory features of MbA's binding mode are further enhanced by the displacement of two elements necessary for substrate binding; that is, D300 and H305. The peripheral sugar groups also participate in an assortment of hydrogen bonds and hydrophobic interactions that increase binding stability. Together, these features exclude substrate from the active site through high affinity binding interactions, rather than attempt to mimic any part of the catalytic process. That other α-glucosidase inhibitors containing the flavonol-sugar-caffeate motif have been found indicates that this π-stacked conformation may be the basis for new, high-affinity inhibitors for other enzymes as well.

Chapter 5

The Foundation of the Nanomolar Inhibition of Mammalian α-Amylases by Amystatin

5.1 Introduction

Amystatin is a high affinity HPA inhibitor isolated from the Caribbean sea anemone, *Stichodactyla helianthus*. It is a small peptide composed of 44 amino acids and it contains 3 disulfide bonds. It inhibits HPA competitively with a K_i of 2 nM, making it a good candidate for structural studies into α-glucosidase inhibition by peptides.

5.1.1 Discovery and Isolation and Characterization of Amystatin

The same search for HPA inhibitors that led to the discovery of a new use for the known molecule, montbretin A, described in the previous chapter, also discovered a heretofore unknown inhibitory peptide that has been designated amystatin.

The screen for HPA inhibitors, conducted by Dr. Chris Tarling, tested natural product extracts and known chemical compounds for HPA inhibitory activity (*2*). In this experiment, the release of chlorophenolate anion from the substrate CNP-G3 was monitored at 402 nm and the residual activity of the enzyme determined by comparing it to uninhibited controls. One of the extracts from a marine natural product library provided by Dr. Raymond Andersen proved to be a particularly potent inhibitor; this extract was from the Caribbean sea anemone, *Stichodactyla helianthus*. The active compound, amystatin, was isolated from this extract by Dr. Rob Keysers.

Kinetic testing of the peptide showed it to be a competitive inhibitor of HPA with a K_i of 2 nM (*251*). Edman degradation identified it as a 44 amino acid peptide with 3 disulfide bonds; its primary sequence is ESGNSCYIYHGVSGICKASCAEDEKAMAGMGVCEGHLCCYKTPW. This original sample was the only one that contained the amylase-inhibiting peptide, and samples of *Stichodactyla helianthus* collected from the same location at a later date failed to produce any more of the peptide. A synthetic peptide was therefore used in all of the structural studies described in this chapter. This peptide was synthesized by AnaSpec, Inc. and its purchase was organized by Suzanne Perry of UBC's Proteomics Core Facility.

5.1.2 Peptides with Three Disulfide Bonds

Short peptides with 3 disulfide bonds are common in nature and been known to have anti-microbial (*266*, *267*), neurotoxic (*268*, *269*), as well as amylase-inhibiting properties (*166*, *270*). These peptides are classified based on the topology of their disulfide bridges: knottins have covalent linkages between cysteines 1 and 4, 2 and 5, and 3 and 6, while defensins are split into two major categories, with α-defensins having bonds between cysteines 1-6, 2-4, and 3-5, and β-defensins having a 1-5, 2-4, 3-6 disulfide bond topology (*170*, *271*). Knottins can vary in secondary structure, whereas almost all defensins share a common fold. Several other categories of defensin do exist: plant defensins (γ-thionins) share a common fold with other defensins, but contain 4 disulfide bridges, and θ-defensins, found in macaques and baboons, are 18 amino acid peptides folded into two antiparallel β-strands stabilized by the three disulfide bonds, one of which joins the N- and C- termini (*272*, *273*).

5.1.2.1 Specific Aims of this Study

The small, disulfide-rich scaffold of amystatin makes it unique among inhibitors of mammalian α-amylases. The goal of the structural study of amystatin inhibition of α-amylase is to determine how this peptide achieves nanomolar inhibition of the enzyme, and to use this informa-

tion about its binding mode to determine features that may contribute to determining specificity for mammalian α-amylases.

5.2 Methods

5.2.1 Unravelling the Disulfide Topology of Synthetic Amystatin

5.2.1.1 Sulphydryl Quantitation for Synthetic Amystatin

Naturally occurring amystatin is a rapid-acting inhibitor of HPA with a K_i of 2 nM. Its synthetic counterpart is a much slower binding inhibitor; however, the K_i remains the same in experiments conducted by Drs. Jacqueline Wicki and Ran Zhang. Since no attempt was made to oxidize the chemically synthesized peptide after purchase to form the disulfide bonds, the implication of these studies is that the synthetic amystatin is at least partially linear and must fold itself into the correct conformation in order to bind to amylase.

To test this hypothesis, I performed a sulphydryl determination for synthetic amystatin using 5,5′-dithio-bis-(2-nitrobenzoic acid) (5,5-dithio-bis-(2-nitrobenzoic acid) (DTNB)) (Figure 5.1) as described by Ellman (*274*). DTNB reacts with sulphydryls to create a yellow-coloured product, TNB^{2-}, that can be monitored at 412 nm (Figure 5.2). The absorbance readings can

then be used to calculate the quantity of free sulphydryl groups in the sample.

A buffer solution was prepared containing 100 mM sodium phosphate, pH 8.0 and 1 mM EDTA (Buffer A). 1.22 mg of lyophilized synthetic RAK01 was dissolved in 1.5 mL of buffer A, and, in a separate vial, 8.42 mg of DTNB was dissolved in 2.04 mL of buffer A. The final concentration of each solution was 1.73×10^{-4} M and 1.04×10^{-2} M, respectively. 1.0 mL samples were prepared in 1 cm plastic cuvettes by diluting the peptide and DTNB solutions with more buffer A. The volume of DTNB solution used was held constant at 20 μL for all samples, but the peptide solution volume was varied between runs from 20 to 100 μL. After mixing, the cuvettes were placed in a Cary 300 spectrophotometer and allowed to incubate for 15 minutes at room temperature. For each run, the samples were prepared in triplicate and were accompanied by peptide and DTNB blanks containing the same concentrations of each reagent as the samples.

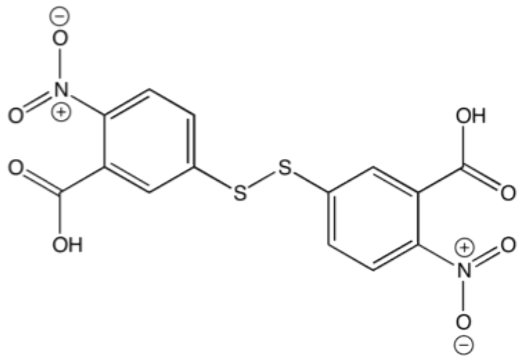

Figure 5.1: Structure of DTNB

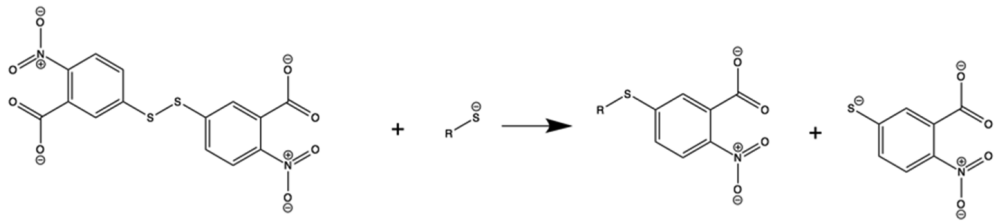

Figure 5.2: The disulfide exchange reaction of DTNB produces a modified peptide and TNB^{2-}.

After 15 minutes, the absorbance of each cuvette was measured 5 times at 412 nm. For each run, the mean of these readings was used to calculate the sulphydryl concentration of the samples using the Beer-Lambert Law and an extinction coefficient of 14150 $M^{-1}cm^{-1}$. This procedure was repeated in five separate runs. The ratio of sulphydryls per amystatin molecule was then calculated (see Table 5.1). All absorbance readings were corrected for both the peptide and DTNB blanks.

The disulfide bridging pattern of the synthetic amystatin peptide was also analysed using mass spectrometry and NMR. The mass spectrometry studies, conducted by Suzanne Perry at The University of British Columbia (UBC)'s Proteomics Core Facility, used both trypsin and endoproteinase GLU-C with and without reduction and alkylation to prepare samples of the synthetic peptide. Maldi-TOF then identified the peptide fragments in the samples that were untreated and those subjected to reductive alkylation. 1d, gDQCOSY, ROESY, WGNOESY and WGTOCSY NMR spectra were collected by Mark Okon of Prof. Lawrence McIntosh's group at 25°C using a Varian Unity 500 MHz NMR spectrometer.

Table 5.1: Sulphydryl Quantitation with DTNB

	Sulphydryl Concentration (M)				
	Run 1	Run 2	Run 3	Run 4	Run 5
Amystatin concentration (M)	1.73×10^{-5}	1.38×10^{-5}	1.04×10^{-5}	6.91×10^{-6}	3.45×10^{-6}
Mean of 5 absorbance readings (A_{412})	0.8087	0.6893	0.5119	0.3308	0.1837
Sulphydryl concentration (M)	5.72×10^{-5}	4.87×10^{-5}	3.62×10^{-5}	2.34×10^{-5}	1.30×10^{-5}
Ratio [SH]:[Amystatin]	3.31	3.53	3.49	3.38	3.76

5.2.2 Crystallization of the Amylase-Amystatin Complex

Crystallization trials initially attempted to co-crystallize amystatin with HPA using both the conditions found in the crystal screening kits, Crystal Screen and Crystal Screen 2 from Hampton Research, and Wizard I and Wizard II from Emerald BioSystems, and by adjusting the known crystallization conditions for wild-type PPA and HPA. Crystals formed under several sets of conditions, but these crystals either did not diffract or degraded rapidly when subjected to x-rays. To circumvent this impasse, and greatly increase the amount of protein available, a sample of porcine pancreatic α-amylase (PPA) was purchased from Sigma (A4268). PPA is a homolog of HPA that shares an 86% sequence identity and 92% similarity with HPA. Both enzymes assume identical folds; the superimposed structures of the two enzymes can be seen in Figure 5.3 (*45*, *109*). One advantage of using PPA over HPA in the crystallization trials is that PPA crystallizes in a form that leaves the active site open, rather than blocked by a symmetry related molecule, thereby increasing the chance that the same crystal packing can accommodate a large inhibtor such as amystatin. Crystallization trials of both the HPA-amystatin and PPA-amystatin complexes then proceeded in tandem. The purchased sample of PPA needed further purification before it could be crystallized. This procedure is described in section 2.2.2 on page 55.

Figure 5.3: The structure of PPA (yellow) is overlaid onto the structure of HPA. HPA shows the enzymes' three domains, with domain A in red, domain B in green and domain C in blue. The calcium ion of HPA is seen in cyan. The chloride ion of PPA is shown as a yellow sphere, and the chloride of HPA sits directly behind it (green sphere). Invisible in this picture is the calcium of PPA, which is obscured by the same atom in HPA.

Diffraction-quality crystals of the PPA-amystatin complex were grown by Nham Nguyen by mixing PPA with amystatin in a 1:2.5 enzyme to amystatin molar ratio. 2 μL drops of the PPA-amystatin solution were then mixed with 2 μL of 0.1 M Tris, pH 8.5, 8% PEG 8000 (mother liquor) on siliconized microscope slides. The slides were then inverted and sealed over a well containing 500 μL of the mother liquor. Using this hanging drop vapour diffusion method, the crystals grew at room temperature in approximately 3 weeks time. The crystals were soaked in a solution of 30% glycerol mixed with the mother liquor before being flash frozen in liquid nitrogen and sent to the SSRL for remote data collection. The crystallization conditions used in this study are new for PPA, and were are based on Hampton Research Crystal Screen kit.

5.2.3 X-Ray Crystallographic Data Collection, Processing and Refinement

Data were collected using a MarMosaic 325 CCD detector on beam line 9-2 at the SSRL using a wavelength of 0.9794 Å and a 1° oscillation (*233*, *235*, *275*). The data were initially processed using Mosflm (*236*) and was the scaled, merged and truncated using Scala (*237*). Molecular replacement was performed using CNS (*238*); the coordinates of PPA with no ligands (*109*, PDB ID: 1PIF) formed the model from which the initial phases were derived.

After rigid body refinement in CNS, sigmaa weighted 2mFo-DFc maps clearly showed a large volume of empty density covering the active site cleft of PPA. Amystatin was built manually into this density using Coot (*239*) and the sequence obtained from Edman degradation of the peptide. Positional refinement of the atoms in CNS was used to maneuver the amino acids into better positions. Individual B-factor refinement, however, caused the thermal factors to decline until many reached the lower threshold of 2 $Å^2$ set in the CNS thermal factor refinement script. This result was unreasonable, but attempts at reprocessing the data using Mosflm and Scala failed to resolve the problem. Eventually, the data were reprocessed using XDS (*216*, *276*). Molecular replacement was performed in Phaser (*277*), again using 1PIF as a starting model. The test set from the initial dataset used in CNS was copied to the new reflection file. Rigid body refinement was performed in Phenix (*278*) and then positional refinement was alternated with manual checks of the position of atoms from the starting model. Where necessary, the positions of the atoms were adjusted in Coot. After no further improvement could be made in this way, thermal factor refinement was added to each round of positional refinement. When the R-value converged again at 24%, the previously built model of amystatin was added to the pdb file and refined. The fit of the inhibitor was then checked with Fo-Fc and sigmaa weighted 2mFo-DFc maps. Seeing that there was good agreement between the model position and density, water was added to the model and refined. The final data processing and refine-

ment statistics can be seen in Table 5.2. The PPA-amystatin binding interface was analysed using Protein interfaces, surfaces and assemblies (PISA) (*279*), which was also used to assign hydrogen bonds. Solvent accessible and buried surface areas were determined using the Protein Structure and Interaction Analyzer (PSAIA) (*280*).

5.3 Results

5.3.1 Sulfhydryl Determination

When Suzanne Perry conducted the mass spectrometric analysis of the synthetic amystatin peptide, she did so assuming that all three disulfide bonds in the peptide had formed. Her analysis showed that the same peptide fragments formed regardless of whether the full peptide had been subjected to reductive alkylation or not. The peptide masses differed only by the mass of the alkylating agent. She interpreted these results to mean that the synthetic peptide contained disulfide bonds between C6 and C16, C20 and C33, and C38 and C39 (i.e. a 1-2, 3-4, 5-6 disulfide topology); however, they can also mean that the original peptide was linear, with no disulfide bonds present.

The sulfhydryl quantitation study was meant to determine which of these possibilities was a more accurate description of the peptide. The result indicating that there were approximately three free sulfhydryl groups

Table 5.2: Data Processing and Refinement Statistics

	PPA-amystatin
Data Collection Parameters	
Space group	$P2_12_12_1$
Unit cell dimensions (Å)	
a	43.75
b	103.28
c	111.90
Resolution range (Å)	49.19-2.6
Highest Resolution Shell (Å)	2.73-2.6
No. of unique reflections	16310 (1177)
Mean $I/\sigma I$[a]	17.3 (7.5)
Multiplicity[a]	7.1 (6.8)
Merging R-factor (%)[a]	10.4 (29.1)
Structure Refinement Values	
Number of reflections	15472
Completeness (%)[a]	95.2 (94.7)
No. protein atoms	3904
No. inhibitor atoms	322
No. solvent atoms	219
Average thermal factors ($Å^2$)	
Protein atoms	16.9
Inhibitor atoms	21.3
Solvent atoms	35.5
Overall	17.2
Final R-free value (%)	22.6
Final R-factor (%)	18.1
Structure Stereochemistry	r.m.s. deviations
bonds (Å)	0.004
angles (°)	0.882

[a] The number in brackets indicates data for the highest resolution shell

per amystatin molecule (see table 5.1) contradicts this and may be due to contamination in the sample provided by AnaSpec or error in weighing small amounts of the peptide.

Since the disulfide bridging pattern of synthetic amystatin was still left unresolved after disulfide determination with DTNB, Mark Okon from Prof. Lawrence McIntosh group collected NMR data on the synthetic amystatin peptide to determine its solution structure. No definable secondary structure elements were found, and it was concluded that the disulfide bonds had not formed and that the peptide assumed random configurations in solution.

5.3.2 Description of the PPA-Amystatin Complex Structure

In the crystal structure of the amystatin PPA-complex, amystatin binds in the active site cleft, covering 5.5% of the enzyme's surface (Figure 5.4). A Procheck Ramachandran plot of the dihedral angles shows that all enzymatic residues, save S414 which is involved in a γ-turn, are well within the allowable limits (Figure 5.5a). The deviation of amystatin serine 2 ("Ser 1002 (B)" in the diagram) is due to the fact that the first residue of amystatin is poorly defined by the electron density. This serine residue, however, is still within allowable limits when main chain dihedral angles are analyzed with Molprobity (*220*, *241*) (Figure 5.5b).

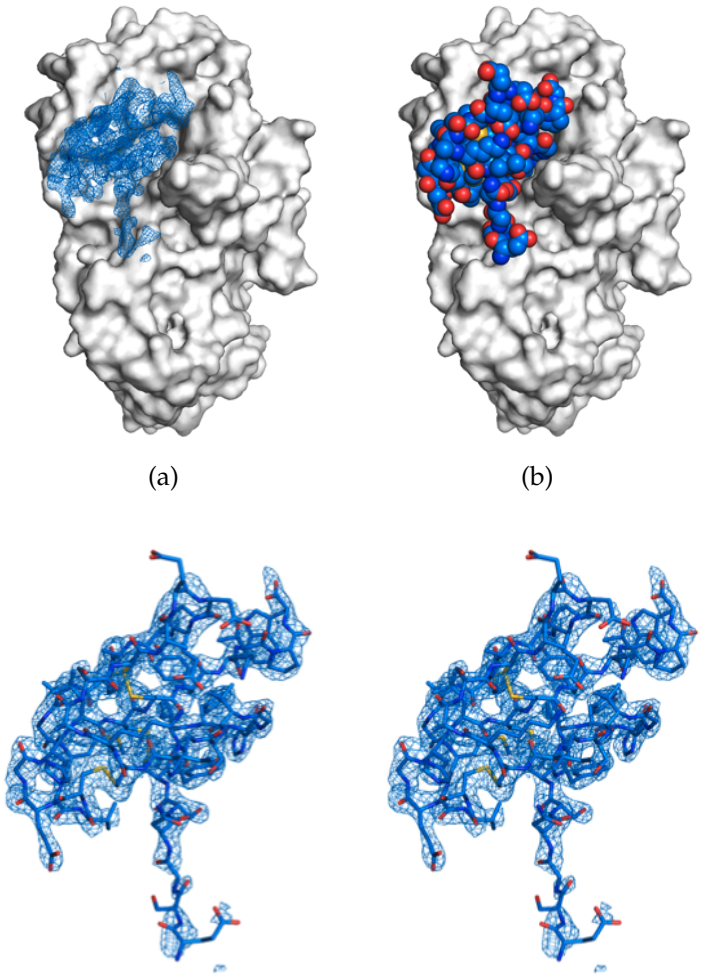

(a) (b)

(c)

Figure 5.4: Amystatin bound to the surface of PPA. The omit map of the inhibitor in (a) is shown at 2.0σ. (b) shows the inhibitor atoms as spheres. (c) is a stereo diagram that shows the same map as (a), only at 3.5σ

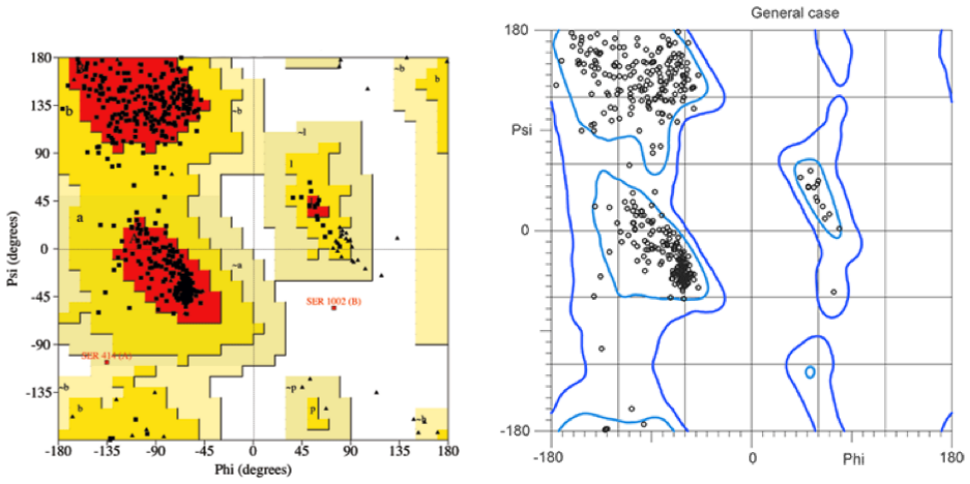

(a) (b)

Figure 5.5: Ramachandran Plots of the Final Coordinates of the PPA-Amystatin Complex Structure.)a) PROCHECK (b) Molprobity

Amystatin shares 13 hydrogen bonds with the enzyme (Table 5.3, Figure 5.6), including interactions with key residues such as the catalytic nucleophile, D197, as well as D300 and H305. The loop from residues 306-310 of PPA also forms a hydrophobic patch that is matched by a corresponding one on amystatin, formed by residues Y7 and V32. Another area of hydrophobic interactions surrounds the side chain of V163 of PPA. Amystatin surrounds this residue with the side chains of I8, V12, and Y40. L162 and L165 extend the size of this hydrophobic patch and form a β-turn that also packs against Y9, T42 and W44. The interactions with residues 162-165 help stabilize both ends of the loop that extends into the active site and interacts with the catalytic carboxylates. D197 shares 2 hydrogen bonds with the inhibitor, and D300 has one. Both hydrogen bond to

H10 of amystatin, which is very likely protonated, creating a salt bridge that further stabilizes the loop. The hydrogen bonding pattern of the PPA-amystatin complex will be discussed in more detail in section 5.3.4.1.

One glycerol molecule is also found in the interface between amystatin and PPA. This forms four hydrogen bonds, three to the enzyme, and one to amystatin. (Figure 5.7). Glycerol was added to the crystallization medium as a cryoprotectant after the crystals had formed, and thus likely displaces several ordered water molecules that would have helped stabilize inhibitor binding.

5.3.3 Amystatin Folding

The most surprising aspect of the crystal structure is that amystatin, which is linear in solution, has spontaneously folded into the conformation that best binds to PPA, and that the distances between the sulphur atoms of its cysteine residues indicate that disulfide bonds have formed. In fact, forcing the refinement to treat these side chains as sulphydryls repositions the peptide's backbone out of alignment with the electron density in both sigmaa weighted 2mFo-DFc and omit electron density difference maps.

The crystallization medium contained 0.1 M Tris, pH 8.5 and 8% PEG 8000. While it is unlikely that PEG 8000 plays any role in the redox chemistry of disulfide formation, Tris buffers above pH 8.0 have been observed to induce crosslinking either in conjunction with copper (*281*), or molecular oxygen (*282*). It can then be supposed that the peptide folds itself into

Table 5.3: Hydrogen Bonds in the Amystatin-PPA Interface

Atoms			
Amystatin	PPA	Distance (Å)	
S2/OG	G308/O	3.85	
S5/OG	H305/O	3.40	
Y9/OH	D197/OD2	2.38	
Y9/OH	Y62/O	3.70	
H10/ND1	D300/OD1	2.75	***
H10/NE2	D197/OD1	2.83	
S13/OG	H305/O	2.73	
A28/N	E149/O	3.00	
W44/NE1	V163/O	2.93	
S2/O	S310/N	3.17	
S5/OG	H305/ND1	3.24	
I8/O	Y151/OH	3.78	
A28/O	Y151/N	2.86	

*** indicates possible salt bridge

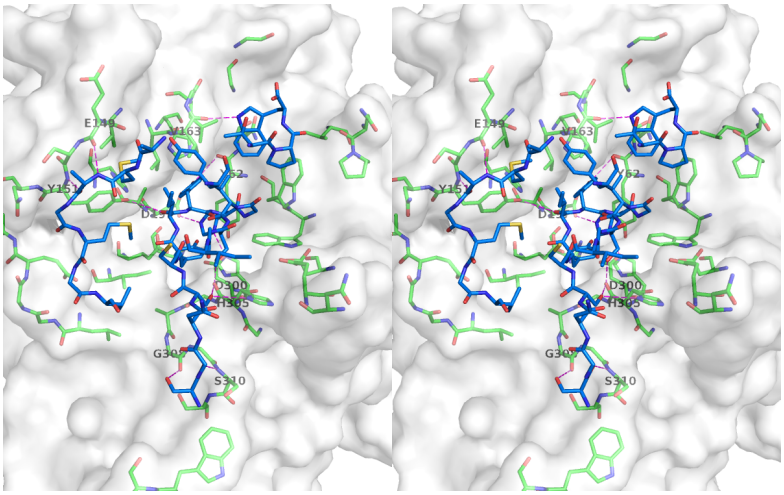

Figure 5.6: Stereo Diagram of the Hydrogen Bonds between Amystatin and PPA. Hydrogen bonds are shown as dashed lines. The labels correspond to the PPA residues in Table 5.3

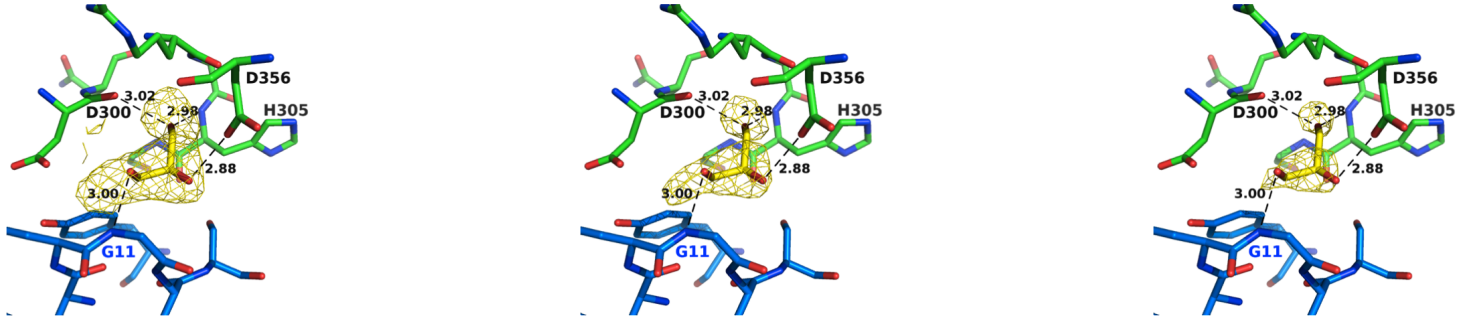

(a) (b) (c)

Figure 5.7: Hydrogen Bonds Formed between a Glycerol Molecule and the Polypeptide Chains in the PPA-Amystatin Interface. PPA is green, amystatin is blue, and glycerol is yellow. Omit maps are shown at 2σ (a), 3σ (b) and 4σ (c). Hydrogen bond distances are shown in Ångstroms

a shape that binds to PPA, and this complex then crystallizes in complex with the protein which stabilizes the peptide fold. The disulfide bonds form within this complex either using molecular oxygen as an oxidizing agent, which would gradually consume any molecular oxygen in the crystallization medium as the crystal grows, or disulfide formation is induced by the x-rays during data collection, the formation of radicals then leading to lower resolution data (as shown with the PPA-amystatin complex at 2.6 Å), or the destruction of the crystals (as observed with the possible HPA-amystatin complexes). The possible role of the buffer in synthetic amystatin disulfide formation remains to be investigated.

The structure that the peptide assumes is a small, antiparallel β-sheet stabilized by disulfide bonds between cysteines 6 and 38, 16 and 33, and 20 and 39 (Figure 5.8), giving it the characteristic 1-5, 2-4, 3-6 disulfide topology of a β-defensin. The β-defensins share little sequence similarity, with the exception of the 6 cysteines that form the disulfide bonds, two of which occur consecutively near the C-terminus of the peptide. All assume the same fold (Figures 5.9, 5.11). Most known β-defensins confer antimicrobial or immunological functions to the host organism; many are toxins (*170*). One plant defensin also has α-amylase inhibitory activity (*171*). The structure of amystatin also contains one α-helical turn from residues 31-34.

Folded amystatin has no hydrophobic core, the role of structural stabilization having been taken over by the disulfide bonds. Indeed, all of its residues are exposed to solvent when folded in solution, leaving any

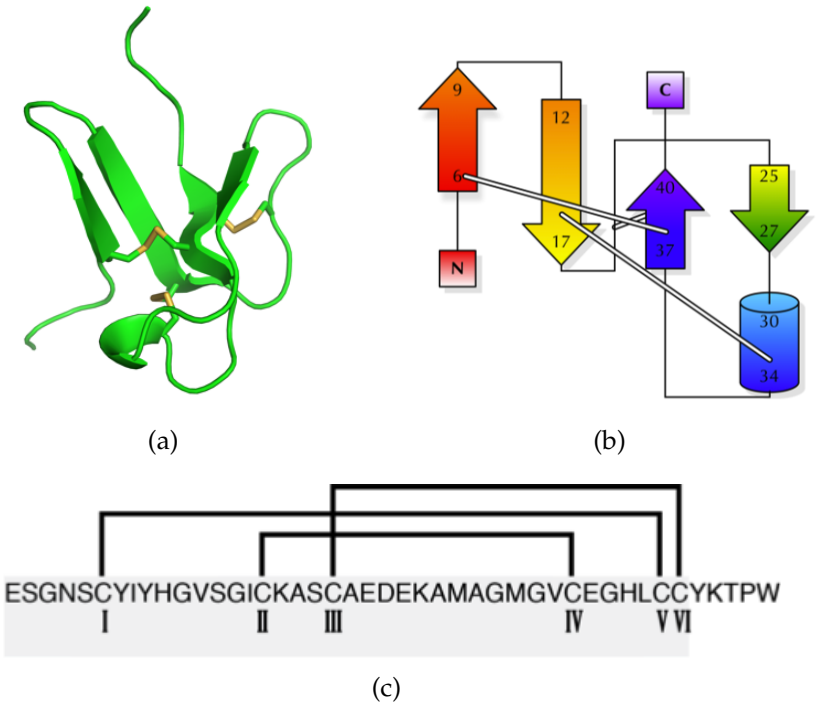

(a) (b)

(c)

Figure 5.8: The Disulfide Topology of Folded Amystatin. (a) Diagram of amystatin derived from the coordinates in the pdb file. The protein backbone is in cartoon format, and the sticks are disulfide bonds. (b) A topology diagram showing the structure of amystatin. Disulfide bonds are shown as white bars, and the rainbow coloration is used to emphasize the knotted conformation of the peptide. (c) The sequence of amystatin, showing the disulfide bonds as black lines.

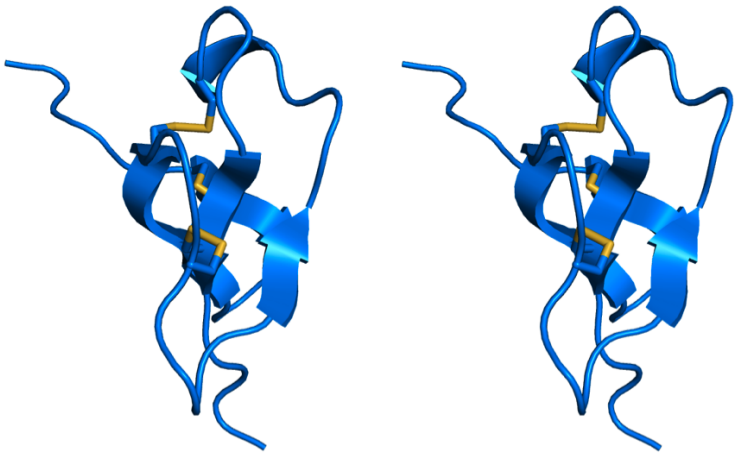

(a)

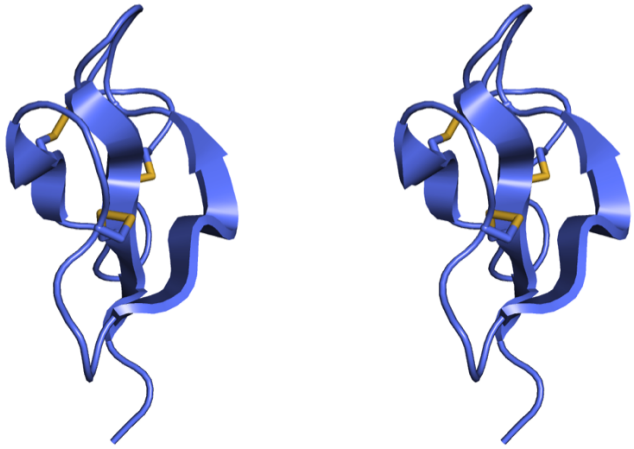

(b)

Figure 5.9: Comparison of the Folded Structure of Amystatin and a β-Defensin. Figure (a) shows a stereo representation of amystatin as bound to PPA, while (b) is the solution structure of spheniscin, a β-defensin found in penguin stomach (PDB ID, 1UT3 *283*). The disulfide bonding structure is the same in both. Amystatin contains an additional β-turn and a short segment of a fourth β-strand. These are due to weak interactions that may be stabilized by interactions with PPA and the cryogenic temperatures of data collection, and may not be present in solution. Disulfide bonds are shown as sticks.

hydrophobic side chains available to interact with other peptides and proteins. This may contribute to the strength of amystatin binding to mammalian α-amylases, where many of the hydrophobic side chains are protected from water through interactions with other aliphatic or aromatic residues on the enzyme's surface.

5.3.4 Amystatin Binding to PPA

5.3.4.1 Hydrogen Bonding

When bound to PPA, amystatin shares 13 hydrogen bonds with the enzyme. A summary of these bonds can be seen in Table 5.3. Surprisingly, these hydrogen bonds involve only 18 residues, 8 in amystatin and 10 in PPA. Of the 3 essential catalytic residues, 2 of them are hydrogen bonded to amystatin (Figure 5.10). The side chain of D197, the catalytic nucleophile, is hydrogen bonded to both Y9 and H10 of the inhibitor, while D300 also shares hydrogen bonds with H10. The carboxylate groups on the side chains of D197 and D300 also stabilize a potential positive charge on H10. This is the only possible salt bridge within the binding interface.

Also important in the binding of amystatin to the enzyme are two amino acids that each form three hydrogen bonds. In amystatin, A28 is hydrogen bonded to E149 and Y151 of PPA (Figure 5.12) One amino acid, H305, forms three hydrogen bonds with PPA; it also forms part of a mobile loop from residues 304-310 that helps stabilize the binding of the natural

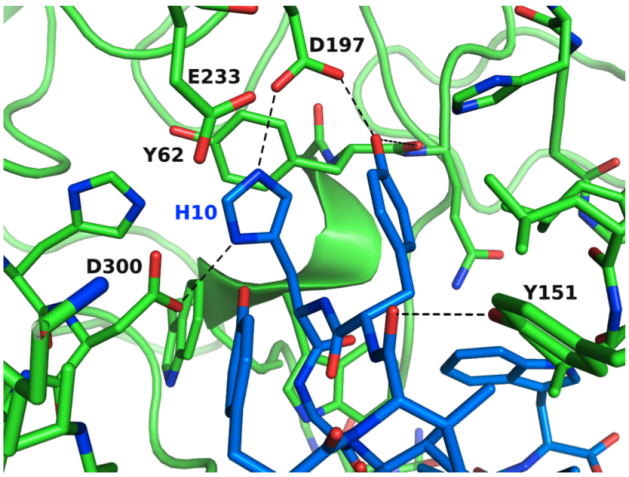

Figure 5.10: Hydrogen bonds formed in the active site between amystatin (blue) and PPA (green). The catalytic nucleophile, D197, hydrogen bonds to both H10 and Y9 of the inhibitor, and D300 also hydrogen bonds to H10, which is very likely protonated.

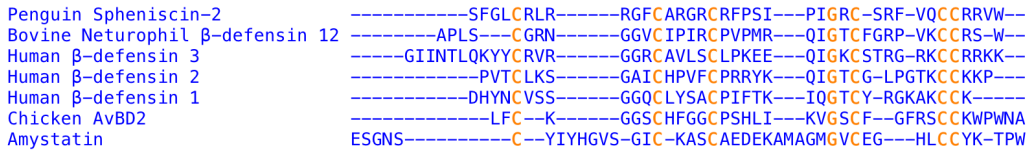

Figure 5.11: Sequence Alignment of β-Defensins Based on the Alignment of their Three-Dimensional Structures. The SuperPose server was used for the structural alignments (http://wishart.biology.ualberta.ca/SuperPose/) (*284*), and the resulting sequence alignment was adjusted manually to better account for the placement of gaps. Amino acids for which there is 100% consensus are marked in orange. The structures used in the alignment can be found in references (*169*, *283*, *285–287*)

substrate in the active site cleft (*50*, *200*) (Figure 5.13). In HPA, this loop is in fact disordered unless a substrate or inhibitor molecule is bound in the active site (*1*, *45*, *50*, *200*). H305 bonds with two amino acids in amystatin, S5 and S13. The side chain of S5 hydrogen bonds to both ND1 and O of H305, whereas S13 binds only to its main chain amide carbonyl.

Two other residues in the mobile loop also interact with amystatin, residues 308, and 310. While both of these residues differ in HPA and PPA, neither change should have a significant impact on amystatin binding. At residue 308, which is a glycine in PPA and an alanine in HPA, the inhibitor interacts with the main chain carbonyl, and a G308A mutation would not interfere. The side chain is also small enough that it would have minimal impact on the packing of residues within the enzyme itself. For the same

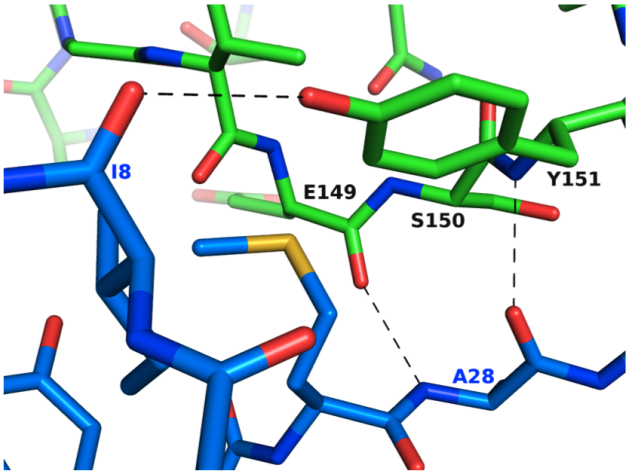

Figure 5.12: Hydrogen bonds formed between PPA (green) and A28 of amystatin (blue). The hydrogen bond from I8 to Y151 is shown in both in this diagram and in Figure 5.10 for reference.

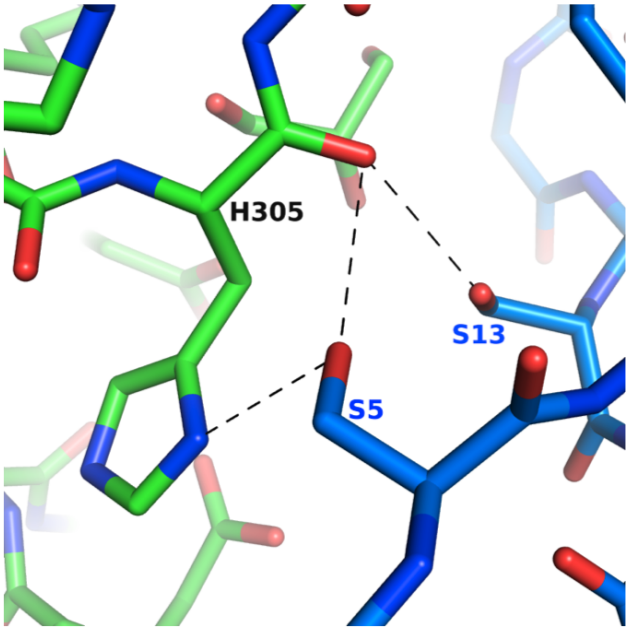

Figure 5.13: Hydrogen bonds between PPA H305 (green) and amystatin (blue). The three hydrogen bonds to this residue show that it is pivotal for amystatin binding. These residues are surrounded by hydrophobic contacts between the enzyme and inhibitor.

reasons, it is also unlikely that the shift from a serine at residue 310 in PPA to an alanine in HPA would have any meaningful effect on inhibitor binding, the hydrogen bond being between the amide nitrogen of S310 and the main chain carbonyl of S2 of the inhibitor.

5.3.4.2 Hydrophobic Interactions between Amystatin and PPA

A third of the solvent accessible surface area of amystatin (34.4%) is buried in the interface with PPA. This amounts to an area of 1110 $Å^2$; the enzyme contributes a slightly smaller solvent accessible area to the interface (956.7 $Å^2$). Hydrophobic contacts contribute significantly to this interface, with

the buried hydrophobic surface area amounting to 339 $Å^2$ for amystatin and 346 $Å^2$ for PPA.

Key hydrophobic interactions contribute to the strong binding of amystatin to PPA. PPA and other amylases, such as HPA, have hydrophobic patches that line the active site cleft. The role of these is to stabilize the position of the amylose chain that is the enzyme's natural substrate by packing against the carbon atoms of the hexose rings that make up the individual glucose monomers. Amystatin takes advantage of the hydrophobicity of the enzyme and packs against a few key residues. The most notable among these are L162 and V163 that pack against the sugars in the +1 and -2 binding subsites, respectively (*50*, *86*, *288*, *289*). In amystatin, the CB of Y9 packs against L162, and the side chain of V12 packs against V163 of PPA. In HPA, there is a V163T substitution that enables the side chain of this residue to interact with the oxygen joining the sugars in the -2 and -3 binding subsites (*50*). In turn, OG1 of this residue could very easily hydrogen bond with the same atom in T42 of the inhibitor in the HPA-amystatin complex.

5.4 Discussion

5.4.1 The Amino Acid Differences of HPA and PPA within the Amystatin Binding Interface

PPA is a close homolog of HPA, having an 86% sequence identity and 92% similar residues. The two enzymes have very nearly identical folds, and a structural alignment using the method of Ye, and Godzik (*290*)) and the Research Collaboratory for Structural Bioinformatics (RCSB) PDB Comparison Tool (*291*) showed that the alignment of HPA (*45*) and PPA (*109*) had an rmsd of 0.36 Å, a number not uncommon between two crystal structures of the same protein. HPA and PPA are thus very similar proteins, structurally (see Figure 5.3). Of the 43 enzyme residues involved in the interface of PPA and amystatin, 35 of them are identical to the residues in the same position in HPA. The only differences occur at residues 52, 106, 150, 163, 241, and 299 and 310. These differences are listed in Table 5.4. None of these residues are involved directly in the hydrogen bonding of amystatin to PPA, nor do they form part of any substantial hydrophobic patch on the binding interface.

Table 5.4: Amino acid differences between HPA and PPA in the PPA-amystatin interface

Residue	PPA	HPA
52	Y	T
106	G	A
150	S	N
163	V	T
241	A	P
299	S	N
308	G	A
310	S	A

5.4.2 Comparison of the PPA-Amystatin and Free PPA Structures

5.4.2.1 Changes to PPA upon the Binding of Amystatin

The positions of the main chain atoms of PPA do not change significantly upon the binding of amystatin (Figure 5.14a): the only peak in the Root mean square deviation (RMSD) graph corresponds to a shift in the position of a surface loop. The graph comparing the thermal factors of the two models also shows that, overall, the two structures are very similar. The first major difference occurs at residue 1, which is poorly defined in the electron density of the PPA-amystatin complex, while the difference seen at residue 350 is due to packing differences in the two crystals. The most striking change, however, is seen in the reduction of thermal factors of domain B upon amystatin binding. This may be due in part to packing differences between the crystals, since domain B in the free PPA structure

(PDB ID 1PIF *109*) has very few symmetry contacts in this region, but the crystal structure by itself cannot rule out the possibility that this change occurs in solution before the crystals are formed.

5.4.3 Comparison of the PPA-Amystatin Structure to other Enzyme-Inhibitor Complexes

5.4.3.1 Comparison to PPA-Acarbose

Acarbose, described in section 1.5.1.1, is transglycosylated by both HPA and PPA, and it is to this elongated inhibitor that the word "acarbose" refers in this discussion.

The secondary structure of PPA is not altered significantly by the binding of either amystatin or acarbose (*85*, *86*). Comparing the two enzyme-inhibitor complexes, most of the observed changes in position of the main chain atoms occur due to flipped peptide bonds in glycine residues (Figure 5.15). The only significant difference occurs in the mobile loop from residue 304 to residue 310. Here, the CA of H305 has moved by 4.5 Å between the two structures. This change is absent when free PPA and the PPA-amystatin complexes are superimposed (see Figure 5.10a).

The high glycine and alanine content of this loop allows it to shift to best bind acarbose, and help stabilize binding along the entire length of the molecule (*50*, *85*, *86*). H305 hydrogen bonds to both amystatin and acarbose, but a shift in the position of the main chain atoms places the

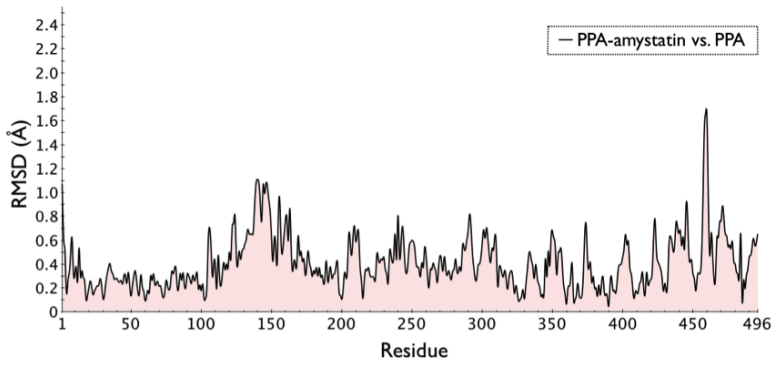

(a)

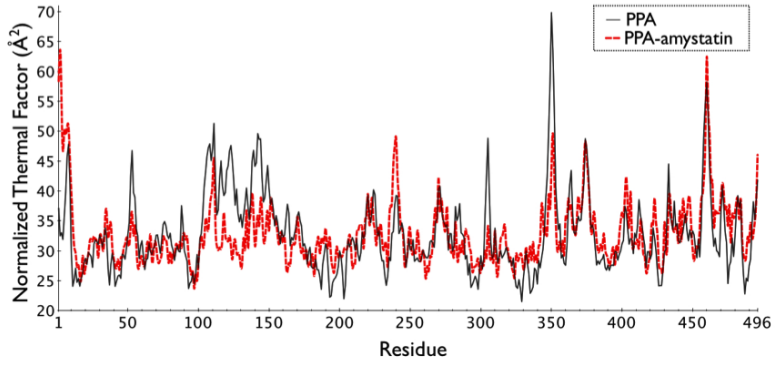

(b)

Figure 5.14: Comparison of Free PPA and the PPA-Amystatin Complex. (a) Graph showing the RMSD in Ångstroms between main chain atoms of the aligned structures. The peak near residue 460 occurs in a surface loop. (b) Graph comparing the thermal factors of PPA and the PPA-amystatin complex. PPA is represented by the black line, and the PPAamystatin structure is red. The most significant difference between the two structures is the reduced thermal motion of domain B, from residues 100-168. The thermal factors have been normalized so that the means are the same. The structure of PPA used for both graphs is PDB code 1PIF (*109*).

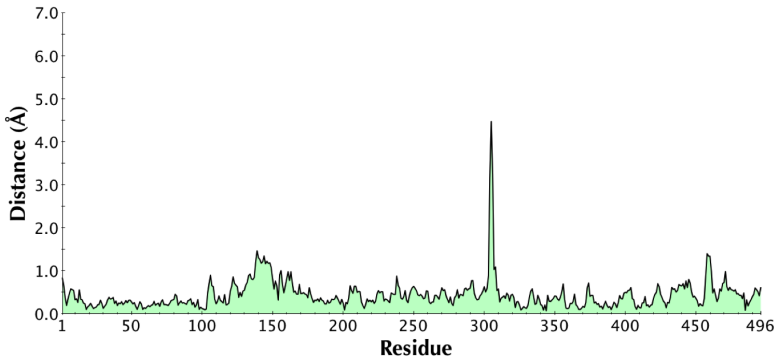

Figure 5.15: Graph of the Distance between Equivalent α-Carbons of the PPA-Acarbose and PPA-Amystatin Structures. The PPA-acarbose structure used in the alignment is PDB code 1OSE (*86*).

mobile loop from residues 304-310 in two very different orientations. (Figure 5.16). This flexibility increases the enzyme's capacity to bind each inhibitor. The PPA-amystatin complex more closely resembles the free enzyme in this region and amystatin resembles the enzyme's starch substrate neither structurally nor functionally.

Two PPA-acarbose complex structures exist in the PDB: 1PPI (*85*) and 1OSE (*86*)). 1OSE binds to PPA with 21 hydrogen bonds, compared to amystatin's 14, with 4 PPA residues hydrogen bonding to both inhibitors: V163, D197, D300, and H305. In the PPA-amystatin complex, the main chain oxygen of V163 hydrogen bonds with NE1 of the inhibitor's C-terminal tryptophan. In 1PPI, the same atom hydrogen bonds to the O4 of the glucose in the -3 subsite while in 1OSE, V163 hydrogen bonds to the nitrogen atom that joins the two rings of the valienamine spanning the -3 and -4

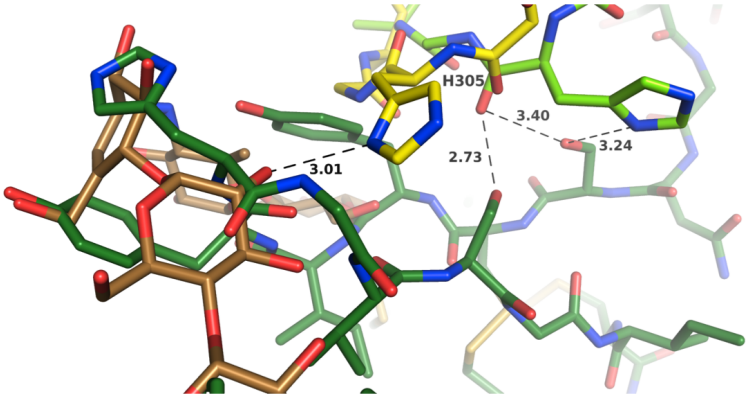

Figure 5.16: The Interactions of H305 with Amystatin and Acarbose. The PPA-acarbose structure is shown in yellow (PPA) and brown (acarbose), and the PPA-amystatin complex, in light green (PPA) and dark green (amystatin). The position of the main chain atoms of H305 is very similar in the free PPA and PPA-amystatin structures, but shifts by 4.5 Å in order to bind the carbohydrate-based acarbose. Hydrogen bonds are shown as dashed lines and distances are in Ångstroms. Of the two PPA-acarbose complex structures available in the PDB, only 1OSE (*86*) is shown.

subsites. This latter interaction more closely resembles that found in the PPA-amystatin complex.

In both of the PPA-acarbose structures, D197 hydrogen bonds to an acarviosine moiety at the O6 position, and the nucleophile sits perfectly in line to attack the anomeric carbon and cleave any labile glycosidic bond (Figure 5.17). The PPA-amystatin complex places the OH of tyrosine 9 in exactly the same location. In addition to this interaction, D197 in the amystatin complex also hydrogen bonds with histidine 10/NE2 of the inhibitor. This is very probably a salt bridge, since H10 also interacts with one of the other catalytic carboxylates, D300, which would significantly increase the

strength of the interaction, and make it more closely resemble the N-linked 'glycosidic' bond of acarbose, which would be protonated at pH 8.5. It has been suggested that this positive charge emulates the transition state of the catalytic mechanism.

D300, the third essential catalytic carboxylate, interacts with H10 of amystatin through ND1. In both PPA-acarbose structures, D300 bonds to the cyclohexenol of valienamine at the O2 position, an interaction made possible by the half-chair conformation of the transition state analogue. The PPA-amystatin complex thus retains many of the key interactions that would be present in the enzyme's Michaelis complex and in its transition state.

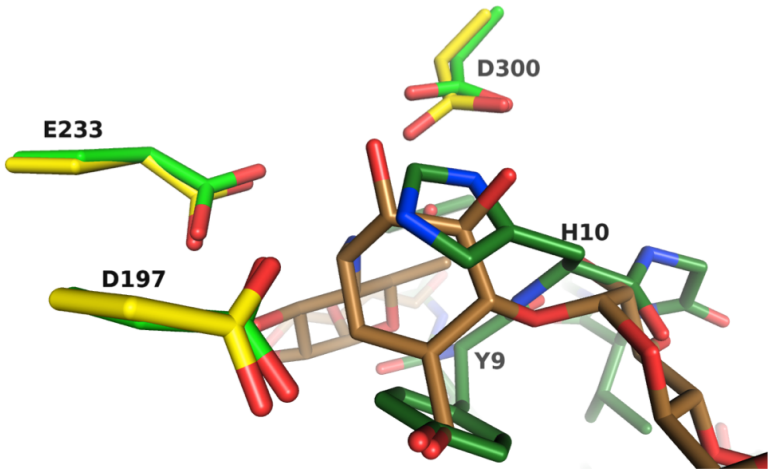

Figure 5.17: Acarbose and Amystatin in the Active Site of PPA. PPA-acarbose is yellow (PPA) and brown (acarbose) while PPA-amystatin is light green (PPA) and dark green (amystatin). The three essential catalytic residues are shown. In both structures, there is a conserved hydrogen bond between D197 OD1 and the inhibitor. Of the two PPA-acarbose structures, only 1OSE (*86*) is shown.

Amystatin also shares one of the same hydrophobic interactions with PPA as its carbohydrate-based counterpart. V12 of the inhibitor packs against V163 of PPA; this residue also interacts with the hydrophobic centre of the glucopyranose ring of modified acarbose in the -3 subsite. The comparison of the PPA-amystatin and PPA-acarbose complexes shows that several key interactions that the enzyme has with a substrate/transition state analogue are retained in the inhibition of PPA by amystatin. These interactions are important for substrate and transition state binding within the active site cleft; amystatin thus capitalizes on the way that the enzyme interacts with carbohydrates to ensure tight nanomolar binding.

5.4.3.2 Comparison to PPA-Tendamistat

Tendamistat is a 74 amino acid peptide identified in the culture filtrate of *Streptomyces tendae* (*152*). It is a powerful inhibitor of mammalian α-amylases and blocks the activity of PPA competitively with a K_i of 9×10^{-12} M when both the purity of the enzyme and the presence of denatured protein were strictly controlled (*152*). Tendamistat has been studied extensively, both in its function as an amylase inhibitor (*152*, *155*, *292*), and as a model of peptide folding (*293*).

The first x-ray crystallographic study of tendamistat in complex with a mammalian amylase was published in 1995 and was then compared to other, carbohydrate-based amylase inhibitors a year later (*109*, *155*). When tendamistat binds to PPA, the peptide blocks the entire active site cleft of

the enzyme with 26.3% of the solvent accessible surface of the peptide inhibitor in contact with the enzyme as determined by PISA (*279*, *294*); amystatin, a much smaller peptide with only 44 amino acids, in contrast, has one third of the water accessible surface in the enzyme-inhibitor interface.

The amino acid sequence of tendamistat bears almost no resemblance to that of amystatin. A BLAST2P (*295*) search comparing the two peptides could align only 7 amino acids, and the sequence similarity does not correspond to any structural resemblance. This region, running from residues 44-50 of tendamistat and 37-43 of amystatin matches LCYAVAP to LCCYKTP in each inhibitor, respectively. While all of the cysteines in these short segments are involved in disulfide bridges, their positions do not coincide when the structures of the enzyme-inhibitor complexes are superimposed. (Tendamistat assumes a 6-stranded β-sandwich topology as opposed to amystatin's 3-stranded β-sheet.) The powerful effect on α-amylase activity of the two peptides is therefore due to similarities in neither sequence nor structure.

PPA does not undergo any significant conformational change upon the binding of either amystatin or tendamistat, and the two enzyme-inhibitor complexes have an RMSD of 0.627 Å between the corresponding Cα atoms of PPA's peptide backbone when overlaid by the method of (*296*). The graph of the distance between corresponding Cα atoms of the two structures can be seen in Figure 5.18. One region of significant difference be-

tween them can be seen at the N-terminus. This occurs because PCA1, a post-translationally modified glutamine, has moved by over 6 Å from where it appears in both the PPA-tendamistat complex structure and the structure of PPA by itself. This residue is very poorly defined in electron density maps, and its movement may demonstrate a natural variability in its placement within the enzyme's structure. The next spike in the RMSD graph, at residue 111, is due to a flipped peptide bond at G110, and occurs in a surface loop. More important, however, is that the enzyme's backbone is seen to shift to accommodate a hydrogen bond between the two oxygens in the side chains of E240 (PPA) and T55 (tendamistat); an equivalent interaction does not exist between PPA and amystatin. The same holds true for the peak at N350. Here, there is a hydrogen bond between the side chains of N350 and T13 of a symmetry-related tendamistat molecule. In the PPA-amystatin complex, N350 is surrounded only by solvent. The final peak near residue 460 is due to variation in the position of a surface loop.

Although the hydrogen-bonding patterns between the enzyme and either amystatin or tendamistat are very different, they do share a few similarities. Firstly, both inhibitors share 14 hydrogen bonds with PPA and, among these, both inhibitors have hydrogen bonds to D149, D151, D300, D305, and S310. For tendamistat, 36% of the hydrogen bonds are to these residues, while for amystatin, these residues comprise 57% of the peptide's hydrogen bonds with the enzyme.

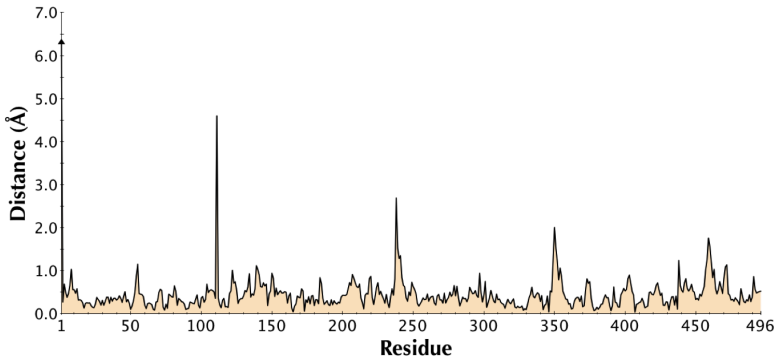

Figure 5.18: Graph showing the distance in Ångstroms between corresponding α-carbon atoms of the enzymes in the PPA-tendamistat and PPA-amystatin complexes.

Each inhibitor complex structure also has 3 hydrogen bonds to two of the three essential catalytic carboxylates. Both tendamistat and amystatin share one hydrogen bond with D300, and tendamistat has two hydrogen bonds to E233, while amystatin shares two with the side chain of D197 (see Table 5.3). Both inhibitors also share hydrogen bonds with the main chain oxygen of E149 (Figure 5.19). H305 plays an important role in the hydrogen bonding patterns of the two inhibitors: the main chain oxygen hydrogen bonds with both S17/N of tendamistat and S13/OG of amystatin. Furthermore, amystatin shares an additional two hydrogen bonds to this histidine, both involving S5 of the inhibitor (see Table 5.3 on page 180 for hydrogen bond distances). The last two residues of PPA that hydrogen bond to both amystatin and tendamistat, Y151 and S310, do so through different atoms in the two structures. S310 of PPA hydrogen bonds to

tendamistat through its side chain oxygen, an interaction that would be impossible with HPA, where this same residue is an alanine.

Both amystatin and tendamistat interact with the hydrophobic patches on the surface of PPA formed by the highly mobile loop from residues 303-311, as well as the beta turn from residues 162-165. These hydrophobic interactions help increase the stability of the hydrogen bonds to H305, and in the case of amystatin help strengthen the interaction between V163/O and W44/NE2, significantly increasing the binding strength of both inhibitors. The difference in binding strength of tendamistat and amystatin near H305 is reflected in the thermal factors of the two structures (Figure 5.20). While one must be cautious in comparing the thermal factors due to differences in crystal packing, it is still interesting to use the graph

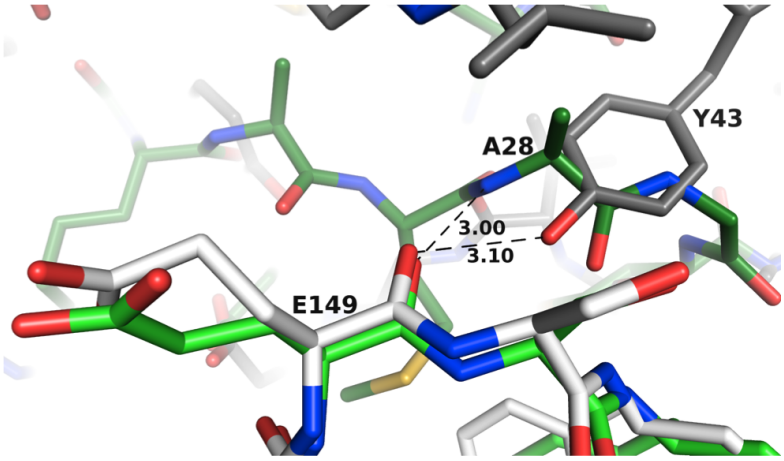

Figure 5.19: Hydrogen Bonds of E149 with Tendamistat (dark gray) and Amystatin (dark green). Hydrogen bonds are shown as dashed lines and distances are in Ångstroms. The light green and white sticks represent PPA in complex with amystatin and tendamistat, respectively.

to gain insight into regions far from contacts with any symmetry-related molecules, and where changes can be easily explained by local variation. In this instance, the thermal factors of the mobile loop from residues 303-311 are much lower in the model of the PPA-amystatin complex. This is likely due to the three hydrogen bonds to H305, two of which are to main chain atoms, and to the hydrophobic interface that surrounds them. This illustrates the remarkable ability of amystatin to capitalize on interactions with just a few key residues in PPA. By doing this, amystatin packs as many interactions as occur in the PPA-tendamistat structure into a much small enzyme-inhibitor interface (1083.6 Å for amystatin versus 1143.4 Å for tendamistat according to a PISA analysis (*279*, *294*).

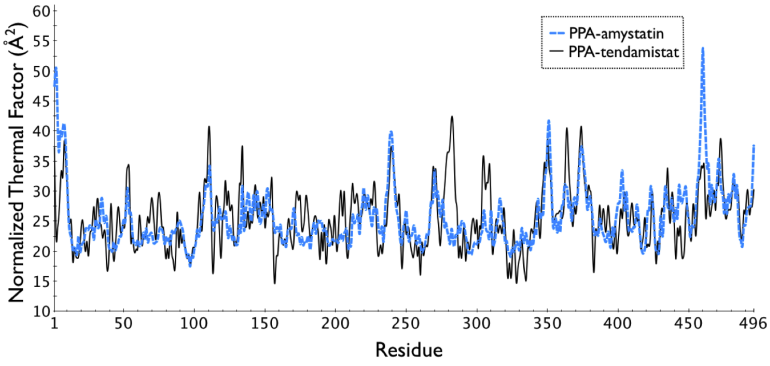

Figure 5.20: Comparison of the Thermal Factors of the PPA-Amystatin (dashed, blue) and PPA-Tendamistat (solid, black) Complexes. The numbers for each structure have been adjusted so that they have the same mean.

5.4.3.3 Comparison to *Tenebrio molitor* Amylase in Complex with Amaranth Amylase Inhibitor

Amystatin is a β-defensin, a small peptide with three disulfide bonds. One other known α-amylase inhibitor is also a small peptide with three disulfide bonds: AAI. AAI is a 32 amino acid peptide having the 1-4, 2-5, 3-6 disulfide connectivity characteristic of a knottin (*163*, *164*). It differs significantly from amystatin both in terms of sequence and structure, but may still shed some light on amystatin inhibition of mammalian amylases such as PPA and HPA. The α-amylase from the yellow meal worm, *Tenebrio molitor*, TMA is a 471 amino acid enzyme that shares only a 51% sequence identity with PPA, but has a nearly identical structural fold. A structural alignment of the two proteins (PDB IDs, 1PIF and 1JAE (*43*, *109*)) found the structures to have an RMSD of only 0.94 Å (*290*, *291*) (Figure 5.21). This degree of structural homology despite a vast sequence difference is common for α-amylases, and all of them retain the three essential catalytic carboxylates in the same orientation (*26*). The key differences between the two enzymes lie in the presence of three loops in the active site cleft that are present in PPA, but absent in TMA: residues 140-148, 304-310, and 342-361. Coincidentally, amystatin interacts with two of the three loops, which provides a means of structurally investigating inhibitor specificity, since AAI is ineffective against mammalian amylases (*163*, *164*).

The binding interfaces of the PPA-amystatin and TMA-AAI (PDB ID: 1CLV, *164*) complexes are remarkably similar, with interactions occurring

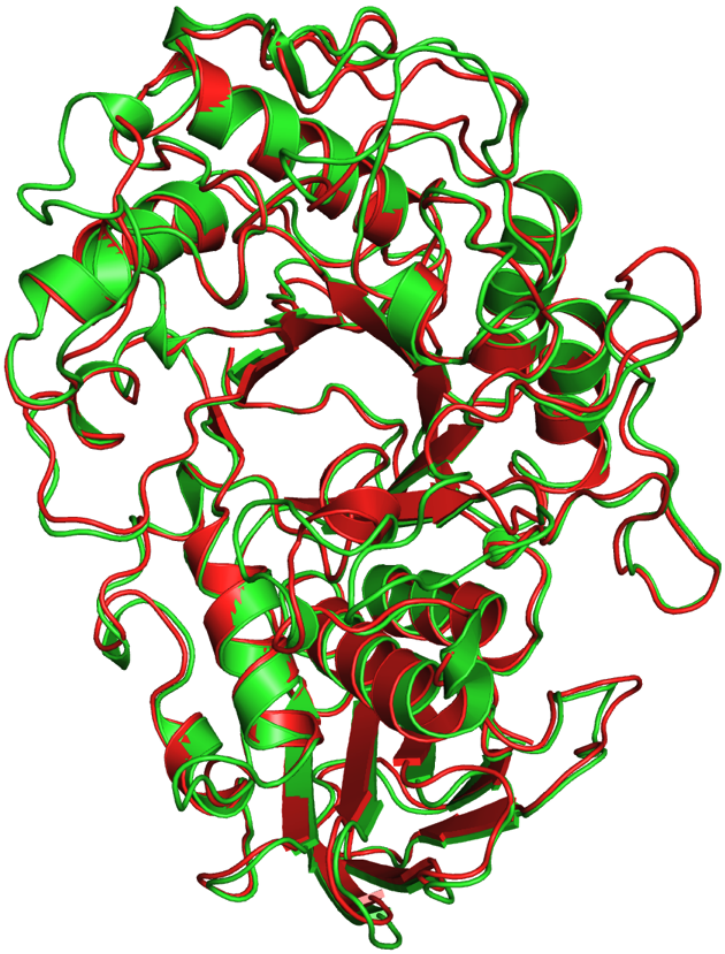

Figure 5.21: The secondary structure of PPA (green) and TMA (red), showing the structural similarity of the two proteins despite large variation in sequence. The two models overlaid in this picture are PDB ID: 1PIF (*109*) and PDB ID: 1JAE (*43*).

in corresponding regions of the active site cleft. In fact, the catalytic nucleophiles in each structure, D197 and D185 in PPA and TMA, respectively, both pack against a tyrosine residue, although only D197 is close enough to hydrogen bond; the TMA equivalent to D300 is also engaged in a salt bridge, albeit to an arginine. The similarities of the binding interactions of amystatin and AAI can be seen in Figure 5.22, which shows a sequence alignment based upon the structural alignment of the two enzymes. The highlighted residues in this figure denote the enzymes' interface with the bound peptide inhibitors, with the residues in green hydrogen bonding to amystatin or AAI. Many of the differences in the binding interfaces of the two enzyme-inhibitor complexes occur precisely in the loops that are present in PPA, yet absent in TMA.

The loop from residues 140-148 in PPA does not come into contact with amystatin, but its shorter counterpart in TMA does hydrogen bond through E135 OE1 to D13 O of AAI. This interaction is impossible in PPA, where the corresponding residue is a glycine. There are no hydrogen bonds in PPA in the region of the loop from 342 to 361, although two residues pack against amystatin. TMA however, hydrogen bonds to its inhibitor at N331 (D356 in PPA), an interaction impossible in PPA, because the loop creates a steric barrier.

The most striking differences between the two structures occur in the loop from residues 304-310. This is due to the essential role that H305 has in binding amystatin, with three hydrogen bonds forming with this one

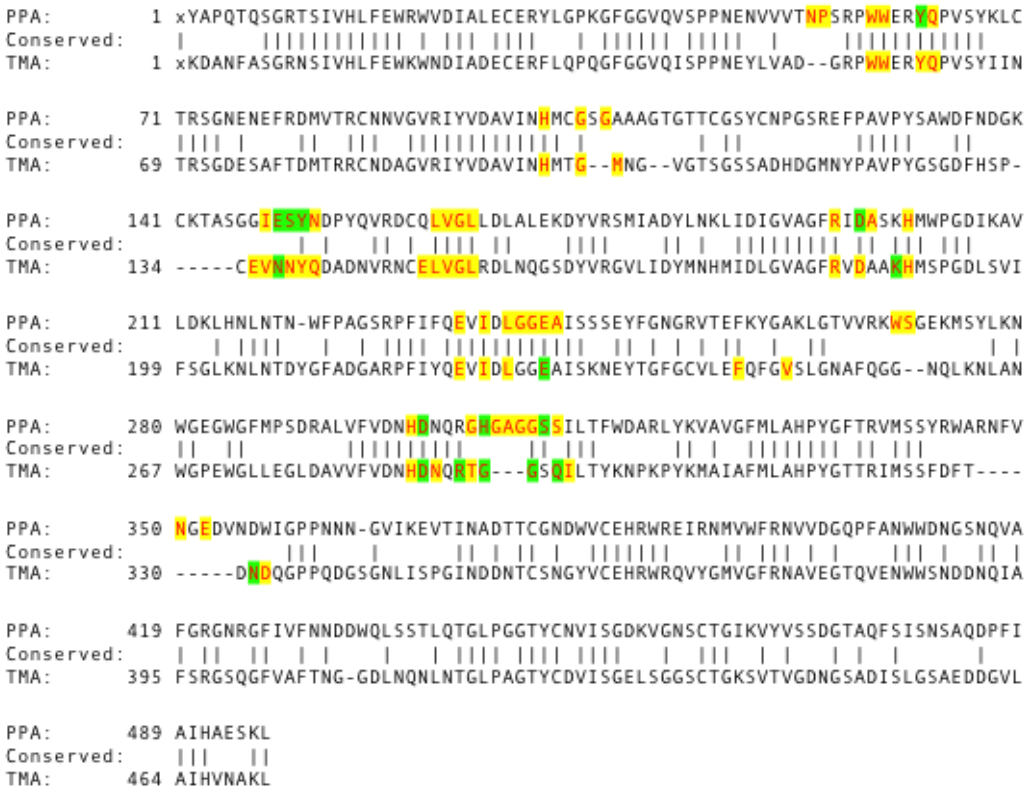

Figure 5.22: Sequence Alignment of PPA and TMA Based on their Structural Alignment. Residues in the PPA-amystatin or TMA-AAI binding interfaces are highlighted in yellow with red text. Green denotes residues of the interface that are involved in hydrogen bonds with the inhibitors.

residue. In addition, when the two structures are superimposed, W5 of AAI extends into the space occupied by residues 306-309 of PPA to pack against I296, P245 and V249 of TMA. The presence of residues 306-310 in PPA would push the small, rigid AAI out of the alignment needed to bind strongly elsewhere in the enzyme's active site cleft. Furthermore, H305 also conflicts sterically with T24 of AAI, further destabilizing any possible

PPA-AAI complex. The absence of an equivalent to H305 in TMA, and the loss of the hydrogen bonds to it indicate that amystatin may bind as poorly to TMA as AAI does to the mammalian α-amylases.

5.4.3.4 Note on Plant Defensins as Amylase Inhibitors

Plant defensins, also known as γ-thionins, are small, cationic peptides that comprise 45-54 amino acids, and contain four conserved disulfide bonds. They all share a common structure made up of a three-stranded anti-parallel β-sheet and an α-helix. Figure 5.23 compares the secondary structure of one such defensin with that of amystatin. VuD1, a defensin from cowpea, *Vigna unguiculata*, has anti-α-amylase activity, and like AAI, shows specificity for insect amylases (*171*). While no crystal structure of a VuD1-insect amylase complex exists in the PDB, *in silico* studies suggest that VuD1's lack of inhibitory activity on mammalian enzymes may be due to steric interference from the mobile loop from residues 304-310 of the mammalian amylases (*171*). This may mean that amystatin's three hydrogen bonds to H305 confer some specificity for mammalian α-amylases over those from other sources.

5.5 Conclusions

The binding of amystatin to PPA capitalizes on a few key features of the enzyme, including the beta turn from residues 162-165 that stabilizes both

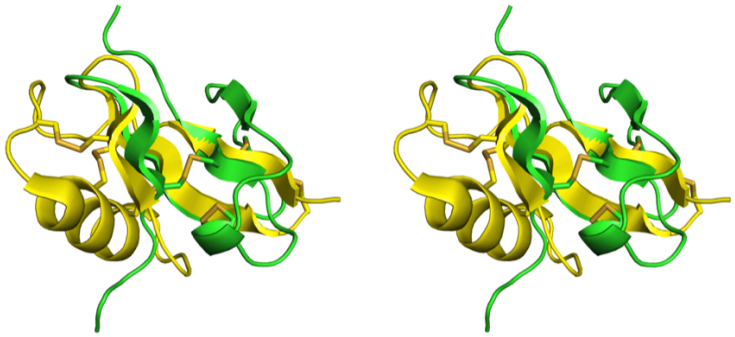

Figure 5.23: Stereo Diagram Comparing the Structure of Amystatin and a Plant Defensin. The only portion of the two structures that aligns well is the small β-sheet. Amystatin is shown in green and *Pisum sativum* defensin 1 is shown in yellow (*297*).

ends of the loop that extends into the active site by interacting with six different hydrophobic amino acids in amystatin, and H305 that makes up 3 of the total of 14 hydrogen bonds with the enzyme. This last interaction may even increase amystatin's specificity for mammalian amylases, and enable us to develop a smaller, more efficient inhibitor that retains amystatin's affinity and specificity for amylase.

Chapter 6

Summary

The work in this thesis focussed on determining the crystal structures of α-amylase-inhibitor complexes in order to bring to light new interaction with the enzyme that may lead to better treatments for type II diabetes. Chapter 3 revealed that voglibose, a derivative of valiolamine, does not act as a substrate mimic for HPA since it does not bind within the enzyme's substrate binding subsites. Myricetin binds adjacent to HPA's catalytic machinery and causes the side chain of D300, an essential catalytic residue, to shift away from the active site cleft. This is accompanied by stabilization of a highly mobile loop (residues 304-310) within the enzyme's active site. Ethyl caffeate, the only noncompetitive inhibitor studied, and the only inhibitor not to bind within the enzyme's active site, appears to disrupt enzyme structure by preventing the formation of a hydrogen bond at the base of helix α6 of the enzyme's β-barrel. This disorder extends the length of the same mobile loop that is stabilized by myricetin binding, and leads to greater thermal motion of D300, and a reduction of enzyme activity.

Chapter 4 describes the crystal structure of the complex between MbA and the HPA H299N variant. Interestingly, the inhibitor assumes a folded

conformation in solution and it is this conformation that binds within the active site of HPA. Binding is stabilized by a complex hydrogen bonding network and hydrophobic interaction with both of the inhibitor's aromatic groups. As in the HPA-myricetin structure, D300 is turned away from the active site, a feature that may be characteristic of flavonol binding.

Chapter 5 describes the binding of amystatin to PPA. A synthetic peptide was used for the crystallization trials, and this peptide lacked the disulfide bonds, and thus the secondary structure of the naturally-sourced peptide. Interaction with PPA selected the folded conformation that best bound to the enzyme, and it is this that we see in the crystal structure. The crystal structure also reveals that the peptide's three disulfide bonds have formed, likely during data collection. These reveal that the peptide has the disulfide topology characteristic of a β-defensin; amystatin therefore constitutes a brand new class of proteinaceous α-amylase inhibitor. Nevertheless, this class maintains the combination of a tyrosine residue and a salt bridge adjacent to the enzyme's catalytic carboxylates, a combination common among many of the peptide inhibitors discussed in Chapter 1.

These insights into novel α-amylase-inhibitor interactions will hopefully lead to high-affinity inhibitors that can become medications to treat type II diabetes.

References

(*1*) Williams, L. K., Li, C., Withers, S. G., and Brayer, G. D. (2012). Order and disorder: differential structural impacts of myricetin and ethyl caffeate on human amylase, an antidiabetic target. *J. Med. Chem.* 55, 10177–10186, DOI: 10.1021/jm301273u.

(*2*) Tarling, C. A., Woods, K., Zhang, R., Brastianos, H. C., Brayer, G. D., Andersen, R. J., and Withers, S. G. (2008). The Search for novel human pancreatic α-amylase inhibitors: high-throughput screening of terrestrial and marine natural product extracts. *Chembiochem* 9, 433–438, DOI: 10.1002%2Fcbic.200700470.

(*3*) Morrish, N. J., Wang, S. L., Stevens, L. K., Fuller, J. H., and Keen, H. (2001). Mortality and causes of death in the WHO Multinational Study of Vascular Disease in Diabetes. *Diabetologia* 44, S2 is supplement 2, S14–S21.

(*4*) World Health Organization Global status report on noncommunicable diseases 2010. [Online] **2011**, http://who.int.nmh/publications/ncd_report2010/en/ (accessed November 4, 2013).

(*5*) World Health Organization Global data on visual impairments 2010. [Online] **2012**, http://www.who.int/blindness/publications/globaldata/en/ (accessed November 4, 2013).

(*6*) Roglic, G., Unwin, N., Bennett, P. H., Mathers, C., Tuomilehto, J., Nag, S., Connolly, V., and King, H. (2005). The burden of mortality attributable to diabetes: realistic estimates for the year 2000. *Diabetes Care* 28, 2130–2135.

(*7*) Danaei, G., Finucane, M. M., Lu, Y., Singh, G. M., Cowan, M. J., Paciorek, C. J., Lin, J. K., Farzadfar, F., Khang, Y.-H., Stevens, G. A., Rao, M., Ali, M. K., Riley, L. M., Robinson, C. A., and Ezzati, M. (2011). National, regional, and global trends in fasting plasma glucose and diabetes prevalence since 1980: systematic analysis of health

examination surveys and epidemiological studies with 370 country-Years and 2.7 million participants. *Lancet* 378, 31–40, DOI: 10.1016/S0140-6736(11)60679-X.

(*8*) World Health Organization Diabetes Action Now: An initiative of the World Health Organization and the International Diabetes Federation.; Geneva, 2004.

(*9*) Puls, W., Keup, U., Krause, H. P., Thomas, G., and Hoffmeister, F. (1977). Glucosidase inhibition. A new approach to the treatment of diabetes, obesity, and hyperlipoproteinaemia. *Die Naturwissenschaften* 64, 536–537.

(*10*) Chiasson, J.-L., Josse, R. G., Gomis, R., Hanefeld, M., Karasik, A., and Laakso, M. (2002). Acarbose for prevention of type 2 diabetes mellitus: the STOP-NIDDM randomised trial. *Lancet* 359, 2072–2077.

(*11*) Hulst, S. G. T., Spooren, P. F. J. M., Smith, P. A., and Hulk, T. Acarbose in insulin-dependent *diabetes mellitus*: efficacy and tolerance. In *Acarbose for the Treatment of Diabetes Mellitus*; Creutzfeldt, W., Ed.; Springer: Berlin, 1988.

(*12*) Eichler, H. G., Korn, A., Gasic, S., Pirson, W., and Businger, J. (1984). The effect of a new specific alpha-amylase inhibitor on post-prandial glucose and insulin excursions in normal subjects and Type 2 (non-insulin-dependent) diabetic patients. *Diabetologia* 26, 278–281.

(*13*) Stark, J. R., and Lynn, A. (1992). Starch granules large and small. *Biochem. Soc. Trans.* 20, 7–12, DOI: 10.1042/bst0200007.

(*14*) Gessler, K., Usón, I., Takaha, T., Krauss, N., Smith, S. M., Okada, S., Sheldrick, G. M., and Sænger, W. (1999). V-amylose at atomic resolution: X-ray structure of a cycloamylose with 26 glucose residues (cyclomaltohexaicosaose). *Proc. Natl. Acad. Sci. U.S.A.* 96, 4246–4251.

(*15*) O'Sullivan, A. C., and Perez, S. (1999). The relationship between internal chain length of amylopectin and crystallinity in starch. *Biopolymers* 50, 381–390, DOI: 10.1002%2F%28SICI%291097-0282%2819991005%2950%3A4%3C381%3A%3AAID-BIP4%3E3.3.CO%3B2-N.

(*16*) Berman, H. M., Westbrook, J., Feng, Z., Gilliland, G., Bhat, T. N., Weissig, H., Shindyalov, I. N., and Bourne, P. E. (2000). The Protein Data Bank. *Nucleic Acids Res.* 28, 235–242, DOI: 10.1093%2Fnar%2F28.1.235.

(*17*) Sarkar, A., and Pérez, S. PolySac3Db: a database of polysaccharide 3D structures., http://polysac3db.cermav.cnrs.fr/home.html, (accessed December 2, 2013).

(*18*) Gray, G. M. (1971). Intestinal digestion and maldigestion of dietary carbohydrates. *Annu. Rev. Med.* 22, 391–404.

(*19*) Ao, Z., Quezada-Calvillo, R., Sim, L., Nichols, B. L., Rose, D. R., Sterchi, E. E., and Hamaker, B. R. (2007). Evidence of native starch degradation with human small intestinal maltase-glucoamylase (recombinant). *FEBS Lett.* 581, 2381–2388, DOI: 10.1016/j.febslet.2007.04.035.

(*20*) Cantarel, B. L., Coutinho, P. M., Rancurel, C., Bernard, T., Lombard, V., and Henrissat, B. (2009). The Carbohydrate-Active EnZymes database (CAZy): an expert resource for glycogenomics. *Nucleic Acids Res.* 37, D233–D238, DOI: 10.1093/nar/gkn663.

(*21*) Levasseur, A., Drula, E., Lombard, V., Coutinho, P. M., and Henrissat, B. Expansion of the enzymatic repertoire of the CAZy database to integrate auxiliary redox enzymes. *Biotechnol. Biofuels* [Online] **2013**, *6*, DOI: 10.1186/1754-6834-6-41, (accessed January 2, 2014).

(*22*) Henrissat, B., and Bairoch, A. (1996). Updating the sequence-based classification of glycosyl-hydrolases. *Biochem. J.* 316, 295–696.

(*23*) Webb, E. C., *Enzyme Nomenclature 1992. Recommendations of the Nomenclature Committee of the International Union of Biochemistry and Molecular Biology on the Nomenclature and Classification of Enzymes*; Academic Press: San Diego, 1992.

(*24*) Janeček, Š., Svensson, B., and MacGregor, E. A. α-Amylase: an enzyme specificity found in various families of glycoside hydrolases. *Cell. Mol. Life Sci.* [Online] **2013**, DOI: 10.1007/s00018-013-1388-z, (accessed December 2, 2013).

(*25*) Davies, G., and Henrissat, B. (1995). Structures and mechanisms of glycosyl hydrolases. *Structure* 3, 853–859.

(*26*) Henrissat, B. (1991). A classification of glycosyl hydrolases based on amino acid sequence similarities. *Biochem. J.* 280, 309–316.

(*27*) Henrissat, B., and Bairoch, A. (1993). New families in the classification of glycosyl hydrolases based on amino acid sequence similarities. *Biochem. J.* 293, 781–788.

(*28*) Henrissat, B., and Davies, G. (1997). Structural and sequence-based classification of glycoside hydrolases. *Curr. Opin. Struct. Biol.* 7, 637–644.

(*29*) Park, K.-M., Jun, S.-Y., Choi, K.-H., Park, K.-H., C-S, P., and Cha, J. (2010). Characterization of an exo-acting intracellular α-amylase from the hyperthermophilic bacterium *Thermatoga neapolitana*. *Appl. Microbiol. Biotechnol.* 86, 555–566, DOI: 10.1007%2Fs00253-009-2284-1.

(*30*) Janeček, Š. (2002). How many conserved sequence regions are there in the α-amylase family. *Biologia (Bratsl)* 57/Suppl. 11, 29–41.

(*31*) MacGregor, E. A., Janeček, Š., and Svensson, B. (2001). Relationship of sequence and structure to specificity in the α-amylase family of enzymes. *Biochim. Biophys. Acta* 1546, 1–20, DOI: 10.1016/S0167-4838(00)00302-2.

(*32*) Stam, M. R., Danchin, E. G. J., Rancurel, C., Coutinho, P. M., and Henrissat, B. (2006). Dividing the large glycoside hydrolase family 13 into subfamilies: towards improved functional annotations of α-amylase-related proteins. *Protein Eng. Des. Sel.* 19, 555–562, DOI: 10.1093/protein/gzl044.

(*33*) Janeček, Š. (1994). Sequence similarities and evolutionary relationships of microbial, plant and animal α-amylases. *Eur. J. Biochem.* 224, 519–524.

(*34*) Kuriki, T., and Imanaka, T. (1999). The concept of the α-amylase family: structural similarity and common catalytic mechanism. *J. Biosci. Bioeng.* 87, 557–565, DOI: 10.1016/S1389-1723(99)80114-5.

(*35*) van der Maarel, M. J. E. C., van der Veen, B., Uitdehaag, J. C. M., Leemhuis, H., and Dijkhuizen, L. (2002). Properties and applications of starch-converting enzymes of the α-amylase family. *J. Biotechnol.* 94, 137–155, DOI: 10.1016/S0168-1656(01)00407-2.

(*36*) Svensson, B. (1994). Protein engineering in the α-amylase family: catalytic mechanism, substrate specificity, and stability. *Plant Mol. Biol.* 25, 141–157, DOI: 10.1007%2FBF00023233.

(*37*) Matsuura, Y., Kusunoki, M., Harada, W., and Kakudo, M. (1984). Structure and possible catalytic resiudes of Taka-amylase A. *J. Biochem.* 95, 697–702.

(*38*) Christiansen, C., Abou Hachem, M., Janeček, S., Viksø-Nielsen, A., Blennow, A., and Svensson, B. (2009). The carbohydrate-binding module family 20 – diversity, structure, and function. *FEBS J.* 276, 5006–5029, DOI: 10.1111/j.1742-4658.2009.07221.x.

(*39*) Machovic, M., and Janeček, Š. (2006). The evolution of putative starch-binding domains. *FEBS Lett.* 580, 6349–6356, DOI: 10.1016/j.febslet.2006.10.041.

(*40*) Dauter, Z., Dauter, M., Brzozowski, A. M., Christensen, S., Borchert, T. V., Beier, L., Wilson, K. S., and Davies, G. J. (1999). X-ray Structure of novamyl, the five-domain "maltogenic" α-amylase from *Bacillus stearothermophilus*: maltose and acarbose complexes at 1.7 Å resolution. *Biochemistry* 38, 8385–8392.

(*41*) Machius, M., Declerck, N., Huber, R., and Wiegand, G. (1998). Activation of *Bacillus licheniformis* α-amylase through a disorder→order transition of the substrate-binding site mediated by a calcium-sodium-calcium metal triad. *Structure* 6, 281–292, DOI: 10.1016/S0969-2126(98)00032-X.

(*42*) Linden, A., Mayans, O., Meyer-Klaucke, W., Antranikian, G., and Wilmanns, M. (2003). Differential regulation of a hyperthermophilic alpha-amylase with a novel (Ca,Zn) two-metal center by zinc. *J. Biol. Chem.* 278, 9875–9884, DOI: 10.1074/jbc.M211339200.

(*43*) Strobl, S., Maskos, K., Betz, M., Wiegand, G., Huber, R., Gomis-Rüth, F. X., and Glockshuber, R. (1998). Crystal structure of yellow meal worm α-amylase at 1.64 Å resolution. *J. Mol. Biol.* 278, 617–628, DOI: 10.1006%2Fjmbi.1998.1667.

(*44*) Kamitori, S., Abe, A., Ohtaki, A., Kaji, A., Tonozuka, T., and Sakano, Y. (2002). Crystal structures and structural comparison of *Thermoactinomyces vulgaris* R-47 α-amylase 1 (TVAI) at 1.6Å resolution and

α-Amylase 2 (TVAII) at 2.3Å resolution. *J. Mol. Biol.* 318, 443–453, DOI: 10.1016/S0022-2836(02)00111-0.

(*45*) Brayer, G., Luo, Y., and Withers, S. G. (1995). The structure of human pancreatic α-amylase at 1.8 Å resolution and comparisons with related enzymes. *Protein Sci.* 4, 1730–1742.

(*46*) Kagawa, M., Fujimoto, Z., Momma, M., Takase, K., and Mizuno, H. (2003). Crystal structure of *Bacillus subtilis* α-amylase in complex with acarbose. *J. Bacteriol.* 185, 6981–6984, DOI: 10.1128/JB.185.23.6981-6984.2003.

(*47*) Sivakumar, N., Li, N., Tang, J. W., Patel, B. K. C., and Swaminathan, K. (2006). Crystal structure of AmyA lacks acidic surface and provide insights into protein stability at poly-extreme condition. *FEBS Lett.* 580, 2646–2652, DOI: 10.1016%2Fj.febslet.2006.04.017.

(*48*) Rydberg, E. H. Mechanistic Studies on Human Pancreatic α-Amylase., Ph.D. Thesis, The University of British Columbia, 2000.

(*49*) Uitdehaag, J. C., Mosi, R., Kalk, K. H., van der Veen, B. A., Dijkhuizen, L., Withers, S. G., and Dijkstra, B. W. (1999). X-ray structures along the reaction pathway of cyclodextrin glycosyltransferase elucidate catalysis in the alpha-amylase family. *Nat. Struct. Biol.* 6, 432–436, DOI: 10.1038/8235.

(*50*) Brayer, G. D., Sidhu, G., Maurus, R., Rydberg, E. H., Braun, C., Wang, Y., Nguyen, N. T., Overall, C. M., and Withers, S. G. (2000). Subsite mapping of the human pancreatic α-amylase active site through structural, kinetic, and mutagenesis techniques. *Biochemistry* 39, 4778–4791.

(*51*) Rydberg, E. H., Sidhu, G., Vo, H. C., Hewitt, J., Côté, H. C., Wang, Y., Numao, S., Macgillivray, R. T. A., Overall, C. M., Brayer, G. D., and Withers, S. G. (1999). Cloning, mutagenesis, and structural analysis of human pancreatic α-amylase expressed in *Pichia pastoris*. *Protein Sci.* 8, 635–643, DOI: 10.1110/ps.8.3.635.

(*52*) Numao, S., Maurus, R., Sidhu, G., Wang, Y., Overall, C. M., Brayer, G. D., and Withers, S. G. (2002). Probing the role of the chloride ion in the mechanism of human pancreatic α-amylase. *Biochemistry* 41, 215–225, DOI: 10.1021%2Fbi0115636.

(*53*) Buisson, G., Duée, E., Haser, R., and Payan, F. (1987). Three dimensional structure of porcine pancreatic α-amylase at 2.9 Å resolution. Role of calcium in structure and activity. *EMBO J.* 6, 3909–3916.

(*54*) Morris, C., Fichtel, S. L., and Taylor, A. J. (2011). Impact of calcium on salivary α-amylase activity, starch paste apparent viscosity, and thickness perception. *Chem. Percept.* 4, 116–122, DOI: 10.1007/s12078-011-9091-7.

(*55*) Tibbot, B. K., Wong, D. W., and Robertson, G. H. (2002). Studies on the C-terminal region of barley α-amylase 1 with emphasis on raw starch-binding. *Biologia* 57(Suppl. 11), 229–238.

(*56*) Tibbot, B. K., Wong, D. W. S., and Robertson, G. H. (2000). A functional raw starch-binding domain of barley α-amylase expressed in *Escherichia coli*. *J. Protein Chem.* 19, 664–669, DOI: 10.1023/A:1007148202270.

(*57*) Holm, L., Koivula, A. K., Lehtovaara, P. M., Hemminki, A., and Knowles, J. K. (1990). Random mutagenesis used to probe the structure and function of *Bacillus stearothermophilus* alpha-amylase. *Protein Eng.* 3, 181–191.

(*58*) Vihinen, M., Peltonen, T., Iitiä, A., Suominen, I., and Mäntsälä, P. (1994). C-terminal truncations of a thermostable *Bacillus stearothermophilus* α-amylase. *Protein Eng.* 7, 1255–1259, DOI: 10.1093/protein/7.10.1255.

(*59*) Koshland Jr, D. (1953). Stereochemistry and the mechanism of enzymatic reactions. *Biol. Rev.* 28, 416–436.

(*60*) Rydberg, E. H., Li, C., Maurus, R., Overall, C. M., Brayer, G. D., and Withers, S. G. (2002). Mechanistic analyses of catalysis in human pancreatic α-amylase: detailed kinetic and structural studies of mutants of three conserved carboxylic acids. *Biochemistry* 41, 4492–4502, DOI: 10.1021/bi011821z.

(*61*) Legler, G. (1993). Mechanism of enzymic glycoside hydrolysis and of glycosyl transfer by glycosidases and glycosyltransferases. *Carbohydr. Res.* 250, vii–xx, DOI: 10.1016/0008-6215(93)84148-Y.

(*62*) Rye, C. S., and Withers, S. G. (2000). Glycosidase mechanisms. *Curr. Opin. Chem. Biol.* 4, 573–580.

(*63*) Vasella, A., Davies, G. J., and Böhm, M. (2002). Glycosidase mechanisms. *Curr. Opin. Chem. Biol.* 6, 619–629, DOI: 10.1016/S1367-5931(02)00380-0.

(*64*) Zechel, D. L., and Withers, S. G. (2000). Glycosidase mechanisms: anatomy of a finely tuned catalyst. *Acc. Chem. Res.* 33, 11–18.

(*65*) McCarter, J. D., and Withers, S. G. (1994). Mechanisms of enzymatic glycoside hydrolysis. *Curr. Opin. Struct. Biol.* 4, 885–892, DOI: 10.1016/0959-440X(94)90271-2.

(*66*) Tao, B. Y., Reilly, P. J., and Robyt, J. F. (1989). Detection of a covalent intermediate in the mechanism of action of porcine pancreatic α-amylase by using ^{13}C nuclear magnetic resonance. *Biochim. Biophys. Acta* 995, 214–220, DOI: 10.1016%2F0167-4838%2889%2990038-1.

(*67*) MacLeod, A. M., Tull, D., Rupitz, K., Warren, R. A., and Withers, S. G. (1996). Mechanistic consequences of mutation of active site carboxylates in a retaining beta-1,4-glycanase from Cellulomonas fimi. *Biochemistry* 35, 13165–13172, DOI: 10.1021/bi00186a042.

(*68*) Wang, Q., Graham, R., Trimbur, D., Warren, R., and Withers, S. (1994). Changing enzymic reaction mechanisms by mutagenesis: conversion of a retaining glucosidase to an inverting enzyme. *J. Am. Chem. Soc.* 116, 11594–11595, DOI: 10.1021/ja00104a060.

(*69*) Zechel, D. L., Reid, S. P., Stoll, D., Nashiru, O., Warren, R. A. J., and Withers, S. G. (2003). Mechanism, mutagenesis, and chemical rescue of a β-mannosidase from *Cellulomonas fimi*. *Biochemistry* 42, 7195–7204, DOI: 10.1021/bi034329j.

(*70*) Zhang, R., Li, C., Williams, L. K., Rempel, B. P., Brayer, G. D., and Withers, S. G. (2009). Directed "*in situ*" inhibitor elongation as a strategy To structurally characterize the covalent glycosyl-enzyme intermediate of human pancreatic α-amylase. *Biochemistry* 48, 10752–10764, DOI: 10.1021/bi901400p.

(*71*) Numao, S., Damager, I., Li, C., Wrodnigg, T. M., Begum, A., Overall, C. M., Brayer, G. D., and Withers, S. G. (2004). *In situ* extension as an approach for identifying novel α-amylase inhibitors. *J. Biol. Chem.* 279, 48282–48291, DOI: 10.1074%2Fjbc.M406804200.

(*72*) MacLeod, A. M., Lindhorst, T., Withers, S. G., and Warren, R. A. (1994). The acid/base catalyst in the exoglucanase/xylanase from *Cellulomonas fimi* is glutamic acid 127: evidence from detailed kinetic studies of mutants. *Biochemistry* 33, 6371–6376.

(*73*) Mosi, R., Sham, H., Uitdehaag, J. C. M., Ruiterkamp, R., Dijkstra, B. W., and Withers, S. G. (1998). Reassessment of acarbose as a transition state analogue inhibitor of cyclodextrin glycosyltransferase. *Biochemistry* 37, 17192–17198, DOI: 10.1021/bi981109a.

(*74*) Schmidt, D. D., Frommer, W., Junge, B., Müller, L., Wingender, W., Truscheit, E., and Schäfer, D. (1977). α-Glucosidase inhibitors. New complex oligosaccharides of microbial origin. *Die Naturwissenschaften* 64, 535–536, DOI: 10.1007%2FBF00483561.

(*75*) Strokopytov, B., Penninga, D., Rozeboom, H. J., Kalk, K. H., Dijkhuizen, L., and Dijkstra, B. W. (1995). X-ray structure of cyclodextrin glycosyltransferase complexed with acarbose. Implications for the catalytic mechanism of glycosidases. *Biochemistry* 34, 2234–2240, DOI: 10.1021%2Fbi00007a018.

(*76*) Krause, H. P., and Ahr, H. J. Pharmakokinetics and metabolism of glucosidase inhibitors. In *Oral Antidiabetics*; Kuhlmann, J., and Puls, W., Eds.; Handbook of Experimental Pharmacology, Vol. 119; Springer: Berlin, 1996; pp 541–545.

(*77*) Brendel, E., and Wingender, W. Clinical pharmacology of glucosidase inhibitors. In *Oral Antidiabetics*; Kuhlmann, J., and Puls, W., Eds.; Handbook of Experimental Pharmacology, Vol. 119; Springer: 1996; pp 611–632.

(*78*) Asano, N. (2003). Glycosidase inhibitors: update and perspectives on practical use. *Glycobiology* 13, 93R–104R, DOI: 10.1093/glycob/cwg090.

(*79*) Svensson, B., Fukuda, K., Nielsen, P. K., and Bønsager, B. C. (2004). Proteinaceous α-amylase inhibitors. *Biochim. Biophys. Acta* 1696, 145–156, DOI: 10.1016%2Fj.bbapap.2003.07.004.

(*80*) Asano, N. (2009). Sugar-mimicking glycosidase inhibitors: bioactivity and application. *Cell. Mol. Life Sci.* 66, 1479–1492, DOI: 10.1007/s00018-008-8522-3.

(*81*) Asano, N. (2003). Naturally occurring iminosugars and related compounds: structure, distribution, and biological activity. *Curr. Top. Med. Chem.* 3, 471–484.

(*82*) Asano, N., Nash, R. J., Molyneux, R. J., and Fleet, G. W. J. (2000). Sugar-mimic glycosidase inhibitors: natural occurrence, biological activity and prospects for therapeutic application. *Tetrahedron–Asymmetr* 11, 1645–1680.

(*83*) Butters, T. D., Dwek, R. A., and Platt, F. M. (2005). Imino sugar inhibitors for treating the lysosomal glycosphingolipidoses. *Glycobiology* 15, 43R–52R, DOI: 10.1093/glycob/cwi076.

(*84*) Lebovitz, H. E. (1997). α-Glucosidase inhibitors. *Endocrinol. Metab. Clin. North Am.* 26, 539–551, DOI: 10.1016/S0889-8529(05)70266-8.

(*85*) Qian, M., Haser, R., Buisson, G., Duée, E., and Payan, F. (1994). The Active center of a mammalian α-amylase: structure of the complex of a pancreatic α-amylase with a carbohydrate inhibitor refined to 2.2-Å resolution. *Biochemistry* 33, 6284–6294, DOI: 10.1021/bi00186a031.

(*86*) Gilles, C., Astier, J.-P., Marchis-Mouren, G., Cambillau, C., and Payan, F. (1996). Crystal structure of pig pancreatic α-amylase isoenzyme II, in complex with the carbohydrate inhibitor acarbose. *Eur. J. Biochem.* 238, 561–569.

(*87*) Brzozowski, A. M., and Davies, G. J. (1997). Structure of the *Aspergillus oryzae* α-amylase complexed with the inhibitor acarbose at 2.0 Å resolution. *Biochemistry* 36, 10837–10845.

(*88*) Brzozowski, A. M., Lawson, D. M., Turkenburg, J. P., Bisgaard-Frantzen, H., Svendsen, A., Borchert, T. V., Dauter, Z., Wilson, K. S., and Davies, G. J. (2000). Structural analysis of a chimeric bacterial α-amylase: high-resolution analysis of native and ligand complexes. *Biochemistry* 39, 9099–9107.

(*89*) Davies, G. J., Brzozowski, A. M., Dauter, Z., Rasmussen, M. D., Borchert, T. V., and Wilson, K. S. (2005). Structure of a *Bacillus halmapalus* family 13 α-amylase, BHA, in complex with an acarbose-derived nonasaccharide at 2.1 Å resolution. *Acta Cryst. D*61, 190–193, DOI: 10.1107/S0907444904027118.

(*90*) Davies, G. J., Wilson, K. S., and Henrissat, B. (1997). Nomenclature for sugar-binding subsites in glycosyl hydrolases. *Biochem. J.* 321, 557–559.

(*91*) Horii, S., Fukase, H., Matsuo, T., Kameda, Y., Asano, N., and Matsui, K. (1986). Synthesis and α-D-glucosidase inhibitory activity of N-substituted valiolamine derivatives as potential oral antidiabetic agents. *J. Med. Chem.* 29, 1038–1046.

(*92*) Matsuo, T., Odaka, H., and Ikeda, H. (1992). Effect of an intestinal disaccharidase inhibitor (AO-128) on obesity and diabetes. *Am. J. Clin. Nutr.* 55, 314S–317S.

(*93*) Horne, G., Wilson, F. X., Tinsley, J., Williams, D. H., and Storer, R. (2011). Iminosugars past, present and future: medicines for tomorrow. *Drug Discovery Today* 16, 107–118, DOI: 10.1016/j.drudis.2010.08.017.

(*94*) *Iminosugars: From Synthesis to Therapeutic Applications*; Compain, P., and Martin, O. R., Eds.; John Wiley and Sons: New York, 2007.

(*95*) Lembcke, B., Fölsch, U. R., and Creutzfeldt, W. (1985). Effect of 1-desoxynojirimycin derviatives on small intestinal disaccharidase activities and on active transport in vitro. *Digestion* 31, 120–127, DOI: 10.1159/000199188.

(*96*) Scott, L. J., and Spencer, C. M. (2000). Miglitol: a review of its therapeutic potential in type 2 diabetes mellitus. *Drugs* 59, 521–549, DOI: 10.2165%2F00003495-200059030-00012.

(*97*) Siriwardena, A. H., Chiaroni, A. l., Riche, C., El-Daher, S., Winchester, B., and Grierson, D. S. (1992). (1R,2S,4S,7aR)-1,2-Dihydroxy-7-thia-3a-thioniaperhydropentalene chloride: a new, biologically active pyrrolizidine alkaloid analogue. *Chem. Commun.* 20, 1531–1533, DOI: 10.1039/C39920001531.

(*98*) Yoshikawa, M., Murakami, T., Shimada, H., Matsuda, H., Yamahara, J., Tanabe, G., and Muraoka, O. (1997). Salacinol, potent antidiabetic principle with unique thiosugar sulfonium sulfate structure from the Ayurvedic traditional medicine *Salacia reticulata* in Sri Lanka and India. *Tetrahedron Lett.* 38, 8367–8370, DOI: 10.1016/S0040-4039(97)10270-2.

(*99*) Mohan, S., and Pinto, B. M. (2007). Zwitterionic glycosidase inhibitors: salacinol and related analogues. *Carbohydr. Res.* 342, 1551–1580, DOI: 10.1016/j.carres.2007.05.014.

(*100*) Williamson, G. (2013). Possible effects of dietary polyphenols on sugar absorption and digestion. *Mol. Nutr. Food Res.* 57, 48–57, DOI: 10.1002/mnfr.201200511.

(*101*) Jung, M., Park, M., Lee, H. C., Kang, Y.-H., Kang, E. S., and Kim, S. K. (2006). Antidiabetic agents from medicinal plants. *Curr. Med. Chem.* 13, 1203–1218.

(*102*) Etxeberria, U., de la Garza, A. L., Campión, J., Martínez, J. A., and Milagro, F. I. (2012). Antidiabetic effects of natural plant extracts via inhibition of carbohydrate hydrolysis enzymes with emphasis on pancreatic alpha amylase. *Expert Opin. Ther. Targets* 16, 269–297, DOI: 10.1517/14728222.2012.664134.

(*103*) Hanhineva, K., Törrönen, R., Bondia-Pons, I., Pekkinen, J., Kolehmainen, M., Mykkänen, H., and Poutanen, K. (2010). Impact of dietary polyphenols on carbohydrate metabolism. *Int. J. Mol. Sci.* 11, 1365–1402, DOI: 10.3390/ijms11041365.

(*104*) Wang, H., Liu, T., and Huang, D. (2013). Starch hydrolase inhibitors from edible plants. *Adv. Food Nutr. Res.* 70, 103–136, DOI: 10.1016/B978-0-12-416555-7.00003-5.

(*105*) Ghosh, S., Ahire, M., Patil, S., Jabgunde, A., Bhat Dusane, M., Joshi, B. N., Pardesi, K., Jachak, S., Dhavale, D. D., and Chopade, B. A. Antidiabetic activity of *Gnidia glauca* and *Dioscorea bulbifera*: potent amylase and glucosidase inhibitors. *Evid. Based Complement. Alternat. Med.* [Online] **2012**, DOI: 10.1155/2012/929051, (accessed December 2, 2013).

(*106*) Misbah, H., Aziz, A. A., and Aminudin, N. Antidiabetic and antioxidant properties of *Ficus deltoidea* fruit extracts and fractions. *BMC Complement. Altern. Med.* [Online] **2013**, *13*, DOI: 10.1186/1472-6882-13-118, (accessed January 3, 2014).

(*107*) Narita, Y., and Inouye, K. (2009). Kinetic analysis and mechanism on the inhibition of chlorogenic acid and its components against porcine pancreas α-amylase isozymes I and II. *J. Agric. Food Chem.* 57, 9218–9225, DOI: 10.1021%2Fjf9017383.

(*108*) Lo Piparo, E., Scheib, H., Frei, N., Williamson, G., Grigorov, M., and Chou, C. J. (2008). Flavonoids for controlling starch digestion: structural requirements for inhibiting human α-amylase. *J. Med. Chem.* 51, 3555–3561, DOI: 10.1021/jm800115x.

(*109*) Machius, M., Vértesy, L., Huber, R., and Wiegand, G. (1996). Carbohydrate and protein-based inhibitors of porcine pancreatic α-amylase: structure analysis and comparison of their binding characteristics. *J. Mol. Biol.* 260, 409–421, DOI: 10.1006/jmbi.1996.0410.

(*110*) Ramasubbu, N., Ragunath, C., and Mishra, P. J. (2003). Probing the role of a mobile loop in substrate binding and enzyme activity of human salivary amylase. *J. Mol. Biol.* 325, 1061–1076, DOI: 10.1016/S0022-2836(02)01326-8.

(*111*) Iwai, K., Kim, M.-Y., Onodera, A., and Matsue, H. (2006). α-Glucosidase inhibitory and antihyperglycemic effects of polyphenols in the fruit of *Viburnum dilatatum* Thunb. *J. Agric. Food Chem.* 54, 4588–4592, DOI: 10.1021/jf0606353.

(*112*) Tsai, H.-Y., Wu, L.-Y., and Hwang, L. S. (2008). Effect of a proanthocyanidin-rich extract from longan flower on markers of metabolic syndrome in fructose-fed rats. *J. Agric. Food Chem.* 56, 11018–11024, DOI: 10.1021/jf801966y.

(*113*) Matsui, T., Ueda, T., Oki, T., Sugita, K., Terahara, N., and Matsumoto, K. (2001). α-Glucosidase inhibitory action of natural acylated anthocyanins. 1. Survey of natural pigments with potent inhibitory activity. *J. Agric. Food Chem.* 49, 1948–1951, DOI: 10.1021/jf001251u.

(*114*) Matsui, T., Ueda, T., Oki, T., Sugita, K., Terahara, N., and Matsumoto, K. (2001). α-Glucosidase inhibitory action of natural acylated anthocyanins. 2. α-Glucosidase inhibition by isolated acylated anthocyanins. *J. Agric. Food Chem.* 49, 1952–1956, DOI: 10.1021/jf0012502.

(*115*) Ishikawa, A., Yamashita, H., Hiemori, M., Inagaki, E., Kimoto, M., Okamoto, M., Tsuji, H., Memon, A. N., Mohammadi, A., and Natori, Y. (2007). Characterization of inhibitors of postprandial hyperglycemia from the leaves of *Nerium indicum*. *J. Nutr. Sci. Vitaminol.* 53, 166–173.

(*116*) Welsch, C. A., Lachance, P. A., and Wasserman, B. P. (1989). Dietary phenolic compounds: inhibition of Na+-dependent D-glucose uptake in rat intestinal brush border membrane vesicles. *J. Nutr.* 119, 1698–1704.

(*117*) Welsch, C. A., Lachance, P. A., and Wasserman, B. P. (1989). Effects of native and oxidized phenolic compounds on sucrase activity in rat brush border membrane vesicles. *J. Nutr.* 119, 1737–1740.

(*118*) Matsui, T., Tanaka, T., Tamura, S., Toshima, A., Tamaya, K., Miyata, Y., Tanaka, K., and Matsumoto, K. (2007). α-Glucosidase inhibitory profile of catechins and theaflavins. *J. Agric. Food Chem.* 55, 99–105, DOI: 10.1021/jf0627672.

(*119*) Yilmazer-Musa, M., Griffith, A. M., Michels, A. J., Schneider, E., and Frei, B. (2012). Grape seed and tea extracts and catechin 3-gallates are potent inhibitors of α-amylase and α-glucosidase activity. *J. Agric. Food Chem.* 60, 8924–8929, DOI: 10.1021/jf301147n.

(*120*) Tadera, K., Minami, Y., Takamatsu, K., and Matsuoka, T. (2006). Inhibition of α-glucosidase and α-amylase by flavonoids. *J. Nutr. Sci. Vitaminol.* 52, 149–153, DOI: 10.3177/jnsv.52.149.

(*121*) Escandón-Rivera, S., González-Andrade, M., Bye, R., Linares, E., Navarrete, A., and Mata, R. (2012). α-Glucosidase inhibitors from *Brikellia cavanillesii*. *J. Nat. Prod.* 75, 968–974, DOI: 10.1021/np300204p.

(*122*) Hanamura, T., Hagiwara, T., and Kawagishi, H. (2005). Structural and functional characterization of polyphenols isolated from acerola (*Malpighia emarginata* DC.) fruit. *Biosci. Biotechnol. Biochem.* 69, 280–286.

(*123*) Manaharan, T., Appleton, D., Cheng, H. M., and Palanisamy, U. D. (2012). Flavonoids isolated from *Syzygium aqueum* leaf extract as potential antihyperglycæmic agents. *Food Chem.* 132, 1802–1807, DOI: 10.1016/j.foodchem.2011.11.147.

(*124*) Kim, J. S., Kwon, C. S., and Son, K. H. (2000). Inhibition of α-glucosidase and α-amylase by luteolin, a flavonoid. *Biosci. Biotechnol. Biochem.* 64, 2458–2461.

(*125*) Yang, Y., Zhan, J., Zhao, H., and Zhou, Y. (2012). A new size-independent score for pairwise protein structure alignment and its application to structure classification and nucleic-acid binding prediction. *Proteins* 80, 2080–2088, DOI: 10.1002/prot.24100.

(*126*) Goto, T., Horita, M., Nagai, H., Nagatomo, A., Nishida, N., Matsuura, Y., and Nagaoka, S. (2012). Tiliroside, a glycosidic flavonoid, inhibits carbohydrate digestion and glucose absorption in the gastrointestinal tract. *Mol. Nutr. Food Res.* 56, 435–445, DOI: 10.1002/mnfr.201100458.

(*127*) Yao, Y., Cheng, X., Suhua Wang, L., and Ren, G. (2011). A Determination of potential α-glucosidase inhibitors from azuki beans (*Vigna angularis*). *Int. J. Mol. Sci.* 12, 6445–6451, DOI: 10.3390%2Fijms12106445.

(*128*) Azuma, T., Kayano, S., Matsumura, Y., Konishi, Y., Tanaka, Y., and Kikuzaki, H. (2011). Antimutagenic and α-glucosidase inhibitory effects of constituents from *Kaempferia parviflora*. *Food Chem.* 125, 471–475, DOI: 10.1016/j.foodchem.2010.09.033.

(*129*) Li, Y., Gao, F., Gao, F., Shan, F., Bian, J., and Zhao, C. (2009). Study on the interaction between 3 flavonoid compounds and α-amylase by fluorescence spectroscopy and enzymatic kinetics. *J. Food Sci.* 74, C199–C203, DOI: 10.1111/j.1750-3841.2009.01080.x.

(*130*) Ryu, H. W., Cho, J. K., Curtis-Long, M. J., Yuk, H. J., Kim, Y. S., Jung, S., Kim, Y. S., Lee, B. W., and Park, K. H. (2011). α-Glucosidase inhibition and antihyperglycemic activity of prenylated xanthones from *Garcinia mangostana*. *Phytochemistry* 72, 2148–2154, DOI: 10.1016/j.phytochem.2011.08.007.

(*131*) Lee, D.-S., and Lee, S.-H. (2001). Genistein, a soy isoflavone, is a potent α-glucosidase inhibitor. *FEBS Lett.* 501, 84–86, DOI: 10.1016/S0014-5793(01)02631-X.

(*132*) Matsui, T., Ebuchi, S., Fukui, K., Matsugano, K., Terahara, N., and Matsumoto, K. (2004). Caffeoylsophorose, a new natural α-glucosidase inhibitor, from red vinegar by fermented purple-fleshed sweet potato. *Biosci. Biotechnol. Biochem.* 68, 2239–2246, DOI: 10.1271/bbb.68.2239.

(*133*) Funke, I., and Melzig, M. F. (2005). Effect of different phenolic compounds on α-amylase activity: screening by microplate-reader based kinetic assay. *Die Pharmazie* 60, 796–797.

(*134*) McDougall, G. J., Shpiro, F., Dobson, P., Smith, P., Blake, A., and Stewart, D. (2005). Different polyphenolic components of soft fruits inhibit α-amylase and α-glucosidase. *J. Agric. Food Chem.* 53, 2760–2766, DOI: 10.1021/jf0489926.

(*135*) Adisakwattana, S., Chantarasinlapin, P., Thammarat, H., and Yibchok-Anun, S. (2009). A series of cinnamic acid derivatives and their inhibitory activity on intestinal α-glucosidase. *J. Enzyme Inhib. Med. Chem.* 24, 1194–1200, DOI: 10.1080/14756360902779326.

(*136*) Chauhan, A., Gupta, S., and Mahmood, A. (2007). Effect of tannic acid on brush border disaccharidases in mammalian intestine. *Indian J. Exp. Biol.* 45, 353–358.

(*137*) Narita, Y., and Inouye, K. (2011). Inhibitory effects of chlorogenic acids from green coffee beans and cinnamate derivatives on the activity of porcine pancreas α-amylase isozyme I. *Food Chem.* 127, 1532–1539, DOI: 10.1016%2Fj.foodchem.2011.02.013.

(*138*) Omar, R., Li, L., Yuan, T., and Seeram, N. P. (2012). α-Glucosidase inhibitory hydrolyzable tannins from *Eugenia jambolana* seeds. *J. Nat. Prod.* 75, 1505–1509, DOI: 10.1021%2Fnp300417q.

(*139*) Ochir, S., Nishizawa, M., Park, B. J., Ishii, K., Kanazawa, T., Funaki, M., and Yamagishi, T. (2010). Inhibitory effects of *Rosa gallica* on the digestive enzymes. *J Nat Med* 64, 275–280, DOI: 10.1007%2Fs11418-010-0402-0.

(*140*) Lee, Y. A., Cho, E. J., Tanaka, T., and Yokozawa, T. (2007). Inhibitory activities of proanthocyanidins from persimmon against oxidative stress and digestive enzymes related to diabetes. *J. Nutr. Sci. Vitaminol.* 53, 287–292, DOI: 10.3177/jnsv.53.287.

(*141*) Schäfer, A., and Högger, P. (2007). Oligomeric procyanidins of French maritime pine bark extract (Pycnogenol®) effectively inhibit α-glucosidase. *Diabetes Res. Clin. Pract.* 77, 41–46, DOI: 10.1016/j.diabres.2006.10.011.

(*142*) Rattanangkool, E., Kittikhunnatham, P., Damsud, T., Wacharasindhu, S., and Phuwapraisirisan, P. (2013). Quercitylcinnamates, a new series of antidiabetic bioconjugates possessing α-glucosidase inhibition and antioxidant. *Eur. J. Med. Chem.* 66, 296–304, DOI: 10.1016%2Fj.ejmech.2013.05.047.

(*143*) Ponnusamy, S., Zinjarde, S., Bhargava, S., Kulkarni-Kale, U., Sawant, S., and Ravikumar, A. (2013). Deciphering the inactivation of human pancreatic α-amylase, an antidiabetic target, by bisdemethoxycurcumin, a small molecule inhibitor, isolated from *Curccuma longa*. *Natural Products Journal* 3, 15–25, DOI: 10.2174%2F2210315511303010005.

(*144*) Yuk, H. J., Lee, J. H., Curtis-Long, M. J., Lee, J. W., Kim, Y. S., Ryu, H. W., Park, C. G., Jeong, T. S., and Park, K. H. (2011). The most abundant polyphenol of soy leaves, coumestrol, displays potent α-glucosidase inhibitory activity. *Food Chem.* 126, 1057–1063, DOI: 10.1016/j.foodchem.2010.11.125.

(*145*) Sengupta, S., Mukherjee, A., Goswami, R., and Basi, S. (2009). Hypoglycemic activity of the antioxidant saponarin, characterized as α-glucosidase inhibitor present in *Tinospora cordifolia*. *J. Enzyme Inhib. Med. Chem.* 24, 684–690, DOI: 10.1080/14756360802333075.

(*146*) Aparna, P., Tiwari, A. K., Srinivas, P. V., Ali, A. Z., Anuradha, V., and Rao, J. M. (2009). Dolichandroside A, a new α-glucosidase inhibitor and DPPH free-radical scavenger from *Dolichandrone falcata* seem. *Phytother. Res.* 23, 591–596, DOI: 10.1002/ptr.2672.

(*147*) Huang, G.-J., Hsieh, W.-T., Chang, H.-Y., Huang, S.-S., Lin, Y.-C., and Kuo, Y.-H. (2011). α-Glucosidase and aldose reductase inhibitory activities from the fruiting body of *Phellinus merrillii*. *J. Agric. Food Chem.* 59, 5702–5706, DOI: 10.1021/jf2003943.

(*148*) Kim, K. Y., Nguyen, T. H., Kurihara, H., and Kim, S. M. (2010). α-Glucosidase inhibitory activity of bromophenol purified from the red alga *Polyopes lancifolia*. *J. Food Sci.* 75, H145–H150, DOI: 10.1111/j.1750-3841.2010.01629.x.

(*149*) Franco, O. L., Rigden, D. J., Melo, F. R., and Grossi-de-Sá, M. F. (2002). Plant α-amylase inhibitors and their interaction with insect α-amylases. *Eur. J. Biochem.* 269, 397–412.

(*150*) Lehtiö, J., Teeri, T. T., and Nygren, P.-A. (2000). Alpha-amylase inhibitors selected from a combinatorial library of a cellulose binding domain scaffold. *Proteins* 41, 316–322, DOI: 10.1002%2f1097-0134(20001115)41%3a3%3c316%3a%3aAID-PROT40%3e3.0.CO%3b2-K.

(*151*) Desmyter, A., Spinelli, S., Payan, F., Lauwereys, M., Wyns, L., Muyldermans, S., and Cambillau, C. (2002). Three camelid VHH domains in complex with porcine pancreatic α-amylase. Inhibition and versatility of binding topology. *J. Biol. Chem.* 277, 23645–23650, DOI: 10.1074/jbc.M202327200.

(*152*) Vértesy, L., Oeding, V., Bender, R., Zepf, K., and Nesemann, G. (1984). Tendamistat (HOE 467), a tight-binding α-amylase inhibitor from *Streptomyces tendae* 4158. Isolation, biochemical properties. *Eur. J. Biochem.* 141, 505–512, DOI: 10.1111/j.1432-1033.1984.tb08221.x.

(*153*) Billeter, M., Kline, A. D., Braun, W., Huber, R., and Wüthrich, K. (1989). Comparison of the high-resolution structures of the α-amylase inhibitor tendamistat determined by nuclear magnetic resonance in solution and by X-ray diffraction in single crystals. *J. Mol. Biol.* 206, 677–687.

(*154*) Kline, A. D., Braun, W., and Wüthrich, K. (1988). Determination of the complete three-dimensional structure of the α-amylase inhibitor tendamistat in aqueous solution by nuclear magnetic resonance and distance geometry. *J. Mol. Biol.* 204, 675–724.

(*155*) Wiegand, G., Epp, O., and Huber, R. (1995). The crystal structure of porcine pancreatic α-amylase in complex with the microbial inhibitor Tendamistat. *J. Mol. Biol.* 247, 99–110, DOI: 10.1006/jmbi.1994.0125.

(*156*) Murai, H., Hara, S., Ikenaka, T., Goto, A., Arai, M., and Murao, S. (1985). Amino acid sequence of protein α-amylase inhibitor from *Streptomyces griseosporeus* YM-25. *J. Biochem. (Tokyo)* 97, 1129–1133.

(*157*) Vértesy, L., and Tripier, D. (1985). Isolation and structure elucidation of an α-amylase inhibitor, AI-3688, from *Streptomyces aureofaciens*. *FEBS Lett.* 185, 187–190, DOI: 10.1016/0014-5793(85)80767-5.

(*158*) Yoshida, M., Nakai, T., Fukuhara, K., Saitoh, S., Yoshikawa, W., Kobayashi, Y., and Nakamura, H. (1990). Three-dimensional structure of an α-amylase inhibitor HAIM as determined by nuclear magnetic resonance methods. *J. Biochem. (Tokyo)* 108, 158–165.

(*159*) Etzkorn, F. A., Guo, T., and Lipton, M. A. (1994). Cyclic hexapeptides and chimeric peptides as mimics of tendamistat. *J. Am. Chem. Soc.* 116, 10412–10425.

(*160*) Bode, W., Greyling, H. J., Huber, R., Otlewski, J., and Wilusz, T. (1989). The refined 2.0 Å X-ray crystal structure of the complex formed between bovine beta-trypsin and CMTI-I, a trypsin inhibitor from squash seeds (*Cucurbita maxima*). Topological similarity of the squash seed inhibitors with the carboxypeptidase A inhibitor from potatoes. *FEBS Lett.* 242, 285–292.

(*161*) Rees, D. C., and Lipscomb, W. N. (1982). Refined crystal structure of the potato inhibitor complex of carboxypeptidase A at 2.5 Å resolution. *J. Mol. Biol.* 160, 475–498, DOI: 10.1016%2F0022-2836%2882%2990309-6.

(*162*) Gelly, J.-C., Gracy, J., Kaas, Q., Le-Nguyen, D., Heitz, A., and Chiche, L. (2004). The KNOTTIN website and database: a new information system dedicated to the knottin scaffold. *Nucleic Acids Res.* 32, D156–D159, DOI: 10.1093/nar/gkh015.

(*163*) Chagolla-Lopez, A., Blanco-Labra, A., Patthy, A., Sánchez, R., and Pongor, S. (1994). A novel α-amylase inhibitor from amaranth (*Amaranthus hypocondriacus*) seeds. *J. Biol. Chem.* 269, 23675–23680.

(*164*) Barbosa-Pereira, P., Lozanov, V., Patthy, A., Huber, R., and Bode, W. (1999). Specific inhibition of insect α-amylases: yellow meal worm α-amylase in complex with the *Amaranth* α-amylase inhibitor at 2.0 Å resolution. *Structure* 7, 1079–1088, DOI: 10.1016/S0969-2126(99)80175-0.

(*165*) Bruix, M., Jimenez, M., Santoro, J., Gonzalez, C., Colilla, F., Mendez, E., and Rico, M. (1993). Solution structure of γ1-H and γ1-P thionins from barley and wheat endosperm determined by ^{1}H-NMR: a structural motif common to toxic arthropod proteins. *Biochemistry* 32, 715–724.

(*166*) Bloch Jr, C., and Richardson, M. (1991). A new family of small (5 kDa) protein inhibitors of insect α-amylases from seeds or sorghum (*Sorghum bicolor* (L) Moench) have sequence homologies with wheat α-purothionins. *FEBS Lett.* 279, 101–104.

(*167*) Selsted, M. E., Szklarek, D., and Lehrer, R. I. (1984). Purification and antibacterial activity of antimicrobial peptides of rabbit granulocytes. *Infect. Immun.* 45, 150–154.

(*168*) Lehrer, R. I., Lichtenstein, A. K., and Ganz, T. (1993). Defensins: antimicrobial and cytotoxic peptides of mammalian cells. *Annu. Rev. Immunol.* 11, 105–128, DOI: 10.1146/annurev.iy.11.040193.000541.

(*169*) Zimmermann, G., Legault, P., Selsted, M., and Pardi, A. (1995). Solution structure of bovine neutrophil β-defensin-12: the peptide fold of the β-defensins is identical to that of the classical defensins. *Biochemistry* 34, 13663–13671, DOI: 10.1021/bi00041a048\x{fffd}\x{fffd}\x{fffd}.

(*170*) Torres, A. M., and Kuchel, P. W. (2004). The β-defensin-fold family of polypeptides. *Toxicon* 44, 581–588, DOI: 10.1016/j.toxicon.2004.07.011.

(*171*) Pelegrini, P. B., Lay, F. T., Murad, A. M., Anderson, M. A., and Franco, O. L. (2008). Novel insights on the mechanism of action of α-amylase inhibitors from the plant defensin family. *Proteins* 73, 719–729, DOI: 10.1002%2Fprot.22086.

(*172*) Liu, Y.-J., Cheng, C.-S., Lai, S.-M., Hsu, M.-P., Chen, C.-S., and Lyu, P.-C. (2006). Solution structure of the plant defensin VrD1 from mung bean and its possible role in insecticidal activity against bruchids. *Proteins* 63, 777–786, DOI: 10.1002/prot.20962.

(*173*) Lin, K.-F., Lee, T.-R., Tsai, P.-H., Hsu, M.-P., Chen, C.-S., and Lyu, P.-C. (2007). Structure-based protein engineering for α-amylase inhibitory activity of plant defensin. *Proteins* 68, 530–540, DOI: 10.1002/prot.21378.

(*174*) Barber, D., Sanchez-Monge, R., García-Olmeda, F., Salcedo, G., and Méndez, E. (1986). Evolutionary implications of sequential homologies among members of the trypsin/α-amylase inhibitor family

(CM-proteins) in wheat and barley. *Biochim. Biophys. Acta* 873, 147–151.

(*175*) Barber, D., Sanchez-Monge, R., Mendez, E., Lazaro, A., García-Olmedo, F., and Salcedo, G. (1986). New α-amylase and trypsin inhibitors among the CM-proteins of barley (*Hordeum vulgare)*. *Biochim. Biophys. Acta* 869, 115–118.

(*176*) Alagiri, S., and Singh, T. (1993). Stability and kinetics of a bifunctional amylase/trypsin inhibitor. *Biochim. Biophys. Acta* 1203, 77–84, DOI: 10.1016%2F0167-4838%2893%2990038-S.

(*177*) Maskos, K., Huber-Wunderlich, M., and Glockshuber, R. (1996). RBI, a one-domain α-amylase/trypsin inhibitor with completely independent binding sites. *FEBS Lett.* 397, 11–16, DOI: 10.1016/S0014-5793(96)01131-3.

(*178*) Iulek, J., Franco, O. L., Silva, M., Trevisan Slivinski, C., Bloch Jr, C., Rigden, D. J., and Grossi de Sá, M. F. (2000). Purification, biochemical characterisation and partial primary structure of a new α-amylase inhibitor from *Secale cereale* (rye). *Int. J. Biochem. Cell Biol.* 32, 1195–1204.

(*179*) García-Olmedo, F., Molina, A., Alamillo, J. M., and Rodríguez-Palenzuéla, P. (1998). Plant defense peptides. *Biopolymers* 47, 479–491.

(*180*) Strobl, S., Maskos, K., Wiegand, G., Huber, R., Gomis-Rüth, F. X., and Glockshuber, R. (1998). A novel strategy for inhibition of α-amylases: yellow meal worm α-amylase in complex with the *Ragi* bifunctional inhibitor at 2.5 Å resolution. *Structure* 6, 911–921, DOI: 10.1016%2FS0969-2126%2898%2900092-6.

(*181*) Gourinath, S., Alam, N., Srinivasan, A., Betzel, C., and Singh, T. (2000). Structure of the bifunctional inhibitor of trypsin and α-amylase from ragi seeds at 2.2 Å resolution. *Acta Cryst. D*56, 287–293.

(*182*) Strobl, S., Mühlhahn, P., Bernstein, R., Wiltscheck, R., Maskos, K., Wunderlich, M., Huber, R., Glockshuber, R., and Holak, T. A. (1995). Determination of the three-dimensional structure of the bifunctional α-amylase/trypsin inhibitor from ragi seeds by NMR spectroscopy. *Biochemistry* 34, 8281–8293, DOI: 10.1021%2Fbi00026a009.

(*183*) Alam, N., Gourinath, S., Dey, S., Srinivasan, A., and Singh, T. P. (2001). Substrate-inhibitor interactions in the kinetics of α-amylase inhibition by ragi α-amylase/trypsin inhibitor (RATI) and its various N-terminal fragments. *Biochemistry* 40, 4229–4233, DOI: 10.1021%2Fbi002537v.

(*184*) Onesti, S., Brick, P., and Blow, D. M. (1991). Crystal structure of a Kunitz-type trypsin inhibitor from *Erythrina caffra seeds. J. Mol. Biol.* 217, 153–176.

(*185*) Vallée, F., Kadziola, A., Bourne, Y., Juy, M., Rodenburg, K. W., Svensson, B., and Haser, R. (1998). Barley α-amylase bound to its endogenous protein inhibitor BASI: crystal structure of the complex at 1.9 Å resolution. *Structure* 6, 649–659, DOI: 10.1016/S0969-2126(98)00066-5.

(*186*) Schimoler-O'Rourke, R., Richardson, M., and Selitrennikoff, C. P. (2001). Zeamatin inhibits trypsin and α-amylase activities. *Appl. Environ. Microbiol.* 67, 2365–2366, DOI: 10.1128%2FAEM.67.5.2365-2366.2001.

(*187*) Batalia, M. A., Monzingo, A. F., Ernst, S., Roberts, W., and Robertus, J. D. (1996). The crystal structure of the antifungal protein zeamatin, a member of the thaumatin-like, PR-5 protein family. *Nat. Struct. Biol.* 3, 19–23, DOI: 10.1038/nsb0196-19.

(*188*) Roberts, W. K., and Selitrennikoff, C. P. (1990). Zeamatin, an antifungal protein from maize with membrane-permeabilizing activity. *J. Gen. Microbiol.* 136, 1771–1778.

(*189*) Le Berre-Anton, V., Bompard-Gilles, C., Payan, F., and Rougé, P. (1997). Characterization and functional properties of the α-amylase inhibitor (α-AI) from kidney bean (*Phaseolus vulgaris*) seeds. *Biochim. Biophys. Acta* 1343, 31–40, DOI: 10.1016/S0167-4838(97)00100-3.

(*190*) Grossi de Sá, M. F., Mirkov, T. E., Ishimoto, M., Colucci, G., Bateman, K. S., and Chrispeels, M. J. (1997). Molecular characterization of a bean α-amylase inhibitor that inhibits the α-amylase of the Mexican bean weevil *Zabrotes subfasciatus*. *Planta* 203, 295–303.

(*191*) Ishimoto, M., Suzuki, K., Iwanaga, M., Kikuchi, F., and Kitamura, K. (1995). Variation of seed α-amylase inhibitors in the common bean. *Theor. Appl. Genet.* 90, 425–429.

(*192*) Mirkov, T. E., Evans, S. V., Wahlstrom, J., Gomez, L., Young, N. M., and Chrispeels, M. J. (1995). Location of the active site of the bean α-amylase inhibitor and involvement of a Trp, Arg, Tyr triad. *Glycobiology* 5, 45–50, DOI: 10.1093/glycob/5.1.45.

(*193*) Bompard-Gilles, C., Rousseau, P., Rougé, P., and Payan, F. (1996). Substrate mimicry in the active center of a mammalian α-amylase: structural analysis of an enzyme-inhibitor complex. *Structure* 4, 1441–1452.

(*194*) Kasahara, K., Hayashi, K., Arakawa, T., Philo, J. S., Wen, J., Hara, S., and Yamaguchi, H. (1996). Complete sequence, subunit structure, and complexes with pancreatic α-amylase of an α-amylase inhibitor from *Phaseolus vulgaris* white kidney beans. *J. Biochem. (Tokyo)* 120, 177–183.

(*195*) Nahoum, V., Roux, G., Anton, V., Rougé, P., Puigserver, A., Bischoff, H., Henrissat, B., and Payan, F. (2000). Crystal structures of human pancreatic α-amylase in complex with carbohydrate and proteinaceous inhibitors. *Biochem. J.* 346, 201–208, DOI: 10.1042/0264-6021:3460201.

(*196*) Nahoum, V., Farisei, F., Le Berre-Anton, V., Egloff, M. P., Rougé, P., Poerio, E., and Payan, F. (1999). A plant-seed inhibitor of two classes of α-amylases: X-ray analysis of *Tenebrio molitor* larvae α-amylase in complex with the bean *Phaseolus vulgaris* inhibitor. *Acta Cryst. D*55, 360–362, DOI: 10.1107/S0907444998010701.

(*197*) Santimone, M., Koukiekolo, R., Moreau, Y., Le Berre, V., Rougé, P., Marchis-Mouren, G., and Desseaux, V. (2004). Porcine pancreatic α-amylase inhibition by the kidney bean (*Phaseolus vulgaris*) inhibitor (α-AI1) and structural changes in the α-amylase inhibitor complex. *Biochim. Biophys. Acta* 1696, 181–190, DOI: 10.1016%2Fj.bbapap.2003.11.001.

(*198*) Powers, J. R., and Whitaker, J. R. (1978). Purification and some physical and chemical properties of red kidney bean *Phaseolus vulgaris* α-amylase inhibitor. *J. of Food Biochem.* 1, 217–238, DOI: 10.1111/j.1745-4514.1978.tb00183.x.

(*199*) Tarling, C. A., [Personal communication], 2008.

(*200*) Li, C., Begum, A., Numao, S., Park, K. H., Withers, S. G., and Brayer, G. D. (2005). Acarbose rearrangement mechanism implied by the kinetic and structural analysis of human pancreatic α-amylase in complex with analogues and their elongated counterparts. *Biochemistry* 44, 3347–3357, DOI: 10.1021/bi048334e.

(*201*) Bischoff, H. (1994). Pharmacology of alpha-glucosidase inhibition. *Eur. J. Clin. Invest.* 24, Suppl. 3, 3–10.

(*202*) Chiasson, J.-L., Josse, R. G., Hunt, J. A., Palmason, C., Rodger, N. W., Ross, S. A., Ryan, E. A., Tan, M. H., and Wolever, T. M. (1994). The efficacy of acarbose in the treatment of patients with non-insulin-dependent diabetes mellitus. A multicenter controlled clinical trial. *Ann. Intern. Med.* 121, 928–935.

(*203*) Yuen, V. G., Brayer, G. D., Withers, S. G., Coleman, J., and McNeill, J. H. (2010). The acute effects of Montbretin A, an α-glucosidase inhibitor, on plasma glucose levels in the Zucker Diabetic Fatty Rat. [unpublished].

(*204*) McPherson, A., *Preparation and Analysis of Protein Crystals*; Robert E. Krieger Publishing Company: Malabar, Florida, 1989.

(*205*) *Protein Crystallization*; Bergfors, T. M., Ed.; International University Line: La Jolla, California, 2009.

(*206*) Blundell, T. L., and Johnson, L. N., *Protein Crystallography*; Academic Press: New York, 1976.

(*207*) Stout, G. H., and Jensen, L. H., *X-ray Structure Determinations: a Practical Guide*; Wiley: New York, 1989.

(*208*) Rhodes, G., *Crystallography Made Crystal Clear: A Guide for Users of Macromolecular Models*, 3rd. ed.; Elsevier: Amsterdam, 2006.

(*209*) McRee, D. E., *Practical Protein Crystallography*; Academic Press: San Diego, 1993.

(*210*) Drenth, J., *Principles of Protein X-ray Crystallography*; Springer: New York, 1999.

(*211*) *Fundamentals of Crystallography*, 3rd.; Giacovazzo, C., Ed.; IUCR Monographs on Crystallography; Oxford Univeristy Press: New York, 2011.

(*212*) Hofmann, A., *The Physics of Synchrotron Radiation*; Cambridge University Press: New York, 2004.

(*213*) Willmott, P., *An Introduction to Synchrotron Radiation: Techniques and Applications*; Wiley: Chicester, 2011.

(*214*) Powell, H. R. (1999). The Rossmann Fourier autoindexing algorithm in MOSFLM. *Acta Cryst. D*55, 1690–1695, DOI: 10.1107%2FS0907444999009506.

(*215*) Leslie, A. G. W. (2006). The integration of macromolecular diffraction data. *Acta Cryst. D*62, 48–57, DOI: 10.1107/S0907444905039107.

(*216*) Kabsch, W. (2010). XDS. *Acta Cryst. D*66, 125–132, DOI: 10.1107/S0907444909047337.

(*217*) Rossmann, M., Leslie, A. G., Abdel-Meguid, S., and Tsukihara, T. (1979). Processing and post-refinement of oscillation camera data. *J. Appl. Crystallogr.* 12, 570–581, DOI: 10.1107/S0021889879013273.

(*218*) Pannu, N., and Read, R. (1996). Improved Structure Refinement Through Maximum Likelihood. *Acta Cryst. A*52, 659–668, DOI: 10.1107%2FS0108767396004370.

(*219*) Brünger, A. T. (1992). Free R value: a novel statistical quantity for assessing the accuracy of crystal structures. *Nature* 355, 472–475.

(*220*) Laskowski, R. A., MacArthur, M. W., Moss, D. S., and Thornton, J. M. (1993). PROCHECK: a program to check the stereochemical quality of protein structures. *J. Appl. Cryst.* 26, 283–291, DOI: 10.1107/S0021889892009944.

(*221*) Davis, I. W., Leaver-Fay, A., Chen, V. B., Block, J. N., Kapral, G. J., Wang, X., Murray, L. W., Arendall III, W. B., Snoeyink, J., Richardson, J. S., and Richardson, D. C. (2007). MolProbity: all-atom contacts and structure validation for proteins and nucleic acids. *Nucleic Acids Res.* 35, W375–W383, DOI: 10.1093/nar/gkm216.

(*222*) Tan, T.-C., Mijts, B. N., Swaminathan, K., Patel, B. K. C., and Divne, C. (2008). Crystal structure of the polyextremophilic α-amylase AmyB from *Halothermothrix orenii*: details of a productive enzyme-substrate complex and an *N* domain with a role in binding raw starch. *J. Mol. Biol.* 378, 852–870.

(*223*) Babu, P. V. A., Liu, D., and Gilbert, E. R. (2013). Recent advances in understanding the anti-diabetic actions of dietary flavonoids. *J. Nutr. Biochem.* 24, 1777–1789, DOI: 10.1016/j.jnutbio.2013.06.003.

(*224*) Selvaraj, S., Krishnaswamy, S., Devashya, V., Sethuraman, S., and Krishnan, U. M. (2013). Flavonoid-metal ion complexes: a novel class of therapeutic agents. *Med. Res. Rev.* n/a–n/a, DOI: 10.1002%2Fmed.21301.

(*225*) Singh, R., Kaur, N., Kishore, L., and Gupta, G. K. (2013). Management of diabetic complications: A chemical constituents based approach. *J. Ethnopharmacol.* 150, 51–70, DOI: 10.1016%2Fj.jep.2013.08.051.

(*226*) Yiannakopoulou, E. C. Effect of green tea catechins on breast carcinogenesis: a systematic review of in-vitro and in-vivo experimental studies. *Eur. J. Cancer Prev.* [Online] **2013**, DOI: 10.1097/CEJ.0b013e328364f23e, (accessed January 11, 2014).

(*227*) Pereira, D. F., Cazarolli, L. H., Lavado, C., Mengatto, V., Figueiredo, M. S. R. B., Guedes, A., Pizzolatti, M. G., and Silva, F. R. M. B. (2011). Effects of flavonoids on α-glucosidase activity: potential targets for glucose homeostasis. *Nutrition* 27, 1161–1167, DOI: 10.1016/j.nut.2011.01.008.

(*228*) Hsu, F. L., Chen, Y. C., and Cheng, J. T. (2000). Caffeic acid as active principle from the fruit of *Xanthium strumarium* to lower plasma glucose in diabetic rats. *Planta Med.* 66, 228–230, DOI: 10.1055/s-2000-8561.

(*229*) Jung, U. J., Lee, M.-K., Park, Y. B., Jeon, S.-M., and Choi, M.-S. (2006). Antihyperglycemic and antioxidant properties of caffeic acid in db/db mice. *J. Pharmacol. Exp. Ther.* 318, 476–483, DOI: 10.1124/jpet.106.105163.

(*230*) Yoshida, K., Hishida, A., Iida, O., Hosokawa, K., and Kawabata, J. (2008). Flavonol caffeoylglycosides as α-glucosidase inhibitors from *Spiraea cantoniensis* flower. *J. Agric. Food Chem.* 56, 4367–4371, DOI: 10.1021/jf8007579.

(*231*) Rubilar, M., Jara, C., Poo, Y., Acevedo, F., Gutierrez, C., Sineiro, J., and Shene, C. (2011). Extracts of maqui (*Aristotelia chilensis*) and murta (*Ugni molinae* Turcz.): sources of antioxidant compounds and α-glucosidase/α-amylase inhibitors. *J. Agric. Food Chem.* 59, 1630–1637, DOI: 10.1021/jf103461k.

(*232*) Shobana, S., Sreerama, Y. N., and Malleshi, N. G. (2009). Composition and enzyme inhibitory properties of finger millet (*Eleusine coracana* L.) seed coat phenolics: Mode of inhibition of α-glucosidase and pancreatic amylase. *Food Chem.* 115, 1268–1273, DOI: 10.1016%2Fj.foodchem.2009.01.042.

(*233*) Soltis, S. M., Cohen, A. E., Deacon, A., Eriksson, T., González, A., McPhillips, S., Chui, H. J., Dunten, P., Hollenbeck, M., Mathews, I. I., Moorhead, P., Phizackerley, R. P., Smith, C., Song, J., van dem Bedem, H., Ellis, P., Kuhn, P., McPhillips, T., Sauter, N., Sharp, K., Tsyba, I., and Wolf, G. (2008). New paradigm for macromolecular crystallography experiments at SSRL: automated crystal screening and remote data collection. *Acta Cryst. D*64, 1210–1221, DOI: 10.1107%2FS0907444908030564.

(*234*) González, A., Moorhead, P., McPhillips, S. E., Song, J., Sharp, K., Taylor, J. R., Adams, P. D., Sauter, N. K., and Soltis, S. M. (2008). Web-Ice: integrated data collection and analysis for macromolecular crystallography. *J. Appl. Crystallogr.* 41, 176–184, DOI: 10.1107/S0021889807057822.

(*235*) McPhillips, T. M., McPhillips, S. E., Chiu, H. J., Cohen, A. E., Deacon, A. M., Ellis, P. J., Garman, E., Gonzalez, A., Sauter, N. K., Phizackerley, R. P., Soltis, S. M., and Kuhn, P. (2002). Blu-Ice and the Distributed Control System: software for data acquisition and instrument control at macromolecular crystallography beamlines. *J. Synchrotron Rad.* 9, 401–406, DOI: 10.1107/S0909049502015170.

(*236*) Leslie, A. G. W. Integration of macromolecular diffraction data. *Acta Cryst. D*55, 1696–1702, DOI: 10.1107/S090744499900846X.

(*237*) Collaborative Computational Project, Number 4 (1994). The CCP4 suite: programs for protein crystallography. *Acta Cryst. D*50, 760–763.

(*238*) Brünger, A. T., Adams, P. D., Clore, G. M., DeLano, W. L., Gros, P., Grosse-Kunstleve, R. W., Jiang, J. S., Kuszewski, J., Nilges, M., Pannu, N. S., Read, R. J., Rice, L. M., Simonson, T., and Warren, G. L. (1998). Crystallography and NMR system: A new software suite for macromolecular structure determination. *Acta Cryst. D*54, 905–921.

(*239*) Emsley, P., and Cowtan, K. (2004). Coot: model-building tools for molecular graphics. *Acta Cryst. D*60, 2126–2132, DOI: 10.1107/S0907444904019158.

(*240*) Schüttelkopf, A. W., and van Aalten, D. M. F. (2004). PRODRG: a tool for high-throughput crystallography of protein-ligand complexes. *Acta Cryst. D*60, 1355–1363, DOI: 10.1107/S0907444904011679.

(*241*) Chen, V. B., Arendall III, W. B., Headd, J. J., Keedy, D. A., Immormino, R. M., Kapral, G. J., Murray, L. W., Richardson, J. S., and Richardson, D. C. (2010). MolProbity: all-atom structure validation for macromolecular crystallography. *Acta Cryst. D*66, 12–21, DOI: 10.1107/S0907444909042073.

(*242*) Ren, L., Cao, X., Geng, P., Bai, F., and Bai, G. (2011). Study of the inhibition of two human maltase-glucoamylases catalytic domains by different α-glucosidase inhibitors. *Carbohydr. Res.* 346, 2688–2692, DOI: 10.1016%2Fj.carres.2011.09.012.

(*243*) Braun, C., Brayer, G. D., and Withers, S. G. (1995). Mechanism-based inhibition of yeast α-glucosidase and human pancreatic α-amylase by a new class of inhibitors: 2-deoxy-2,2-difluoro-α-glycosides. *J. Biol. Chem.* 270, 26778–26781.

(*244*) Maurus, R., Begum, A., Williams, L. K., Fredriksen, J. R., Zhang, R., Withers, S. G., and Brayer, G. D. (2008). Alternative catalytic anions differentially modulate human α-amylase activity and specificity. *Biochemistry* 47, 3332–3344, DOI: 10.1021/bi701652t.

(*245*) Maurus, R., Begum, A., Kuo, H., Racaza, A., NUMAO, S., Andersen, C., Tams, J., Vind, J., Overall, C., Withers, S., and Brayer, G. (2005). Structural and mechanistic studies of chloride induced activation of human pancreatic α-amylase. *Protein Sci.* 14, 743–755, DOI: 10.1110%2Fps.041079305.

(*246*) Liu, I.-M., Tzeng, T.-F., Liou, S.-S., and Lan, T.-W. (2007). Myricetin, a naturally occurring flavonol, ameliorates insulin resistance induced by a high-fructose diet in rats. *Life Sci.* 81, 1479–1488, DOI: 10.1016/j.lfs.2007.08.045.

(*247*) Kim, J. H., Ryu, Y. B., Kang, N. S., Lee, B. W., Heo, J. S., Jeong, I.-Y., and Park, K. H. (2006). Glycosidase inhibitory flavonoids from *Sophora flavescens*. *Biol. Pharm. Bull.* 29, 302–305.

(*248*) Ong, K. C., and Khoo, H. E. (2000). Effects of myricetin on glycemia and glycogen metabolism in diabetic rats. *Life Sci.* 67, 1695–1705, DOI: 10.1016/S0024-3205(00)00758-X.

(*249*) Ramasubbu, N., Paloth, V., Luo, Y., Brayer, G., and Levine, M. (1996). Structure of human salivary α-amylase at 1.6 Å resolution: implications for its role in the oral cavity. *Acta Cryst. D*52, 435–446, DOI: 10.1107%2FS0907444995014119.

(*250*) Y, A., Hirayama, Y., and Furuya, T. (1988). Acylated flavonols from *Crocosmia crocosmiflora*. *Phytochemistry* 27, 1497–1501.

(*251*) Wicki, J. Personal Communication., 2010.

(*252*) Woods, K. Bioactive natural products., Ph.D. Thesis, University of British Columbia, 2010.

(*253*) Lincez, P., and Hii, C. Alpha-amylase inhibitors for Type-2 diabetes: Isolation, Purification, and Kinetic Analysis of Montbretins from *Crocosmia sp.*, *Presented at the CDRD, University of British Columbia, 2008*, Vancouver, BC.

(*254*) Morris, G. M., Goodsell, D. S., Halliday, R. S., Huey, R., Hart, W. E., Belew, R. K., and Olson, A. J. (1998). Automated docking using a Lamarckian genetic algorithm and emipirical binding free energy function. *J. Comput. Chem.* 19, 1639–1662, DOI: 10.1002%2F%28SICI%291096-987X%2819981115%2919%3A14%3C1639%3A%3AAID-JCC10%3E3.0.CO%3B2-B.

(*255*) Evans, P. (2006). Scaling and assessment of data quality. *Acta Cryst. D*62, 72–82, DOI: 10.1107/S0907444905036693.

(*256*) Winn, M. D., Ballard, C. C., Cowtan, K. D., Dodson, E. J., Emsley, P., Evans, P. R., Keegan, R. M., Krissinel, E. B., Leslie, A. G. W., McCoy, A., McNicholas, S. J., Murshudov, G. N., Pannu, N. S., Potterton, E. A., Powell, H. R., Read, R. J., Vagin, A., and Wilson, K. S. (2011). Overview of the CCP4 suite and current developments. *Acta Cryst. D*67, 235–242, DOI: http://dx.doi.org/10.1107%2FS0907444910045749.

(*257*) Brünger, A. T. (2007). Version 1.2 of the Crystallography and NMR system. *Nature Protocols* 2, 2728–2733, DOI: 10.1038/nprot.2007.406.

(*258*) Kleywegt, G. J., and Jones, T. A. (1998). Databases in protein crystallography. *Acta Cryst. D*54, 1119–1131, DOI: 10.1107/S0907444998007100.

(*259*) Kleywegt, G. J. (2007). Crystallographic refinement of ligand complexes. *Acta Cryst. D*63, 94–100, DOI: 10.1107/S0907444906022657.

(*260*) Ramsay, A. G., Scott, K. P., Martin, J. C., Rincon, M. T., and Flint, H. J. (2006). Cell-associated α-amylases of butyrate-producing Firmicute bacteria from the human colon. *Microbiology* 152, 3281–3290, DOI: 10.1099/mic.0.29233-0.

(*261*) Martinez, C. R., and Iverson, B. L. (2012). Rethinking the term "pi-stacking". *Chemical Science* 3, 2191–2199, DOI: 10.1039/c2sc20045g.

(*262*) Zhang, X. Personal communication., 2012.

(*263*) Borges de Melo, E., da Silveira Gomes, A., and Carvalho, I. (2006). α- and β-Glucosidase inhibitors: chemical structure and biological activity. *Tetrahedron* 62, 10277–10302, DOI: 10.1016/j.tet.2006.08.055.

(*264*) Kameda, Y., Asano, N., Yoshikawa, M., and Matsui, K. (1980). Valienamine as an alpha-glucosidase inhibitor. *J. Antibiot. (Tokyo)* 33, 1575–1576.

(*265*) He, Q., Lv, Y., and Yao, K. (2006). Effects of tea polyphenols on the activities of α-amylase, pepsin, trypsin and lipase. *Food Chem.* 101, 1178–1182, DOI: 10.1016/j.foodchem.2006.03.020.

(*266*) Selsted, M. E., and Ouellette, A. J. (2005). Mammalian defensins in the antimicrobial immune response. *Nat. Immunol.* 6, 551–557, DOI: 10.1038/ni1206.

(*267*) White, S. H., Wimley, W. C., and Selsted, M. E. (1995). Structure, function, and membrane integration of defensins. *Curr. Opin. Struct. Biol.* 5, 521–527, DOI: 10.1016/0959-440X(95)80038-7.

(*268*) Bohlen, C. J., Priel, A., Zhou, S., King, D., Siemens, J., and Julius, D. (2010). A bivalent tarantula toxin activates the capsaicin receptor, TRPV1, by targeting the outer pore domain. *Cell* 141, 834–845, DOI: 10.1016/j.cell.2010.03.052.

(*269*) Peigneur, S., Billen, B., Derua, R., Waelkens, E., Debaveye, S., Béress, L., and Tytgat, J. (2011). A bifunctional sea anemone peptide with Kunitz type protease and potassium channel inhibiting properties. *Biochem. Pharmacol.* 82, 81–90, DOI: 10.1016%2Fj.bcp.2011.03.023.

(*270*) Carugo, O., Lu, S., Luo, J., Gu, X., Liang, S., Strobl, S., and Pongor, S. (2001). Structural analysis of free and enzyme-bound amaranth α-amylase inhibitor: classification within the knottin fold superfamily and analysis of its functional flexibility. *Protein Eng.* 14, 639–646.

(*271*) Pallaghy, P. K., Nielsen, K. J., Craik, D. J., and Norton, R. S. (1994). A common structural motif incorporating a cystine knot and a triple-stranded β-sheet in toxic and inhibitory polypeptides. *Protein Sci.* 3, 1833–1839, DOI: 10.1002%2Fpro.5560031022.

(*272*) Tang, Y. Q., and Selsted, M. E. (1993). Characterization of the disulfide motif in BNBD-12, an antimicrobial β-defensin peptide from bovine neutrophils. *J. Biol. Chem.* 268, 6649–6653.

(*273*) Trabi, M., Schirra, H. J., and Craik, D. J. (2001). Three-dimensional structure of RTD-1, a cyclic antimicrobial defensin from rhesus macaque leukocytes. *Biochemistry* 40, 4211–4221, DOI: 10.1021/bi002028t.

(*274*) Ellman, G. L. (1959). Tissue sulfhydryl groups. *Arch. Biochem. Biophys.* 82, 70–77.

(*275*) Cohen, A. E., Ellis, P. J., Miller, M. D., Deacon, A. M., and Phizackerley, R. P. (2002). An automated system to mount cryo-cooled protein crystals on a synchrotron beamline, using compact sample cassettes and a small-scale robot. *J. Appl. Cryst.* 35, 720–726.

(*276*) Kabsch, W. (2010). Integration, scaling, space-group assignment and post-refinement. *Acta Cryst. D*66, 133–144, DOI: 10.1107/S0907444909047374.

(*277*) McCoy, A. J., Grosse-Kunstleve, R. W., Adams, P. D., Winn, M. D., Storoni, L. C., and Read, R. J. (2007). *Phaser* crystallographic software. *J. Appl. Cryst.* 40, 658–674, DOI: 10.1107/S0021889807021206.

(*278*) Adams, P. D., Afonine, P. V., Bunkóczi, G., Chen, V. B., Davis, I. W., Echols, N., Headd, J. J., Hung, L. W., Kapral, G. J., Grosse-Kunstleve, R. W., McCoy, A. J., Moriarty, N. W., Oeffner, R., Read, R. J., Richardson, D. C., Richardson, J. S., Terwilliger, T. C., and Zwart, P. H. (2010). PHENIX: a comprehensive Python-based system for macromolecular structure solution. *Acta Cryst. D*66, 213–221, DOI: 10.1107/S0907444909052925.

(*279*) Krissinel, E., and Henrick, K. (2007). Inference of macromolecular assemblies from crystalline state. *J. Mol. Biol.* 372, 774–797, DOI: 10.1016/j.jmb.2007.05.022.

(*280*) Mihel, J., Šikić, M., Tomić, S., Jeren, B., and Vlahoviček, K. PSAIA – Protein Structure and Interaction Analyzer. *BMC Struct. Biol.* [Online] **2008**, *21*, DOI: 10.1186/1472-6807-8-21, (accessed December 12, 2013).

(*281*) Takahashi, M., Takano, M., and Asada, K. (1981). Tris-induced cross-linking of thylakoid peptides; thiol oxidation catalyzed by Tris-Cu2+ complexes as a possible mechanism. *J. Biochem.* 90, 87–94.

(*282*) Koundal, K. R., Sawhney, S. K., and Sinha, S. K. (1983). Oxidation of 2-mercaptoethanol in the presence of tris buffer. *Phytochemistry* 22, 2183–2184.

(*283*) Landon, C., Thouzeau, C., Labbée, H., Bulet, P., and Vovelle, F. (2004). Solution structure of Spheniscin, a β-Defensin from the Penguin Stomach. *J. Biol. Chem.* 279, 30433–30439, DOI: 10.1074/jbc.M401338200.

(*284*) Maiti, R., van Domselaar, G. H., Zhang, H., and Wishart, D. S. (2004). SuperPose: a simple server for sophisticated structural superposition. *Nucleic Acids Res.* 32, W590–W594, DOI: 10.1093/nar/gkh477.

(*285*) Schibli, D. J., Hunter, H. N., Aseyev, V., Starner, T. D., Wiencek, J. M., McCray, P. B., Tack, B. F., and Vogel, H. J. (2002). The solution structures of the human β-defensins lead to a better understanding of the potent bactericidal activity of HBD3 against *Staphylococcus aureus*. *J. Biol. Chem.* 277, 8279–8289, DOI: 10.1074%2Fjbc.M108830200.

(*286*) Derache, C., Meudal, H., Aucagne, V., Mark, K. J., Cadène, M., Delmas, A. F., Lalmanach, A. C., and Landon, C. (2012). Initial insights into structure-activity relationships of avian defensins., English *J. Biol. Chem.* 287, 7746–7755, DOI: 10.1074/jbc.M111.312108.

(*287*) Bauer, F., Schweimer, K., Klüver, E., Conejo-Garcia, J. R., Forssmann, W. G., Rösch, P., Adermann, K., and Sticht, H. (2001). Structure determination of human and murine β-defensins reveals structural conservation in the absence of significant sequence similarity. *Protein Sci.* 10, 2470–2479, DOI: 10.1110%2Fps.24401.

(*288*) Qian, M., Haser, R., and Payan, F. (1995). Carbohydrate binding sites in a pancreatic alpha-amylase-substrate complex, derived from X-ray structure analysis at 2.1 Å resolution. *Protein Sci.* 4, 747–755, DOI: 10.1002/pro.5560040414.

(*289*) Qian, M., Spinelli, S., Driguez, H., and Payan, F. (1997). Structure of a pancreatic α-amylase bound to a substrate analogue at 2.03 Å resolution. *Protein Sci.* 6, 2285–2296, DOI: 10.1002/pro.5560061102.

(*290*) Ye, Y., and Godzik, A. (2003). Flexible structure alignment by chaining aligned fragment pairs allowing twists. *Bioinformatics* 19, ii246–ii255, DOI: 10.1093%2Fbioinformatics%2Fbtg1086.

(*291*) Prlic, A., Bliven, S., Rose, P. W., Bluhm, W. F., Bizon, C., Godzik, A., and Bourne, P. E. (2010). Pre-calculated protein structure alignments at the RCSB PDB website. *Bioinformatics* 26, 2983–2985, DOI: 10.1093/bioinformatics/btq572.

(*292*) König, V., Vértesy, L., and Schneider, T. (2003). Structure of the α-amylase inhibitor tendamistat at 0.93 Å. *Acta Cryst. D*59, 1737–1743, DOI: 10.1107/S0907444903015828.

(*293*) Qin, M., Zhang, J., and Wang, W. (2006). Effects of disulfide bonds on folding behavior and mechanism of the β-Sheet protein tendamistat. *Biophys. J.* 90, 272–286, DOI: 10.1529%2Fbiophysj.105.063552.

(*294*) Krissinel, E. (2010). Crystal contacts as nature's docking solutions. *J. Comput. Chem.* 31, 133–143, DOI: 10.1002/jcc.21303.

(*295*) Altschul, S. F., Gish, W., Miller, W., Myers, E. W., and Lipman, D. J. (1990). Basic Local Alignment Search Tool. *J. Mol. Biol.* 215, 403–410.

(*296*) Kabsch, W. (1976). A solution for the best rotation to relate two sets of vectors. *Acta Cryst. A*32, 922.

(*297*) Almeida, M. S., Cabral, K. M. S., Kurtenbach, E., Almeida, F. C. L., and Valente, A. P. (2002). Solution structure of *Pisum sativum* defensin 1 by high resolution NMR: plant defensins, identical backbone with different mechanisms of action. *J. Mol. Biol.* 315, 749–757, DOI: 10.1006/jmbi.2001.5252.

(*298*) Koropatkin, N. M., Martens, E. C., Gordon, J. I., and Smith, T. J. (2008). Starch catabolism by a prominent human gut symbiont is directed by the recognition of amylose helices. *Structure* 16, 1105–1115, DOI: 10.1016/j.str.2008.03.017.

(*299*) Gasteiger, E., Hoogland, C., Gattiker, A., Wilkins, M. R., Appel, R. D., and Bairoch, A. Protein identification and analysis tools on the ExPASy server. In *The Proteomics Protocols Handbook*; Walker, J. M., Ed.; Humana Press: Totowa, N.J., 2005; pp 571–607.

Appendix A

Enzyme Kinetics

The work in this thesis characterizes reversible inhibitors of HPA. Kinetic studies of inhibition are used to establish how well, as well as the manner in which the inhibitor impedes the enzymes activity. Enzyme kinetics is the study of the rates of enzyme-catalyzed reactions under varying conditions. The reaction rates give us information about the enzymes catalytic mechanism, and how its activity is regulated.

A.1 Michaelis-Menten Kinetics

The rate of an enzyme catalysed reaction is not a constant and depends on the concentration of the enzyme, substrate and products. The rate measured in kinetics experiments is usually the initial rate, ν_o, where the effects of products binding to the enzyme are negligible. Under this condition, the enzyme binds the substrate and transforms it into products. For a single-step, unimolecular reaction, the scheme is as follows:

$$E + S \underset{k_{-1}}{\overset{k_1}{\rightleftharpoons}} ES \xrightarrow{k_2} P + E$$

Measuring the initial reaction rates at different substrate concentrations, results in a saturation curve like that in Figure A.1. This can be used to help determine V_{max} and K_m.

The Michaelis-Menten equation (Eq. A.1) describes the dependence of the initial reaction rate on the substrate concentration. This equation assumes a steady state for the enzyme-substrate complex (i.e. $d[ES]/dt = 0$)

$$\nu_\circ = \frac{V_{max}[S]}{K_m + [S]} \tag{A.1}$$

A Lineweaver-Burk plot (Figure A.2) is a double reciprocal plot showing $1/o$ vs. $1/[S]$. Although much used, it does have the fault of compressing data at high substrate concentrations. Kinetic results are often reported in terms of an enzymes catalytic efficiency (k_{cat}/K_m) where $k_{cat} \equiv V_{max}/[E]_{total}$, and $K_m \equiv (k_{-1} + k_2)/k_1$. In the simplest case of a single step, unimolecular reaction, $k_2 = k_{cat}$.

A.2 Enzyme Inhibition

Enzyme inhibitors can be divided into two broad categories: reversible and non-reversible inhibitors. This thesis deals exclusively with reversible enzyme inhibitors. Reversible enzyme inhibition can be competitive, uncompetitive, or noncompetitive; each type of inhibition affects K_m, and V_{max} in specific ways (Table A.1).

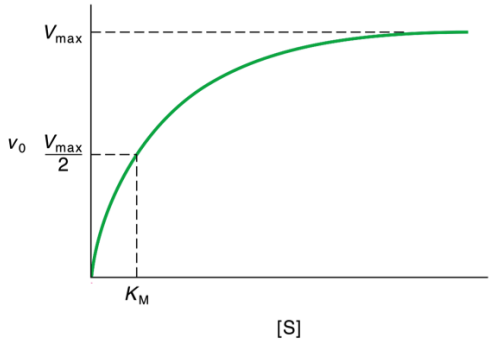

Figure A.1: Example of a Saturation Curve in an Enzyme Kinetics Experiment. The curve is extrapolated from the initial rate of many different reactions at various substrate concentrations.

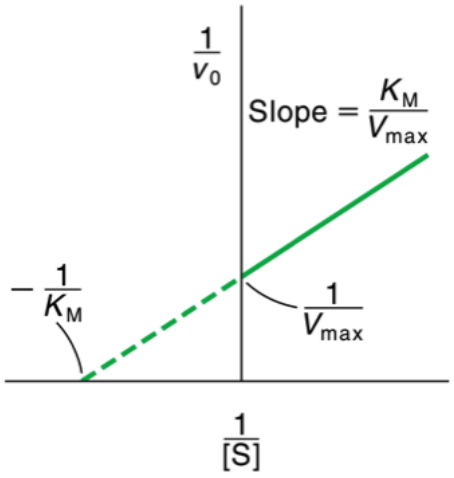

Figure A.2: Example of a Lineweaver-Burk Double Reciprocal Plot.

Table A.1: Effect of reversible inhibitors on V_{max} and K_m

	Type of inhibition			
Apparent value	Competitive	Uncompetitive	Linear Mixed	Noncompetitive
V^*_{max}	No effect	Decrease	Decrease	Decrease
K^*_m	Increase	Decrease	Increase or decrease	No effect

A.2.1 Competitive Inhibition

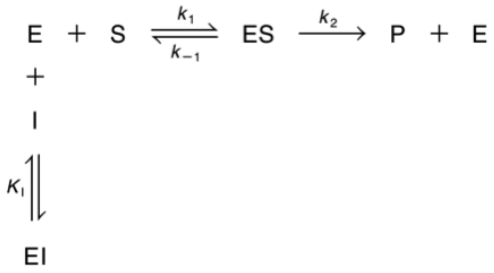

In competitive inhibition, the inhibitor competes with the substrate to bind to the enzyme. The enzyme-inhibitor complex cannot react with the substrate to form products. When we apply the steady state approximation for [ES],

$$\nu_\circ = \frac{V_{max}[S]}{K_m\left(1 + \frac{[I]}{K_i}\right) + [S]} \tag{A.2}$$

This is the same as the Michaelis Menten equation, only the K_m term has been modified by $(1+[I]/K_i)$, where $K_i = ([E][I]/[EI])$. V_{max} does not change during competitive inhibition, but the amount of substrate needed to reach

half maximum velocity (K_m) increases. A Lineweaver-Burk plot of competitive inhibition is shown in Figure A.3. Since V_{max} does not change, all of the lines from experiments at different inhibitor concentrations intercept on the y-axis.

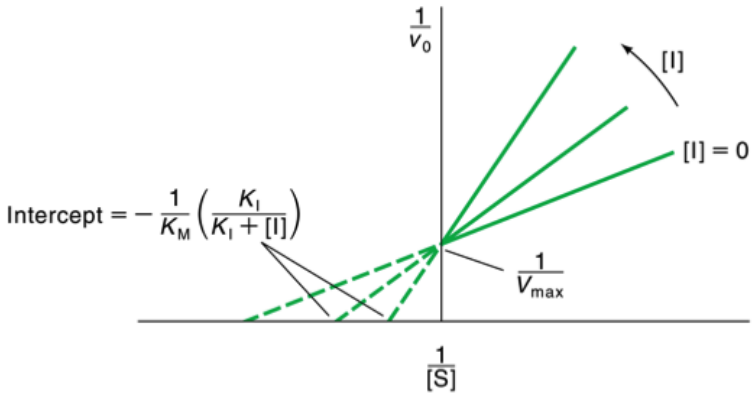

Figure A.3: Double reciprocal plot of a Competitive Inhibition Experiment.

A.2.2 Uncompetitive Inhibition

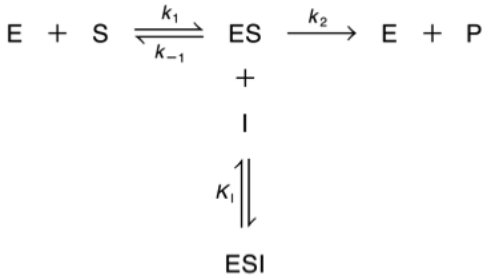

An uncompetitive inhibitor cannot bind to the free enzyme and only forms an enzyme-substrate-inhibitor complex. No product can be formed

while the inhibitor is bound. The presence of the inhibitor does not affect the formation of the enzyme-substrate complex. Equation A.3 gives the initial rate for uncompetitive inhibition:

$$\nu_\circ = \frac{\frac{V_{max}}{1+\frac{[I]}{K_i}}[S]}{\frac{K_m}{\left(1+\frac{[I]}{K_i}\right)} + [S]} \tag{A.3}$$

Here, both V_{max} and K_m are reduced by the factor $(1 + [I]/K_i)$, where $K_i = ([ES][I]/[ESI])$. In a Lineweaver-Burk plot of uncompetitive inhibition at various inhibitor concentrations shows that both V_{max} and K_m change, but the slope remains constant, producing parallel lines (Figure A.4).

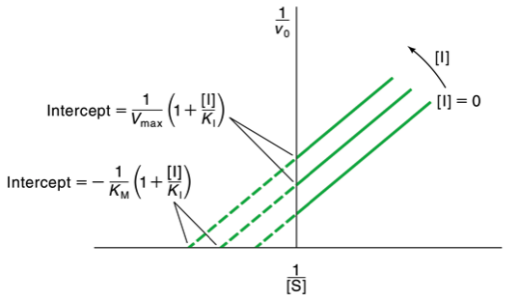

Figure A.4: Double reciprocal plot of Uncompetitive Inhibition

A.2.3 Linear Mixed Inhibition

In this type of inhibition, an inhibitor can interact with both the free enzyme and the enzyme-substrate complex. This results in an apparent decrease of V_{max}, and an apparent increase or decrease in K_m. Under steady state conditions, the initial rate is

$$\nu_\circ = \frac{\frac{V_{max}}{1+\frac{[I]}{K_i'}}[S]}{\frac{1+\frac{[I]}{K_i}}{1+\frac{[I]}{K_i'}} + [S]} \tag{A.4}$$

Here, $K_i = ([E][I])/[EI]$, $K_i' = ([ES][I]/[ESI])$ and $K_i \neq K_i'$. The appearance of a Lineweaver-Burk plot changes depending on the relationship between K_i and K_i', and does not produce a distinct pattern, as that seen for competitive and uncompetitive inhibition.

A.2.4 Noncompetitive Inhibition

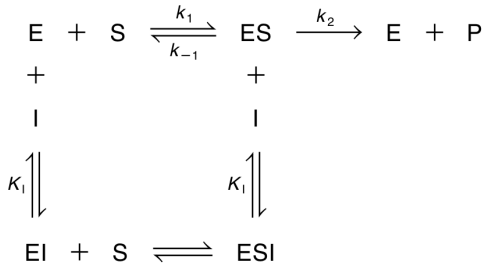

Noncompetitive inhibition is a special case of mixed inhibition where $K_i = K_i'$. A noncompetitive inhibitor can bind to either the free enzyme or the enzyme-substrate complex. The binding of either the substrate or inhibitor to the enzyme does not affect the ability of the other to bind. In this scheme, neither the EI or ESI complexes can react to form products. Unlike in competitive inhibition, where the effect of the inhibitor can be overcome by adding more substrate, this is not possible for noncompetitive inhibition, and the equation for the initial rate is altered:

$$\nu_\circ = \frac{\frac{V_{max}}{1+\frac{[I]}{K_i}}[S]}{K_m + [S]} \tag{A.5}$$

In this equation, V_{max} is reduced by a factor of $(1 + [I]/K_i)$, where $K_i = ([E][I])/[EI] = ([ES][I])/[ESI]$; K_m remains the same. If multiple experiments are carried out at different inhibitor concentrations, a distinctive Lineweaver-Burk plot is again produced. Here, all lines intersect on the x-axis (Figure A.5).

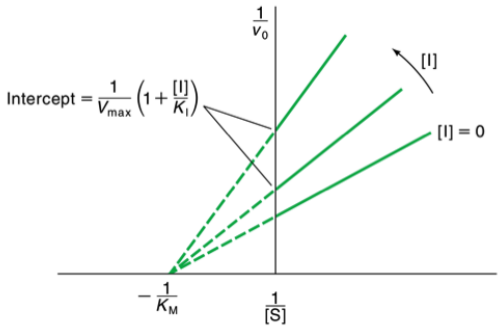

Figure A.5: Double Reciprocal Plot of a Noncompetitive Inhibition Experiment.

A.2.5 Irreversible Inhibitors

Michaelis-Menten kinetics do not apply to irreversible inhibitors. The effectrivenes of these inhibitors is not determined by equilibrium constants, such as the K_i of reversible inhibition, but by the rate at which a covalent bond between the enzyme and inhibitor forms.

Appendix B

Isolation and Crystallization Trials of Two α-Amylases from *Roseburia inulinivorans* and *Butyrivibrio fibrisolvens*

B.1 α-Amylases from *Roseburia inulinivorans* and *Butyrivibrio fibrisolvens*

The side effects associated with the clinical use of α-glucosidase inhibitors for the treatment of type II diabetes may be alleviated by the inhibition of α-amylases produced by bacteria in the human gut. Enzymes from *Roseburia inulinivorans* and *Butyrivibrio fibrisolvens* were chosen as models for MbA inhibition of bacterial α-amylases.

Amy13A from *R. inulinivorans* and Amy13B from *B. fibrisolvens* are approximately three times the size of HPA (more than 150 kDa vs. 52 kDa) and are associated with the bacterial cell wall (*260*). Analysis of the amino acid sequence of each of these enzymes has revealed that both have several modules that include a signal peptide, a catalytic domain homologous to domain A of HPA, and a C-terminal module that includes a sortase sig-

nal indicating that it should be attached to the cell's peptidoglycan wall. Previous structural studies have concentrated on the Gram negative *Bacteriodes thetaiotaomicron* (*298*). This would thus be the first structural glimpse of starch processing in Gram positive *Firmicutes*.

B.1.1 Isolation of Amy13A from *Roseburia inulinivorans*

50 μL of *Escherichia coli* BL21 cell stock was mixed with 1 μL of a solution of the pet30 plasmid carrying the *R. inulinivorans* Amy13A gene (10 ng/μl). The cells were electroporated (2.5 kvolt, 400 Ω, 25 μF) then transferred to 1 ml of LB medium (1% tryptone (w/v), 0.5% yeast extract (w/v), 1% NaCl (w/v), pH 7.0) and allowed to incubate for 1 hour at 37°C. They were then plated on agar plates inoculated with kanamycin (50 mg/ml). After this first hour, the cultures were scaled up to 50 ml, and 50 μl of kanamycin was added to each flask. These were allowed to incubate at 37°C overnight.

The next day, the 7 ml of these small cultures were transferred to 700 ml LB medium, and 700 μl kanamycin, and then incubated at 30°C and 225 rpm for 6 hours. At this point, 700 μl IPTG solution (100 mM) was added to each flask and the cells were allowed to grow overnight at 30°C and 225 rpm. The cells were then centrifuged for 30 minutes at 5000 rpm and 4°C. The supernatant was discarded and the cell pellets were frozen at -80°C.

Four days later, the cells were resuspended in 15 ml of binding buffer (20 mM Tris, pH 8.0; 500 mM NaCl; 5 mM imidazole, pH 8.0), and 4 μl of

benzonase was added before using the french press to lyse the cells. After lysing, 35 ml of binding buffer was added and the lysate was centrifuged for 40 minutes at 15000 rpm and 4°C. The supernatant was collected and the cells were discarded. A GE HisTrapFF column was used in conjunction with an AKTA system to purify the protein (binding buffer: 50 mM sodium phosphate, pH 8.0, 5 mM imidazole, 0.5 M NaCl; elution buffer: 50 mM sodium phosphate, pH 8.0, 500 mM imidazole, 0.3 M NaCl). Protein purity was checked using SDS-PAGE (figure B.1), and the protein was transferred to a storage buffer (50 mM sodium phosphate, 20 mM NaCl, 1 mM CaCl2, pH 7.0). This sample was then concentrated to 12 mg/ml with the protein concentration being determined by absorbance at 280 nm. The extinction coefficient was generated by Protparam (*299*).

B.1.2 Isolation of Amy13B from *Butyrivibrio fibrisolvens*

The same procedure was used to isolate Amy 13A from *Roseburia inulinivorans* (section B.1.1) and Amy13B from *Butyrivibrio fibrisolvens*. After purification with the HisTrap column, a protein contaminant remained in the solution, but the Amy13B was still active. This sample also produced a brown precipitate when concentrated. I attempted to remove the rogue protein using Q-sepharose, phenyl-sepharose and cobalt columns. While the cobalt column removed more contaminant than either of the others, the mixture was still unsuitable for crystallization trials. Throughout this

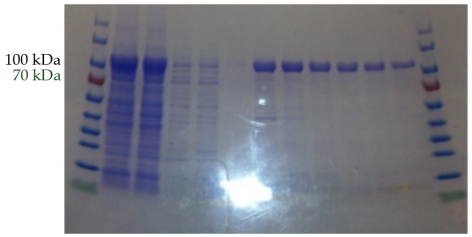

(a) Amy13A

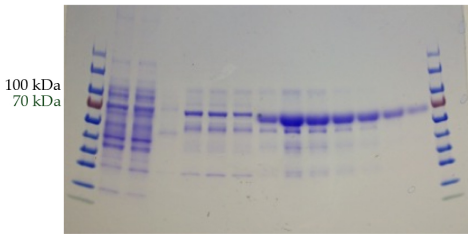

(b) Amy13B

Lane	(a) Amy13A	(b) Amy13B
1	ladder	
2	flowthrough	
3	flowthrough	
4	fraction 8	fraction 1
5	fraction 9	fraction 9
6	fraction 19	fraction 10
7	fraction 22	fraction 11
8	fraction 24	fraction 17
9	fraction 28	fraction 18
10	fraction 31 *	fraction 19
11	fraction 34 *	fraction 20
12	fraction 38 *	fraction 21
13	ladder	fraction 24 *
14		fraction 32 *
15		ladder

Figure B.1: SDS-PAGE of Amy13A and Amy13B. Both purifications used a 5ml HisTrap FF column. Lanes 2 and 3 are what eluted from the column after rinsing the with 10 ml (Lane 1) and 50 ml (Lane 2) of 20mM imidazole. Fractions 31-42 of Amy13A, and 24-34 of Amy13B were collected for crystallographic study.

process, Amy13B activity decreased at a fairly steady rate until the sample had to be discarded.

Some of the cells from the agar plates had been frozen for future use. These were then grown and the expression and purification protocol repeated. This time the contaminant was not present, and the HisTrap column succeeded in purifying the mixture (Figure B.1). The sample was then transferred to the storage buffer (50 mM sodium phosphate, 20 mM NaCl, 1 mM $CaCl_2$, pH 7.0) to be used for crystallization trials.

B.1.3 Crystallization Trials of Amy13A and Amy13B

Crystallization trials were begun to determine the three dimensional structures of Amy13A from *R. inulinivorans* and Amy13B from *B. fibrisolvens*. The proteins were stored in a buffer consisting of 50 mM sodium phosphate, 20 mM NaCl, 1mM CaCl2, pH 7.0. To begin crystallization trials, the buffer was changed to 50 mM sodium cacodylate and 1 mM $CaCl_2$, pH 7.0 and the enzymes were concentrated in this new buffer until A280 readings indicated that they were at 13 mg/ml (Amy13A) and 9.8 mg/ml (Amy13B). The Amy13B solution would produce a brown precipitate if concentrated beyond 10 mg/ml in either the phosphate or cacodylate buffer. Screening was performed using the sitting drop vapour diffusion method in 96 well plates. Screening kits based upon Crystal Screen I and Crystal Screen II (Hampton Research) and Wizard I, Wizard II and Wizard III (Emerald Biosystems) and prepared by Nham Nguyen were used as start-

ing conditions. The sitting drops contained 1 μl of protein solution and 1 μl of crystallization medium from the screening kit and the wells were filled with 100 μl of this same medium. Each drop was produced in duplicate and sealed within the same well. The most promising condition for both enzymes after allowing the plates to equilibrate for one month consisted of 0.05 M cesium chloride, 0.1 M MES monohydrate, pH 6.5 and 30% (v/v) Jeffamine M-600 which produced small clusters of crystals. A grid search around these conditions, varying the Jeffamine M-600 concentration from 16-40%, or the pH in 0.1 unit increments from 5.9-7.1. The protein remained in the cacodylate buffer. The volume of the components was scaled up so that the final drop was 4 μl with the protein and mother liquor solutions in a 1:1 (v/v) ratio. The amount of solution in each well was increased to 1 ml. These screens did not result in any crystals of Amy13A.

The Amy13B samples also crystallized into 2-dimensional plates in an unbuffered solution of 35% (v/v)1,4-dioxane. These formed over two weeks, gradually incorporating protein that precipitated when the 1,4-dioxane was first added. Again a grid screen was carried out, increasing the precipitant concentration to coax the crystals into 3-dimensional form. The amount of 1,4-dioxane was varied from 35% to 60% in 2% increments. These drops contained 2 μl of mother liquor and 2 μl of Amy13B solution. All of these drops produced a yellow or brown precipitate, but none re-

sulted in diffraction quality crystals. Further screening and optimization will be needed to obtain crystals of WT Amy13A and Amy13B.